

UNIVERSIDAD NACIONAL DE COLOMBIA

SEDE MEDELLÍN
FACULTAD DE MINAS

SYNTHESIS OF CALCIUM SILICATES BY FLAME SPRAY PYROLYSIS

Natalia Betancur-Granados

Universidad Nacional de Colombia
School of Mines
Department of Materials and Minerals
Medellin, Colombia

2019

SYNTHESIS OF CALCIUM SILICATES BY FLAME SPRAY PYROLYSIS

Natalia Betancur-Granados

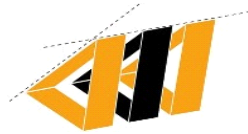
**A dissertation submitted in partial fulfillment
of the requirements of the degree of
Doctor of Engineering in Materials Science and Technology**

Advisor:

Oscar Jaime Restrepo Baena, Ph.D.

Co-advisor

Jorge Iván Tobón, Ph.D.



Group of Cement and Building Materials

School of Mines

Department of Materials and Minerals

Medellin, Colombia

2019

Acknowledgements

I would like to express my sincere gratitude to my advisor Oscar Jaime Restrepo Baena for his accompaniment, support and patience during all my graduate studies. I also thank to my co-advisor Jorge Iván Tobón for his guidance and support during my doctoral studies.

I specially thank to Sergio Medina for all his unfailing academic, moral and emotional support during all this process. This thesis would not be the same without your support

I am grateful to Juan José Toro, Doña Mery, Valeria Medina, Oscar Zapata, Andrés Pinto, Weimar Ávila and Yeisson Vahos for all their help during my experimentation and all my friends, including them, for making this time more bearable.

A very special gratitude for Professors Santiago Franco, from the Organic Chemistry Department in the Universidad de Zaragoza-Spain, Professor Herbert Pöllmann from the Institute of Geosciences and Geography in the Martin-Luther Universität-Germany and Professor Steven Tidrow from the Kazuo Inamori School of Engineering of Alfred University-United States for received me in their research groups and gave me their support and guidance during my internships. I would like to thank to Professor Juan Maria Menendez from the Universidad de Oviedo for the morphological measurements provided.

I would like to thank all the people in the Organic Chemistry Department in the Universidad de Zaragoza-Spain, who patiently taught me to work in their laboratories and shared with me long interesting talks.

I would like to thank all the people who helped me in the Martin-Luther Universität. I am very thankful with Frau Gabriele Kummer, Frau Diana Becher, Juri Buchantschenko and all the members of the group of Mineralogie for all their help, patience and accompaniment. I am especially grateful with the “petrology team” who fill me with coffee every day and made my time in Germany more amusing and entertaining.

I must express my very deep gratitude to my family for their emotional support and understanding my little presence all these years.

Finally, I would like to acknowledge the program *Enlaza Mundos 2018* and the *Agencia Española de Cooperación Internacional para el Desarrollo y al Ministerio de Asuntos Exteriores y de Cooperación*, for their financial support for my internships; and to COLCIENCIAS for my doctoral scholarship (call 647 of 2014).

Declaration of originality

I, Natalia Betancur-Granados, declare that:

- i)** The thesis presented for the degree of Doctor in Engineering: Material Science and Technology has been composed entirely by me.
- ii)** The thesis has not been submitted for any other degree or professional qualification.
- iii)** The figures were by own elaboration, except where states otherwise by reference or acknowledgment.
- iv)** All data and references to texts, research, books, journals, thesis, among others, already published, are properly referenced and cited.
- v)** The work presented in Chapter 2 was previously published in Civil Engineering Research Journal as “Alternative Production Processes of Calcium Silicate Phases of Portland Cement: A Review” by Natalia Betancur-Granados, Jorge Iván Tobón and Oscar Jaime Restrepo Baena. This study was conceived by all of the authors.
- vi)** The work presented in Chapter 3, Section 3.1.2.2, was previously published in Ceramics International as “Dicalcium silicate ($2\text{CaO}\cdot\text{SiO}_2$) synthesized through Flame Spray Pyrolysis and Solution Combustion Synthesis methods” by Natalia Betancur-Granados, Juan Camilo Restrepo, Jorge Iván Tobón and Oscar Jaime Restrepo Baena. This study was conceived by all of the authors.

RESUMEN

El cemento Portland es un material de construcción tradicionalmente obtenido por la calcinación hasta fusión parcial de piedra caliza, arcillas y correctores para obtener clinker, el cual se combina con una fuente de sulfato de calcio para dar lugar al cemento. El clinker se compone de silicatos de calcio (Ca_3SiO_5 y Ca_2SiO_4) y aluminatos de calcio ($\text{Ca}_3\text{Al}_2\text{O}_6$ y $\text{Ca}_4\text{Al}_2\text{Fe}_2\text{O}_{10}$). Las fases de silicato de calcio son responsables del desarrollo de propiedades mecánicas, como resistencia a la compresión, por lo que varias investigaciones se han desarrollado para comprender sus características y propiedades.

Entender las propiedades de los silicatos de calcio de tamaño nanométrico es de gran importancia dada la posibilidad de obtener materiales altamente reactivos que permitan reducir el consumo energético y los impactos negativos generados durante la producción del cemento. Un método importante para la fabricación de nanopartículas es pirólisis de aerosol en llama (FSP), el cual permite controlar las características de las partículas mediante la manipulación de los parámetros del proceso.

En esta tesis se presenta el estudio exploratorio de los efectos de algunas de las condiciones intrínsecas y extrínsecas del proceso pirólisis de aerosol en llama y su influencia sobre las características y propiedades de las partículas, durante la producción de silicato dicálcico como una de las fases principales del cemento Portland. Las propiedades de los silicatos dicálcicos producidos se evaluaron como fases de interés en la industria del cemento. Durante los procesos de síntesis, los precursores metalorgánicos se disolvieron en mezclas de disolventes orgánico-inorgánico, obteniendo la solución de partida. La solución se dirigió hacia una llama de oxi-acetileno, dando como resultado la evaporación y posterior reacción de los precursores. Finalmente, los productos se colectaron en un precipitador electrostático. Los parámetros evaluados durante los procedimientos de síntesis fueron la carga cerámica de la solución, el gas de dispersión, la presión del gas de dispersión, el flujo de los precursores y el disolvente, utilizando un diseño de experimentos tipo factorial fraccionado de dos niveles con resolución III, 2^{5-2}_{III} , el cual permite estudiar los efectos principales y su interacción.

Las respuestas evaluadas fueron la composición mineralógica obtenida mediante el método de Rietveld, el área superficial específica y la liberación de flujo de calor de las muestras durante la reacción de hidratación. Las muestras anhidras se caracterizaron por difracción de rayos x (XRD), espectroscopia infrarroja con transformada de Fourier (FT-IR), análisis térmico acoplado a espectrometría de masas (TGA-DSC/MS-IR), análisis BET por adsorción-desorción de nitrógeno, microscopia electrónica de barrido (SEM), microscopía electrónica de transmisión (TEM) y calorimetría, mientras que las muestras hidratadas se caracterizaron por XRD, SEM y TEM.

Los resultados obtenidos permiten demostrar la influencia de las condiciones del proceso sobre la mineralogía y el comportamiento hidráulico de las muestras. La aplicación de un diseño de experimentos permitió observar cuáles parámetros tienen más importancia en las características de los productos y se obtuvo una tendencia de las condiciones intrínsecas y extrínsecas del proceso. Aplicando estos resultados fue posible tener una metodología para producir nanopartículas de silicatos dicálcicos con propiedades hidráulicas, desarrollando la reacción de hidratación en 24 horas después del contacto con agua, lo cual podría ser escalado a altos volúmenes de producción.

ABSTRACT

Portland cement is a construction material traditionally obtained by the calcination until partial fusion of limestone, clays and correctors to obtain clinker, which is combine with a source of calcium sulfate to produce cement. Clinker is composed by calcium silicates (Ca_3SiO_5 and Ca_2SiO_4) and calcium aluminates ($\text{Ca}_3\text{Al}_2\text{O}_6$ and $\text{Ca}_4\text{Al}_2\text{Fe}_2\text{O}_{10}$). These calcium silicate phases are responsible of the development of mechanical properties, such as compressive strength; therefore, several research have been developed to understand its features and properties.

Understand the properties of nanosized calcium silicates are very important since the possibility to obtain highly-reactive materials which allow the reduction of the energy consumption and negative impacts of production in cement. An important method to manufacture the nanoparticles is by flame spray pyrolysis (FSP), which allows the control of the particles features by controlling the process parameters.

In this thesis is presented the study of the effects of some intrinsic and extrinsic conditions of the process and their influence over the particle features and properties, during the production of dicalcium silicate, as one of the main phases of Portland cement. The properties of dicalcium silicates phases were evaluated as phases of interest in the cement industry. During the synthesis processes, metallorganic precursors were dissolved in organic-inorganic mixtures of solvents, obtaining the starting solution. The solution was sprayed in a premixed oxy-acetylene flame, resulting in the evaporation and subsequent reaction of the precursors. Finally, the powders were manually collected in an electrostatic precipitator. The parameters evaluated during the synthesis procedures were the ceramic loading of the starting solution, dispersion gas, pressure of dispersion gas, precursors flow rate and solvent, using an experimental design of two-levels fractional factorial design with resolution III, 2^{5-2}_{III} , allowing to study the main effects and their interaction.

The responses evaluated were the mineralogical composition obtained by Rietveld refinement, the specific surface area and the heat flow release of the samples during the hydration reaction. The anhydrous samples were characterized by XRD, FT-IR, TGA-DSC/MS-IR, nitrogen adsorption-desorption BET, SEM, TEM and calorimetry, while hydrated samples were characterized by XRD, SEM and TEM.

Results show a strong influence of the process conditions over the mineralogy and hydraulic behavior of the samples. The application of experimental designs allowed to observe which parameters have more significance in the features of the products, and a tendency of the intrinsic and extrinsic conditions of the process were obtained. Applying these results was possible to have a methodology to produce nanoparticles of dicalcium silicates with hydraulic properties, developing the hydration reaction in 24 hours after contact with water, which could be scale-up to high volumes of production.

Academic products

Publications in journals

1. Pinto A. F, Tobón J. I, *Betancur-Granados N*, Restrepo-Baena O. J. "Evaluation of the reactivity of artificial mixtures of Portland cement clinker obtained by flame spray pyrolysis". *Mat. Sci. Res. India*; 16 (2), 2019.
2. *N. Betancur-Granados*, J. C. Restrepo, J. I. Tobón, O. J. Restrepo-Baena. "Dicalcium Silicate ($2\text{CaO}\cdot\text{SiO}_2$) Synthesized through Flame Spray Pyrolysis and Solution Combustion Synthesis Methods (CB-6:IL10)." *Ceram. Int.*, no. July, pp. 1–7, 2018.
3. *N. Betancur-Granados*, J. I. Tobón, O. J. Restrepo-Baena. "Alternative Production Processes of Calcium Silicate Phases of Portland Alternative Production Processes of Calcium Silicate Phases of Portland Cement: A Review." *Civil Engineering Research Journal* 5(3): 1–6, 2018.
4. *N. Betancur-Granados*, O. J. Restrepo-Baena. "Flame Spray Pyrolysis Synthesis of Ceramic Nanopigments CoCr_2O_4 : The Effect of Key Variables." *Journal of the European Ceramic Society* 37(15): 5051–56, 2017.

Publication in proceedings

1. *N. Betancur-Granados*, J. I. Tobón, O. J. Restrepo "C₃S and C₂S nanoparticles synthesized by flame spray pyrolysis (FSP)" *Proceeding of International Congress on the Chemistry of Cement, Czech Republic, September 16 – 20, 2019.*
2. J. C. Restrepo, *N. Betancur-Granados*, J. I. Tobón, O. J. Restrepo "Hydraulic reactivity of calcium silicates synthesized by combustion in solution – SCS" *Proceeding of International Congress on the Chemistry of Cement, Czech Republic, September 16 – 20, 2019.*

Conferences

1. **Poster presentation:** *N. Betancur-Granados*, A. F. Pinto, N. Marín, J. I. Tobón, O. J. Restrepo "Study of the formation of tricalcium silicate after thermal treatments of particles made by flame spray pyrolysis" X Congreso Internacional de Materiales - CIM 2019, Bucaramanga, Colombia
2. **Poster presentation:** *N. Betancur-Granados*, N. Marín, H. A. Estupiñan, J. I. Tobón, O. J. Restrepo, "Synthesis of tricalcium aluminate through the alternative method flame spray pyrolysis" X Congreso Internacional de Materiales - CIM 2019, Bucaramanga, Colombia.
3. **Oral presentation:** W. D. Avila, *N. Betancur-Granados*, J. I. Tobón, O. J. Restrepo-Baena "Evaluación de la adición de nanopartículas de silicatos dicálcicos obtenidos por el método de Pirólisis" X Congreso Internacional de Materiales - CIM 2019, Bucaramanga, Colombia
4. **Poster presentation:** *N. Betancur-Granados*, J. I. Tobón, O. J. Restrepo "C₃S and C₂S nanoparticles synthesized by flame spray pyrolysis (FSP)" *International Congress on the Chemistry of Cement, Czech Republic, September 16 – 20, 2019.*

5. **Poster presentation:** J. C. Restrepo, N. Betancur-Granados, J. I. Tobón, O. J. Restrepo "Hydraulic reactivity of calcium silicates synthesized by combustion in solution – SCS" International Congress on the Chemistry of Cement, Czech Republic, September 16 – 20, 2019.
6. **Poster presentation:** N. Betancur-Granados, H. Pöllmann, J.I. Tobón, O.J. Restrepo-Baena. "Nanosized calcium silicate phases of Portland cement: assessment of synthesis conditions by flame spray pyrolysis" in 6th Nano Today Conference. Lisbon-Portugal, June 16-20, 2019.
7. **Oral Presentation:** N. Betancur Granados, J. I. Tobón, O. J. Restrepo Baena. "Estudio de la hidraulicidad de silicatos dicálcicos realizados mediante el método alternativo de pirólisis de aerosol en llama (FSP)" XIV SIMPOSIO INTERNACIONAL DE ENERGÍAS, Institución Universitaria Pascual Bravo - Sede Robledo. Medellín-Colombia, October 25-26, 2018.
8. **Oral Presentation:** A. F. Pinto, J. I. Tobón, O. J. Restrepo Baena, N. Betancur-Granados. "Evaluación de la reactividad de mezclas artificiales de Clinker de cemento Portland obtenidas mediante Pirolisis de aerosol en llama". XIV SIMPOSIO INTERNACIONAL DE ENERGÍAS, Institución Universitaria Pascual Bravo - Sede Robledo. Medellín-Colombia, October 25-26, 2018.
9. **Oral Presentation:** N. Betancur-Granados, J. C. Restrepo, O. J. Restrepo Baena. "Alternative Methods of Synthesis of Calcium Silicates" 14th International ceramics congress CIMTEC 2018. Perugia, Italia, June 4-8, 2018
10. **Poster presentation:** N. Betancur-Granados, J. I. Tobón, O. J. Restrepo Baena. "Síntesis de nanopartículas usando el proceso de pirolisis de aerosol con llama (FSP)". IX Congreso Internacional de Materiales – CIM 2017. Barranquilla, Colombia. November 14-16, 2017.
11. **Poster presentation:** N. Betancur Granados, O. J. Restrepo Baena. "Synthesis and characterization of the CoCr_2O_4 spinel structure made by Flame Spray Pyrolysis (FSP)" International Meeting on Ferroelectricity IMF 2017. San Antonio, United States of America, September 4- 8, 2017.
12. **Poster presentation:** N. Betancur Granados, O. J. Restrepo Baena. "Synthesis of the ceramic pigment zinc chromite, ZnCr_2O_4 , through the alternative method in flame reaction and the traditional ceramic route" International Congress on Metallurgy and Materials CONAMET/SAM. Concepción, Chile. November 17-20, 2015.

Attendance of courses and seminars

1. Cuantificación de fases por el método Rietveld. Grupo del cemento y materiales de Construcción. Universidad Nacional de Colombia. August, 2018 .
2. Difracción de polvo de Rayos-X y el método de Rietveld aplicado en el sector cementero. X-Ray Data Services S.L. Rietveld. Universidad de Málaga - Spain, March, 2018.
3. Frontiers in Physical Sciences. Organized by International Center for Advanced Studies (ICAS) and the Max Planck Liason Office for Latin America. Buenos Aires - Argentina, November, 2016.
4. Bio-inspired materials. Organized by CONAMET/SAM, Universidad de Concepción. Concepción – Chile, November, 2015.
5. Advanced School on Glasses and Glass-ceramics. Organized by CeRTEVin, Universidade de São Paulo. São Carlos - Brazil, August, 2015.

Internships

1. Alfred University, New York, United States of America. September 1 – October 31, 2019.
2. Martin-Luther-Universität Halle-Wittenberg, Germany. Institute of Geosciences and Geography. Project: “Calcium silicate materials made by flame spray pyrolysis”. December 3, 2018- June 30, 2019.
3. Universidad de Zaragoza, Spain. Organic Chemistry Department-Institute of Materials Science of Aragon. Electro and Photoactive Molecular Materials, Research group. Project: “*Síntesis orgánica de materiales transportadores de huecos*” January – June, 2015.

Projects

1. Research in Project “*Fabricación de silicatos dicálcicos del cemento portland mediante pirólisis de aerosol en llama*”. Uniminuto - Universidad Nacional de Colombia sede Medellín. 12 Months, 2019- 2020.
2. Research in Project “*Producción de silicatos cálcicos para la industria del cemento por medio de Pirólisis de aerosol en llama*”. Fundación para la Promoción de la Investigación y la Tecnología (FPIT) – Banco de la República agreement 201716- Universidad Nacional de Colombia sede Medellín. 12 Months, 2018- 2019.
3. Research in Project “*Diseño, construcción y puesta a punto del equipo FSP para la síntesis de nanopartículas: Escalamiento del proceso de pirólisis de aerosol en llama*” Prototypes project 37005, Universidad Nacional de Colombia sede Medellín. 12 Months, 2017-2018

Grants or honors

1. Distinction “Cruz del Carbón” Resolution N° 3987 (August 24 of 2019) awarded by the Mayor of Amagá. 2019.
2. Scholarship Enlaza Mundos 2018 awarded by SAPIENCIA program and the Mayor of Medellín, 2018.
3. Best Speaker Award. XIV Simposio Internacional de Energías, Institución Universitaria Pascual Bravo - Sede Robledo. Medellín-Colombia, October 25-26, 2018.
4. “University and Scientific Cooperation for Development” scholarship, awarded by Agencia Española de Cooperación Internacional para el Desarrollo y al Ministerio de Asuntos Exteriores y de Cooperación, Spain, 2015.
5. Best Poster design award. International Congress on Metallurgy and Materials CONAMET/SAM. Concepción, Chile. November, 17-20, 2015.
6. COLCIENCIAS scholarship (call 647 of 2014), “National Doctorate Scholarship”, awarded by Sistema Nacional de Ciencia, Tecnología e Innovación, Colombia, 2015.

CONTENTS

ACKNOWLEDGEMENTS	5
DECLARATION OF ORIGINALITY	6
RESUMEN	7
ABSTRACT	8
ACADEMIC PRODUCTS	9
CONTENTS	12
LIST OF FIGURES	15
LIST OF TABLES	18
CHAPTER 1. INTRODUCTION	20
CHAPTER 2. CALCIUM SILICATES	22
2.1. CALCIUM SILICATE PHASES OF PORTLAND CEMENT	22
2.1.1. TRICALCIUM SILICATE	23
2.1.2. DICALCIUM SILICATE	24
2.2. SYNTHESIS OF CALCIUM SILICATE PHASES	25
CHAPTER 3. FLAME SPRAY PYROLYSIS	30
3.1. FLAME SPRAY PYROLYSIS METHOD.....	30
3.1.1. STARTING SOLUTION FOR FSP	31
3.1.2. FSP EQUIPMENT	32
3.1.3. EFFECTS OF SYNTHESIS CONDITIONS	38
3.2. PARTICLE FORMATION IN FLAME.....	42
3.2.1. EVAPORATION, DECOMPOSITION AND REACTION.....	42
3.2.2. NUCLEATION	44
3.2.3. SURFACE GROWTH.....	46
CHAPTER 4. FSP EQUIPMENT DESIGN AND CONSTRUCTION	49

4.1. SET-UP OF THE EQUIPMENT	49
4.1.1. AEROSOL SYSTEM DESIGN AND CONSTRUCTION	49
4.1.2. BURNER SYSTEM DESIGN AND CONSTRUCTION.....	54
4.1.3. ELECTROSTATIC PRECIPITATOR DESIGN AND CONSTRUCTION	57
4.1.4. DESIGN OF ADDITIONAL ELEMENTS IN THE REACTOR.....	58

CHAPTER 5. MATERIALS AND METHODS..... 61

5.1. METHODOLOGY.....	61
5.2. PRECURSORS	62
5.2.1. TETRAETHYL ORTHOSILICATE.....	63
5.2.2. CALCIUM 2-ETHYLHEXANOATE.....	64
5.2.3. CALCIUM PROPIONATE.....	66
5.2.4. CALCIUM NITRATE TETRAHYDRATE	67
5.2.5. TRIETHANOLAMINE.....	67
5.2.6. SOLVENTS.....	68
5.3. CHARACTERIZATION TECHNIQUES	68
5.4. SET-UP OF THE SYNTHESIS PROCESS.....	69
5.4.1. STARTING SOLUTION PREPARATION.....	70
5.4.2. GENERAL SYNTHESIS PROCEDURE	71
5.4.3. RESULTS OF THE EVALUATION OF DIFFERENT CHEMICAL SYSTEMS.....	72
5.5. EXPERIMENTAL DESIGN.....	78

CHAPTER 6. CALCIUM SILICATES OBTAINED BY FLAME SPRAY PYROLYSIS 82

6.1. MINERALOGICAL COMPOSITION.....	82
6.2. DEGREE OF REACTIVITY	93
6.3. MORPHOLOGICAL CHARACTERIZATION	100
6.4. DISCUSSION	111

CHAPTER 7. EFFECTS OF THE OPERATION VARIABLES ON THE CALCIUM SILICATE PROPERTIES..... 116

7.1. EFFECTS ON MINERALOGICAL, PHYSICAL AND CHEMICAL RESPONSES	116
7.2. OPTIMIZATION OF THE RESPONSES	124
7.3. CORRELATION BETWEEN THE RESPONSES.....	126
7.4. DISCUSSION	129

CHAPTER 8. FORMATION OF CALCIUM SILICATES BY FLAME SPRAY PYROLYSIS 133

8.1. MECHANISM OF FORMATION OF CALCIUM SILICATES BY FSP.....	133
--	-----

8.2. METHODOLOGY OF SYNTHESIS CONDITIONS IN FLAME SPRAY PYROLYSIS.....	140
CHAPTER 9. CONCLUSIONS AND FUTURE WORK	143
9.1. CONCLUSIONS.....	143
9.2. RECOMMENDATIONS.....	144
CHAPTER 10. ANNEXES.....	146
10.1. RATIO OF COMBUSTION GASES	146
10.2. PHOTOGRAPHIC RECORD OF THE BUILDING AND USE OF THE FSP EQUIPMENT	147
10.3. RIETVELD REFINEMENT DURING THE EVALUATION OF DIFFERENT CHEMICAL SYSTEMS.....	150
10.4. DIFFRACTOGRAMS OF RIETVELD REFINEMENT OF CALCIUM SILICATES BY FSP AS-PREPARED.....	151
10.5. DIFFRACTOGRAMS OF RIETVELD REFINEMENT OF CALCIUM SILICATES BY FSP WITH INTERNAL STANDARD.....	152
10.6. ASSUMPTIONS OF THE ANALYSIS OF VARIANCE (ANOVA)	153
10.6.1. POLYMORPHS OF BELITE.....	153
10.6.2. AMORPHOUS	154
10.6.3. SECONDARY PHASES	155
10.6.4. SPECIFIC SURFACE AREA	156
10.6.5. P1 – CUMULATIVE HEAT FLOW	157
10.6.6. P2 – CUMULATIVE HEAT FLOW	158
10.6.7. P1 – MAX HEIGHT.....	159
10.6.8. P2 – MAX HEIGHT.....	160
REFERENCES.....	161

List of figures

FIGURE 2-1. TRICALCIUM SILICATE POLYMORPHIC TRANSFORMATIONS	23
FIGURE 2-2. DICALCIUM SILICATE POLYMORPHIC TRANSFORMATIONS.....	24
FIGURE 2-3. SOL-GEL SYNTHESIS PROCEDURE	26
FIGURE 2-4. SOLUTION COMBUSTION SYNTHESIS PROCEDURE	27
FIGURE 2-5. FLAME SPRAY PYROLYSIS SYNTHESIS PROCEDURE	28
FIGURE 3-1. SCHEME OF FLAME SPRAY PYROLYSIS SYSTEM	32
FIGURE 3-2. OXY-ACETYLENE FLAME TYPES.....	35
FIGURE 3-3. COMPILATION OF EFFECTS OF SYNTHESIS CONDITIONS. DATA FOR FEED FLOW RATE FROM [108], [113], [125]–[127], FOR FLOW RATE OF DISPERSION GAS FROM [72], [84], [106], [125] AND FOR CONCENTRATION FROM [128]–[130].	38
FIGURE 3-4. MECHANISMS OF PARTICLE FORMATION DURING FSP (ADAPTED FROM [70])	42
FIGURE 4-1. ATOMIZATION NOZZLE USED DURING IN THE FLAME SPRAY PYROLYSIS SYNTHESIS	50
FIGURE 4-2. MAIN DIMENSIONS OF THE AIRBLAST NOZZLE	50
FIGURE 4-3. INTERNAL NOZZLE TO CONDUCT THE STREAM OF LIQUID	51
FIGURE 4-4. SPRAY CONE	54
FIGURE 4-5. DUAL-FLAME BURNER.....	55
FIGURE 4-6. DISTANCE BETWEEN THE TIPS IN THE DUAL-FLAME BURNER.....	56
FIGURE 4-7. SUPPORTS OF THE WELDING HANDLES AND NOZZLE.....	56
FIGURE 4-8. SCHEMA OF THE ELECTROSTATIC PRECIPITATOR (ESP).....	58
FIGURE 4-9. PRIMARY BURNING ZONE	58
FIGURE 4-10. FRAME OF THE FSP EQUIPMENT	59
FIGURE 4-11. COOLING SYSTEM IN THE FSP EQUIPMENT	59
FIGURE 4-12. SCHEMA OF THE FSP EQUIPMENT FOR THE SYNTHESIS OF NANOPARTICLES.....	60
FIGURE 4-13. IMAGE OF THE FSP EQUIPMENT FOR THE SYNTHESIS OF NANOPARTICLES	60
FIGURE 5-1. METHODOLOGY OF THE EXPERIMENTAL SECTION OF THE PROJECT	62
FIGURE 5-2. TETRAETHYL ORTHOSILICATE STRUCTURE	63
FIGURE 5-3. CALCIUM 2-ETHYLHEXANOATE STRUCTURE	64
FIGURE 5-4. SYNTHESIS OF CALCIUM 2-ETHYLHEXANOATE.....	65
FIGURE 5-5. FT-IR SPECTRUM OF CALCIUM 2-ETHYLHEXANOATE.....	65
FIGURE 5-6. DSC-TGA CURVE OF CALCIUM 2-ETHYLHEXANOATE.....	66
FIGURE 5-7. CALCIUM PROPIONATE STRUCTURE	66
FIGURE 5-8. GENERAL SYNTHESIS PROCEDURE.....	71
FIGURE 5-9. XRD PATTERNS DURING THE EVALUATION OF DIFFERENT CHEMICAL SYSTEMS.....	72
FIGURE 5-10. FT-IR SPECTRA DURING THE EVALUATION OF DIFFERENT CHEMICAL SYSTEMS	73
FIGURE 5-11. CALORIMETRY MEASUREMENTS OF THE CHEMICAL SYSTEMS EVALUATED.....	76
FIGURE 5-12. XRD PATTERNS OF HYDRATED SAMPLES USING DIFFERENT CHEMICAL SYSTEMS.....	76
FIGURE 5-13. MICROGRAPHS OF PROP/ETOH-W-TEA ANHYDROUS AND HYDRAULIC SAMPLES AFTER 40 D.....	77
FIGURE 5-14. NOMENCLATURE OF THE SAMPLES IN THE DESIGN.....	81
FIGURE 6-1. XRD PATTERNS OF ALL SAMPLES IN THE EXPERIMENTAL DESIGN	83
FIGURE 6-2. RIETVELD REFINEMENT OF SAMPLE 30E _{5%} -A ₁₀₀	84
FIGURE 6-3. RIETVELD REFINEMENT OF SAMPLE 10E _{5%} -O ₂₀₀	84
FIGURE 6-4. RIETVELD REFINEMENT OF SAMPLE 30E _{2%} -O ₂₀₀	85
FIGURE 6-5. RIETVELD REFINEMENT OF SAMPLE 30M _{5%} -A ₂₀₀	85
FIGURE 6-6. CHEMICAL COMPOSITION OF THE PRODUCTS.....	87
FIGURE 6-7. THERMAL ANALYSIS COUPLED TO MASS SPECTROMETER OF 30E _{5%} -A ₁₀₀	88

FIGURE 6-8. THERMAL ANALYSIS COUPLED TO MASS SPECTROMETER OF 10E _{5%} -O ₂₀₀	89
FIGURE 6-9. FOURIER TRANSFORM INFRARED SPECTROSCOPY SPECTRA OF CALCIUM SILICATES.....	91
FIGURE 6-10. FIRST PEAK OF HEAT FLOW CURVES OF CALCIUM SILICATES.....	96
FIGURE 6-11. SECOND PEAK OF HEAT FLOW CURVES OF CALCIUM SILICATES.....	97
FIGURE 6-12. SECOND PEAK OF SAMPLES WITH HYDRAULIC BEHAVIOR.....	98
FIGURE 6-13. XRD PATTERS OF THE SAMPLES AFTER 2 DAYS OF HYDRATION.....	99
FIGURE 6-14. XRD PATTERS OF THE SAMPLES AFTER 28 DAYS OF HYDRATION.....	100
FIGURE 6-15. MICROGRAPHS OF ANHYDROUS 10M _{5%} -O ₁₀₀	101
FIGURE 6-16. MICROGRAPHS OF ANHYDROUS 10M _{2%} -A ₂₀₀ R.....	102
FIGURE 6-17. MICROGRAPHS OF LATE-HYDRAULIC SAMPLES AFTER 40 D. (A - B) 30M _{5%} -A ₂₀₀ ; (C - D) 10M _{5%} -O ₁₀₀	103
FIGURE 6-18. MICROGRAPHS OF EARLY-REACTIVE SAMPLES AFTER 40 D. (A - B) 30E _{2%} -O ₂₀₀ ; (C - D) 10M _{2%} -A ₂₀₀ , (E - F) 10M _{2%} -A ₂₀₀ R.....	104
FIGURE 6-19. TEM IMAGES OF SAMPLE 30E _{2%} -O ₂₀₀	107
FIGURE 6-20. TEM IMAGES OF SAMPLE 10M _{2%} -A ₂₀₀	108
FIGURE 6-21. SAED PATTERNS OF ANHYDROUS SAMPLES. (A, B, C) SAMPLE 30E _{2%} -O ₂₀₀ ; (D, E, F) SAMPLE 10M _{2%} -A ₂₀₀	109
FIGURE 6-22. TEM IMAGES OF HYDRATED SAMPLES (2 DAYS). (A, B, C) SAMPLE 30E _{2%} -O ₂₀₀ ; (D, E, F) SAMPLE 10M _{2%} -A ₂₀₀	110
FIGURE 6-23. SAED PATTERNS OF HYDRATED SAMPLES (2 DAYS). (A, B, C) SAMPLE 30E _{2%} -O ₂₀₀ ; (E, F, G) SAMPLE 10M _{2%} -A ₂₀₀	111
FIGURE 6-24. MINERALOGICAL RESULTS OF THE SECONDARY PHASES IN THE CHRONOLOGICAL ORDER OF SYNTHESIS ..	112
FIGURE 7-1. EFFECTS PLOT OF POLYMORPHS OF BELITE.....	116
FIGURE 7-2. INTERACTION PLOT FOR POLYMORPHS OF BELITE	117
FIGURE 7-3. EFFECTS PLOT OF AMORPHOUS	118
FIGURE 7-4. INTERACTION PLOT FOR AMORPHOUS.....	119
FIGURE 7-5. EFFECTS PLOT OF SECONDARY PHASES.....	119
FIGURE 7-6. EFFECTS PLOT OF SPECIFIC SURFACE AREA	120
FIGURE 7-7. PARETO CHARTS OF THE FIRST PEAK RESPONSES.....	121
FIGURE 7-8. MAIN EFFECTS PLOT OF THE FIRST PEAK RESPONSES.....	122
FIGURE 7-9. INTERACTION PLOT FOR FIRST PEAK – CUMULATIVE HEAT FLOW.....	122
FIGURE 7-10. PARETO CHARTS OF THE SECOND PEAK RESPONSES.....	123
FIGURE 7-11. MAIN EFFECTS PLOT OF THE SECOND PEAK RESPONSES.....	124
FIGURE 7-12. OPTIMIZATION PLOT.....	125
FIGURE 7-13. STANDARD DEVIATION OF THE RESPONSE VARIABLES (*SECONDARY PHASES NAMED AS IMPURITIES).....	127
FIGURE 7-14. CORRELATION BETWEEN THE VARIABLES.....	128
FIGURE 7-15. VARIATIONS IN THE AVERAGE PARTICLE SIZE USING AIR AS DISPERSION GAS.....	131
FIGURE 8-1. SOLVATION OF PRECURSORS	133
FIGURE 8-2. COMPLEX OF TEA; A – MONOMER COMPLEX SI- TEA, B- DIMER COMPLEX CA-TEA (ADAPTED FROM [179], [180]).....	134
FIGURE 8-3. SCHEMA OF THE REACTION PROCESS	140
FIGURE 8-4. METHODOLOGY OF SYNTHESIS OF CALCIUM SILICATES BY FSP	141
FIGURE 10-1. PARTICLES OBTAINED WITH FLAME 1 (1:1.5).....	146
FIGURE 10-2. PARTICLES OBTAINED WITH FLAME 2 (1:1.67)	147
FIGURE 10-3. RESIDUAL PLOTS FOR POLYMORPHS OF BELITE	153
FIGURE 10-4. RESIDUAL PLOTS FOR AMORPHOUS.....	154
FIGURE 10-5. RESIDUAL PLOTS FOR SECONDARY PHASES.....	155
FIGURE 10-6. RESIDUAL PLOTS FOR SPECIFIC SURFACE AREA.....	156
FIGURE 10-7. RESIDUAL PLOTS FOR P1 – CUMULATIVE HEAT FLOW	157

FIGURE 10-8. RESIDUAL PLOTS FOR - P2 - CUMULATIVE HEAT FLOW	158
FIGURE 10-9. RESIDUAL PLOTS FOR - P1 - MAX HEIGHT	159
FIGURE 10-10. RESIDUAL PLOTS FOR - P2 - MAX HEIGHT	160

List of tables

TABLE 3-1. THERMOCHEMICAL DATA [119], [120]	36
TABLE 3-2. ADIABATIC FLAME TEMPERATURES	37
TABLE 3-3. PROCESS CONDITIONS OF DIFFERENT RESEARCH DURING THE SYNTHESIS OF NANOPARTICLES BY FSP	41
TABLE 4-1. ALR VALUES AT DIFFERENT PROCESS CONDITIONS.....	52
TABLE 4-2. MEAN DROP SIZE CALCULATIONS.....	53
TABLE 5-1. CHEMICAL SYSTEMS EVALUATED IN THE SYNTHESIS OF CALCIUM SILICATES BY FSP	69
TABLE 5-2. PROCESS CONDITIONS USED DURING THE SET-UP OF THE SYNTHESIS	70
TABLE 5-3. STOICHIOMETRY OF CHEMICAL REACTIONS	70
TABLE 5-4. MINERALOGY QUANTIFICATION FOR DIFFERENT CHEMICAL SYSTEMS	75
TABLE 5-5. SPECIFIC SURFACE AREA (SSA) OF THE SAMPLES DURING THE SET-UP	75
TABLE 5-6. PREPARATION OF THE STARTING SOLUTION.....	78
TABLE 5-7. ALIAS STRUCTURE OF THE EXPERIMENTAL DESIGN.....	79
TABLE 5-8. FACTORS AND LEVELS OF THE PARAMETERS IN THE EXPERIMENTAL DESIGN	79
TABLE 5-9. ENTHALPY OF VOLATILITY OF THE MIXTURE OF SOLVENTS.....	80
TABLE 5-10. EXPERIMENTAL MATRIX	81
TABLE 6-1. RIETVELD REFINEMENT OF THE CALCIUM SILICATE PHASES WITH INTERNAL STANDARD OF RUTILE	86
TABLE 6-2. THERMAL DECOMPOSITION OF THE SAMPLES.....	90
TABLE 6-3. PERCENT OF CALCIUM OXIDE FORMED DURING THE REACTION PROCESSES	93
TABLE 6-4. SPECIFIC SURFACE AREA AND AVERAGE PARTICLE SIZE DISTRIBUTION.....	94
TABLE 6-5. HEAT FLOW RELEASED DURING THE HYDROLYSIS OF CALCIUM SILICATES	95
TABLE 6-6. EDS RESULTS FOR THE ANHYDROUS SAMPLE 10M _{2%} -A ₂₀₀ (ATOMIC %)	105
TABLE 6-7. EDS RESULTS FOR THE HYDRATED SAMPLE 10M _{2%} -A ₂₀₀	106
TABLE 6-8. EDS RESULTS FOR THE HYDRATED SAMPLE 10M _{2%} -A ₂₀₀ R.....	106
TABLE 6-9. GENERAL EVALUATION OF THE FAVORABLE PROCESS CONDITIONS TO OBTAIN SMALL PARTICLES.....	114
TABLE 7-1. SUMMARIZE OF THE VARIABLES WITH SIGNIFICANT EFFECTS ON THE RESPONSES	130
TABLE 8-1. CALCULATED STOICHIOMETRY COEFFICIENTS OF THE PRODUCTS	138
TABLE 8-2. VARIATIONS IN THE RESPONSES WITH THE VARIATION OF CERAMIC LOADING.....	141
TABLE 10-1. FLAMES TESTED IN THE PRODUCTION OF PARTICLES WITH A TERODYN SYSTEM.....	146
TABLE 10-2. ANALYSIS OF VARIANCE OF POLYMORPHS OF BELITE	153
TABLE 10-3. MODEL SUMMARY OF POLYMORPHS OF BELITE	153
TABLE 10-4. ANALYSIS OF VARIANCE OF AMORPHOUS.....	154
TABLE 10-5. MODEL SUMMARY OF AMORPHOUS.....	154
TABLE 10-6. FITS AND DIAGNOSTICS FOR UNUSUAL OBSERVATIONS OF AMORPHOUS.....	154
TABLE 10-7. ANALYSIS OF VARIANCE OF SECONDARY PHASES.....	155
TABLE 10-8. MODEL SUMMARY OF SECONDARY PHASES.....	155
TABLE 10-9. FITS AND DIAGNOSTICS FOR UNUSUAL OBSERVATIONS OF SECONDARY PHASES.....	155
TABLE 10-10. ANALYSIS OF VARIANCE OF SSA	156
TABLE 10-11. MODEL SUMMARY OF SSA	156
TABLE 10-12. ANALYSIS OF VARIANCE – P1 – CUMULATIVE HEAT FLOW	157
TABLE 10-13. MODEL SUMMARY - P1 – CUMULATIVE HEAT FLOW	157
TABLE 10-14. ANALYSIS OF VARIANCE – P2 – CUMULATIVE HEAT FLOW	158
TABLE 10-15. MODEL SUMMARY – P2 – CUMULATIVE HEAT FLOW	158
TABLE 10-16. FITS AND DIAGNOSTICS FOR UNUSUAL OBSERVATIONS – P2 – CUMULATIVE HEAT FLOW	158
TABLE 10-17. ANALYSIS OF VARIANCE- P1 – MAX HEIGHT	159
TABLE 10-18. MODEL SUMMARY- P1 – MAX HEIGHT	159

TABLE 10-19. ANALYSIS OF VARIANCE P2 – MAX HEIGHT	160
TABLE 10-20. MODEL SUMMARY – P2 – MAX HEIGHT.....	160

CHAPTER 1. INTRODUCTION

Cement industry is one of the main industries around the world with a production above 4.000 Mton/year, satisfying the infrastructure system all over the world. The cement production involves the formation of 0.81 kg CO₂ per kg cement produced [1], being an important emission source of greenhouse gases (GHGs) and contributing with the 5-8% of the total anthropogenic CO₂ emissions. In addition, its energy demand is around 2-3% of the total energy produced in the world. Therefore, important members of the cement sector adopted plans to address the industry necessities related to sustainability and set out to “make a difference” to decrease the environment impacts, focusing on resource productivity, climate protection, emission reduction, ecological stewardship, employee well-being, community well-being, regional development and shareholder value [2], [3].

The first three strategies are mainly addressed to mitigate the negative impacts on the environment, considering the develop of new technologies, the reduction of energy consumption in the process, the use of alternative fuels and raw materials [4], improvements in clinker performance and nanotechnological developments [5], [6]. High performance cement can be produced by making improvements in the process production of clinker, main component of the cement. Clinker production is an energy-intensive process, requiring temperatures up to 1600 °C to generate chemical reactions in solid-state, which result in the formation of four main phases corresponding to tricalcium silicate, dicalcium silicate, calcium aluminate and calcium ferro-aluminate, where the calcium silicates play an important role since are responsible of the compression strength and durability of the structures [7], [8].

The study of calcium silicates requires the study of more simple systems, their behavior and influence over reactivity and mechanical properties, enabling the improvement of cement properties in macroscopic systems and providing more information about the influence of atomic position on the level of reactivity of the structure in single crystal systems [7], [8]. These phases have been traditionally synthesized by solid-state reaction with temperatures above 1200 °C, requiring a high-energy consumption that has led researchers to propose new production alternatives. Alternative synthesis methods as Pechini, sol-gel and self-combustion are becoming important because of the possibility of reduce the energetic consumption process and produce nanoparticles with superior features than traditional powders, however all of them are batch methods, which is a limitation to scale-up the processes [9]–[17].

One of the most promising methodologies to powders production is flame spray pyrolysis method, which has been studied during the last decades to obtain nanopowders at high production level [18], [19]. Despite the few studies in cement applications, this method seems as an efficient process to obtain calcium silicate phases, because the reaction takes place in short time giving as a result metastable oxide phases. However, the effect of the process conditions over the products needs to be study to each solvent-chemical precursors system, because each formulation has a specific combustion environment [19].

Production improvements and performance of cementitious materials allow the reduction of energy consumption and mitigate the negative impacts of cement industry. Flame spray pyrolysis is an excellent alternative to produce nanomaterials in continuous, which has not yet been used in the production of cement phases as calcium silicates, hence the effects of this process on hydration properties is almost unknown. Therefore, the hypothesis raised in this project is that it is possible to develop a methodology for synthesis of nanoparticles of calcium silicates, through flame spray pyrolysis process, with cementitious properties and possible application in the cement industry. This hypothesis leads to the following questions about the project, ¿Do the changes of the FSP process's variables have an effect over the formation of calcium silicates? ¿How the mineralogy, specific surface area and reactivity of the phases are affected by these variables changes?

Hence, to the successful production of clinker phases, it is necessary to understand the effect of the process conditions over the products, due to cement formulations are complex systems that could be affected under these combustion environments. For instance, the main objective of this research was to establish a synthesis methodology of calcium silicates nanoparticles by flame spray pyrolysis route, with possible uses in cement industry. To achieve this objective, it was necessary develop the follow specific objectives:

- Evaluate the effect of the process variables over mineralogy, particles diameter and degree of reactivity of calcium silicates compounds.
- Formulate a correlation among operation process variables and features of the reaction products.
- Propose a mechanism of particles formation for calcium silicate phases made by flame spray pyrolysis.

This thesis book is divided in 10 chapters in which are resolved the objectives set out in this section. In the chapters 1 to 3 is given theoretical information about the topics covered in this project, in order to present background knowledge. Chapter 4 covers the design and manufacturing of the synthesis equipment as main apparatus during the project development. Chapter 5 shows the materials and methods established to the synthesis processes, while Chapter 6 address the characterization of the samples obtained after evaluate the process parameters of flame spray pyrolysis during the synthesis of dicalcium silicates and their hydration. Chapters 7 and 8 present the effects of process parameter on the synthesis products and the mechanisms of formation. Finally, results are concluded in Chapter 9, while in Chapter 10 is shown the annexes of the project, as supporting information of some results obtained in this research.

CHAPTER 2. CALCIUM SILICATES

General information of the composition of Portland cement is presented in this chapter. Initially, it is described the importance of the calcium silicate phases and their production by different techniques as main components in cement. Then, as most abundant components in cement, some crystal structure information the anhydrous phases, tricalcium silicate and dicalcium silicate are addressed. The information of this chapter is already-published material in Civil Engineering Research Journal (ISSN: 2575-8950) and it must be cited as:

N. Betancur-Granados, J. I. Tobón, O. J. Restrepo-Baena. 2018. "Alternative Production Processes of Calcium Silicate Phases of Portland Alternative Production Processes of Calcium Silicate Phases of Portland Cement: A Review." Civil Engineering Research Journal 5(3): 1–6.

Page: <https://juniperpublishers.com/cerj/pdf/CERJ.MS.ID.555665.pdf>

2.1. Calcium silicate phases of Portland cement

Portland cement is a construction material traditionally obtained by the calcination until partial fusion of limestone, clays and correctors to obtain clinker, which is combine with a source of calcium sulfate to produce cement. The clinker is composed by four phases corresponding to alite (Ca_3SiO_5 or C_3S), belite (Ca_2SiO_4 or C_2S), celite ($\text{Ca}_3\text{Al}_2\text{O}_6$ or C_3A) and ferrite ($\text{Ca}_4\text{Al}_2\text{Fe}_2\text{O}_{10}$ or C_4AF). The calcium silicate phases, alite and belite, are responsible of the development of mechanical properties such as compressive strength in construction structures, therefore many research have been developed to understand their features and properties [8].

Cement phases with nanometric size have been obtained also by non-conventional methods such as Pechini, sol-gel and self-propagating combustion, which showed good results to the formation of the cement matrix. The first work in the study of pure cement phases was done by R. Roy and Oyefebesi in 1977 using the sol-gel method [9]. Since then, different research had been done in the study of the process effects on the formation of cement polymorphs and their reactivity, considering the anhydrous and hydrated compounds [10]–[17].

S.C. Halim et al., prepared a typical clinker formulation in 2007 by FSP method, resulting in a highly reactive material as a consequence of the reduction of particle size in comparison with traditional clinker [20]. This research shows solid bases to believe that hydraulic calcium silicates could be synthesized by flame spray pyrolysis method, even when the production of alite and belite has not been studied.

In Portland cement, calcium silicates are a group of compounds formed by complex reactions between calcium and silicon oxides, commonly with presence of foreign ions. The crystal structure of calcium silicate compounds depends of length and angle in the Si-O and Ca-O bonds,

giving rise to the formation of polymorphs with different features as hydration behavior, which are quite affected by the chemical composition and the temperature of synthesis [21]. To study the chemical and physical properties of these materials, are available different characterization techniques such as x-ray diffraction (XRD), Fourier transform infrared spectroscopy (FT-IR), scanning electron microscopy (SEM), Thermal analysis (TG-DSC), microcalorimetry, among others.

2.1.1. Tricalcium silicate

Tricalcium silicate, named alite (C_3S), is the main active component in clinker, which has high hydration rates and is the main responsible of strength development during ages up to 28 days [22]–[24]. This compound has a nesosilicate structure, which means that is composed by the binding of a silicon atom with four oxygen atoms to form a tetrahedral structure by covalent bonds, $[SiO_4]^{4-}$, and it could have ionic bonds with metals as calcium, magnesium, iron, among others [25]. Alite presents a large grade of polymorphism, which depends mainly of temperature and impurities, having an effect on the silicate tetrahedral orientations. The reported structures are in triclinic (T), monoclinic (M) and rhombohedral (R) lattice systems, which have reversible transformations. During the cooling process at room temperature, the pure compound T1 is obtained at 620 °C corresponding to the triclinic system, other transformations for monoclinic system occur at 980 °C and finally at 1070 °C for rhombohedral (Figure 2-1), where the last one presents the smallest unit cell and the highest symmetry [26]–[29].

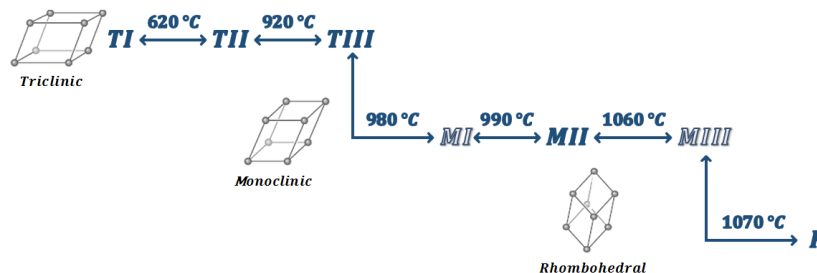


Figure 2-1. Tricalcium silicate polymorphic transformations

The polymorphic structures are T1, T2, T3, M1, M2, M3 and R. Polymorphs M1 and M3 are commonly found in clinker due to the incorporation of foreign ions as Mg^{2+} and could be identify by birefringence measurements while the polymorph T2 is rarely found; at room temperature pure tricalcium silicate present the triclinic structure T1 [8], [25], [27], [30]. The crystal structure of the polymorphs T1, M3 and R have been determinate and there are models for T2, T3, M1 and R [25]. To study the polymorphs, researchers have used impure alite by the addition of foreign ions as zinc, phosphorus, aluminum, magnesium and others, getting different stabilization effects depending of the amount and type of foreign ions [25], [30]. Also, the

models used to get information about the crystal structure of polymorphs, take into account the shape of the unit cell and the space group, based on metric relation and the deformation of unit cell, considering vector directions and planes [27].

For example, using XRD data of polymorphs, Regourd et al. [31], studied the evolution of the cell parameters. They found the existence of an average unit cell or superstructures. Based on it, they could propose structures for triclinic and monoclinic polymorphs, considering the displacements of calcium atoms and the orientations of silicon-oxygen tetrahedral [27]–[29], [32]. The main differences of the polymorphs of alite using XRD are shown from 29 to 38 (2θ), when Cu source is used. The triclinic polymorph shows four peaks overlapped between 31.7–33 (2θ) with a main and higher peak at $\sim 32(2\theta)$. On the other hand, the monoclinic polymorph (M3) shows two well defined peaks in the range 32–33 (2θ) and a small peak up of 33 (2θ), while the rhombohedral have a well-defined peak between 31–32(2θ) and another peak up to 32(2θ). Other important peaks are share by the polymorphs itself [33]. In addition, these polymorphs are influenced by the presence of foreign ions as S^{6+} and Mg^{2+} , resulting in the formation of polytypes as M1 (MgO <0.8 wt%), M2 and M3 (~ 0.6 wt% SO_3 , >1.2 wt%) for the monoclinic crystal system [33].

2.1.2. Dicalcium silicate

Dicalcium silicate or belite (C_2S) is a clinker phase that provides slow reactivity in early ages with a slow setting time; however, this compound plays an important role in the final compressive strength of the structures. Also, the presence of C_2S in cements improves the resistance to chemical attack, drying shrinkage and, allowing the elaboration of most durable Portland cements [34]. The melting point of this phase is 2130 °C. From room temperature until melting point, belite presents several phase transformations, giving place to five polymorphs, (α , β and γ families) where the most common polymorph is β - C_2S . α and β families of polymorphs present a close crystal structure, while γ polymorph is noticeably different. The polymorph γ - C_2S is not desired during the clinker formation, since it is the only phase that is non-reactive with water [8], [35]. Figure 2-2 shows the polymorphic transformations of dicalcium silicate [24], [36].

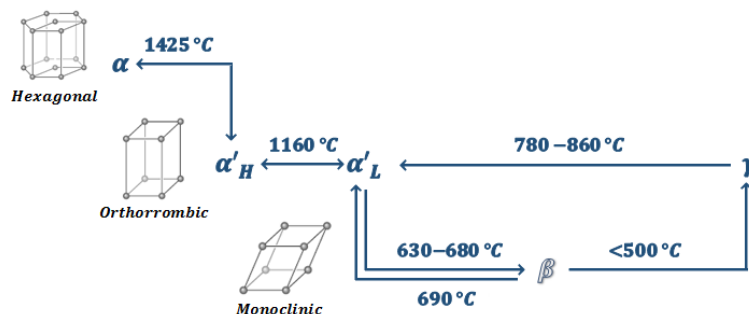


Figure 2-2. Dicalcium silicate polymorphic transformations

To produce better cementitious materials with lower footprint, the reactivity of belite had been strongly studied during the last decades [25]. Research shows two polymorphs with higher reactivity than alite, with the same composition of other polymorphs. One of them, called $x\text{-C}_2\text{S}$, presents a different crystal structure in comparison with the other polymorphs, and has the presence of “tunnels” which could be the responsible of the high reactivity [25]. As alite, C_2S allows the incorporation of foreign ions in order to modify its activity. Foreign ions as phosphorous, aluminum, boron, sulfur, etc., have been studied to know the effect on the reactivity of the impure belite. In the case of sulfur, e.g., some investigations showed an increase in the hydraulic activity, while others report a decrease in the reactivity [25].

2.2. Synthesis of calcium silicate phases

Different synthesis methods to obtain materials with well-defined stoichiometry has been developed and studied. The classification of these processes could be divided in *top-down* and *bottom-up* approaches, which considers the growth processes of the particles. *Top-down* approach is used when the chemical reactions to generate the particle are confined in a delimited space or the starting products are limited as in a drop. These processes are controlled by kinetic mechanisms. *Bottom-up* approach is refer to processes in which the particle is generated molecule-to-molecule or atom-to-atom, being governed by thermodynamic mechanisms which give rise to nucleation of particles [37].

Cementitious phases have been commonly made by solid-state reaction or fusion process, which is considers a *top-down* approach. The main advantage of this method is the simplicity of the process, however, it presents some important difficulties as the high energy consumption and the slow diffusion process which could leads to non-homogeneous phases [10], [38].

This decomposition method presents highly complex reactions, since physical and chemical processes as solid-state decomposition, gas-solid reactions, desorption, diffusion, sublimations and others, are involved simultaneously. The presence of crystal defects is fundamental because the solid reactivity increase as a consequence of these high energy regions [39], [40]. Therefore, the chemical transformations take place in restricted zones of the solid, generating local reactivity areas where the mobility of the ions and molecules controls the reactivity [18], [41], [42].

Research about the production of simple cement systems by solid state reaction method were done by Hasen (1928), Carlson (1930), Philips (1959) and Welch (1977), where are reported the formation and decomposition processes of tricalcium and dicalcium silicate, the stability of chemical systems and the thermodynamic behavior of pure phases of cement [43]–[46]. Looking for improvement of the synthesis of powders by solid-state reactions, it has been used strategies as the addition of mineralizers, wet milling and additional energy resources as microwaves. F. A. Rodrigues et al., [47], evaluated the effect of different compositions of barium additions in the formation of dicalcium silicate, using wet milling and ultrasonic bath to improve the precursors interaction, obtaining belite at 800°C without the presence of residual CaO . Similarly, Quéméneur et al., Shizong Long et al., and Haoxuan Li et al., applied microwaves during the sintering to improve the interaction between the solid starting materials and

decrease the temperature and duration of the process, achieving temperature reductions close to 100°C [48]–[52].

Even when cement phases are successfully obtained by solid state reactions, the high energy demand and CO₂ emissions resulted during this process had led to researchers to propose new alternatives. To overcome these problems, alternative batch methods as Pechini, sol-gel, solution combustion, have been used and to a lesser extent continuous processes as aerosol methodologies. These alternative methods start from suspensions or solutions which allow the production of high surface area powders. However, some of these methods require high-cost starting materials and specialized equipment [53].

Methods as Pechini and sol-gel show good results, since hydration products are part of the synthesis process, allowing the formation of C-S-H gel, which gives place to cement matrix. Sol-gel has been one of the most widely used alternative methods, which can be performed by gelation of a solution of colloidal particles, hydrolysis and polycondensation of alkoxides or nitrates followed by a hypercritical drying of the gel or by hydrolysis and polycondensation of an alkoxide followed by curing and drying of gel at atmospheric temperature (Figure 2-3) [54].

One of the main alternative synthesis methods is sol-gel, which was developed for R. Roy 1954 [54]. In 1977 Roy and Oyefebesi presented the first research in preparation of dicalcium silicate phases by the alternative methods sol-gel and spray drying. They studied the mechanical behavior of highly reactive belite showing increases of around 20 MPa in compressive strength compared to powders produced by high-temperature sintering, since this method starts from precursors in solution or colloidal form allowing a close interaction between the ions and, as a consequence, the production of particles with high surface area and a defined composition [9]. Researchers as Stephan et al. [10], Anikó Meiszterics [11], [12] and R. Chrysafi et al. [13] evaluated process parameters as pH, concentration and temperature, over the specific surface area and their effects on the reactivity and G. Laudisio y F. Branda [55] studied the crystallization behavior of 3CaO.2SiO₂ during the synthesis. Other research focused in biomaterials presented by Zhougru Gou et al. [56], [57], Wenyuan Zhao et al. [58], [59] and Chun-Cheng Chen et al. [60], used dicalcium silicate polymorphs and tricalcium silicate to study the behavior during the sintering process, mechanical properties and *in vitro* bioactivity using simulated body fluid (SBF).

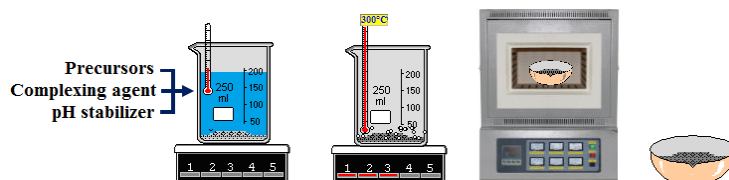


Figure 2-3. Sol-gel synthesis procedure

A similar methodology of sol-gel is the Pechini method, develop and patented by Maggio P. Pechini in 1967 [61]. In the synthesis of cementitious materials, I. Nettleship et al. [14] and

Seong-Hyeon Hong et al. [15], prepared different polymorphs of dicalcium silicate by changing the process temperature and, in a similar way, they evaluated the products reactivity [53]. I. Nettleship et al. studied the $\beta \rightarrow \gamma$ transformation to Ca_2SiO_4 while Seong-Hyeon Hong et al. prepared the α' - Ca_2SiO_4 , β - Ca_2SiO_4 and γ - Ca_2SiO_4 polymorphs by changing the process conditions. Both studies conclude about the increment in the reactivity because of the increment in the specific surface area. Besides, calcium aluminate phases related with setting time in Portland cement systems have also been done by alternative methods. A. Gaki et al. [62] and G. Voicu et al. [7] prepared calcium aluminate phases using Pechini method while D. A. Fumo et al, [53] and A. Cüneyt Tas et al [63] prepared the same family of compounds by a close methodology called solution combustion synthesis (SCS) starting from metal nitrates and urea as fuel, analyzing the relation oxidants/fuel and decreasing considerably the synthesis temperature.

Self-combustion synthesis start in 1972 for the production of refractory inorganic materials by A.G.Merzhanov and I.P. Borovinskaya, using oxidizing and reducing agents to fabricate particles after a heat and self-ignited process [64]. During self-combustion or solution combustion synthesis, a redox reaction is produced, heating a solution containing metal nitrates, pH stabilizers and a fuel up to the autoignition temperature, resulting in a quick reaction in a self-produced flame (Figure 2-4). Researchers as Xiang-Hui Huang et al. [16] and Restrepo et al. [17], [65], prepared β - Ca_2SiO_4 using colloidal SiO_2 and calcium nitrate as precursors and, glycine, citric acid and other organic compounds as fuels, resulting in the formation of products with different reactivity rates because of the changes in the specific surface area of the powders which is influenced by the energy given by the fuel. This method allows the production of calcium silicates without hydrate products in the structure, but when it comes into contact with water, the reaction occurs resulting in the formation of C-S-H gel [17].



Figure 2-4. Solution combustion synthesis procedure

Hideki Ishida et al., [66], M. Georgescu et al., [67], Larbi Kacimi et al., [68] and Nakshatra B. Singh et al., [34] prepared β - Ca_2SiO_4 by hydrothermal synthesis. These studies analyzed the influence of process conditions such as pressure, temperature, stir, concentration and heating time, in the formation of highly reactive belite. Hideki Ishida's work studied the phase formation with temperature variations at atmospheric pressure similarly than Larbi Kacimi but using fly ashes as starting materials instead of Hillebrandite as Ishida's work, while M. Georgescu used pressures of 1 atm and 16 atm at constant temperature. On the other hand, Nakshatra B. Singh's research considers both conditions, analyzing the influence of pressure and temperature.

As noticed above, mentioned methods such as Pechini, sol-gel, hydrothermal and self-combustion are batch processes, which often require later treatments as filtration, drying and calcination, making them less attractive to industrial applications [69], [70]. Considering the high cement production volumes, it is necessary to propose alternative scalable manufacturing processes, whereby aerosol technologies have a great potential since they are continuous processes and can be easily taken to industrial production, allowing the production from g/h to kg/h without disturbing particles features [71], [72].

In aerosol flame methods, the solution is subjected under an energetic resource which achieves high temperatures in few minutes, resulting in nanopowders formation (Figure 2-5). By flame spray pyrolysis (FSP) there have been not investigations of calcium silicates for cementitious applications, however, S.C. Halim shows the preparation of ultra-fast binding material, preparing a typical clinker formulation. Results showed a highly reactive material as a consequence of high surface area by the reduction of particle size in comparison with traditional clinker. However, mechanical properties showed unfavorable results due to high porosity in the cement blocks prepared to make measurements [20]. Furthermore, Tobias J. Brunner et al., prepared bioglasses and calcium phosphates cements changing the stoichiometry by addition of different cations. Bioactivity and strategies to control the setting rate of calcium phosphate phases formed by the manipulation of process conditions were evaluated for medical applications [73]–[75]. Hongbin Zhong et al., also evaluated the *in vitro* bioactivity of β - Ca_2SiO_4 made through spark plasma sintering (SPS) in a process with high heating rate, high pressure, high energy activity and short sintering time [76]. During this process, resulting powders show a bending strength ten times higher than conventional made materials as a consequence of the quick particles densification. Shekhar Nath et al., [77] evaluated apatite formation in β - Ca_2SiO_4 in powders made by metallorganic chemical vapor deposition (MOCVD), achieving the formation of apatite in the material surface after immersion in Hank's solution.

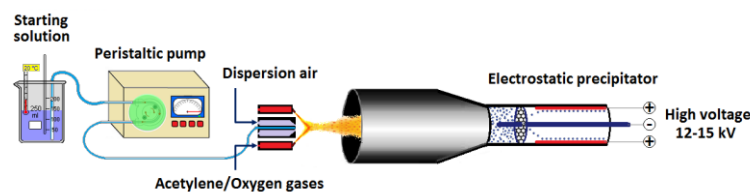


Figure 2-5. Flame spray pyrolysis synthesis procedure

As shown above, several research has been proposed to overcome the problems observed in the traditional method, allowing the improvement of cementitious materials, however, most of the studied processes present strong limitations to scale-up to industrial applications. Therefore, it is important to give attention to continuous processes such as aerosol flame methods. One of the most promising aerosol methodologies to powders production is flame spray pyrolysis method, which has been studied during the last decades to obtain nanopowders at high production level. This method seems as an efficient process to obtain calcium silicate

phases because the reaction takes place in a short time, giving as a result metastable oxide phases. However, the effect of the process conditions over the products needs to be studied in each solvent-chemical precursors system, because each formulation has a specific combustion environment [78]. In addition, the alternative methods mentioned above, allow the formation of nanoparticles, which has strong influence in the material features. The use of nanoscale systems in cement industry allows to develop a fundamental understanding which could be transferred to macroscopic systems, and at the same time, allows the development of stronger, durable and environmentally friendly materials [6].

CHAPTER 3. FLAME SPRAY PYROLYSIS

The calcium silicates produced in this research were prepared by the non-conventional method, flame spray pyrolysis. This chapter provides fundamental information about the synthesis method, addressing the importance of the starting solution in the process, the machine parts and phenomena during the reaction stages.

3.1. Flame spray pyrolysis method

Aerosol technologies are methods in which a discrete phase is dispersed by a continuous gas phase, resulting in the formation of droplets. Using an external energy resource, the droplets suffer evaporation/decomposition processes to form particles with spherical shape. The advantages of the process in the fabrication of nanosized inorganic particles are related to the process efficiency and product quality allowing the production of multicomponent particles from a stoichiometry controlled solution [79]–[84].

Aerosol flame processes began in 1977 with the research of M. Sokolowski in the synthesis of nanosized Al_2O_3 particles. These bottom-up processes generate nanopowders with precise compositional control, where the processing conditions have an important impact over the material properties. Factors such as precursors flow rate, dispersion gas flow and solution concentration have been studied to understand their role in the process and influence over powders features as specific surface area and morphology [85], [86].

One of the most important aerosol flame processes is called flame spray pyrolysis (FSP) highly developed in the University of Michigan [87]–[93]. In this method, the process starts from a liquid solution where the precursors are mixed in a molecular level. The solution is subjected under an energetic resource achieving high temperatures in milliseconds and resulting in the vaporization of the precursors. This phenomenon gives place to the decomposition of the precursors and formation of monomers, which react to form nuclei or primary particles. The primary particles grow by nucleation, coagulation and agglomeration processes, to result in the formation of aggregates of nanoparticles [19].

Flame spray pyrolysis method has been successfully applied in the production of complex oxides, however it is necessary to understand deeply the phenomena inside the process. For this reason, the challenge of FSP is to understand the relation between intrinsic and extrinsic conditions and their influence over the particle features and properties, obtaining an integral vision of the process. Researchers have studied the influence of individual parameters such as precursors flow rate, dispersion gas flow, concentration, solvent, between others, however this

process is strongly affected by at least ten parameters, and their possible combination effects [19]. Considering that cement systems are highly complex and the mineralogy of the compounds could be affected by the amount of energy give it to the particles during the reaction and quenched processes, it is very important to study the effects of the process conditions of flame spray pyrolysis over calcium silicates.

3.1.1. Starting solution for FSP

Currently, they are available a large variety of organic and inorganic compounds which can be used as solutes and solvents. Some of the most used solutes are acetates, nitrates and organometallics and to a lesser extent metallorganics [87], [94]. Inorganic salts as nitrates are commonly used because of their low-cost, high solubility in polar solvents and high availability. However, the use of nitrates leads to non-spherical morphologies and large particles, because of the droplets are dried instead of vaporized [94]–[96]. Otherwise, the metallorganics and organometallics compounds are stable in solution and allow the vaporization of the metal precursors before the solvent vaporization to permitting the subsequent gas reactions [97], [98].

The choice of the solvents for FSP process depends on the solubility of the precursors, the enthalpy of vaporization and the cost. The most used solvent is ethanol, however, other solvents as methanol, toluene, tetrahydrofuran and xylene have been used [99]. The relationship between the boiling temperature ($T_{bp(solvent)}$) and the decomposition temperature of the precursors ($T_{d/p(precursors)}$) are important parameters to choose the solvent. The proper evaporation of the metallic precursors required a solvent with slower volatility point than the precursors, allowing the gaseous reaction. Contrarily, if the solvent is vaporized before the precursors, large and/or hollow particles are formed because of the precipitation of the starting materials [99].

In addition, the concentration of metals in the solution is an important parameter, which can depend of the precursor's solubility and viscosity. The size and morphology of the particles is also affected by these parameters, so that at high concentrations hollow, encapsulated and large particles are formed. Thus, researchers suggest that to obtain nanosized and spherical particles, the ceramic loading of the solution should be lower than 10 wt. % [83], [99]–[101].

The relation $T_{bp(solvent)}/T_{d/p(precursors)}$ could determines the mechanism of formation of the particles. For high boiling points solvents, ($T_{bp}/T_{d/p}>1.05$) the precursors are completely evaporate allowing the formation of ultrafine nanoparticles (gas-to-particle mechanism). In contrast, using low boiling point solvents ($T_{bp}/T_{d/p}<1.05$), the solvent evaporates before the precursors, resulting in their precipitation and later formation of hollow, shell-like or larger particles, corresponding to the droplet-to-particle mechanism. Other important criterion to chose the solvent, is the combustion specific enthalpy, where high combustion specific enthalpy

upon to $4.7 \text{ kJ/g}_{\text{gas}}$ is the enough heat to evaporate the precursors to form homogeneous fine particles, even if $T_{\text{bp}}/T_{\text{d/p}} < 1.05$ [99], [102].

3.1.2. FSP equipment

Flame spray pyrolysis machine is divided in atomization system, reaction zone and collector system (Figure 3-1). Each component plays an important role in the process, having an impact on the features of the materials.

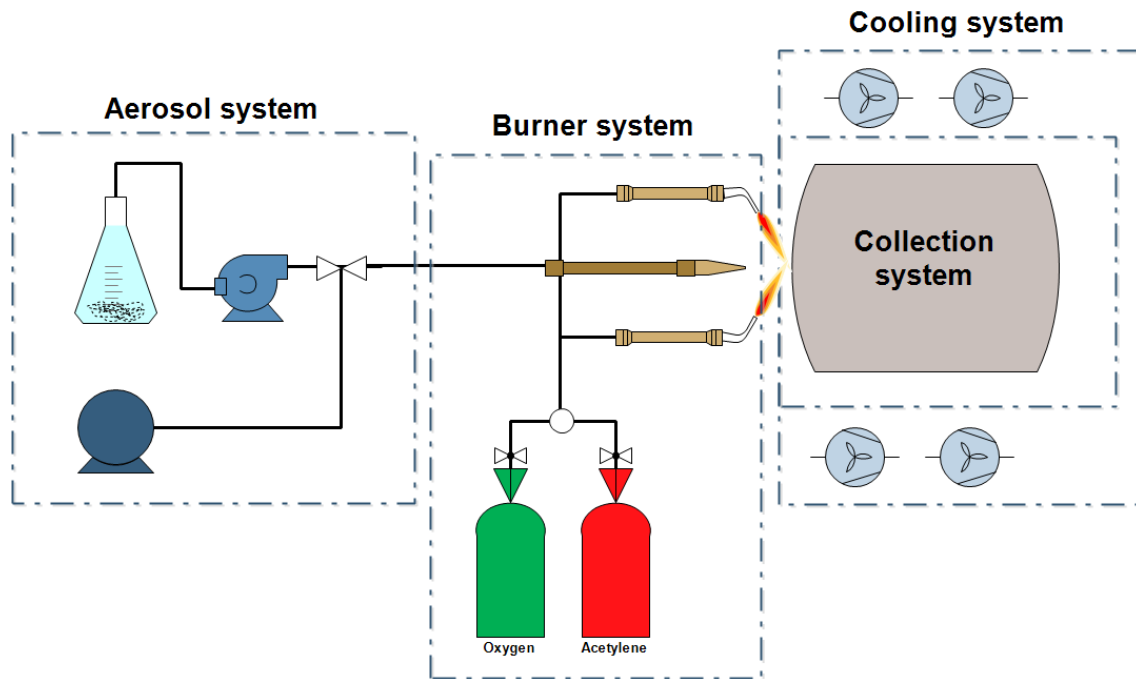


Figure 3-1. Scheme of flame spray pyrolysis system

3.1.2.1. Atomization system

The spraying process during flame spray pyrolysis can be considered a critical stage when low volatile precursors are used, although for high volatile precursors their influence decrease [103]. Different atomization devices are used to the generation of droplets, whose uniformity depends of the solution features, nozzle geometry and process conditions [103]. The atomization processes consist of the liquid disintegration in small drops when the surface tension forces of the liquid are overcome by a surrounding gas phase with high kinetic energy. An effective atomization allows the increment of the specific surface area of the liquid phase resulting in higher efficiencies in the follow evaporation processes. Characteristics as number of density, drop speed and drop size distribution are strongly affected by the nozzle geometry, gaseous medium and liquid properties [104].

The drop size is an important factor to describe the spray quality, which can be expressed by different equations, where the most relevant are *Sauter Mean Diameter* (SMD) and *the Mass Median Diameter* (MMD). From these two equations, the *Sauter Mean Diameter* (SMD) is considered the most appropriate equation in aerosol processes with mass transfer and heat transfer [105]. The empirical equation of *Sauter mean diameter* (SMD) described by Nukiyama and Tanasawa for airblast nozzles is shown in equation (1). This equation is formed by two terms, dominated by the air velocity and the viscosity of the liquid phase and can be used to small nozzles with a maximum hole size of 2 mm [106], [107]. From this equation it is possible to observe that the flow features of the spray are strongly influenced by the density, viscosity and surface tension forces of the liquid/gas phases [104].

$$SMD = \frac{0.585}{U_R} \left(\frac{\sigma_L}{\rho_L} \right)^{0.5} + 53 \left(\frac{\mu_L^2}{\sigma_L \rho_L} \right)^{0.225} \left(\frac{Q_L}{Q_A} \right)^{1.5} \quad (1)$$

Where U_R is the relative velocity of air to liquid, σ_L is the liquid surface tension, ρ_L is the liquid density, μ_L is the liquid viscosity and Q_L and Q_A are the volumetric flow rate of the liquid and air, respectively.

A spray can be defined in terms of the increment of the surface area of the liquid after the atomization process. The surface area before the atomization is defined as the liquid cylinder area that goes out the nozzle. After the atomization, the surface area is the sum of the surface area of each drop. The multiplication of these factors provides a direct indication of the atomization level reached, which is used in processes with surface phenomena as evaporation. On the other hand, the surface tension of the liquid represents the force that the liquid resists to form a new surface area. For instance, the minimum energy required during the atomization is equal to the surface tension multiplied by the increment of surface area of the liquid [104].

A broadly used atomization device is the airblast nozzle, which has two concentric tubes in axial direction, heading the gas and liquid with high amounts of air at low velocity (velocities lower than 100 m/s). The most important feature of the nozzle is the external or discharge hole diameter, where the mean diameter of the drop is close to the square root of the external diameter hole of the liquid. In airblast nozzles, the liquid speed is usually lower than air speed, reason why the droplets size is less sensitive to viscosity and density variations of the liquid due to the high pressures in the system [104].

The dispersion velocity during the atomization process depends of the feed flow rate of the starting solution and the pressure of the dispersion gas. These factors also have an influence over the drop size. The droplet size is an important characteristic since small droplets allow rapid evaporation and lower residence time in the reaction. Studies about the effects of the dispersion gas flow show that its increment leads to small primary particles since a decrease in the residence time in the flame and high energies to break the flow cylinder [81], [108].

3.1.2.2. Reaction zone

The reaction zone of the FSP process can have different configurations. The flame can be exposed to the air or enclosed [109]. The enclosed flames allow a better control of the process conditions since the heat losses by convection and radiation are lower, however this facilitates the particles coalescence inside the reactor resulting in the formation of larger particles than in open-air systems. Otherwise, the open-air systems enable the gas-to-particle conversion, allowing higher synthesis performance since the airflow minimizes the particle deposition in the reactor [109].

The co-flow diffusion flame burner has been a configuration widely employed for commercial production. One of these configurations is the coaxial multi-annulus, which have three concentric stainless-steel tubes, corresponding to separate streams of fuel, oxidizer and metal precursors. The classic configuration for this burner uses the outermost tube for the oxidizer, the middle tube for the fuel and the inner tube for the precursor/dispersion gas mix. However, other stream configurations had been studied, putting the fuel in the outermost tube and the oxidizer in the middle tube, demonstrating higher potential to obtain finer particles, going from 105 nm to 11 nm. This configuration has as disadvantage the longer high temperature zone, after the flame, resulting in large particles by sintering processes or high agglomerate particles. Nevertheless, this problem can be resolved by the use of better quenching processes, which can stop the growth phenomena downstream [99]. Other widely use burner is the McKenna burner, which producer premixed flat flames, with uniform distribution of temperature [110]. The advantage of this burner is the simple and standard geometry. The premixed flames, allow the formation of high concentration of radical which take place in the oxidation reactions of the precursors, but do not affect the arrangement of species for mixed-oxides [99]. Other premixed flame widely used is the dual-flame burner in which two individual pre-mixed flames collide, forming a mid-point with high temperature, in which the aerosol is decomposed to result in the nanoparticles formation [96].

It is important to note that the energy released in the reaction zone comes from the flame, precursors and solvent, but the main source of energy comes from the flame. The flame is one of the most important variables during the FSP process, because of its influence in the size of the particles. The fuels usually used in FSP process are methane, hydrogen and acetylene, which can offer different combustion environments and energies values to the reaction [106]. The hydrogen allows the formation of very pure materials since its combustion does not produce carbon radicals [106]; however, the installation of hydrogen systems is very expensive and demanding. On the other hand, acetylene is an inexpensive gas which provide higher combustion enthalpies than other fuels [111].

The oxy-acetylene flame can be mix at different acetylene/oxygen ratios (Figure 3-2), allowing three different combustion environments corresponding to reducing, oxidizing or neutral atmospheres [18].

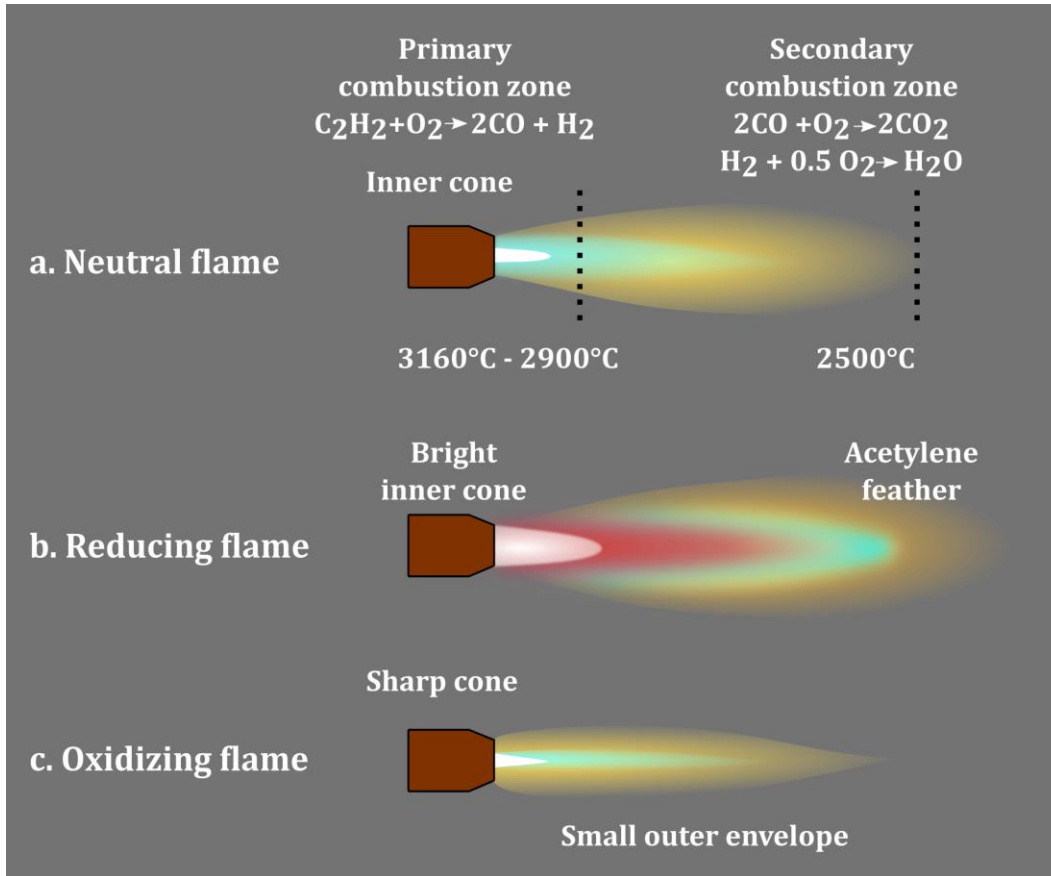
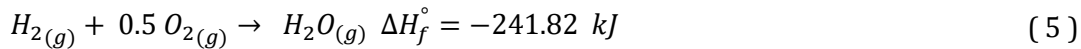
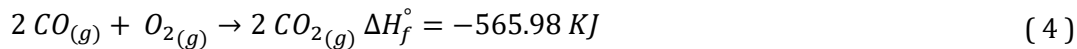
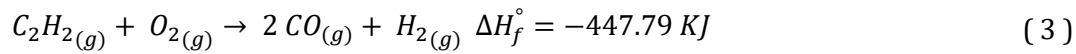
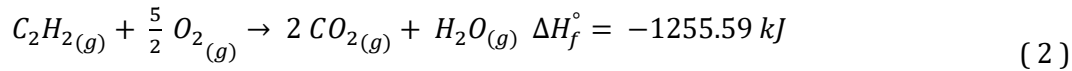


Figure 3-2. Oxy-acetylene flame types

The neutral flame is produced by a stoichiometry mix of the gases as is shown in the Figure 3-2. This flame is characterized by having a well-defined inner cone, different to the reducing flame, which is characterized by having a bright inner cone and a feather surrounding the flame due to the excess of acetylene. Contrary to the reducing flame, the oxidizing flame is rich in oxygen, avoiding the formation of residual carbon. This flame is quite blue with a sharp inner cone. The gases flow proportion ($C_2H_2:O_2$) determines the final temperature of the flame as it is supported below by thermodynamic calculations of adiabatic flame temperature (Table 3-2) [112]. Increments in the flame temperature could lead to increments of the specific surface area, by the increase of nucleation points [100]. However, it also could lead to an increase of the particle size whether there is not a rapid cooling of the particles [103], [111], [113].

The Figure 3-2 (a) shows the reactions of a neutral oxy-acetylene flame. The combustion occurs in two stages presenting two different zones: a primary combustion zone, where oxygen for combustion is supplied, achieving the highest temperatures of the flame ($2900-3160^\circ C$) [114]. First, a reaction between equal molar quantities of oxygen and acetylene occurs, resulting in the formation of carbon monoxide and hydrogen. Then, in the secondary combustion zone, the carbon monoxide reacts with oxygen from the air to form CO_2 , while hydrogen reacts with oxygen from the air to form water, achieving temperatures close to $2500^\circ C$ [112], [115]–[117].

The thermochemical reactions for oxy-acetylene combustion are shown in equations (2) to (5) [117]. The standard enthalpy of formation of the overall reactions corresponds to the sum of the enthalpy changes of the individual reaction steps. Equation (2) shows the overall gases combustion and equations (3) to (5) show the combustion reaction stages. To generate the flame, the supplied oxygen is just the required to give rise to the first stage of the combustion (equation (3)), since the rest of the oxygen is taken from the air. Depending on the stoichiometry of the flame, a reducing or oxidizing environment will be produced [106], [117].



Thermodynamic calculations of the adiabatic flame temperature were done using the equation (6) and the thermochemical data of the compounds in Table 3-1. Adiabatic flame temperatures for flame spray pyrolysis are shown in Table 3-2. These theoretical results are higher than the experimental maximum temperatures of the flames, as it was expected since it considers that no energy is lost to the outside environment and the temperature depends on the quantity of nitrogen in the mixture. The highest temperature values are obtained using pure oxygen for FSP flames. The experimental data for reducing, oxidizing or neutral flames using oxy-acetylene, were taken from WeldCor Supplies Inc. Encyclopedia [118].

Table 3-1. Thermochemical data [119], [120]

Compound	ΔH_f (KJ/mol)	C_p (J/mol·K)
$C_{(ref)}$	0.00	8.52
$C_2H_{2(g)}$	226.73	44.10
$C_2H_{4(g)}$	52.47	42.89
C_2H_5OH	-277.05	65.21
$C_8H_{20}O_4Si_{(l)}$	-1408.00	364.40
$Ca(NO_3)_2 \cdot 4H_2O_{(s)}$	-2132.30	149.40
$Ca_2SiO_{4(s)}$	-2304.82	128.61

CaO _(l)	-683.92	62.76
CO _(g)	-110.53	29.14
CO _{2(g)}	-393.52	37.73
H _{2(g)}	0.00	28.84
H _{2O_(g)}	-241.82	33.59
H _{2O_(l)}	-285.83	75.35
N _{2(g)}	0.00	29.12
NO _(g)	90.29	29.85
NO _{2(g)}	33.10	36.97
O _{2(g)}	0.00	29.38
SiO _{2(l)}	-935.34	85.77

(6)

$$\sum_{Reac} n_i(\Delta\bar{h}_{f,298}^{\circ} + \bar{h}_T - \bar{h}_{298})_i = \sum_{Prod} n_i(\Delta\bar{h}_{f,298}^{\circ} + \bar{h}_T - \bar{h}_{298})_i$$

Table 3-2. Adiabatic flame temperatures

Type of flame	Adiabatic temperature (°C)	Experimental temperature (°C)
Neutral flame	4513	3100
Reducing flame	4399	3065
Oxidizing flame	4892	3315

3.1.2.3. Particles collection

The collection of the particles has been done using different systems. The commonly used systems are filter chambers, electrostatic precipitator, thermophoretic precipitators and cyclones, offering different yield values to the synthesis process. During the collecting process, the particles are still suffering growth phenomena, due to the high temperatures of the process. For that reason, the collectors are usually equipped with a cooling system to quickly quench the particles avoiding sintering processes [103].

One of the most efficient collector systems for nanoparticles are the electrostatic precipitator (ESP), due to the small particle size. This dispositive, electrically charge the particles resulting in a deposition in the surface of the collector. During the operation of the ESP an electric field, created by the application of a high voltage difference, charge the particles inside of the dispositive, which are affected by gas ions and random Brownian motion of negative air ions and their collisions with small particles [121].

A simple configuration of these collector systems are the wire-in-cylinder systems, which allow continuous operation and could achieve collection efficiency upon 65 %. This system is preheated using ethanol to form the spray, avoiding the condensation of water inside the system [122]. Other systems are the countercurrent scrubber [123]. In flame aerosol methods,

it is also requires an efficient cooling system, due to the high temperatures in the aerosol stream allowing the growth of the particles by coagulation [101]. Other method for collecting the particles is using commercial filters as Jet filter. For this method it is necessary to use baghouse filters which collect the powders on the outside surface using air suction ventilators, which is removed by using air pressure shocks of 5 bar absolute pressure [124].

3.1.3. Effects of synthesis conditions

Several research had been developing in order to evaluate the effect of the process conditions on the features of the products, however, most of the parameters are evaluated as individual factors and some discrepancies in the effects had being observed. Table 3-3 shows the synthesis conditions used for different researchers to evaluate the effects of the process conditions, while Figure 3-3 shows the tendency of the particle size and specific surface area of different materials, obtained by them. The data from one research to another is a bit spread since the differences between the equipment and specific conditions of synthesis.

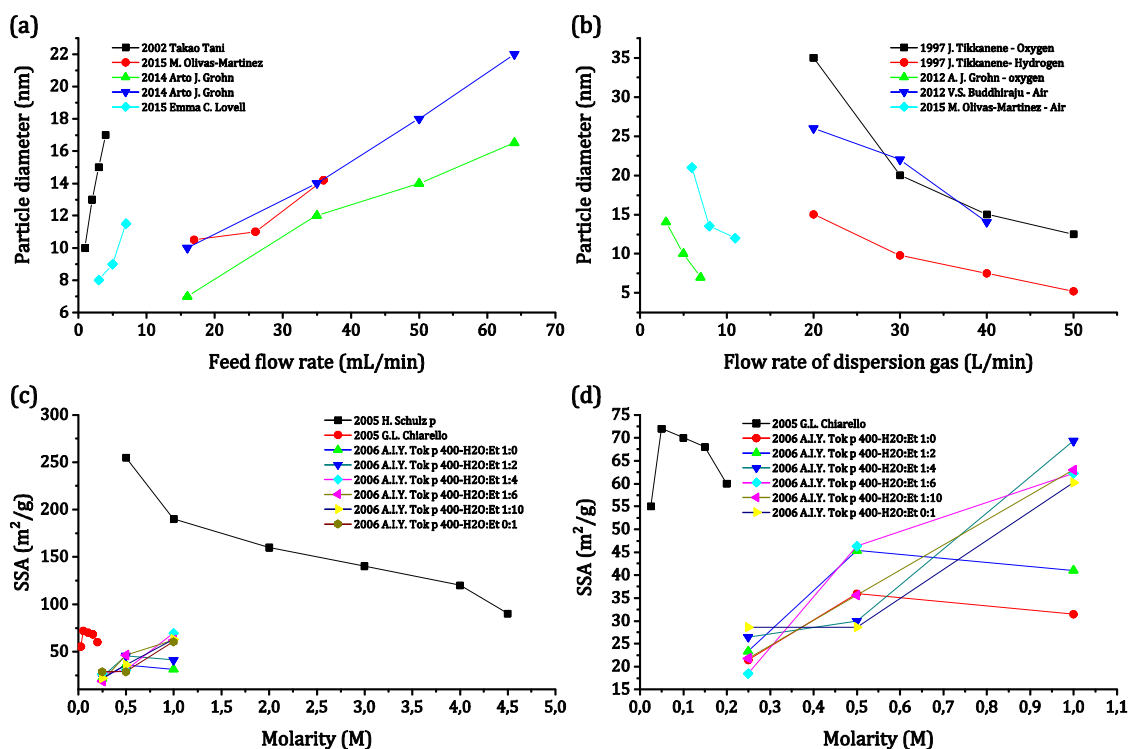


Figure 3-3. Compilation of effects of synthesis conditions. Data for Feed flow rate from [108], [113], [125]–[127], for Flow rate of dispersion gas from [72], [84], [106], [125] and for concentration from [128]–[130].

Figure 3-3 (a) shows the increment of the particle size by increasing the feed flow rate independently of the material and chemical system used during the synthesis process. High feed flow rates leads to longer flames due to the higher amounts of fuel in the combustion environment, decreasing the specific surface area of the particles by coalescence and growth processes between the particles [113], [127]. The solvent as fuel could increase the temperature of the flame whether the solvent provides energy; otherwise, a solvent as water will require energy decreasing the temperature of the flame. Additionally, under high feed flow rate the concentration of ions in the flame is high, increasing the number of collision between the particles, therefore, the sintering processes [108], [113], [126], [127].

Olivas *et al.* [125], presents a model of particle formation, predicting a increase in particle size with the increase of the feed flow, since an increment in the nucleation points which allow the formation of nanosized particles. H. Chang *et al.*, M. Aromaa *et al.* and Lovell *et al.* [81], [127], [131] report that the increment in the feed flow rate leads to increments in the particle size, due to a high concentration of particles in the high temperature zone allowing coalescence processes.

A. Purwanto *et al.* [132], report that the particle size can be predicted using a mass balance equation (Equation (7)), using the physical properties of the precursor as follows:

$$d_p = \left[\frac{C_D d_D^3 MW}{n \cdot \rho} \right]^{1/3} \quad (7)$$

Where C_D is the droplet concentration, d_D is the droplet diameter, MW is the molecular weight of the particles, n is the stoichiometric ratio and ρ is the particle density [132].

The flow rate of dispersion gas (Figure 3-3 (b)) shows an opposite effect in the particle size, regarding to the feed flow rate (Figure 3-3 (a)). This process parameter decrease the flame length when the pressure of dispersion gas increases, as consequence, the gas phase reactions are improve since better mixing of gases and faster consumption of the species take place [125]. This phenomena imply that the combustion rate of the species is governed by the parameters of the process and no by the reaction kinetics [125]. During the reaction, the lifetime of the droplets can be divided in two stages, corresponding to the heat-up of the droplets and subsequent evaporation. The heat-up of the droplets could take around 1 ms, while the evaporation depends of the feed flow of dispersion gas. High pressures of dispersion lead to shorter lifetime, since the formation of turbulent environments which improve the heat transfer rates [125].

Figure 3-3 (c) shows the relationship between the concentration of the starting solution and the specific surface area, while the Figure 3-3 (d) is an enlargement of it, for low molarities. In contrary with the other variables, the concentration of the solution does not show the same effect in the specific surface area of the powders for these research, increasing the specific surface area with the increment of the molarity in the work of A. I. Y. Tok *et al* (2006). They attributed this behavior to a high rate of solvent in the flame, which could result in high flame

temperatures, however, at the same time they agree that high concentration leads to high number of particles collision against to the experimental results, where the SSA should decrease. Even when the explanation is not clear, the results indicate a contrary behavior from the expected results. Otherwise, Chiarrello et al (2005) and Schulz et al (2005) research, showed a decrement of the SSA with the increase of the molarity, due to the particle collisions and subsequent sintering processes. Additionally, A. I. Y. Tok et al (2006) shows the use of mixtures of water:ethanol a different ratios, as solvents. The results do not show a clear effect of the addition of water, but the higher surface area was obtained with a ratio water:ethanol of 1:4 at high concentration, while at low concentrations, the SSA using this mixture of solvents was comparative with the results obtained using only ethanol as solvent, suggesting a good proportion between these liquids whether the use of water is required during the reactions ([113], [125], [127], [129], [130]).

Summarizing, the particle size of the powders in flame spray pyrolysis increase by increasing the residence time of the droplets in the flame, which can be given by too low feed flow rates or too low pressure of dispersion. Likewise, high flame temperatures increase the particle size, which could be a consequence of high feed flow rates due to the increment of fuel fed to the flame from the solvent. Finally, high precursor concentrations implies high concentrations of primary particles in the reaction environment, increasing the number of collisions which promotes the sintering of the particles [113], [127].

Table 3-3. Process conditions of different research during the synthesis of nanoparticles by FSP

Reference	Compound	Feed flow rate (mL/min)	Dispersion gas	Flow of dispersion (L/min)	Concentration	Fuel/Oxidant	Flow Fuel-Oxidant (L/min)	Solvent	Precursors
T. Tani et al (2002)	ZnO	1-4	Oxygen	-	-	Methane/Oxygen	1.58-1.52	Methanol:Acetic acid	Zinc acrylate
E. C. Lovell et al (2015)	SiO ₂	3, 5, 7	-	-	-	-	-	-	Organometallic
M. Olivas (2015)	SiO ₂	18.3, 26.2, 35.8	Air	0.011	50 % TEOS	Hydrogen/Oxygen	0.38-3.66	Ethanol	TEOS
	SiO ₂	26.2		0.006, 0.0083, 0.011	30 % TEOS				
A. Grohn (2014)	ZrO ₂	16, 32, 64	Oxygen	0.02, 0.04, 0.08	1 M	Methane/Oxygen	2-4.5	Xylenes	Zirconium 2-ethylhexanoate
A. Grohn (2014)	ZrO ₂	4	Oxygen		1 M	Methane/Oxygen	1.25-2.5	Xylenes	Zirconium 2-ethylhexanoate
A. Grohn (2012) (810)	ZrO ₂	4	Oxygen	3-7	0.5, 1 M	Methane/Oxygen	1.25-2.5	Ethanol/1-propanol	Zirconium n-propoxide
Tikkaneer (1997)	Al ₂ O ₃	6.2	Helium	20-50	-	Hydrogen/Oxygen	35-20	Isopropanol	Aluminium nitrate nonahydrate
Baddhiraju (2012)	SiO ₂		Air	-	-	Hydrogen/Oxygen	6-15	-	TEOS
Chiarello (2005)	LaCoO ₃	1	Oxygen	5	0.025-0.2 M	Methane/Oxygen	0.5-1	Propionic acid	La(CH ₃ COO) ₃ Co(CH ₃ COO) ₂
Schulz (2005)	Ta ₂ O ₅ /SiO ₂	5	Oxygen/Air	5	0.5-4.5 M	Methane/Oxygen	1.1-2.5	Hexano	Ta Butoxide/TEOS
I. Y. Tok (2006)	ZrO ₂		Combustion gases		0.25-1M	C ₂ H ₂ /O ₂	65-70 psi	H ₂ O:ethanol	Nitrates

3.2. Particle formation in flame

The synthesis processes with *bottom-up* approach start by a supersaturated solution followed by nucleation and growth processes governed through thermodynamic equilibrium [37]. During the synthesis process, the formation of the particles depends of the time residence of the drop in the flame, which can result in droplet-to-particle conversion or gas-to-particle conversion as is shown in Figure 3-4 [109].

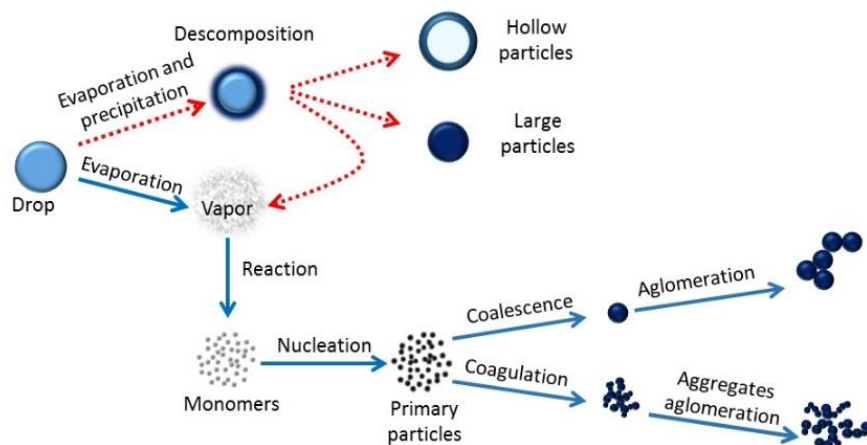


Figure 3-4. Mechanisms of particle formation during FSP (Adapted from [70])

The droplet-to-particle conversion leads to the formation of large or hollow particles, while the gas-to-particle conversion leads to the formation of nanosized and dense particles. The mechanism gas-to-particle is the ideal way to produce nanoparticles through flame spray pyrolysis, having as formation stages the evaporation/decomposition of the starting solution, the gases reactions, nucleation, coagulation and coalescence processes [19], [133].

3.2.1. Evaporation, decomposition and reaction

The evaporation is an important stage since it determines the conversion mechanism of the particles in droplet-to-particle or gas-to-particle. Whether the evaporation is properly done, the resulting gas phases give rise to the subsequent nucleation and growth stages [37]. Heat transfer phenomena starts when the droplets cross the flame, leading to evaporation of the solvent, condensation of the precursors and chemical reactions [134]. During this stage, the droplets can cross the flame before a complete vaporization, being vaporized by the surrounding hot gas.

In flame spray pyrolysis the model of Sirignano (1999) has been used to describes the droplet combustion, after spraying the starting solution [135]. This model considers the liquid-vapor phase equilibrium when the droplets are in contact with fuels and oxidizer species. However, this model

does not consider droplet interactions, liquid fuel solubility with gases and the gas phases are formed only by fuel, oxidizer and combustion products. In addition, it is assumed that the fuel and oxidizer react instantaneously and the mass diffusivity and thermal conductivity of the products are constant, allowing the calculation of the droplet velocity, v_d , and diameter, d_d . Equations (8) and (9) are in terms of the Nusselt number (10), Nu, the transfer number, $B_{0,q}$ (11), Reynolds number, Re (12), and the drag coefficient in non-Stokesian regime, C_D (15) [136].

$$\frac{dv_d}{dx} = \frac{3 \rho_g C_D}{4 \rho_d d_d} (v_{rel}) |v_{rel}| \frac{1}{v_d} \quad (8)$$

$$\frac{dd_d}{dx} = - \left(\frac{8k_g}{\rho_l c_{pg}} \ln(1 + B_{0,q}) \frac{Nu}{2} \right) \frac{1}{d_d} \frac{1}{v_d} \quad (9)$$

$$Nu = 2 + \frac{0.555 Re^{1/2} Pr^{1/3}}{\left[1 + 1.232 / (Re Pr^{4/3}) \right]^{1/2}} \quad (10)$$

$$B_{0,q} = \frac{\frac{\Delta h_c}{v} + c_{pg}(T_\infty - T_d)}{q_{i-l} + h_{ig}} \quad (11)$$

$$Re = \frac{d_d v_{rel}}{\eta} \quad (12)$$

$$v_{rel} = u_f - v_d \quad (13)$$

To obtain the value of the gas velocity u_f is necessary use a correlation for turbulent jets issuing from a round nozzle,

$$u_f = \begin{cases} u_0 & x/d_n \leq 5.27, \\ \frac{5.27 u_0}{x/d_n} & x/d_n > 5.27 \end{cases} \quad (14)$$

$$C_D = \frac{24}{Re} + \frac{6}{1 + \sqrt{Re}} + 0.4 \quad (15)$$

Whether the energy resource is insufficient, the rate of evaporation of the solution components can be different, resulting in different reactions velocities for the ions. If the energy is enough, the new gas phase will give place to the reaction stage.

The precursor in contact with the flame starts a chemical decomposition as a primary gaseous phase. The kinetic of the combustion reactions are weakly coupled to the precursor decomposition and particle formation processes; nevertheless, it can be interactions between them by reactions of radicals.

During the decomposition of the spray are formed radicals, intermediaries and monomers species that can polymerize and create nuclei. The thermodynamic stable nuclei will continue the nucleation process [137]. If the precursors decomposition rate is very different, it results in the formation of particles with an component *A*, surrounded by a different component *B*, with slow decomposition rate [137]. The rate of the precursor's decomposition is represented by the equation (16),

$$S = \frac{d[\text{Monomero}]}{dt} \alpha - \frac{d[\text{precursores}]}{dt} \quad (16)$$

Where, α is a proportionality constant.

Because the residence time of the species in the flame is extremely short, the particle formation processes are very fast and the chemical reaction is supposed instantaneous (microseconds) [138]. Fristrom and Westenberg, proposed in 1965 an empirical relationship to premixed flames shown in equation (17), which shows that the required time (τ) at atmospheric pressure for both preheat and primary chemical reaction in a flame is inversely proportional to the square of the flame velocity (*V*) [138].

$$\tau = \frac{3}{V^2} \quad (17)$$

3.2.2. Nucleation

The growth of the nanoparticles by FSP assumes homogeneous nucleation, i.e. when the concentration of solute in the solvent exceeds the equilibrium solubility rising to a new phase. After the evaporation and decomposition of the precursors in the first stage, the medium is rich of radicals, intermediaries and monomers. Consequently, the medium possesses high Gibbs free energy allowing a polymerization and nucleus formation in order to reduce the overall energy of the system. Thus, the total energy of the system is reduced by the formation of a new phase keeping an equilibrium concentration in the media. Then, the driving force for the nucleation and the growth of the particles is the reduction of the Gibbs free energy. Equation (18) shows the change of the Gibbs free energy per unit volume of the solid phase.

$$\Delta G_v = \frac{-KT}{\Omega} \ln C/C_0 = \frac{-KT}{\Omega} \ln(1 - \sigma) \quad (18)$$

Where, C is the concentration of the solute, C_0 is the equilibrium concentration or solubility, T is the temperature, K the Boltzmann constant, Ω is the atomic volume and σ is the supersaturation describe in the equation (19).

$$\sigma = \frac{C-C_0}{C_0} \quad (19)$$

In the equation (20), a system without saturation, i.e. $\sigma=0$, has a $\Delta G_v = 0$ and the nucleation won't happen. When $C>C_0$, $\Delta G_v < 0$, and the process is spontaneous. Considering a spherical nucleus with radius r , the change in the volume energy, $\Delta\mu_v$, is,

$$\Delta\mu_v = \frac{4}{3}\pi r^3 \Delta G_v \quad (20)$$

By decreasing the super saturation, the energy is reduced, which is countered by the introduction of surface energy of the new solid phase. This energy is expressed as,

$$\Delta\mu_s = 4\pi r^2 \gamma \quad (21)$$

Where, γ is the surface energy per unit area. The total change of the chemical potential for the formation of the nucleus is the sum of the volume and surface energies. The energy reduction will result in the formation of primary particles if the radius exceeds a critical size, r^* . If the particle is smaller than r^* , it will be dissolved into the medium, whereas a larger nucleus would continue the nucleation and growth process [37], [112]. The equations of homogeneous nucleation in terms of the Gibbs free energy, ΔG_v , are,

$$\Delta G^* = \frac{16\pi\gamma}{(3\Delta G_v)^2} \quad (22)$$

$$r^* = -\frac{2\gamma}{\Delta G_v} \quad (23)$$

Where equation (22) represents the critical energy which must be overcome to allow a nucleation process and equation (23) the critical radio of the particles, where γ is the surface energy per unit area. In processes with supersaturate media, low viscosity and low critical energy (ΔG^*) favored the formation of large number of nucleation sites, implying smaller nuclei sizes [37].

The nucleation rate per volume and time unit, R_N , is estimated by

$$R_N = nP\Gamma \quad (24)$$

Where, n is the number of growth species per unit volume, P is the probability of a thermodynamic fluctuation of critical free energy and Γ is the jump frequency of growth species. Where the last two terms are defined in equations (25) and (26).

$$P = \exp\left(\frac{-\Delta G^*}{KT}\right) \quad (25)$$

$$\Gamma = \frac{KT}{3\pi\lambda^3\eta} \quad (26)$$

Where, λ is the diameter of growth species and η is the viscosity of the solution. For homogeneous nucleation, the number of growth species is equal to the initial concentration of the solute, $n=C_0$, then,

$$R_N = C_0 \frac{KT}{3\pi\lambda^3\eta} \exp\left(\frac{-\Delta G^*}{KT}\right) \quad (27)$$

3.2.3. Surface growth

The growth mechanisms in flame spray pyrolysis are mainly divided in two phenomena corresponding to coagulation, also call collision or agglomeration, referred to the particle collision and sticking together, and coalescence, also called sintering, referred to the merge of coagulates to form a large particle [125]. These phenomena are difficult to separate, because both of them happen at the same time.

Ulrich studied in 1971 sintering processes considering coalesce and coagulation as separate processes, formulating equations for the particle size and specific surface area evolution [138], [139]. Kock and Frielander (1990), modeled the primary particle size evolution in the free molecular regime, considering the effects of coagulation over sintering processes, by assuming that the collision of the aggregates happens at the same velocity than the primary particles with the same volume [140]. Xong and Pratsinis (1993), including the sintering term in the General dynamic equation for aerosol, developing a model in two dimensions for a free molecule in the continuous regime, which describes the evolution of the aggregate volume by simultaneous coagulation and sintering in non-isothermal conditions, assuming a mono dispersed aggregate and without suppositions about the particle size [133][141].

After the instantaneous chemical reaction in the previous stage, the molecules and primary particles start to growth by successive collisions. Initially, the rate of coalescence of the particles is higher than the collision rate, allowing the formation of spherical particles. Assuming that all the aggregates have the same number of primary particles with the same size, the evolution of the particle size distribution of the aggregates is represents by the equation (28).

$$\frac{dN}{dt} = -\frac{1}{2}\beta N^2 \quad (28)$$

Where β , is the frequency function for the collision between aggregates or the collision probability and N is the number of particles per gas volume area. The aggregates surface area increases by coagulation (first term in the equation) and decrease by sintering (second term in the equation) as is described in the equation (29).

$$\frac{da}{dt} = -\frac{1}{N} \frac{dN}{dt} a - \frac{1}{\tau} (a - a_s) \quad (29)$$

Where, τ is the sintering time necessary to reduce approx. the 63% of the excess surface area of an aggregate over the surface area of a sphere with the same mass and a_s is the surface area of an aggregate completely melted in spherical shape as is shows in equation (30).

$$a_s = \left(\frac{v}{v_0}\right)^{2/3} a_0 \quad (30)$$

Where a_0 corresponds to the monomer surface area, v_0 is the monomer volume and v is the aggregate volume, which is only affected by coagulation. Also, the particle size (d_p) and number of particles (n_p) in an aggregate are describe in the equations (36) and (37), where $v_p = (\pi d_p^3)/6$ is the primary particle volume.

$$d_p = \frac{6v}{a} \quad (31)$$

$$n_p = \frac{v}{v_p} \quad (32)$$

The coagulation happens between adjacent primary particles, reducing the number of particles in the aggregates. The morphology of the particles is determinates by the coagulation rate, β , and the characteristic sintering time τ [141]. An accepted model to coagulation is the collision Kernel or coagulation of Kernel. In this model, when the aggregates of particles are submitted to high temperature processes, they are treated as fractal-like, using a relationship between the aggregate volume and the radius of gyration or collision radius [141]. The fractal-like concept in the description of aggregates obtained by aerosol methods facilitates the understanding of the collision rate and their

morphologies [141]. Matsoukas and Friedlander (1991) proposed the relationship of the aggregates volume and collision radius, r_c , show in the equation (33),

$$r_c = r_p \left(\frac{v}{v_p} \right)^{1/D_f} = r_p (n_p)^{1/D_f} \quad (33)$$

Where, r_p is the primary particle radius and D_f is the mass fractal-like dimension.

To calculate the coagulation rate, β , it is used the Fuchs equation ((34)) proposed in 1964, for Brownian collisions in the free-molecular and continuum regime [84], [141].

$$\beta = 8\pi D r_c \left[\frac{r_c}{2r_c + \sqrt{2}g} + \frac{\sqrt{2}D}{c r_c} \right]^{-1} \quad (34)$$

Where g is the transition parameter described below in equations (35) to (39), c is the particle velocity, r_c is the collision radius and D is the particle diffusion coefficient.

$$g = \left[\frac{1}{6r_c l} \right] \left[(2r_c + l)^3 - (4r_c^2 + l^2)^{3/2} \right] - 2r_c \quad (35)$$

$$l = \frac{8D}{\pi c} \quad (36)$$

$$c = \sqrt{\frac{8K_b T}{\pi \rho_p v}} \quad (37)$$

$$D = \frac{K_b T}{6\pi r_c \mu} \left[\frac{5 + 4K_n + 6K_n^2 + 18K_n^3}{5 - K_n + (8 + \pi)K_n^2} \right] \quad (38)$$

$$K_n = \frac{\lambda}{r_c} \quad (39)$$

As described above, the coagulation and coalescence growth processes play an important role in the formation of particles in aerosol technologies. Their determination involve the formation of spherical and non-spherical particles by collisions of particles-particles, particles-molecular clusters and particles-vapor molecules, which are systems mainly governed by the collision kernel of particles [142].

CHAPTER 4. FSP EQUIPMENT DESIGN AND CONSTRUCTION

The equipment to carry out the synthesis processes by flame spray pyrolysis was build-up during the development of this thesis. The design and construction steps followed in this stage are describe in this chapter, however, the optimization of the equipment design was out of the objectives of this project; consequently, basic element designs of the systems were used.

4.1. SET-UP OF THE EQUIPMENT

To build-up the reactor for production of nanoparticles by flame spray pyrolysis was necessary to consider three parts of it: aerosol, burner and collector system, which will be described in depth below. The aerosol system was defined as an airblast nozzle considering the state of the art. This kind of nozzle shows advantages over other nozzles, since the construction simplicity, the manageability of viscous liquids, the formation of fines spray using low pressures and the low production of soot in the combustion of fuels [105]. Otherwise, two different burner systems were analyzed based on the design used by the main research groups in this topic. To collect the products of the synthesis process, the first option was scratch the materials deposited in the surface of the reactor. However, the yields of the reactions were lower than 5 %, leading to consider an electrostatic precipitator as collector system, since expect particles to collect are in the nanosized range.

4.1.1. Aerosol system design and construction

The aerosol system was made-up by an airblast nozzle with coaxial gas flow (atomizer with concentric double air nozzle), in which an slow moving liquid is expose to a high velocity airstream (Figure 4-1) [105]. In general, the efficiency of atomizers is low, with typical values between 2% to 5%, however, the rest of the energy is converted to kinetic energy in the spray, allowing the movement of the particles throughout the collector. Researchers studied the effects of the fluids properties on the mean drop size, concluding that the mass median drop size is mainly governed by the air/liquid mass ratio (ALR), being and important operation factor [104], [105].

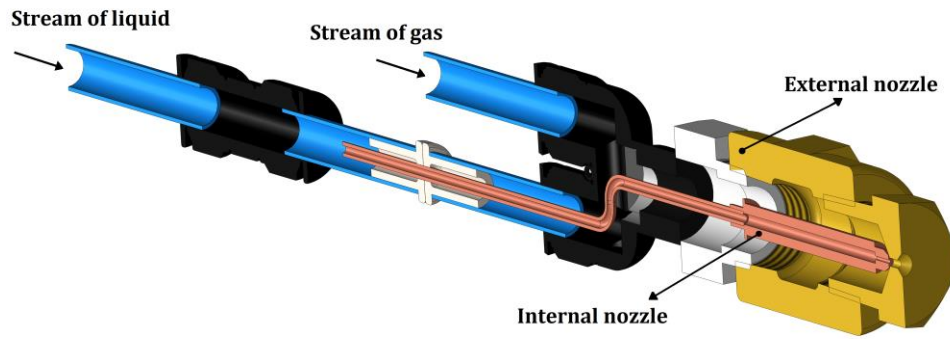


Figure 4-1. Atomization nozzle used during in the flame spray pyrolysis synthesis

The airblast nozzle used during the experimentation was composed by an internal nozzle conducting the stream of liquid, surrounded by a covering nozzle with the stream of gas, in order to break the jet of liquid and form the droplets. Figure 4-2 shows the main characteristics of the airblast nozzle build up to the spray formation. The external nozzle diameter is 11 mm with an internal orifice of ~6 mm of diameter (28.27 mm² of area) in which is located an internal nozzle with an external diameter of 4.1 mm, leaving a free area to the has stream of ~14.2 mm².

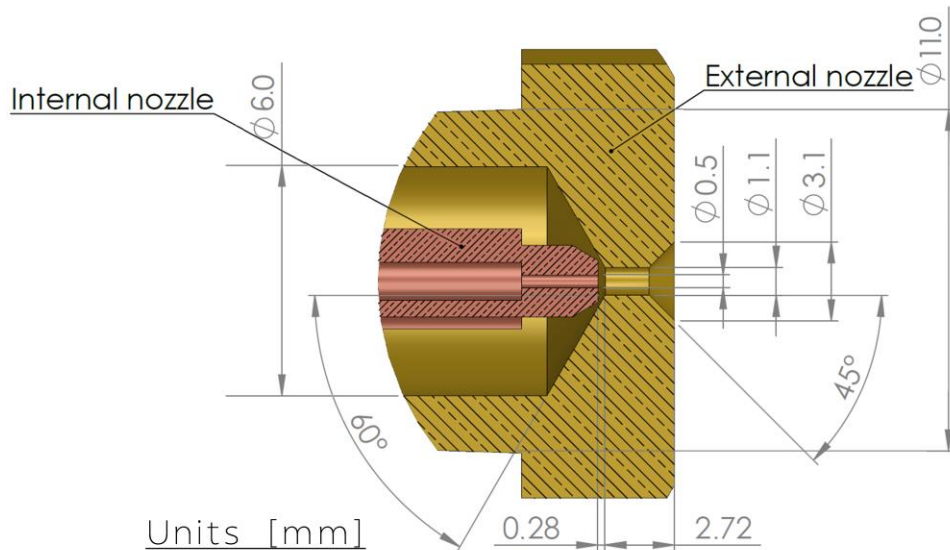


Figure 4-2. Main dimensions of the airblast nozzle

The internal nozzle was manufactured in copper, while the external nozzle was manufacture with commercial brass pipe fittings parts. The main dimension in the liquid-nozzle (internal nozzle) was the outer diameter, D_w , establishing as $D_w \cong 0.5$ mm, which was the smallest diameter that was possible to manufacture using a conventional lathe. The whole dimensions of the internal nozzle are described in Figure 4-3. Defined this dimension, the dimension of the outer gas-diameter nozzle was

evaluated conserving all the nozzle dimensions, using equal or greater diameters values than the D_w . In this sense, the air diameter nozzles evaluated were $D_a \cong 0.5, 0.7, 0.9, 1.1$ and 1.3 mm. The gases used as dispersants were air and oxygen; the air was supplied through a compressor (DeWalt – Model D2002M-WK 150 psi, 6 gal), with air tank pressure of 345 kPa coupled to a commercial pressure gauge to control the pressure in the nozzle. Similarly, the oxygen was supplied through a gas cylinder with a cylinder pressure of 345 kPa coupled in the same way as the air supplied pressure gauge.

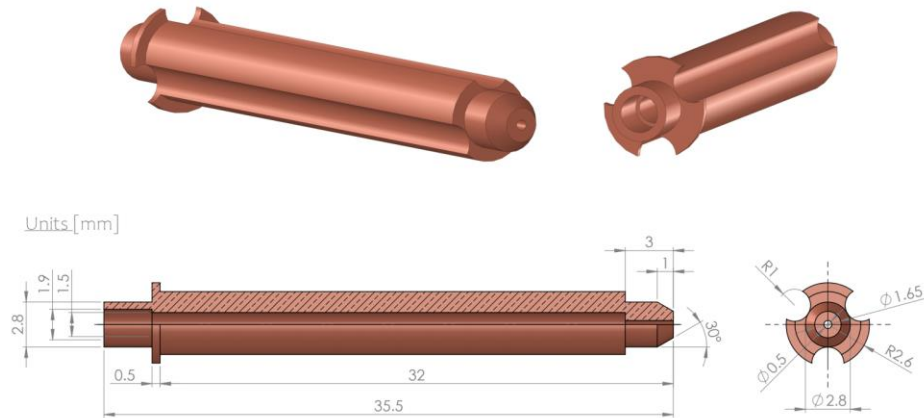


Figure 4-3. Internal nozzle to conduct the stream of liquid

The literature suggested that the air/liquid mass ratio (ALR) must be between 0.1 to 10, due to lower values will not produce proper drops, while higher values waste energy [105]. The ALR values for outer diameters of 0.5, 0.7 mm, 0.9 mm, 1.1 and 1.3 mm (Table 4-1) were calculated at different mass flow rates of starting solution and dispersion gas, having water and air as fluids and using the equations (41), (40), (42) and (43) [143]. The feed flow and pressure of dispersion gas were chosen considering the operation values of the parts of the equipment (peristaltic pump, compressor, welding handles) and the sensibility of the control systems (pressure gauge, rotameter and flow rates controller). The obtained ALR values fitted in the suggested range, whereby the degree of atomization was experimentally tested and observed with each one, considering the build simplicity and low production costs.

$$P = \frac{1}{2} \rho V^2 \quad (40)$$

$$Q = V \cdot S \quad (41)$$

$$\dot{m} = \rho Q \quad (42)$$

$$ALR = \frac{\dot{m}_{air}}{\dot{m}_{liq}} \quad (43)$$

Where, Q is the volumetric flow rate, V is the flow velocity, S is the cross-sectional area of the nozzle, ρ is the density, \dot{m} is the mass flow rate and ALR is the air/liquid mass ratio.

Table 4-1. ALR values at different process conditions

Flow rate (mL/min)- Dispersion pressure (kPa)	ALR(D _{0.5})	ALR(D _{0.7})	ALR(D _{0.9})	ALR(D _{1.1})	ALR(D _{1.3})
10-100	0.60	1.17	1.93	2.89	4.03
10-150	0.73	1.43	2.37	3.53	4.94
10-200	0.84	1.65	2.73	4.08	5.70
10-250	0.94	1.85	3.05	4.56	6.37
20-100	0.30	0.58	0.97	1.44	2.01
20-150	0.37	0.72	1.18	1.77	2.47
20-200	0.42	0.83	1.37	2.04	2.85
20-250	0.47	0.92	1.53	2.28	3.19
30-100	0.20	0.39	0.64	0.96	1.34
30-150	0.24	0.48	0.79	1.18	1.65
30-200	0.28	0.55	0.91	1.36	1.90
30-250	0.31	0.62	1.02	1.52	2.12
40-100	0.15	0.29	0.48	0.72	1.01
40-150	0.18	0.36	0.59	0.88	1.23
40-200	0.21	0.41	0.68	1.02	1.42
40-250	0.24	0.46	0.76	1.14	1.59

The degree of atomization for each air-nozzle diameter was experimentally observed. Even when the nozzles with a diameter of 0.5 mm and 0.7 mm had the ALR values in the theoretical range, the systems showed water hammer phenomenon during the atomization making impossible the control of the pressure gauge, as consequence, these two diameters were discarded. By using the air-nozzle with a diameter of 0.9 mm, the water hammer was solved, however the control of the pressure was difficult due to the large pressure changes with the application of small changes in the pressure gauge. Otherwise, the air-nozzles with diameter of 1.1 mm and 1.3 mm did not show these problems, but the degree of atomization observed with the diameter of 1.3 mm was poor, showing a prolonged jet cylinder at the beginning of the spray. For these reasons, the external diameter was defined as 1.1 mm.

The mean drop sizes for D=1.1 mm were calculated using the *Sauter Mean Diameter* (SMD) equations for plain-jet airblast atomizers described by Nukiyama & Tanasaw, in which are not consider effects of the nozzle dimensions or air density (equation (44)); and Lorenzetto & Lefebvre (equation (45)) and Jasuja (equation (46)) in which the SMD is independent of initial jet diameter for low viscosity liquids [105].

$$SMD = 0.585 \left(\frac{\sigma_L}{\rho_L U_R^2} \right)^{0.5} + 53 \left(\frac{\mu_L^2}{\sigma_L \rho_L} \right)^{0.225} \left(\frac{Q_L}{Q_A} \right)^{1.5} \quad (44)$$

$$SMD = 0.95 \left[\frac{(\sigma_L W_L)^{0.33}}{\rho_L^{0.37} \rho_A^{0.30} U_R} \right] \left(1 + \frac{W_L}{W_A} \right)^{1.70} + 0.13 \left(\frac{\mu_L^2 D_o}{\sigma_L \rho_L} \right)^{0.5} \left(\frac{Q_L}{Q_A} \right)^{1.5} \left(1 + \frac{W_L}{W_A} \right)^{1.70} \quad (45)$$

$$SMD = 0.19 \left(\frac{\rho_L}{\rho_L \rho_A} \right)^{0.35} (1/U_A) \left(1 + \frac{W_L}{W_A} \right)^{0.25} + 0.127 \left(\frac{\mu_L^2 D_o}{\sigma_L \rho_L} \right)^{0.5} \left(1 + \frac{W_L}{W_A} \right) \quad (46)$$

Where U_R is the relative velocity of air to liquid, σ_L is the liquid surface tension, ρ_L is the liquid density, ρ_A is the air density, μ_L is the liquid viscosity, D_o is liquid orifice diameter, or initial jet diameter (m), Q_L and Q_A are the volumetric flow rate of the liquid and air, respectively and W_L and W_A are the mass flow rate of the liquid and air, respectively,

Table 4-2. Mean drop size calculations

Flow rate (mL/min)-Dispersion pressure (kPa)	SMD (mm) (Nukiyama & Tanasawa)	SMD (mm) Lorenzetto & Lefebvre	SMD (mm) Jasuja
10-100	0.19	0.57	0.47
10-150	0.14	0.53	0.44
10-200	0.12	0.50	0.43
10-250	0.10	0.48	0.42
20-100	0.52	0.85	0.59
20-150	0.39	0.74	0.54
20-200	0.31	0.68	0.51
20-250	0.26	0.64	0.49
30-100	0.95	1.18	0.71
30-150	0.70	0.99	0.64
30-200	0.57	0.89	0.60
30-250	0.48	0.82	0.57
40-100	1.45	1.54	0.83
40-150	1.07	1.27	0.74
40-200	0.87	1.12	0.68
40-250	0.73	1.02	0.65

These equations are considered better to describe the drop formation in plain-jet airblast nozzles [105]. The values obtained for the mean drop sizes considering a water-nozzle diameter of $D=1.1$ mm are shown in Table 4-2. The results obtained for each equation differs due to particular assumptions consider for each one. There is possible to observe that the increment in the dispersion pressure leads to smaller drop sizes, opposed to the increment of the liquid flow rate, which increase the drop mean size. The Nukiyama & Tanasawa equation suggest the formation of droplets under 0.95 mm for feed flow rates under 30 mL/min, providing a liquid fed with enough surface area to improve the vaporization processes required in the formation of the particles.

The cone angle of the spray is a factor slightly affected by the nozzle dimensions, being mainly governed by fluids properties as viscosity and surface tension of the liquid [104]. The cone angle observed during the formation of the spray was around 4° , as is shown in Figure 4-4.

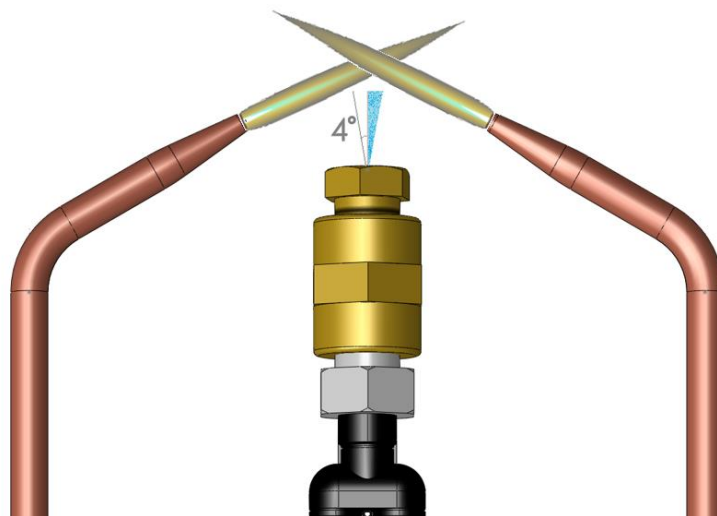


Figure 4-4. Spray cone

4.1.2. Burner system design and construction

The configuration of the burner system was experimentally defined. The most used flame configurations correspond to coaxial flow flame and a cross-flow, considering the spray direction. In both systems were used industrial gases for the combustion (oxygen and acetylene), which are inexpensive and highly accessible.

Initially, a coaxial flame was evaluated as burner system, however the high consumption of gases and the small amount of collected material during the synthesis leads to propose an alternative system

with cross-flames in perpendicular direction of the aerosol. The coaxial flame assemble is show in the annex section. Nevertheless, with the results obtained by using this coaxial flame, it was defined the ratio of the combustion gases ($C_2H_2:O_2$ ($m^3: m^3$) 1:1.67).

4.1.1.1. Dual-flame perpendicular to the spray direction

The dual-flame burner consists in two crossed flames perpendicular to the spray of precursors. To join up the dual-flame burner were used two Victor® torch handles with tips N°1. This kind of tip was chosen because of it allows the minimum flow gases of the Victor® torch handles, allowing a lower gases consumption during the synthesis process. The delivery pressure of the cylinders was choose following the specifications in the torchers manual as 35 psi for O_2 and 7 psi for C_2H_2 [144] (Figure 4-5).

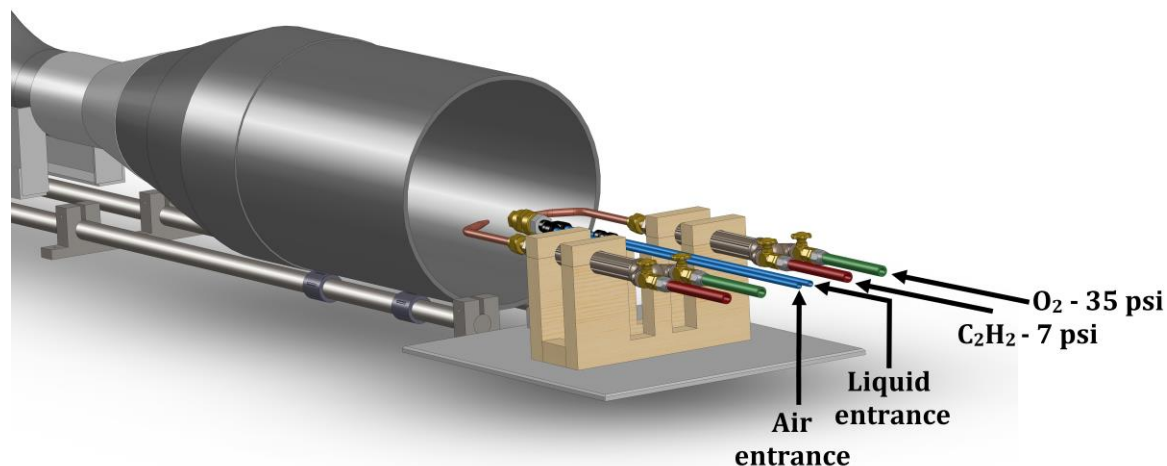


Figure 4-5. Dual-flame burner

The distance of the tips (Figure 4-6) was determinates considering the interference between flames and contact with the aerosol, joining the outer envelope or acetylene feather to make it as small as it was possible without affecting the integrity of the welding nozzles. In addition, in the meeting point of the flames, it is formed a flame with higher area, which must have complete contact with the spray to have a proper vaporization process. In this sense, it was also considering the contact of the spray cone and the flame.

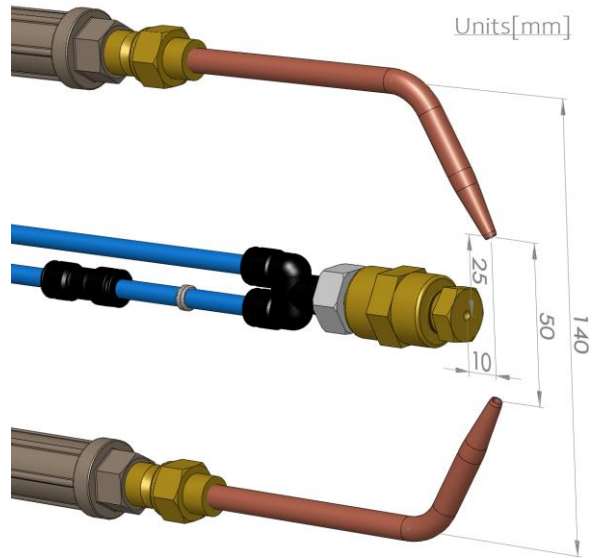


Figure 4-6. Distance between the tips in the dual-flame burner

The nozzle is supported in an aluminum frame, which allows the adequacy of the distance to the flames and the height of the nozzle with respect to the midpoint of the flames, in order to ensure that all the spray was ignited. Likewise, the welding handles were supported in wood frame as it is shown in (Figure 4-7).

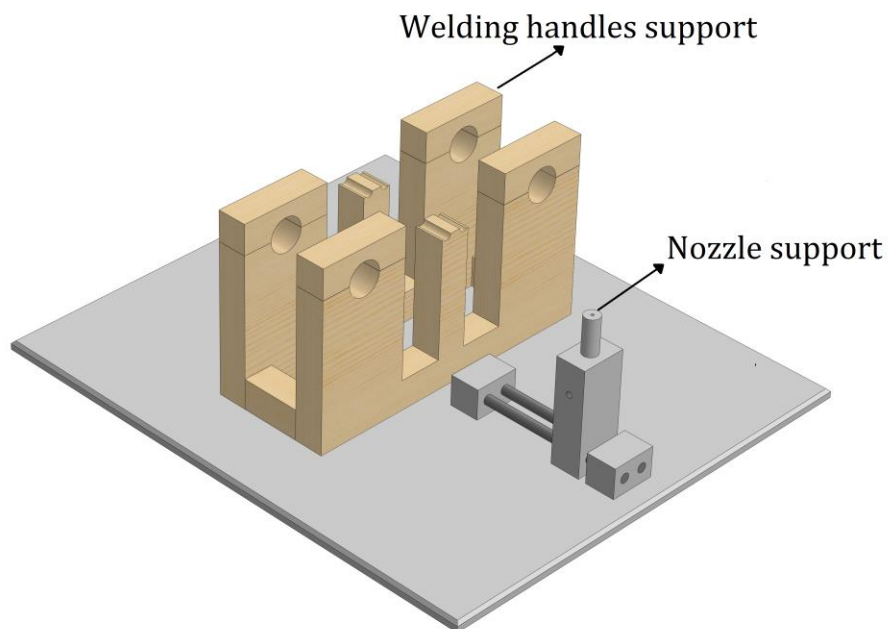


Figure 4-7. Supports of the welding handles and nozzle

4.1.3. Electrostatic precipitator design and construction

To collect the nanoparticles was made a tubular electrostatic precipitator of aluminum because of its durability, availability, thermal and electrical conductivity. The precipitator was formed by four tubes of 75 cm of length and 7.6 cm of diameter, resulting in a specific collecting area of 0.72 m². A rigid aluminum rod of ¼ in of diameter and 85 cm of length connected to a metal mesh at the ends of the rod, was used as discharge electrode, hold in a glass coupling located at both ends of each tube. The voltage between the places was placed between 12-15 kV (AC). This voltage was achieving with a high voltage power supply CXDZ Model CX-150A, with an output voltage DC: 2kV-15kV. The schema of the electrostatic precipitator is show in Figure 4-8.

The efficiency of the precipitator depends of the total collecting area and the amount of independent electrical energization. The efficiency of the ESP is determined by the Deutsch-Anderson equation, show in the equation (47).

$$\eta = 1 - e\left(-\frac{V_{pm}A_c}{Q}\right) \quad (47)$$

Where η is the collection efficiency of the precipitator, A_c is the effective collection area (m²), V_{pm} is the particle migration velocity (m/s) and Q is the volumetric flow rate of gas (m³/s). This equation does not consider the particle size and particle distribution of the powders, assuming a uniform migration velocity, neglecting that larger particles have higher migration velocity than smaller particles. In addition, particles deposition in the surface of the precipitator or sneakeage factor through the system is not contemplate. Considering a constant migration velocity (m/s) of 0.04, determinate for calcium carbonate particles [145], [146] and assuming a volumetric flow rate of air of 0.0133 m³/s measured with an anemometer (Wavetek Meterman TAQ10) at the beginning of the electrostatic precipitator, using an air-nozzle with 1.1 mm of diameter and a dispersion pressure of 275 kPa, the efficiency of the precipitator calculated with the Deutsch-Anderson equation is the 88.4 %.

The particle migration velocity in Deutsch-Anderson equation depends on the main forces acting in the particle, corresponding to gravitational, electric, viscous and inertial forces. Whereby, the particle migration velocity equation is expressed as (48),

$$V_{pm} = \frac{qEC}{3\pi\mu d} \quad (48)$$

Where, q corresponds to the charge of the particle, C is the Cunningham correction factor, E is the collector electric field, μ is the viscosity and d is the particle size. From equations (47) and (48) is possible to observe that higher volumetric flow rates (Q) and small particle sizes leads to lower

efficiencies in the precipitator. Also, higher collecting area increase the efficiency but increase the production costs and hinders the cleaning process.

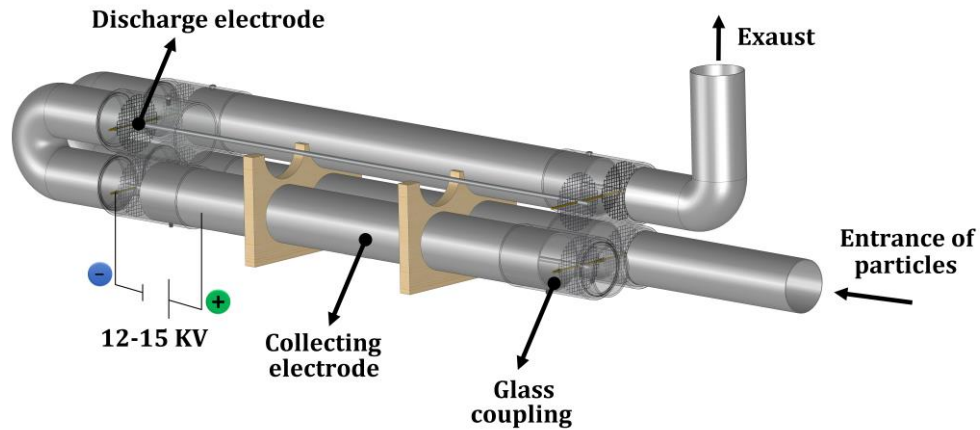


Figure 4-8. Schema of the electrostatic precipitator (ESP)

4.1.4. Design of additional elements in the reactor

In order to collect the powders in the reactor after the ignition of the starting solution in the flame, the primary burning zone is formed by a cylinder of low carbon steel which is allow to support the high temperatures at the beginning of the reaction. The cylinder was commercially obtained with an internal diameter of 22.32 cm (8 in), and a thickness of ~ 1 cm (3/8 in) with a length of 40 cm. Then, the reaction deposition area is reduced with cone of 29,2 cm of height from 22 cm of diameter to 8.8 cm of diameter, corresponding to the internal diameter of a low carbon steel commercial tube, which was deformed in shape of S to have a velocity drop of the gas flow rate and drop in temperature before the entrance in the electrostatic precipitator.

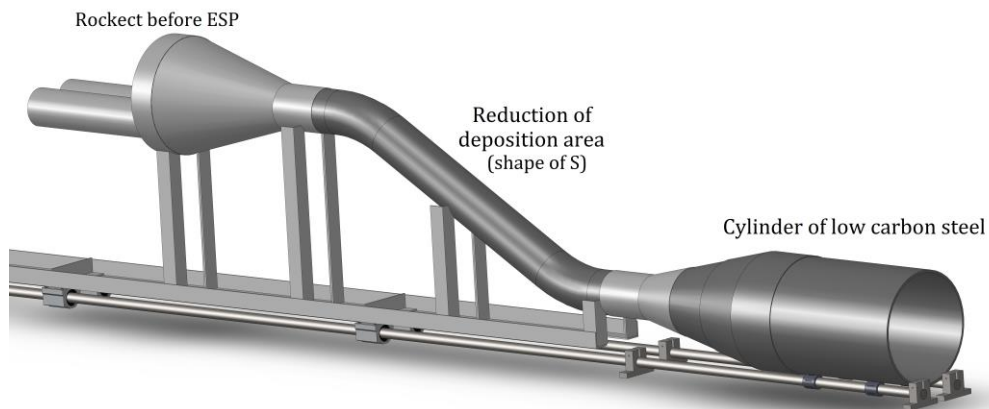


Figure 4-9. Primary burning zone

The chassis to support the system was built with aluminum angle profiles of 38.10x38.10 cm (1 ½x1 ½ in) (Figure 4-10). The total length of the chassis is 1.65 m with five perpendicular bars distributed in the main horizontal line to hold the parts. The whole frame can be moved forward or backward because it is supported on four linear ball bearing sealed, in order to avoid contamination of soot in the inside of the reactor when the flame is lit and adjusted.

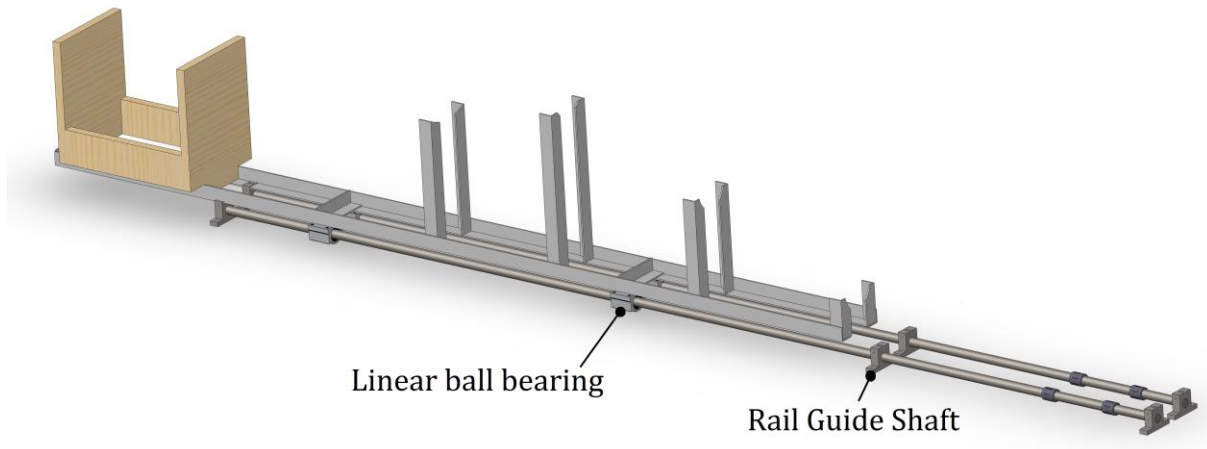


Figure 4-10. Frame of the FSP equipment

The cooling system of the equipment is formed by four fans (Kalley - High Power Fan Model K-VP20HS) located behind the equipment (Figure 4-11). These fans keep the temperature of the electrostatic precipitator below 30 °C and significantly decrease the temperature in the primary burning zone to values below than 500 °C, avoiding sintering process, which could increase the particle size in the reactor.

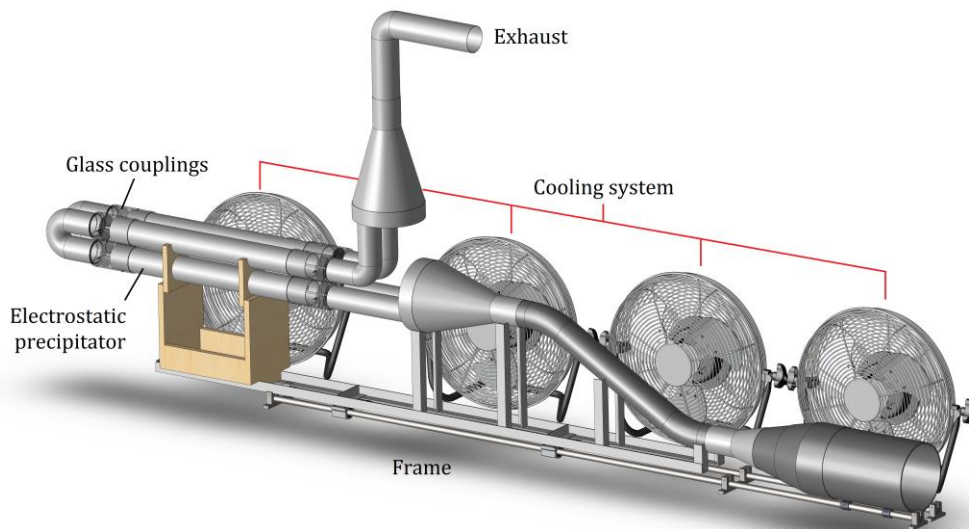


Figure 4-11. Cooling system in the FSP equipment

In the whole system, a fraction of the particles is collected in the electrostatic precipitator (15-20%) and the rest is collected from the surface of the equipment, where the particles are deposited by impact. The total efficiency of the system was 30-45 %, where the large particles are obtained from the surface, while the smaller particles are obtained in the ESP [100]. The full equipment schema and a picture of the real system are shown in Figure 4-12 and Figure 4-13, respectively.

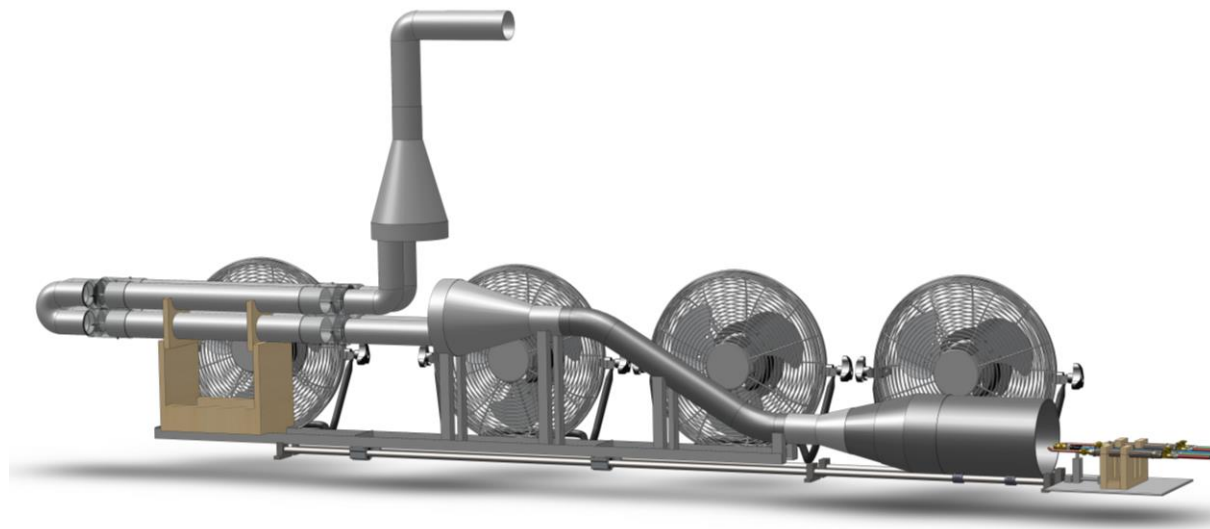


Figure 4-12. Schema of the FSP equipment for the synthesis of nanoparticles



Figure 4-13. Image of the FSP equipment for the synthesis of nanoparticles

The equipment presented in this chapter was used for all the synthesis processes described in this research and later related projects developed in the research group. Additional photographs of the final equipment and building stages are shown in the annex (Chapter 10, Section 10.2).

CHAPTER 5. MATERIALS AND METHODS

Chapter 5 is concerned to the initial experimentation and its conditions. The general methodology followed during the experimentation is described in this section. The starting materials used during the reactions, their decomposition processes and the set-up of the synthesis process to define the final conditions to study the effects of the process in the materials are discussed. Finally, the experimental design and the characterization techniques used are described.

5.1. Methodology

The design and construction of the FSP equipment was carried out as first stage of this project. The equipment has gases flow, gases pressure and feed flow rate controllers. After the set-up of the equipment and previous experimental tests, the tasks to carry out the experimentation of this project are described and summarized in the flow diagram below (Figure 5-1).

- Set-up of the synthesis process by the definition of the chemical systems and process parameters was performed. For this, different inorganic and organic calcium resources were tested in order to define an adequate precursor to obtain calcium silicate phases. In the same way, the solvents to prepare the starting solution were defining. As silicon resource, tetraethyl orthosilicate was used.
- Identification of process parameters, which have a strong influence on the powders to be manufactured. This research evaluated the effect of five process parameters and their combination effects over the final products of synthesis. The chosen parameters were precursors flow rate, dispersion gas pressure, ceramic loading of the solution, solvent and dispersion gas. The values of each factor were chosen based in the literature and previous experience.
- Synthesis processes to evaluate the effects of the process were executed by using a random matrix of the experimental design, under the conditions previously defined. For this purpose, a two-level fractional factorial design with resolution III, 2^{5-2} , which permit estimation of all the main effects with no aliasing by two-factor interactions was used. The statistical analyses of the data were performed in the Minitab® software.
- Characterization of anhydrous and hydrated products by different techniques:
 - Phases composition identification were carried out using X-ray diffractometer with Rietveld refinement. Thermal analysis coupled to mass spectrometer and infrared spectroscopy (TGA/DSC+MS/FTIR) and Fourier transform infrared spectroscopy FT-IR were used to identify the additional chemical information of the powders.

- Scanning electron microscopy (SEM), Transmission electron microscopy (TEM) and Brunauer-Emmett-Teller (BET) surface area analysis was carried out to identify the differences in the specific surface area and morphology of the particles to evaluate the effects of the process conditions.
- The reactivity of the samples was carried out using a calorimeter which allows the measurement of very small heat changes, giving information to study the hydraulic behavior of the samples.
- The analysis of data was carried out using different software. The process information was analyzed using Minitab® statistical software, in order to identify the influence of process parameters on samples structural properties. XRD data were processed with X'Pert High Score Plus. Other data processing were performance using OriginPro.
- Finally, with the data obtained from the characterization, it was proposed the correlation between the properties of the powders with the process parameters and the mechanism of formation of the calcium silicates obtained during the synthesis processes.

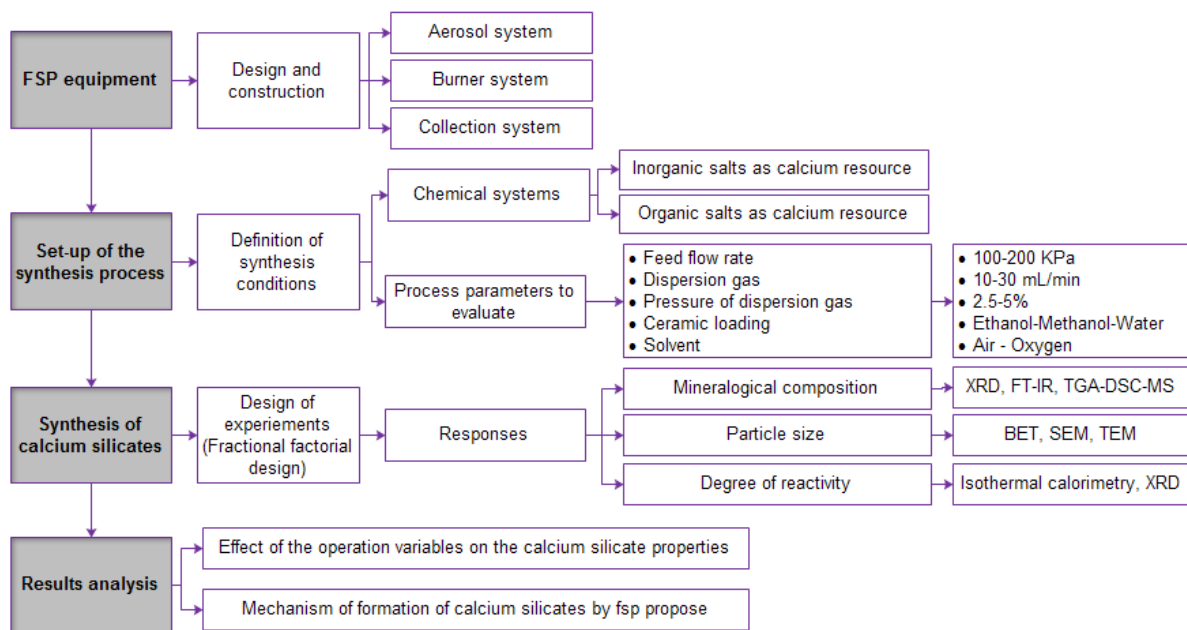


Figure 5-1. Methodology of the experimental section of the project

5.2. Precursors

The most common precursors used during flame spray pyrolysis synthesis, correspond to carboxylates, nitrates and acetates as it was mentioned above in Chapter 3. The use of

organometallics and metallorganic compounds is preferred since the volatility of these compounds is usually lower than the volatility of the solvents, favoring the gas-to-particle conversion after the ignition and during the growth process.

To produce calcium silicates phases by FSP were proved four chemical systems by the combination of different raw materials and solvents, which will be describe below. During the synthesis process, three calcium resources corresponding to calcium nitrate, calcium 2-ethylhexanoate and calcium propionate, and three solvents corresponding to ethanol, methanol and water were evaluated. Additionally, the use of emulsifiers was considered.

5.2.1. Tetraethyl orthosilicate

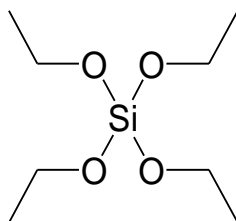
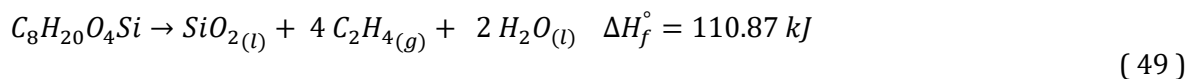


Figure 5-2. Tetraethyl orthosilicate structure

Tetraethyl orthosilicate, Si(OC₂H₅)₄, (called also TEOS or tetraethoxisilane) is an important reagent used during the synthesis of silica and silicon-based nanoparticles. This compound is a volatile liquid at room temperature and presents low toxicity. Several studies had been developed to understand its thermal decomposition kinetics, since its large demand in the industry. This compound is widely used as silicon resource in the synthesis of ceramics nanoparticles by flame spray pyrolysis. Seshu et al., found that during TEOS thermal decomposition analysis at 700 °C and 33.33 Pa, take place the formation of acetaldehyde, ethylene, ethanol, ethane and diethyl ether [147], while Chu et al., suggested the formation of diethoxy silicate, ethanol and ethylene [148]. D. Nurkowski et al. 2013, concluded that the dominant decomposition of TEOS, results in the elimination of ethylene and C-C bonds, which allows the formation of silanols and silicic acid [148]. Spitzmüller et al., 1998, found by STM and XPS analysis, that TEOS start the decomposition into a triethoxysiloxane and ethyl groups, bounded to Si atoms. Then, at elevated temperatures, the ethyl groups are broken resulting in the formation of diethoxysiloxane and ethyl groups. Later, at 690 K, the ethyl groups are decomposed in H_{adsorbed} and hydrocarbons as ethylene, and finally at 850 K, the diethoxysiloxane decomposition take places resulting in hydrogen release and carbide formation [149]. During the synthesis of calcium silicates, TEOS (Si(OC₂H₅)₄, 98%) from Sigma Aldrich was used as silicon resource. The decomposition reaction of TEOS is show in (49) [125].



5.2.2. Calcium 2-ethylhexanoate

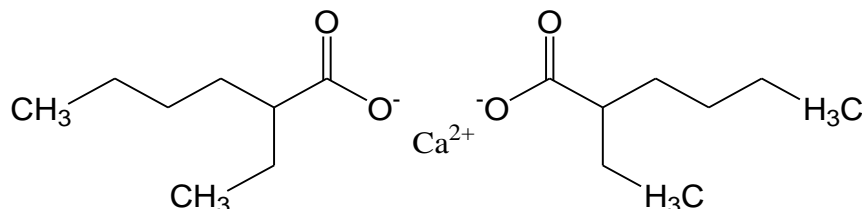
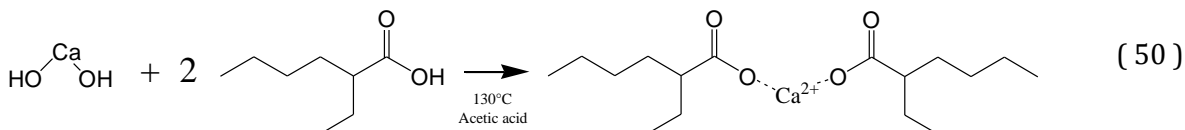


Figure 5-3. Calcium 2-ethylhexanoate structure

Calcium 2-ethylhexanoate is a metallorganic compound belonging to the carboxylates or ester of a carboxylic acids, which is insoluble in ethanol and soluble in water and toluene. This compound is widely used in commercial applications related to the production of nanoparticles and thin films. Other applications include food, pharmaceutical and cosmetic industries [150].



Calcium 2-ethylhexanoate was prepared in the laboratory of Chemistry of Cement by heating a metal hydroxide-alkanoic acid mixture to promote ligand exchange (Figure 5-4) as is shown in reaction (50). For this, a distillation system under nitrogen atmosphere was charged with calcium hydroxide (11.1572 g, 0.0342 mol) and 2-ethylhexanoic acid (56 mL) in anhydrous acetic acid (76 mL). The mixture was heated at 130 °C for 6 hours under stirring. The solution was distilled off of 2-ethylhexanoic acid, acetic acid and water to complete the reaction. A clear solution was obtained when the reaction was complete. After cooling at room temperature, the metal carboxylate was filtered by suction and washed with hexane. The solid is dried, ground and stored (22.7855 g, 46 %). The product was analyzed by TGA and FT-IR.

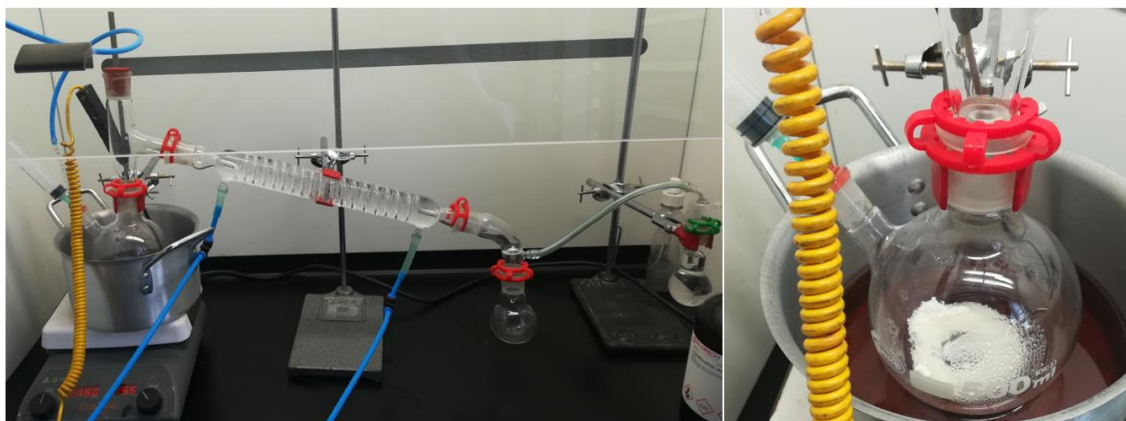


Figure 5-4. Synthesis of calcium 2-ethylhexanoate

In Figure 5-5 is observed the Fourier transform infrared spectrum of the product of synthesis of calcium 2-ethylhexanoate. The spectrum shows the presence of residual starting materials from the synthesis process. At the beginning, the presence of these compounds, acetic acid and 2-ethylhexanoic acid, do not affect the stoichiometry by FSP, since all of them are organic materials, which were evaporated during the ignition process. However, it is necessary to determine the ceramic yield of the precursor, to determine the stoichiometry during the reaction. To obtain this value, thermal analysis is required. In the FT-IR spectra are observed a group of bands between 715-740 cm^{-1} belonging $-\text{C}-\text{H}$ vibrations of the organic chain. In addition, two bands at 1448 cm^{-1} and 1546 cm^{-1} attributed to $\text{C}=\text{O}$ vibrations of the carboxylic acid are observed, while the bands between 2870-3000 cm^{-1} correspond to $\text{C}-\text{H}$ stretching vibrations of the alkyl chain and the band at 3562 cm^{-1} correspond to $\text{Ca}-\text{O}$ vibrations. The other bands are attributed to 2-ethylhexanoic acid and anhydrous acetic acid used during the synthesis process.

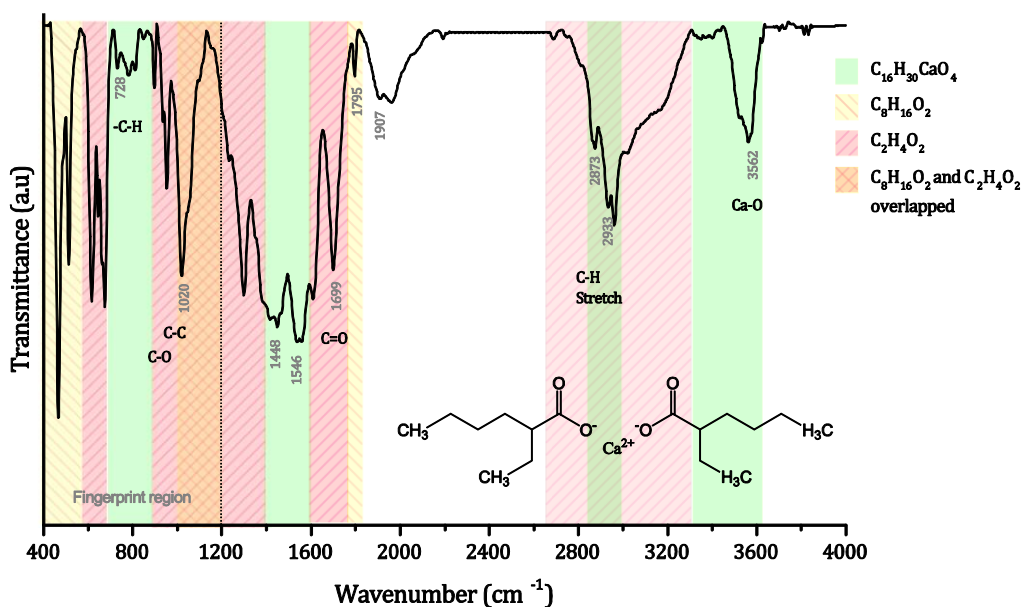


Figure 5-5. FT-IR spectrum of calcium 2-ethylhexanoate

In Figure 5-6 is shown the DSC-TGA plot of calcium 2-ethylhexanoate. The curve shows three losses of mass around 200, 405 and 730 °C. The first mass loss of 23.52 %, until 200 °C correspond to the loss of external methyl groups of the 2-ethylhexanoate group. Then, at 405 °C a loss of mass of 31.92 % occurs in two small steps (~16 % and ~15.92%) corresponding to the loss of alkyl radicals. Finally, at 600 °C starts the last mass loss, corresponding to RC=O radicals closer to the calcium, giving place to the formation of CaO. The residual mass after the thermal decomposition corresponds to the ceramic yield of the compound, which indicates the percentage of organic precursor, which will be converted in a ceramic material. This value is used to calculate the stoichiometry of the compound to flame spray pyrolysis synthesis.

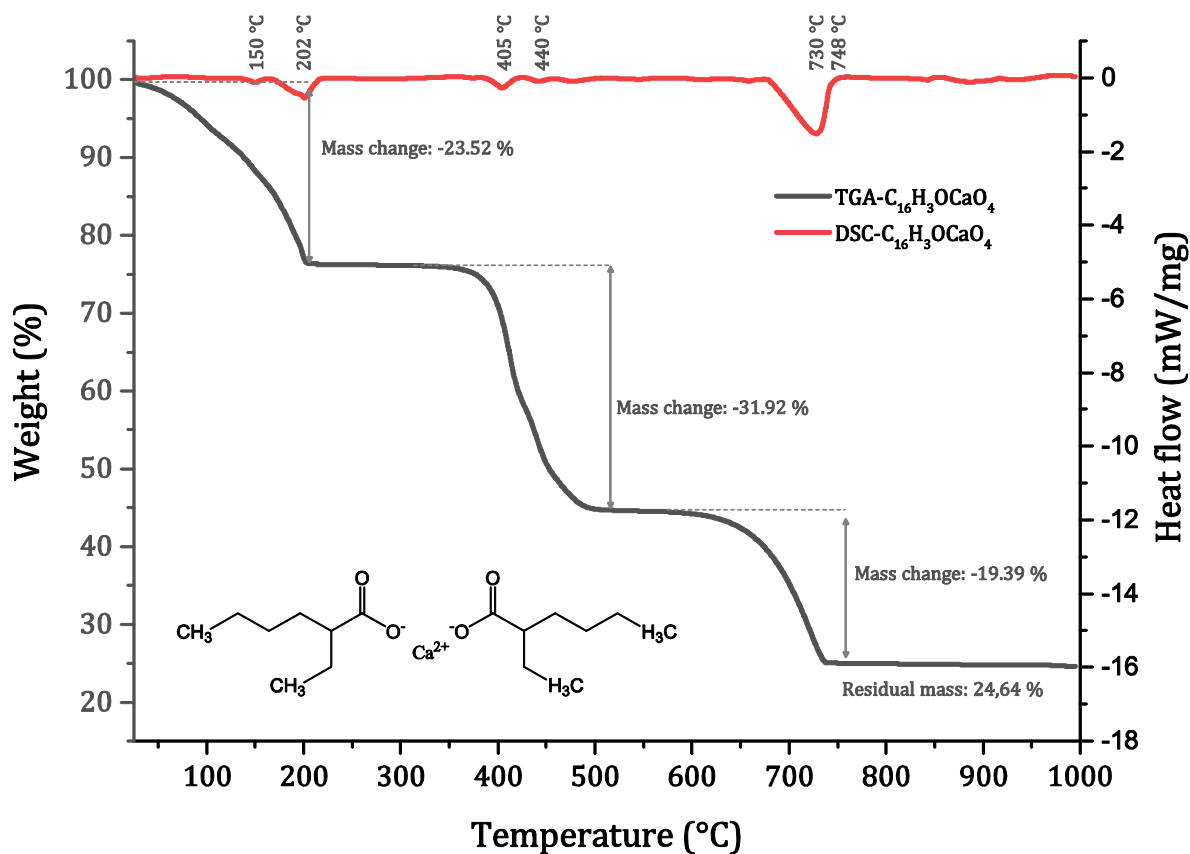


Figure 5-6. DSC-TGA curve of calcium 2-ethylhexanoate

5.2.3. Calcium propionate

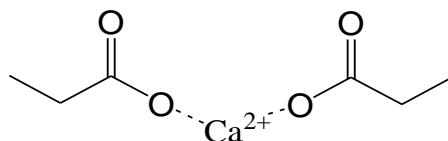
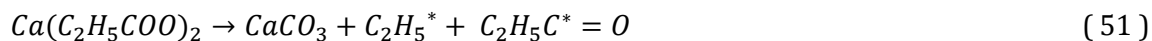


Figure 5-7. Calcium propionate structure

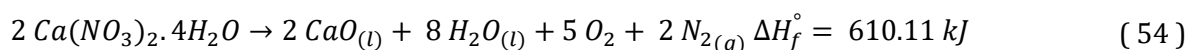
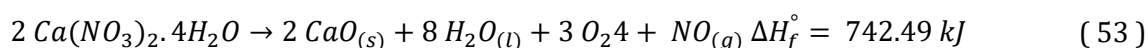
Calcium propionate is a metallorganic compound belonging to the carboxylates or ester of a carboxylic acids, widely used as preservative in the food industry, antifungal agent in bakery and sorbent of sulfur dioxide and nitric oxide emissions in coal-fired power plants [151]. This reagent is soluble in water and slightly soluble in ethanol.

During the thermal decomposition of calcium propionate, calcium carbonate is formed, which is decomposed by increasing the temperature upon 570 °C. This reaction is followed by the decomposition of the alky chains formed during the reactions, which are shown in equations (51) and (52) [151]–[153]. Calcium propionate was purchased from Protokimika S.A.



5.2.4. Calcium nitrate tetrahydrate

Calcium nitrate tetrahydrate is an inorganic salt obtained with nearly stoichiometry water content and high purity, which possess low price and high availability. It melts at low temperature, achieving liquid phase before decomposition (42.5 °C melting temperature) and it is very hygroscopic [154]. The thermal processes depend of the experimental conditions used during the decomposition [155]. Calcium nitrate tetrahydrate decompose commonly in HNO₃, NO, NO₂, O₂ and calcium oxide. In reactions (53) and (54) is shown the decomposition of this inorganic salt resulting in the partial or total decomposition of NO₃ radials in NO, O₂ and N₂ [155].



During the synthesis processes to obtain calcium silicates, calcium nitrate tetra-hydrate (Ca(NO₃)₂·4H₂O, 98%) from J.T Baker® Avantor Performance Materials, Inc., was used as one of the calcium resources evaluated, due to its low price, availability and high solubility in polar solvents as ethanol, methanol and water.

5.2.5. Triethanolamine

Triethanolamine, with chemical formula C₆H₁₅NO₃, is a ternary amine extensively used for agricultural, construction and cosmetic applications. In addition, this compound is widely used as complexing agent and emulsifier in chemist industry, because of its versatility to form coordination compounds with transition metals.

During the formation of coordination compounds, triethanolamine usually acts as an N,O,O'-tridentate ligand, however it can act as N,O,O',O''-tetradentate ligand with metal ions of large ionic radii, to form -atranes compounds (heterocyclic structures) [156]. During this project, triethanolamine (USP-NF) pure, pharma grade from PanReac AppliChem was used.

5.2.6. Solvents

Ethanol and methanol are organic solvents, which directly react in the flame, releasing heat, while water is an inorganic solvent, which take heat away from the flame during the evaporation. The use of water was necessary due to the limited solubility of the precursors in organic solvents. Ethanol from Protokimica, 96% purity, methanol from Sigma-Aldrich (99.8% of purity) and deionized water where used as solvents during the reaction processes.

5.3. Characterization techniques

Chemical and physical characterization of samples prepared by flame spray pyrolysis was perform. Qualitative and quantitative phases determination of anhydrous and hydrated samples were carried out by X-Ray diffraction in an PANalytical EMPYREAN X-ray diffractometer, with an X'Celerator detector Bragg Brentano geometry (CuK α λ = 1.5418 Å) operated at 45 kV / 40 mA (1800 W), with a diffraction interval between 5 and 70 ° (2 θ), with steps of 0.013 ° (2 θ) and time per step of 38 s. The software X'Pert-HighScore plus was used to identify the crystalline phases and their quantification was carried out through the Rietveld method using the free software GSAS.

Chemistry qualitative information was obtained by Fourier transform infrared spectroscopy analysis (FT-IR). The measurements were carried out under ambient conditions in a Shimadzu FT-IR spectrometer (model IRTracer-100 and model FTIR 8400S) between 400 cm⁻¹ to 4000 cm⁻¹ (spectral resolution 2 cm⁻¹). Additionally, Raman Spectrometer measurements were carried out in a LabRam HR, HORIBA, Confocal Raman Microscope, using a He-Ne Laser (532 nm) with a measurement wavelength range from 200 nm to 2000.

Thermal analysis of the precursors (TGA) were carried out in a TA Instruments Hi-Res TGA 2950 equipment, with nitrogen atmosphere (40 mL/min), with temperature variations from 30 to 700 °C at a heating rate of 10 °C/min. On the other hand, the thermal analysis of the samples was carried out from room temperature to 1000 °C in a thermobalance STA 449 F3 Jupiter® Netzsch, equipped with two furnaces on a double hoisting gear, coupled with a FT-IR unit of Bruker Optics and a mass spectrometer of Netzsch.

Morphologies of the samples were evaluated by scanning electron microscopy (SEM) in an equipment Model EVO MA10, Carl Zeiss. Powders were dispersed in acetone during 10 minutes using an ultrasonic bath and deposited in a silicon polished holder. Samples were coated with gold using a QT150R sputter, Quorum Technologies. Additionally, Transmission Electron Microscope (TEM) were

carried out in a JEOL JEM-2100 equipped with a field emission cannon (FEG) and a high resolution CCD camera (Gatan).

Specific surface area measurements (BET) were carried out in a Flowsorb II 2300 with multigas manifold, by determining the quantity of gas adsorbed as a single layer of molecules on the sample, by the single point procedure, using a Nitrogen:Helium mixture of 30:70 (% volume) and a cold bath of liquid nitrogen.

The calorimetry measurements were carried out in an isoperoboilc arrangement equipped with three measuring stations and one reference station. During the measurements, 0.2000 g of each sample were weight and deposit in copper vials. After 24 hours of stabilization, the samples were hydrated with deionized water using a w/s of 5.0, without stirring. The hydration was stopped after 48 and 168 hours, and XRD measurements of the hydrated product were made.

5.4. Set-up of the synthesis process

In order to define the most appropriate chemical system to produce calcium silicates, four different combinations of raw materials showed in Table 5-1 were evaluated. It is well-know that metal nitrates in ethanol tends to produce nanosized particles as large particles, however its evaluation was done considering that the use of low-cost fuels as acetylene, which possess high combustion enthalpy and allows the production of homogeneous nanopowders when low enthalpy precursors are used [111].

Table 5-1. Chemical systems evaluated in the synthesis of calcium silicates by FSP

Nomenclature	Calcium resource	Silicon resource	Solvent
Nit/EtOH	$\text{Ca}(\text{NO}_3)_2 \cdot 4\text{H}_2\text{O}$	$\text{Si}(\text{C}_8\text{H}_{20}\text{O}_4)$	Ethanol
EH/EtOH-W	$\text{C}_{16}\text{H}_3\text{OCaO}_4$	$\text{Si}(\text{C}_8\text{H}_{20}\text{O}_4)$	Ethanol + Water
Prop/EtOH-W	$\text{Ca}(\text{O}_2\text{CCH}_2\text{CH}_3)_2$	$\text{Si}(\text{C}_8\text{H}_{20}\text{O}_4)$	Ethanol + Water
Prop/EtOH-W-TEA	$\text{Ca}(\text{O}_2\text{CCH}_2\text{CH}_3)_2$	$\text{Si}(\text{C}_8\text{H}_{20}\text{O}_4)$	Ethanol + Water + $\text{C}_6\text{H}_{15}\text{NO}_3$

The combustion enthalpy of the process depends of the chemical system and the flame properties. For this reason, the process parameters of the synthesis were kept constant in order to observe the isolated effects of the chemical system in the products. The process parameters used in this stage are listed in Table 5-2.

Table 5-2. Process conditions used during the set-up of the synthesis

Process parameters	Value
Feed flow rate (mL/min)	10
Dispersion gas	Oxygen
Pressure of dispersion gas (kPa)	200
Ceramic loading (% wt.)	5
Acetylene flow	0.011 m ³ /min
Oxygen flow	0.019 m ³ /min

5.4.1. Starting solution preparation

The preparation of the starting solution for each system is shown below. The stoichiometric quantities of calcium and silicon resources used during the synthesis set-up to produce 10 g of Ca₂SiO₄ are mentioned in Table 5-3.

Table 5-3. Stoichiometry of chemical reactions

Precursors	Nit/EtOH	EH/EtOH-W	Prop/EtOH-W	Prop/EtOH-W-TEA
Ca(NO ₃) ₂ ·4H ₂ O (g)	27.9820	-	-	-
C ₁₆ H ₃ O ₄ CaO ₄ (g)	-	29.4661	-	-
Ca(O ₂ CCH ₂ CH ₃) ₂ (g)	-	-	22.0699	22.0640
Si(C ₈ H ₂₀ O ₄) (g)	12.2174	12.2179	12.2188	12.2172
Ethanol (mL)	246	125	190	190
Water (mL)	-	81	50	50
C ₆ H ₁₅ NO ₃ (mL)	-	-	-	2

Starting solution of Nit/EtOH - Calcium nitrate tetra hydrate, Ca(NO₃)₂·4H₂O, 98%, (27.9820 g, 0.1184 mol) is dissolved in 100 mL of ethanol. Then, tetraethyl orthosilicate, Si(OC₂H₅)₄, 99%, (12.2174 g, 0.0586 mol) is dissolved in 146 mL of ethanol and added slowly to the calcium solution. The solution is stirred during 10 minutes and then, it is brought to the synthesis equipment.

Starting solution of EH/EtOH-W - Calcium 2-ethylhexanoate, C₁₆H₃O₄CaO₄, ceramic yield 0.25, (27.13161, 0.0831 mol) is dissolved in 81 mL of distilled water. Then, tetraethyl orthosilicate, Si(OC₂H₅)₄, 99%, (12.2179 g, 0.0586 mol) is dissolved in 125 mL of ethanol and added slowly to the calcium solution. The solution is stirred during 10 minutes and then, it is brought to the synthesis equipment.

Starting solution of Prop/EtOH-W - Calcium propionate, Ca(O₂CCH₂CH₃)₂, 98 %, (22.0699 g, 0.1185 mol) is dissolved in 50 mL of distilled water. Then, tetraethyl orthosilicate, Si(OC₂H₅)₄, 99%, (12.2188 g, 0.0586 mol) is dissolved in 190 mL of ethanol and added slowly to the calcium solution. The

solution is stirred during 5 minutes and then, it is quickly brought to the synthesis equipment. The solution precipitate after a while.

Starting solution of Prop/EtOH-W-TEA - Calcium propionate, $\text{Ca}(\text{O}_2\text{CCH}_2\text{CH}_3)_2$, 98 %, (22.0640 g, 0.1184 mol) is dissolved in 50 mL of distilled water. Then, tetraethyl orthosilicate, $\text{Si}(\text{OC}_2\text{H}_5)_4$, 99%, (12.2172 g, 0.0586 mol) is dissolved in 190 mL of ethanol and added slowly to the calcium solution. Triethanolamine, $\text{C}_6\text{H}_{15}\text{NO}_3$, (USP-NF) pure, pharma grade, is added dropwise (~2 mL) to avoid the formation of emulsions and precipitates in the starting solution. The solution is stirred during 10 minutes and then, it is brought to the synthesis equipment.

5.4.2. General synthesis procedure

To start the synthesis, all process parameters must be previously defined. After prepare the starting solution, the general synthesis procedure (Figure 5-8) consists in light up and adjust the oxy-acetylene torches to a slightly oxidizing flame. Then, the cooling system and the electrostatic precipitator must be light up. Having turned overall equipment, the solution is pumped using a dispensing peristaltic pump, model NE-9000G, and aerosolized with an airblast nozzle through the flames, resulting in the evaporation/reaction of the precursors and subsequent formation of the ceramic particles.

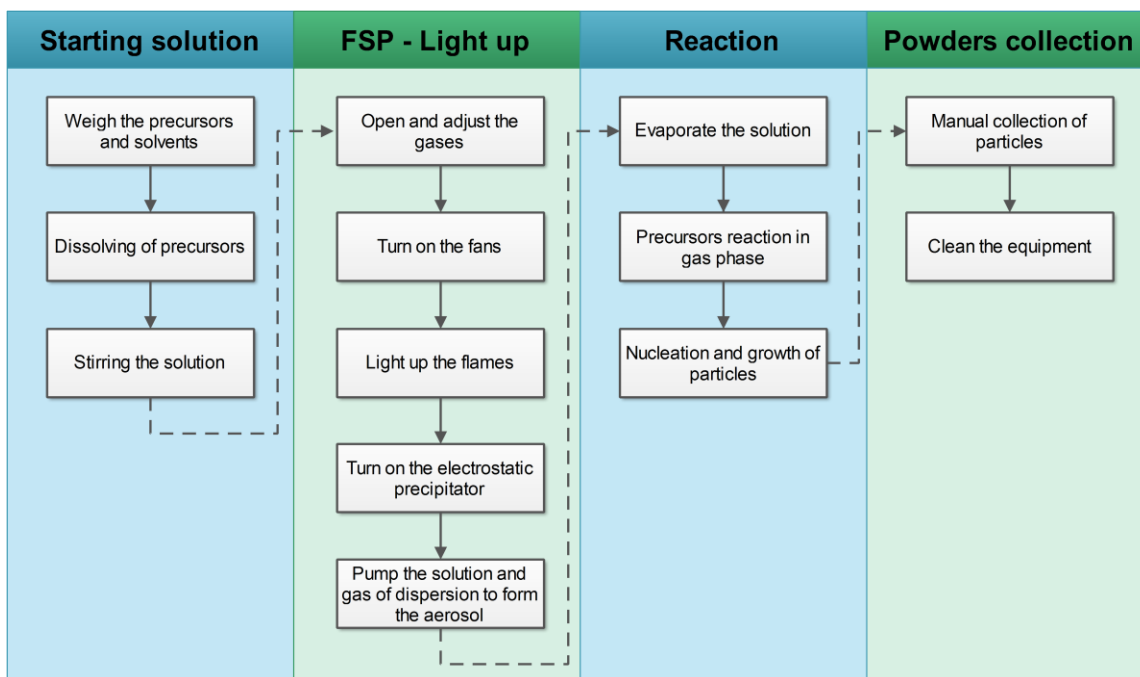


Figure 5-8. General synthesis procedure

The instruments for monitoring the flow of combustion gases and dispersion gas were mechanical flowmeters, implying the manual determination of the flows using an arrangement of moving parts.

Despite that, the flows were kept as constant as possible; however, some small differences in the final characteristics of the samples can be observed, as result of human errors during the definition of the conditions in the synthesis processes.

5.4.3. Results of the evaluation of different chemical systems

Figure 5-9 show the XRD patterns obtained for the synthesis of Ca_2SiO_4 by FSP using the chemical systems Nit/EtOH, EH/EtOH-W, Prop/EtOH-W and Prop/EtOH-W-TEA. The phases were identified and quantified using Rietveld refinement with internal standard (rutile), in order to identify the amorphous material. The XRD pattern of Nit/EtOH, show the presence of 15.6 % of α' - Ca_2SiO_4 (ICSD-34241), 4.4 % of CaO (ICSD-51409), 26.1 % of $\text{Ca}(\text{OH})_2$ (Portlandite) (ICSD-81097), 6.4 % CaCO_3 (ICSD-80869) and 47.5 % of amorphous material.

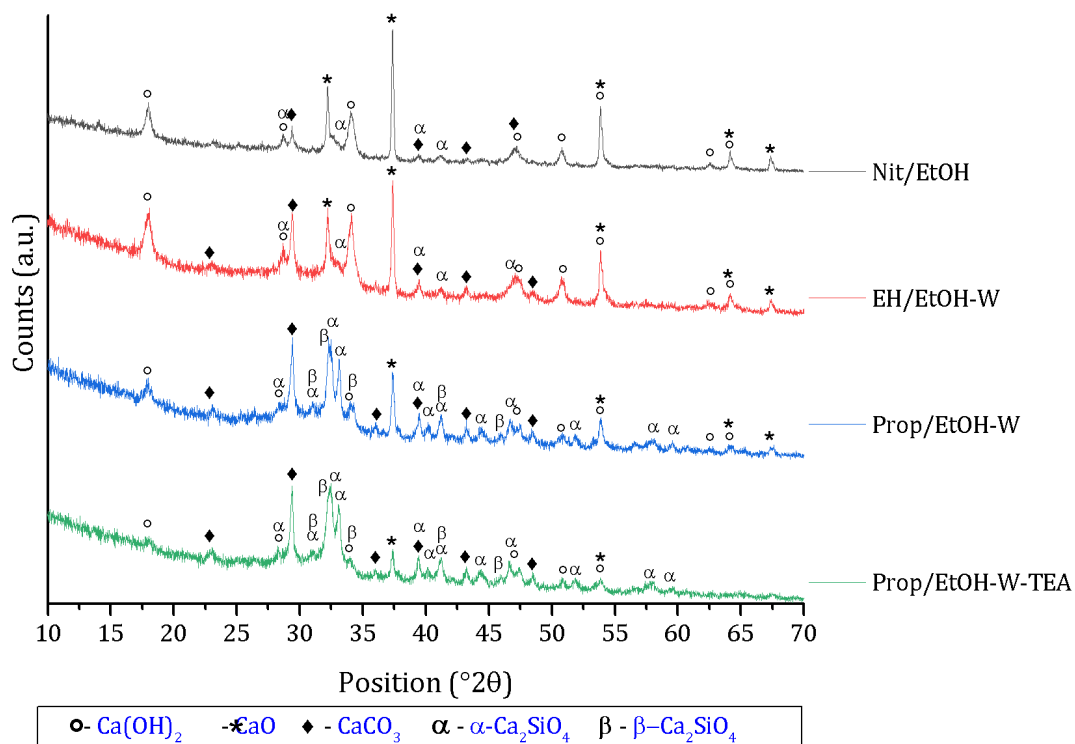


Figure 5-9. XRD patterns during the evaluation of different chemical systems

There are observed large amounts of $\text{Ca}(\text{OH})_2$ in comparison with the main phase, belite. Considering the temperatures reached during the process and the mineralogy of the products, it is possible to say that the presence of $\text{Ca}(\text{OH})_2$ and CaCO_3 cannot be product of the synthesis process. However, the CaO can be formed during the reaction due to the differences of enthalpy of the decomposition products, considering that the calcium nitrate is dried before to be decomposed in the flame, while the tetraethyl orthosilicate is volatilized with the solvent, favoring the formation of calcium oxide instead of dicalcium silicate. Then, this calcium oxide is transformed in $\text{Ca}(\text{OH})_2$ and CaCO_3 by

reacting with the water and carbon dioxide in the environment. Besides, the solution was stoichiometry defined, whereby, the rest of the silicon resource should have favored the formation of silicon oxide as part of the non-diffracting percentage of the sample, considering that no silica peaks are observed in the XRD.

To confirm it, FT-IR measurements were carried out (Figure 5-10-a), showing the two main bands of silicate compounds under between 500-1000 cm^{-1} corresponding to bending vibrations of Si-O-Si and symmetrical Si-O stretching vibrations of SiO_4 [157]–[159]. Additionally, the spectrum shows a band at 1618 cm^{-1} and a small band at 1384 cm^{-1} belonging to vibrations of ionic NO_3^- of calcium nitrate, while the sharp band in 3640 cm^{-1} and the broad band around 3426 cm^{-1} belong to O-H vibrations from humidity in the sample and the hydroxyl ions of portlandite. The bands at 874 cm^{-1} and 1440 cm^{-1} belong to CO_3^{2-} calcite confirming the XRD results.

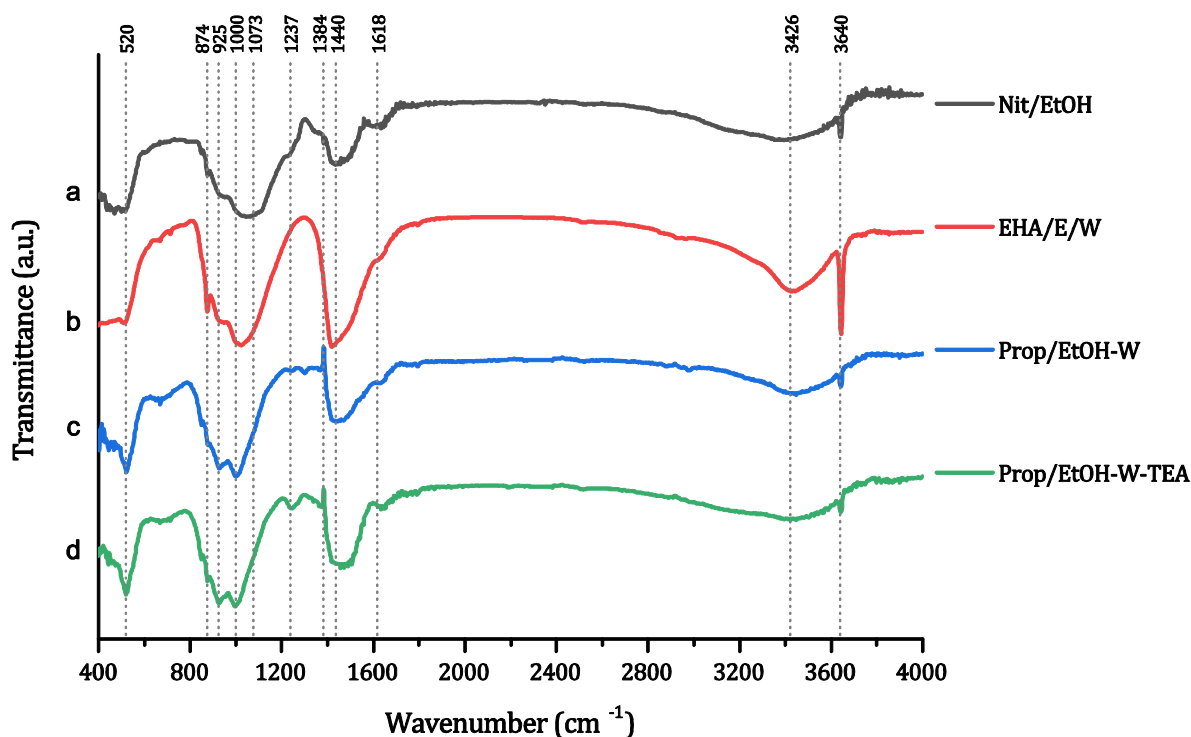


Figure 5-10. FT-IR spectra during the evaluation of different chemical systems

Using a metallorganic compound with high enthalpy as calcium 2-ethylhexanoate instead of calcium nitrate dissolved in a mixture of water and ethanol, the XRD pattern (sample EH/EtOH-W) showed a similar behavior than Nit/EtOH, but with higher amount of amorphous material and lower amount of calcium silicates. The Rietveld refinement show the presence of 7.4 % of α' - Ca_2SiO_4 (ICSD-81097), 2.8 % of CaO (ICSD-51409), 18.2 % of $\text{Ca}(\text{OH})_2$ (Portlandite) (ICSD-202225), 11.0 % of CaCO_3 (ICSD-80869) and 60.6 % of amorphous material. In this sample, the high presence of calcium hydroxide and calcium carbonate is also attributed to the reaction of calcium oxide with the environment, while the presence of calcium oxide and its derivatives could be the result of the use of water as solvent in

the preparation of the starting solution, nevertheless, the properties of the carboxylic acid forced the use of water.

As described above, calcium 2-ethylhexanoate is also soluble in toluene, hence, an additional reaction using toluene as unique solvent was done, however, the product was a black powder due to the high amount of soot produced during the reaction, which could be attributed to the chemical decomposition of the solvent, which has seven carbon ions, (C₇H₈), the high quantity of carbon in the precursor (32 carbon ions) and the decomposition of the fuel (C₂H₂). The FT-IR spectrum of EH/EtOH-W (Figure 5-10-b), show a big band at 1440 cm⁻¹ indicating a high presence of calcium carbonate as well as a big and sharp band at 3640 cm⁻¹ attributed to O-H vibrations in calcium hydroxide. The two bands corresponding to Si-O vibrations are also observed in the spectrum, confirming the presence of calcium silicates and possible formation of silicon oxide in the amorphous fraction of the sample, in coherence with the initial stoichiometry.

Considering the previous results, a salt of carboxylic acid with shorter alkyl chain than calcium 2-ethylhexanoate was proved, looking for compounds easier to dissolve. This system was constituted by calcium propionate and TEOS dissolved in water and ethanol (sample name: Prop/EtOH-W). The use of water as solvent was necessary to dissolve the propionate, but in lower amount. In this case, the XRD pattern shows the formation of 20.0 % of α'-Ca₂SiO₄ (ICSD-81097), 5.8 % of β-Ca₂SiO₄ (ICSD-245076), 2.6 % of CaO (ICSD-51409), 6.2 % of Ca(OH)₂ (Portlandite) (ICSD-34241), 7.4 % of CaCO₃ (ICSD-80869) and 58 % of amorphous material.

In this sample is observed the presence of two polymorphs of belite as main phases, decreasing the percentage of calcium oxide and its derivatives. In addition, this pattern presents higher noise and a hump, which could be attributed to particles in nanoscale and the formation of amorphous material. Even when the mineralogy obtained with this chemical system was better, the stability of the starting solution was poor, leading to the formation of two liquid phases and after a while, the precipitation of the precursors. For this reason, triethanolamine (TEA) was tested in the starting solution. This compound can act as emulsifier and surfactant, improving the stability of the solution by bonding the molecules to the metal ions. The solution made with TEA shows good chemical stability, whereby the reaction was carried out (sample name: Prop/EtOH-W-TEA), resulting in the formation of 20.8 % α'-Ca₂SiO₄ (ICSD-81097), 10.9 % of β-Ca₂SiO₄ (ICSD-245076), 1.3 % of CaO (ICSD-51409), 2.7 % of Ca(OH)₂ (Portlandite) (ICSD-34241), 7.0 % of CaCO₃ (ICSD-80869) and 57.3 % of amorphous material.

The amount of calcium oxide, calcium hydroxide and calcium carbonate of this sample, was slightly lower in comparison with the samples Prop/EtOH-W, while the quantity of β-Ca₂SiO₄ was slightly higher, which could be attributed to the presence of the complexing agent. On the other hand, the number of amorphous material and α'-Ca₂SiO₄ remain constant. The FT-IR results (Figure 5-10 -c, d) of the samples obtained using calcium propionate do not show big differences by the use of TEA. For these samples, the two bands at 925 cm⁻¹ and 1000 cm⁻¹ corresponding to silicon-oxygen vibrations of tetrahedral silicate units are more defined than in the other spectra. Bands corresponding to C-O vibrations of calcium carbonate are observed at 1440 cm⁻¹ in smaller proportion than EHA/E/W. Furthermore, the sharp band located in 3640 cm⁻¹ attributed to O-H vibrations in Portlandite and a

broad band at 3426 cm^{-1} corresponding to O-H vibrations, belonging to absorbed water are also observed.

The samples in which the calcium resource was a carboxylic acid showed high amounts of amorphous material, which could indicate the formation of smaller particle sizes than using inorganic salts. Table 5-4 summarizes the results of the Rietveld refinement, while the plots of the quantification are shown in the annex.

Table 5-4. Mineralogy quantification for different chemical systems

Sample	Rwp	Amorphous	$\alpha\text{-C}_2\text{S}$	$\beta\text{-C}_2\text{S}$	CaCO_3	CaO	Ca(OH)_2
Nit/EtOH	8.0	47.5	15.6	0.0	6.4	4.4	26.1
EH/EtOH-W	8.1	60.6	7.4	0.0	11.0	2.8	18.2
Prop/EtOH-W	7.6	58.0	20.0	5.8	7.4	2.6	6.2
Prop/EtOH-W-TEA	7.4	57.3	20.8	10.9	7.0	1.3	2.7

R_{wp}: Weighted profile R-factor

The specific surface area of the samples was measured by BET. The lower specific surface area was obtained for Nit/EtOH, due to the low enthalpy of volatility of the calcium nitrate. On the other hand, the SSA for samples using carboxylic acids without complexing agents, EH/EtOH-W and Prop/EtOH-W, have a similar behavior, but the SSA is slightly higher when calcium 2-ethylhexanoate is used, which could be a consequence of the higher energy release in the reaction for the longer carbon chain of this compound. Furthermore, the sample with higher SSA was obtained using a propionic acid with a complexing agent, suggesting that the use of chelators favor the formation of particles with smaller sizes.

Table 5-5. Specific surface area (SSA) of the samples during the set-up

Samples	SSA (m^2/g)
Nit/EtOH	22.74
EH/EtOH-W	34.41
Prop/EtOH-W	30.01
Prop/EtOH-W-TEA	47.66

Finally, the hydraulic behavior of the samples was evaluated by calorimetry and XRD, while micrographs of the hydrated material were observed. Figure 5-11 shows the first and second peaks of the samples after contact with water. The samples prepared with propionate as starting material show the higher heat flow release. Otherwise, the samples Nit/EtOH and EH/EtOH-W do not show

the formation of the second peak until 48 hours, while the other samples had finished the hydraulic reaction.

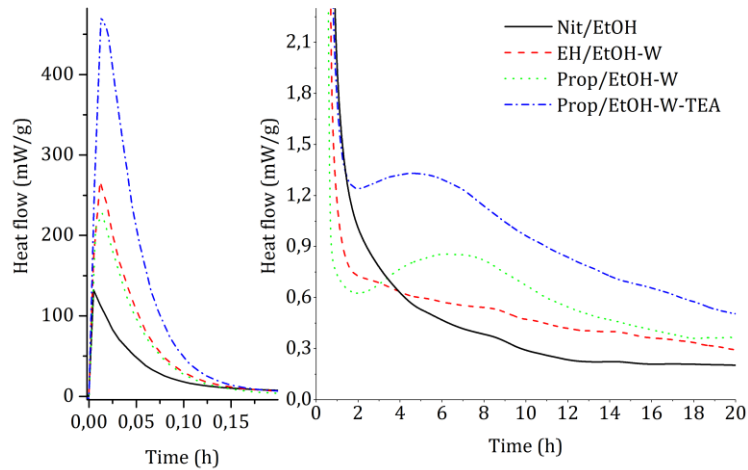


Figure 5-11. Calorimetry measurements of the chemical systems evaluated

Figure 5-12 present the XRD patterns of the samples after 48 hours of hydration. All the samples show a defined peak at $29.5^\circ(2\theta)$, which is associated to the presence of calcium carbonate in the samples, however the peaks between $29^\circ(2\theta)$ to $35^\circ(2\theta)$ corresponding to calcium silicates disappear, indicating a chemical reaction with water. In this case, the gel C-S-H is part of the amorphous material, for this reason, not diffraction peaks were observed.

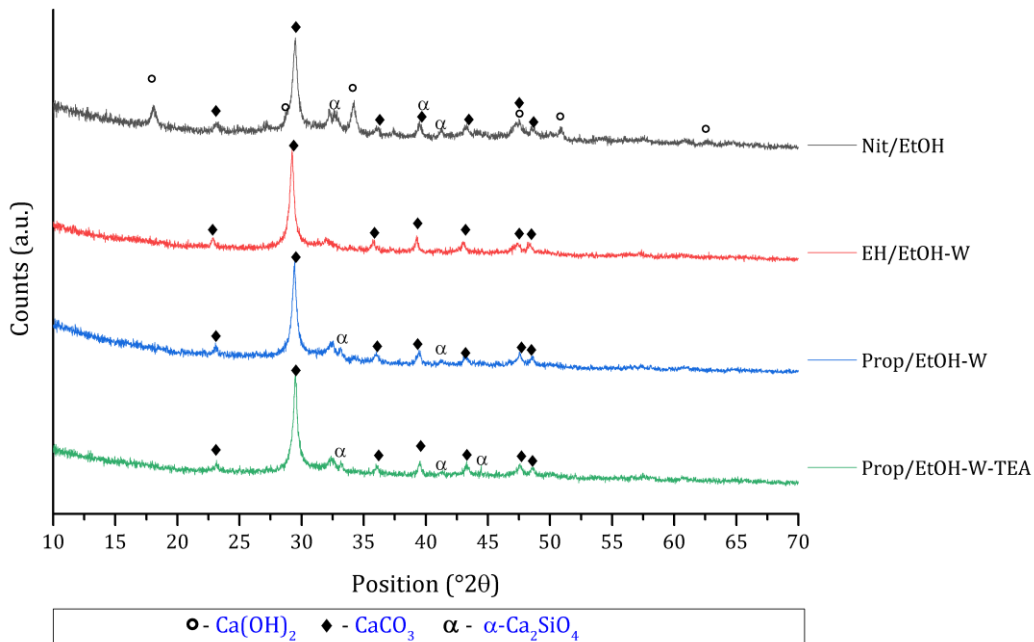


Figure 5-12. XRD patterns of hydrated samples using different chemical systems

Figure 5-13 shows the morphology of sample Prop/EtOH-W-TEA as-prepare and after hydration. Micrographs **a** and **b** correspond to the anhydrous sample, in which is possible to observe the formation of aggregates of small particles surrounding a sphere of $\sim 12\ \mu\text{m}$ of diameter (image **a**) and the formation of hollow particles, in which the shell is formed by agglomerates of smaller particles (image **b** and **b1**). Micrographs **c**, **d**, **e** and **f** show the morphology of the hydrated sample. Image **c** shows the formation of a non-dense matrix and hollow spheres, as it was observed in the anhydrous sample. Image **d** is a magnification of the surface of this hollow sphere, in which is observed the formation of spider-like shapes associated with the formation of C-S-H (enlargement **d1**). On the other hand, it was observed the formation of crystals in the matrix (images **e** and **f**), also associated to calcium silicate hydrates.

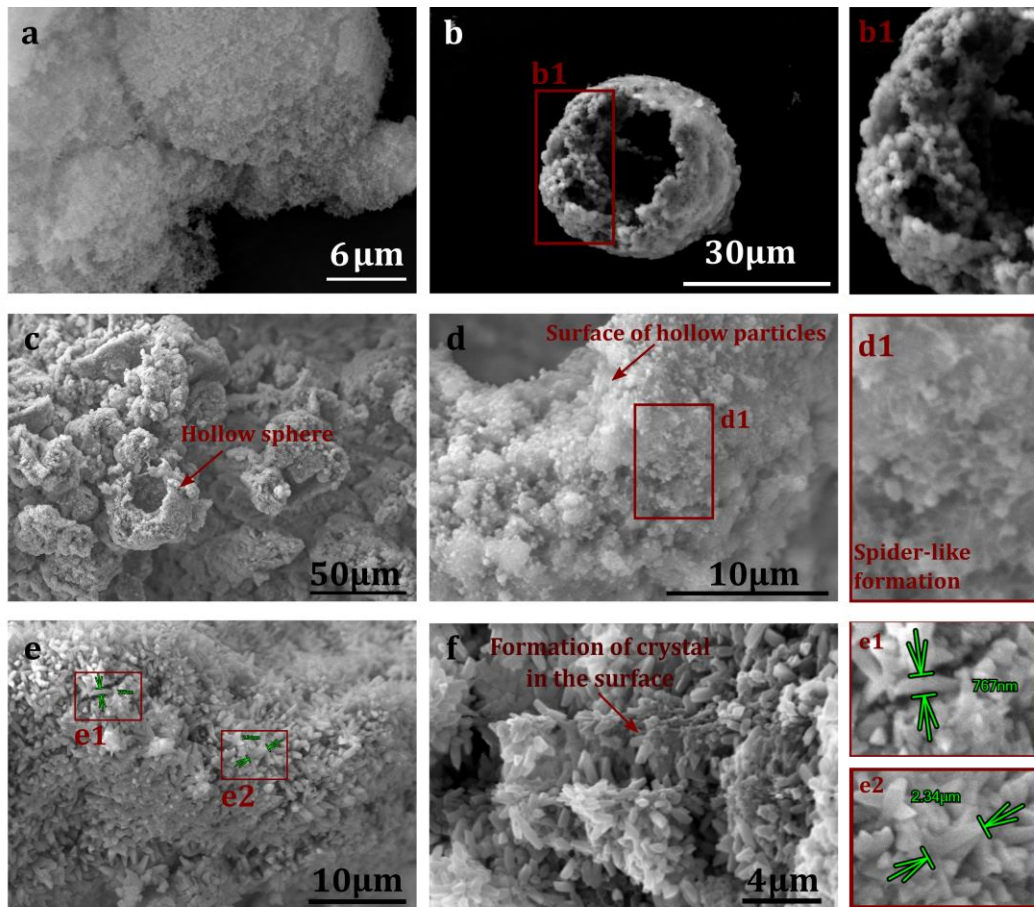


Figure 5-13. Micrographs of Prop/EtOH-W-TEA anhydrous and hydraulic samples after 40 d

Considering the results of the set-up of the synthesis process, the chemical system formed by calcium propionate, TEOS, water, ethanol and triethanolamine (Prop/EtOH-W-TEA) was chosen to the evaluation of the process conditions in the final properties of the products, during the synthesis of calcium silicate phases.

During the evaluation of these starting solutions, the energy released during the ignition changes as consequence of differences in the enthalpy of combustion of the precursors. Additionally, it is observed the tendency to form heterogeneous powders by using inorganic salts as calcium nitrate tetrahydrate or by the use of water as solvent, due to the differences in the rate of decomposition of the components [80]. Nevertheless, the decrease in the flame energy due to the use of water as solvent, can be solved by the use of a high enthalpy flame obtain by the use of oxy-acetylene mixture, instead of methane or other fuel with lower combustion enthalpy [111].

Regarding to the chemical composition of the precursors, it is important consider the amount of CO₂ formed by the oxidation and decomposition of them, because precursors with low carbon content could be more advantageous than that with high molarity with respect to the total of carbon concentration. (Calcium propionate Ca:C= 1:6, while Calcium- 2 ethylhexanoate Ca:C= 1:32) [160].

5.5. Experimental design

In order to evaluate the effects of the process parameters in the formation of calcium silicate phases it was used an experimental design as statistical tool, which allows the study of the main effects of the parameters and their interactions during the synthesis process.

As described in the previous section, the chemical system was defined by a mixture of Ca(O₂CCH₂CH₃)₂/Si(C₂H₅O)₄ dissolved in ethanol/water/TEA. The starting solution to obtain 6 g of product, considering an equipment yield of 30 %, was prepared by dissolving calcium propionate, Ca(O₂CCH₂CH₃)₂, 98 % (44.1287 g, 0.2369 mol), in 200 mL of distilled water in 1 L beaker. Tetraethyl orthosilicate, Si(C₂H₅O)₄, 99% (24.4353 g, 0.1172 mol) was dissolved in 200 mL of ethanol and added slowly to the calcium propionate solution. Then, triethanolamine, C₆H₁₅NO₃, 98% was added dropwise to avoid the formation of emulsions in the starting solution (3.5 mL, 0.0263 mol are added to ceramic loadings of 5 % and 7 mL, 0.0527 mol are added to ceramic loadings of 2.5 %). The mixture of solvents was corrected according to the experimental conditions of the chemical system (solvent and ceramic loading) as it is show in Table 5-6. The solution is stirred during 10 minutes and then, it was brought to the synthesis equipment.

Table 5-6. Preparation of the starting solution

Solvent mixtures		Ceramic loading	
		2.5 %	5 %
Solvent 1	Ethanol (mL) (0.7)	710	355
	Water (mL) (0.25)	200	100
	Methanol (mL) (0.05)	51	25.5
Solvent 2	Ethanol (mL) (0.75)	200	100
	Water (mL) (0.25)	760	380

The experimentation was defined using a two-level fractional factorial design, resolution III, 2^{5-2} , studying the interaction effects and main effects of the process parameters, with an alias structure as shown in Table 5-7.

Table 5-7. Alias Structure of the experimental design

Aliases
I - ACE - BDE + ABCD
A - CE + BCD - ABDE
B - DE + ACD - ABCE
C - AE + ABD - BCDE
D - BE + ABC - ACDE
E - AC - BD + ABCDE
AB + CD - ADE - BCE
AD + BC - ABE - CDE

The process parameters evaluated were the feed flow rate, dispersion gas, pressure of dispersion gas, ceramic loading and solvent, while the responses were the phases composition obtained by Rietveld refinement, the specific surface area of the powders obtained by BET and the reactivity of the samples evaluated by microcalorimetry. The low and high levels of the parameters are shown in Table 5-8.

Table 5-8. Factors and levels of the parameters in the experimental design

Symbol	Process parameters	Levels	
		Low level	High level
A	Ceramic loading (%)	2.5	5
B	Pressure of dispersion gas (kPa)	100	200
C	Feed flow rate (mL/min)	10	30
D	Solvent	Ethanol:Water (E)	Methanol:Ethanol:Water (M)
E	Dispersion gas	Oxygen (O)	Air (A)

The levels of the factors were defined during the set-up of the equipment and synthesis, considering the most common ranges used for others researchers and previous experiences. In addition, the time of the reaction was considered as an important factor, looking for conditions with good contact between the flame and precursors, but in short time. In that way, flow rates of 30, 40 and 50 mL/min were tested, however, upon 30 mL/min some amounts of solution crossed the flame without a proper

evaporation, resulting in the formation of a thick layer of precursors or a gel in the reactor. Regarding to the pressure of dispersion gas, it was defined a limit up to 276 kPa, in which the velocity of the solution was available to break the flame, resulting in the non-evaporation of the precursors. Having this into account and the results obtained for the ALR values at different process conditions in Table 4-1, the maximum high level of study was defined as 200 kPa, and the minimum was 100 kPa since it was the lower pressure to get a good spray of the solution. Concerning to the ceramic loading of the solution, using calcium propionate, the solution was limited by the solubility of the precursors in the solvent. A ceramic loading of 5 % was close to the limit of solubility, therefore, to evaluate the effect of this parameter it was used as low level a ceramic loading of 2.5 %. Values lower than 2.5 % of ceramic loading were avoided due to the high amount of solvent for the solution preparation, increasing the time for the reaction. In addition, the decrease of precursor's concentration leads to lower enthalpy content in the starting solution.

The mixture of solvents to produce the nanoparticles in this chemical system required the use of water due to the nature of the precursors. Calcium propionate is easily soluble in water and slightly soluble in ethanol, for this reason, it was necessary to use water in the less amount possible, due to it decreases the enthalpy of volatility in the mixture. Therefore, it was use 25 % of distill water in the mixture of solvents allowing the formation of a homogeneous solution. In addition, 5% of ethanol was replaced by 5 % of methanol. The replacement of ethanol by water slightly decreases the enthalpy of the mixture, reducing the residence time of droplets and particles in high temperatures, influencing in the growth rate. The enthalpies of the mixture of solvents used during the synthesis processes are shown in Table 5-9.

Table 5-9. Enthalpy of volatility of the mixture of solvents

Mixture of solvents	Abbreviation	Proportion (wt)	Enthalpy of volatility
Ethanol:Water	E	0.75:0.25	-13.60 kJ/mL
Methanol:Ethanol:Water	M	0.05:0.70:0.25	-13.30 kJ/mL

Two dispersion gases were evaluated. The most common gas used in flame spray pyrolysis is oxygen since this gas allows greater flame enthalpies as main oxidizing agent during combustion processes. The use of air can dilute the flame, resulting in the decrease of the flame temperature and decreasing the enthalpy density of it. However, its use was evaluated, because its high availability and low price. The experimentation matrix was randomly defined using the statistical software Minitab® as it is shown in Table 5-10.

The compound names were made up considering the conditions of the synthesis, being divided in two terms (solution conditions-spraying conditions). In that sense, the first term (solution conditions) is composed by a combination of Number-Letter-Number, in which the first number (30 or 10) correspond to the feed flow rate, the letter (E or M) correspond to the mixture of solvents and the third term (2 % or 5 %) correspond to the ceramic loading of the solution. The second term (spraying conditions) is composed by Letter-Number, where the letter (A or O) correspond to the

dispersion gas and the number to the pressure of the dispersion gas. Finally, if it is a R at the end of the name, means that this compound is a replication of an experiment in the matrix.

Table 5-10. Experimental matrix

Compound name	Feed rate (mL/min)	Mixture of Solvents	Ceramic loading (Weight %)	Dispersion gas	Dispersion pressure (kPa)
30E _{5%} -A ₁₀₀	30	E	5	Air	100
30E _{2%} -O ₂₀₀	30	E	2.5	Oxygen	200
30M _{2%} -O ₁₀₀	30	M	2.5	Oxygen	100
10M _{2%} -A ₂₀₀	10	M	2.5	Air	200
10M _{5%} -O ₁₀₀	10	M	5	Oxygen	100
30M _{5%} -A ₂₀₀	30	M	5	Air	200
10E _{5%} -O ₂₀₀	10	E	5	Oxygen	200
10E _{2%} -A ₁₀₀	10	E	2.5	Air	100
30E _{5%} -A ₁₀₀ R	30	E	5	Air	100
30M _{5%} -A ₂₀₀ R	30	M	5	Air	200
10M _{2%} -A ₂₀₀ R	10	M	2.5	Air	200
10E _{2%} -A ₁₀₀ R	10	E	2.5	Air	100
10E _{5%} -O ₂₀₀ R	10	E	5	Oxygen	200
10M _{5%} -O ₁₀₀ R	10	M	5	Oxygen	100
30E _{2%} -O ₂₀₀ R	30	E	2.5	Oxygen	200
30M _{2%} -O ₁₀₀ R	30	M	2.5	Oxygen	100

The anhydrous products of this experimental matrix were characterized by X-ray diffraction, BET and isothermal calorimetry to obtain the main values and responses to run the experimental design. However, these results were supported by thermal analysis coupled to mass spectrometer and infrared spectroscopy (TGA/DSC+MS/FTIR), Fourier transform Infrared spectroscopy (FT-IR), scanning electron microscopy and X ray diffraction of hydrated phases after calorimetry.

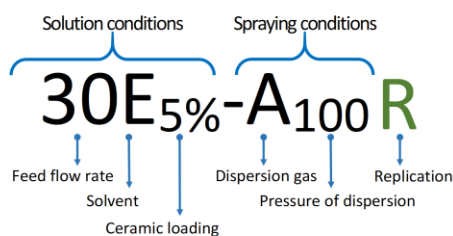


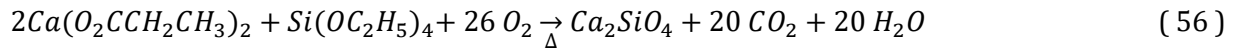
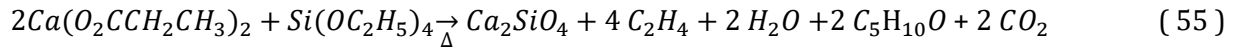
Figure 5-14. Nomenclature of the samples in the design

CHAPTER 6. CALCIUM SILICATES OBTAINED BY FLAME SPRAY PYROLYSIS

Experimental conditions defined in the statistical design in Chapter 5 were used to produce 16 compounds of dicalcium silicate under different process conditions. The present chapter addresses the mineralogical, physical and chemical characterization results of these compounds, obtained through flame spray pyrolysis by changing the process conditions.

6.1. Mineralogical composition

After run the experimental matrix presented in Table 5-10, were obtained 16 samples with an initial stoichiometry in order to produce dicalcium silicate using a Ca:Si ratio of 2:1, as it shows in the equations (55) and (56),



The XRD patterns of all the samples in the design are shown Figure 6-1. These XRD patterns were analyzed and quantified by Rietveld refinement as-prepared and with internal standard of rutile to determine the fraction of amorphous material, using the GSAS software. The amorphous fraction was calculated by the spiking method by the over- estimation of an internal crystalline standard using the equation (57) [161]. Rietveld refinement curves for the samples 30E_{5%}-A₁₀₀, 30E_{2%}-O₂₀₀, 10E_{5%}-O₂₀₀ and 30M_{5%}-A₂₀₀R are shown from Figure 6-2 to Figure 6-5 as representative measurements of all the samples in the design. The rest of the graphs (as-prepared and with internal standard) are shown in annex.

$$ACn (\%) = \frac{1 - W_s/R_s}{100 - W_s} \times 10^4 \quad (57)$$

Where W_s (%) is the weighed concentration of the internal standard and R_s (%) is the over-estimate value during the Rietveld analysis [161].

The diffraction patterns of the eight main experimental runs of the design and their replication were graphed overlade, with a total of 16 samples (Figure 6-1). There are observed four diffraction

patterns tendencies, corresponding to samples, 30E_{5%}-A₁₀₀, 30E_{2%}-O₂₀₀, 10E_{5%}-O₂₀₀ and 30M_{5%}-A₂₀₀R, which will be described below. Additionally, it is possible to observe the coherence between the original run and the replication, indicating the reproducibility of the method during the synthesis processes. Nevertheless, the samples 10M_{5%}-O₁₀₀ and 10E_{5%}-O₂₀₀, presented slight differences with their replication, mainly related to the formation of amorphous material and calcium carbonate in the sample.

The samples show the presence up to five crystalline phases and the formation of a hump which indicates the presence of non-diffracting material, as it was expected considering the particle size of the samples. The phases identified correspond to α -Ca₂SiO₄ (ICSD-81097), β -Ca₂SiO₄ (ICSD-245076-ICSD-245078 and ICSD-79550), CaCO₃ (ICSD-80869), CaO (ICSD-90486 and ICSD-51409) and Ca(OH)₂ (ICSD-202225, ICSD-202226 and ICSD-34241), where the CaCO₃, CaO and Ca(OH)₂ will be called secondary phases, considering the quantities of them and their undesired formation. The major components after the amorphous material are the dicalcium silicate polymorphs with peaks between 31-34 °(2 θ) and the calcium carbonate with a main peak ~29 °(2 θ). The sample 10E_{5%}-O₂₀₀ presented the lower quantity of calcium carbonate (3.8 %), which is part of the unwanted phases in the system. Then, it follows by samples 30E_{2%}-O₂₀₀ (4%) and 30E_{2%}-O₂₀₀R (4.3%). These samples have as common factor the use of high pressure of dispersion gas, suggesting an important effect of this parameter. Additionally, observing globally the effect of the variables involved in the samples 30E_{2%}-O₂₀₀ and 10E_{5%}-O₂₀₀, four variables are in the high level of the design, where they bring more energy to the system.

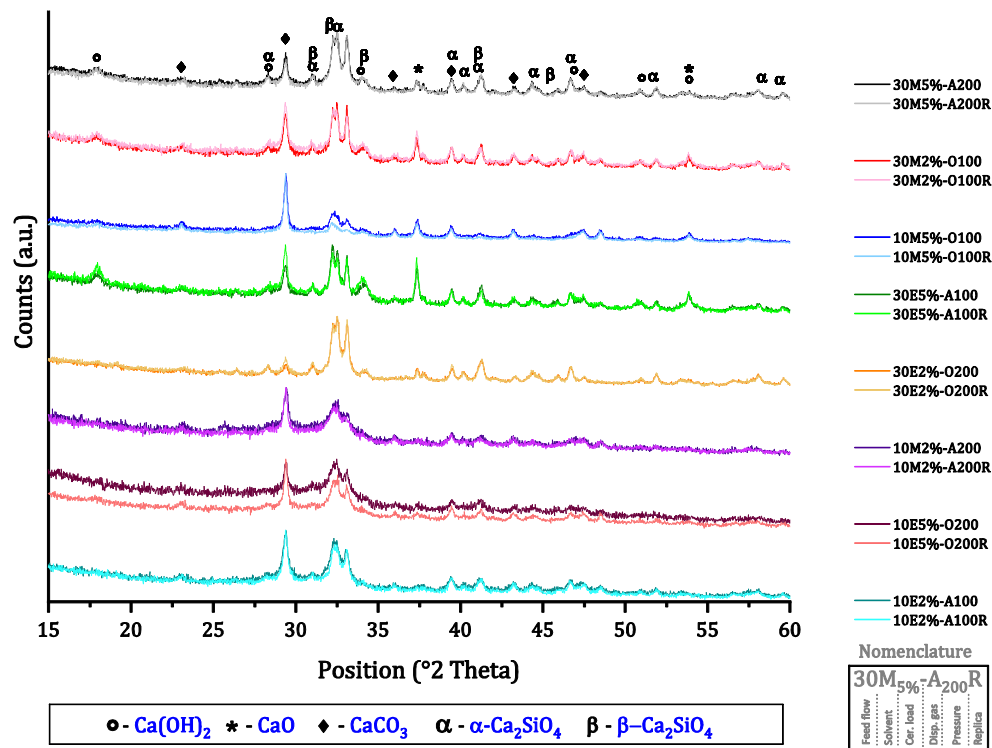


Figure 6-1. XRD patterns of all samples in the experimental design

Figure 6-2 shows the X-ray diffractogram of the sample 30E_{5%}-A₁₀₀ refined by the Rietveld method. It shows the formation of well-defined peaks in the diffraction pattern, permitting the identification of five crystalline phases, corresponding to 13.8 % of α -Ca₂SiO₄ (ICSD-81097), 21.5 % of β -Ca₂SiO₄ (ICSD-245076), 6.2 % of CaCO₃ (ICSD-80869), 3.1 % of CaO (ICSD-51409) and 6.4 % Ca(OH)₂ (ICSD-34241), with a percent of non-diffracting material of 49 %, mainly composed by amorphous materials and nanoparticles.

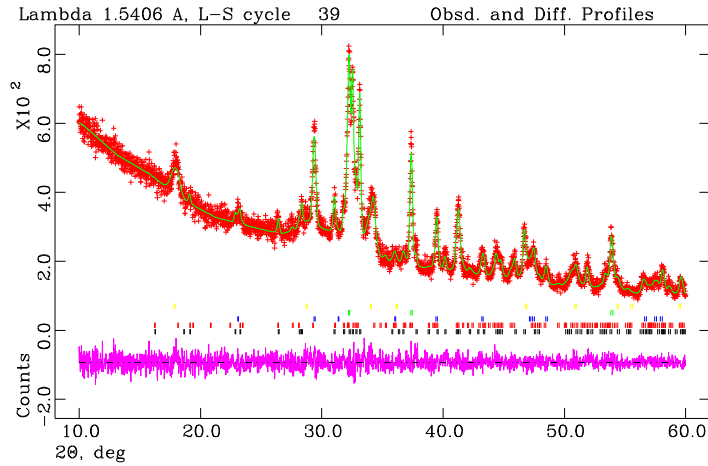


Figure 6-2. Rietveld refinement of sample 30E_{5%}-A₁₀₀

In contrast with sample 30E_{5%}-A₁₀₀, the XRD pattern of the sample 10E_{5%}-O₂₀₀, (Figure 6-3) shows broad peaks with a high noise level, which are possible related to the particle size of the samples. Despite this, it was possible to identify the three crystalline phases, corresponding to 16.3 % of α -Ca₂SiO₄ (ICSD-81097), 5.6 % of β -Ca₂SiO₄ (ICSD-245076) and 3.8 % of CaCO₃ (ICSD-80869), with a high percent of non-diffracting material of 74.3 %.

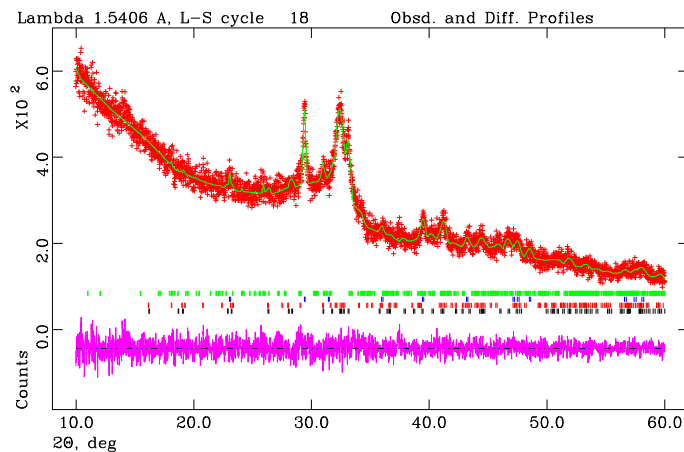


Figure 6-3. Rietveld refinement of sample 10E_{5%}-O₂₀₀

Otherwise, the Rietveld refinement of the sample 30E_{2%}-O₂₀₀, (Figure 6-4), shows a similar behavior than sample 30E_{5%}-A₁₀₀, however, this sample do not show any peak around 17.9 °(2θ), indicating that there is not portlandite in the sample. Similarly, the peak of calcium carbonate is smaller for this sample, in comparison with the rest of the samples. The phases identified correspond to 34.6 % of α-Ca₂SiO₄ (ICSD-81097), 28.1 % of β-Ca₂SiO₄ (ICSD-79550), 4.0 % of CaCO₃ (ICSD-80869) and 2.1 % of CaO (ICSD-90486), with 31.1 % percent of non-diffracting material. The process conditions of this two samples coincide in the solvent and feed flow rate, but differ in the pressure of dispersion gas, which could be the cause of the lower presence of secondary phases.

The Rietveld quantification of the sample 30M_{5%}-A₂₀₀ (Figure 6-5), permitted the identification of five crystalline phases, corresponding to 23.9 % of α-Ca₂SiO₄ (ICSD-81097), 22 % of β-Ca₂SiO₄ (ICSD-245078), 5.9 % of CaCO₃ (ICSD-80869), 1.7 % of CaO (ICSD-90486) and 5.4 % Ca(OH)₂ (ICSD-202225), with a percent of non-diffracting material of 41 %. The X-ray pattern of this sample is also similar to the pattern of sample 30E_{5%}-A₁₀₀, in which the ceramic loading, the dispersion gas and flow rate of the solution are the same.

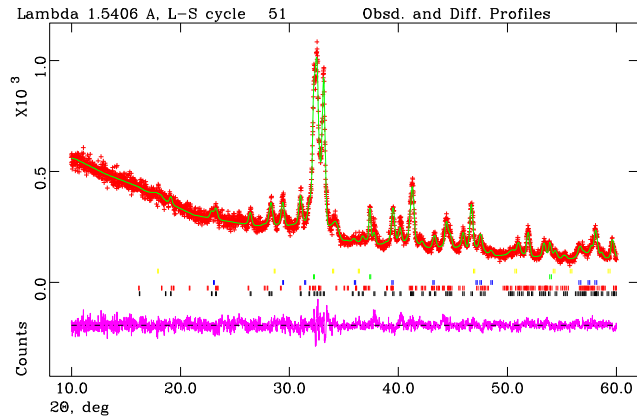


Figure 6-4. Rietveld refinement of sample 30E_{2%}-O₂₀₀

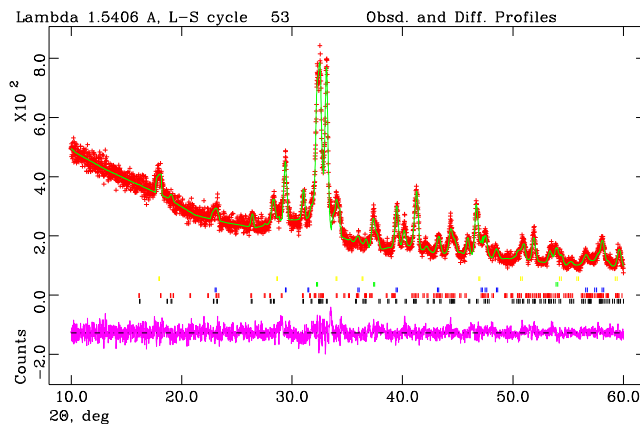


Figure 6-5. Rietveld refinement of sample 30M_{5%}-A₂₀₀

The composition obtained for all the samples considering the non-diffracting material or amorphous are shown in Table 6-1. All the samples present a high percent of non-diffracting material, while the crystalline fraction is formed for α -Ca₂SiO₄, β -Ca₂SiO₄, CaCO₃, CaO and Ca(OH)₂. The R_{wp} obtained from the Rietveld refinement for all the samples were below 10 %, with a good shape of the difference curve (close to flat). The refined overall parameters were phase scale factors, background coefficients, unit cell parameters, zero-shift error, peak shape parameters, and preferred orientation coefficient when it was necessary [162]. The amount of the non-diffracting material was indirectly obtained by the addition of a crystalline standard of rutile.

Table 6-1. Rietveld refinement of the calcium silicate phases with internal standard of rutile

Sample	Rwp	Amorphous (%)	α -C ₂ S (%)	β -C ₂ S (%)	CaCO ₃ (%)	Ca(OH) ₂ (%)	CaO (%)
30M _{5%} -A ₂₀₀	7.5	48.1	20.3	19.3	7.2	3.5	1.6
30M _{5%} -A ₂₀₀ R	6.8	41.1	23.9	22.0	5.9	5.4	1.7
30M _{2%} -O ₁₀₀	7.5	46.2	20.2	17.0	9.8	4.8	2.0
30M _{2%} -O ₁₀₀ R	7.4	50.7	21.3	8.4	10.9	6.1	2.6
10M _{5%} -O ₁₀₀	7.8	51.7	12.2	12.1	18.3	3.3	2.4
10M _{5%} -O ₁₀₀ R	7.7	48.5	22.5	1.2	21.3	4.9	1.6
30E _{5%} -A ₁₀₀	6.8	49.0	13.8	21.5	6.2	6.4	3.1
30E _{5%} -A ₁₀₀ R	7.4	56.1	7.7	17.2	8.5	9.4	1.1
30E _{2%} -O ₂₀₀	7.9	31.2	34.6	28.1	4.0	-	2.1
30E _{2%} -O ₂₀₀ R	7.8	33.5	16.7	44.3	4.3	-	1.2
10M _{2%} -A ₂₀₀	6.80	78.4	12.9	3.8	4.5	-	0.4
10M _{2%} -A ₂₀₀ R	7.5	77.1	12.3	4.6	6.0	-	-
10E _{5%} -O ₂₀₀	6.77	74.3	16.3	5.6	3.8	-	-
10E _{5%} -O ₂₀₀ R	7.7	64.5	16.9	7.7	9.4	-	1.5
10E _{2%} -A ₁₀₀	7.4	59.8	16.8	11.0	12.4	-	-
10E _{2%} -A ₁₀₀ R	7.5	61.0	18.3	12.4	7.9	0.4	-

All the samples present high numbers of non-diffracting material with values between 78.3 % and 31.1 %, for the samples 10M_{2%}-A₂₀₀ and 30E_{2%}-O₂₀₀, respectively. Figure 6-6 shows the distribution of the components of the samples in a stacker bar chart, where the original run of the experiment is followed by its respective replication. This figure suggests that the combination 30 mL/min - 100 kPa

(feed flow rate vs pressure of dispersion gas) favor the formation of calcium oxide, which is an undesired compound in the samples. The relationship between the quantification of the phases and the process conditions used in each reaction will be explained in more detail in the next chapter, using an analysis of variance (ANOVA).

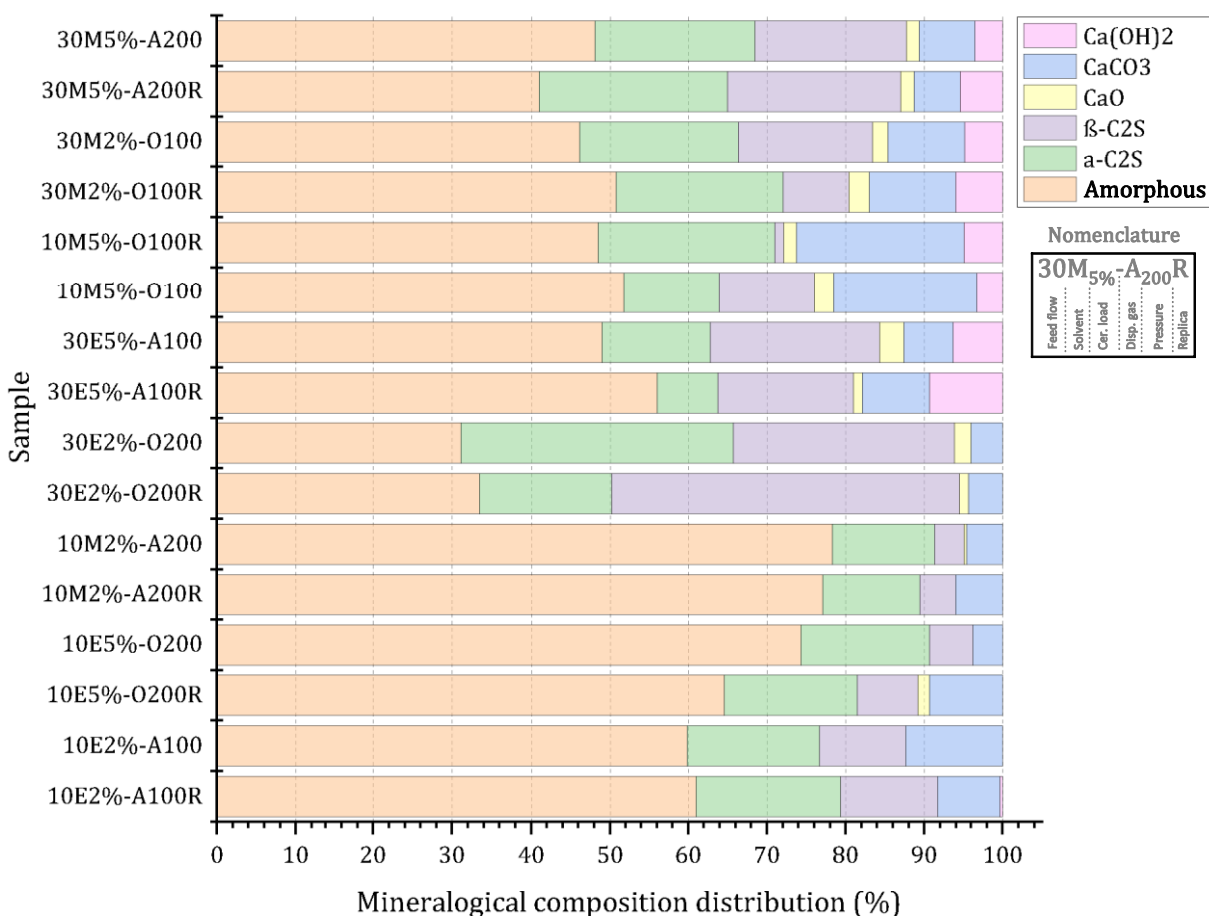


Figure 6-6. Chemical composition of the products

Phases as Ca(OH)_2 and CaCO_3 in nanometric size could be undetectable by XRD analysis, being part of the non-diffracting material, but their identification can be possible by thermal techniques as TGA. Therefore, the samples were submitted to thermal analysis coupled to mass spectrometer and infrared spectroscopy, (TGA/DSC+MS/FTIR) under a nitrogen atmosphere. This technique allows the study of thermal behavior of the samples, giving complementary results to understand and corroborate the Rietveld percentages obtained in the mineralogical analysis. In addition, the use of mass spectrometer and infrared spectroscopy give chemical information about the thermal process of the samples.

In Figure 6-7 are presented the TGA-DSC-MS curves of the sample $30\text{E}_{5\%}\text{-A}_{100}$. The TGA curve shows two main losses of mass around $400\text{ }^\circ\text{C}$ and $730\text{ }^\circ\text{C}$ and three small losses from water and soot in the

sample. The gases evolved during the decomposition were identified by mass spectrometry and infrared spectroscopy. The first significant loss of mass between 319 - 416 °C with a value of 3.66 % is associated to the dehydration of portlandite present in the sample. In this range, the mass spectrometer results indicate the release of gases with 16 and 18 UMA attributed to the hydroxyl groups of $\text{Ca}(\text{OH})_2$. Two small losses of mass of 1.03 % and 0.99 % are produced around 400-600 °C, in which mass spectrometer signals with 12, 14, 28, 29 and 30 UMA from dissociation of carbon monoxide; these gases could be attributed to the decomposition of residual soot produced during the combustion. The second major loss of mass of 6.68 % is associated with the decarbonation of CaCO_3 with a release of gases corresponding to CO_3^{2-} with 12, 16, 22 and 44 UMA, with a remarkable proportion of 44 UMA.

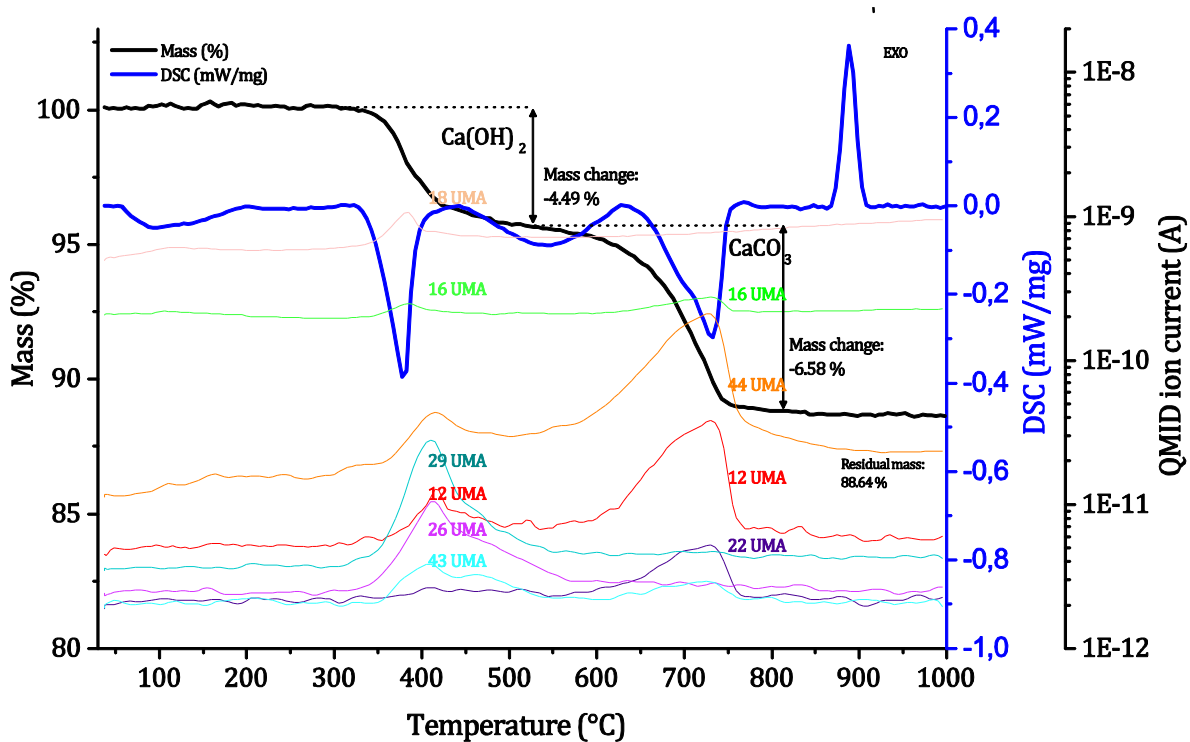


Figure 6-7. Thermal analysis coupled to mass spectrometer of 30E_{5%}-A₁₀₀

In addition, an exothermic and four endothermic transitions were observed on the heating of the sample. The first endothermic peak is attributed to the decomposition of water in the sample with a release of energy of -23.92 J/g. The second endothermic peak corresponding to the decomposition of portlandite release -70.63 J/g, while the peak attributed to soot decomposition released -51 J/g. The enthalpy released during the decomposition of calcium carbonate achieve the higher value of -89.85 J/g, and finally, was observed an exothermic peak releasing 39.1 J/g between 864 °C - 915°C, which could be attributed to a recrystallization of calcium silicates in the sample, considering the availability of amorphous material and calcium oxide from the other decompositions.

Figure 6-8 shows the TGA-DSC-MS curves of the sample 10E_{5%}-O₂₀₀. In this case, the slope of the TGA curve goes down softly, nevertheless, there are also identified two major losses of weight at 400 °C

and 730 °C, and three small losses of mass attributed to water, soot and possible alkyl chains. The first loss of weight of 3.15 % corresponds to the free water decomposition until 250 °C evolving gases with 18 UMA. In this range, the DSC curve shows an endothermic transition with an enthalpy of -59.42 J/g.

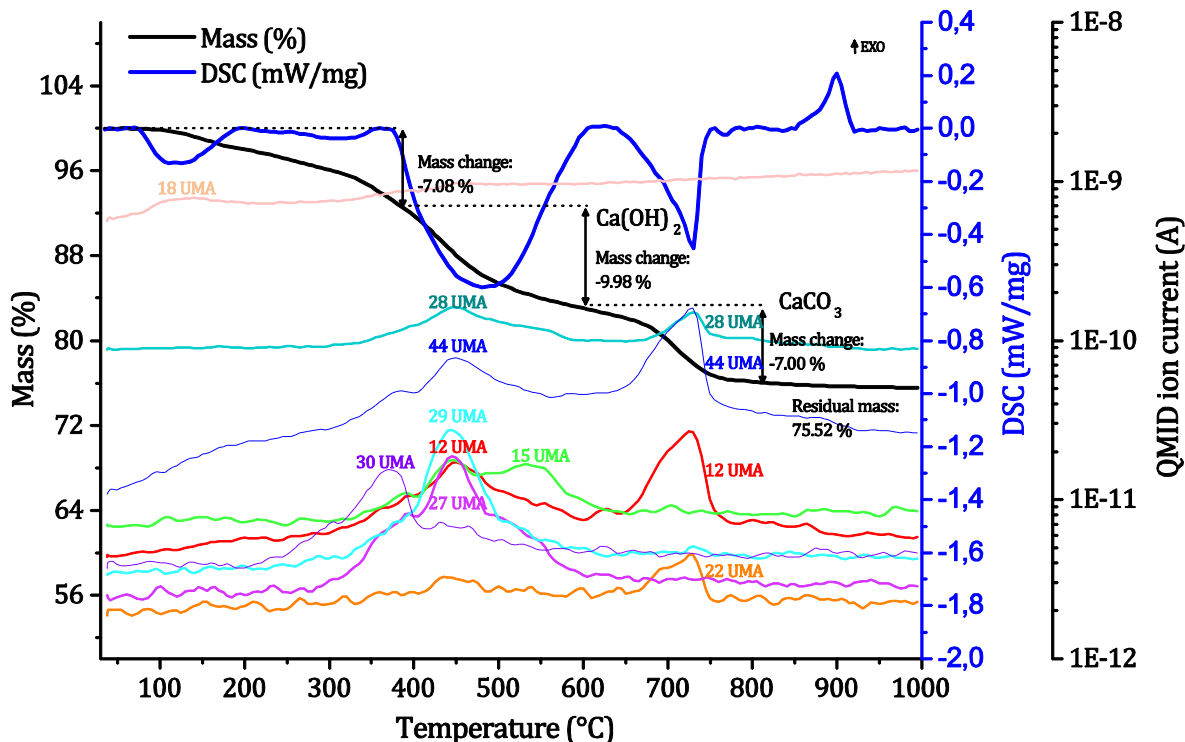


Figure 6-8. Thermal analysis coupled to mass spectrometer of 10E₅%-O₂₀₀

A major loss of mass take place between 260 – 600 °C, which can be divided in three overlaid decompositions, which are possible to identify supported in the released gases. The first weight loss between 260 – 390 °C has a value of 3.33 % where are released gases with a 30 UMA possible for alkyl chains decomposition. In this range, the DSC curve shows a small endothermic transition of -13.24 J/g. The second weight loss between 370 – 499 °C, with a value of 8.18 %, cannot be attributed to a single decomposition, because the soot and portlandite decomposed in the same range of temperatures, how is supported by the gas spectrometer measurements. However, the gases with higher concentration correspond to dehydration reactions by the release of gases with 16, 17 and 18 UMA. In lower concentration were identified gases with 22, 27, 28, 29 and 44 UMA associated to carbon monoxide and carbon dioxide. The third mass loss between 500 – 600 °C, has a value of 2.51 %, in which was identify the release of gases with 15 and 28 UMA, attributed also to soot decomposition. In this broad range, the DSC curve shows a broad endothermic peak with a high enthalpy of -448.2 J/g.

Finally, a second significant loss of weight of 6.23 % occurs between 610 – 750 °C, with an endothermic transition, which releases -117 J/g. In this range were identified gases corresponding to CO₃²⁻ with 12, 22, 28, 29 and 44 UMA, from the decarbonation of CaCO₃. An exothermic peak

releasing an enthalpy of 32.08 J/g was also observed around 900 °C, probably from a recrystallization of calcium silicates in the sample. These two graphs are used as representative examples of the TGA-DSC-MS curves. In Table 6 2 is presented a comparison between the amounts of calcium carbonate and calcium hydroxide obtained by Rietveld refinement and thermal analysis. The slight differences in the percentages of portlandite and calcium carbonate from TGA results and Rietveld refinement can be explained by the formation of nanosized phases, which cannot be identify by XRD, being part of the amorphous and crystalline not-quantified (ACn) material in the samples.

Table 6-2. Thermal decomposition of the samples

Sample	Ca(OH) ₂		CaCO ₃	
	Rietveld refinement	Thermal analysis	Rietveld refinement	Thermal analysis
30M _{5%} -A ₂₀₀	3.5	3.7	7.2	5.9
30M _{5%} -A ₂₀₀ R	5.4	3.8	5.9	8.8
30M _{2%} -O ₁₀₀	4.8	4.6	9.8	10.8
30M _{2%} -O ₁₀₀ R	6.1	4.0	10.9	10.8
10M _{5%} -O ₁₀₀	3.3	7.2	18.3	14.6
10M _{5%} -O ₁₀₀ R	4.9	14.0	21.3	19.2
30E _{5%} -A ₁₀₀	6.4	4.5	6.2	6.6
30E _{5%} -A ₁₀₀ R	9.4	7.0	8.5	9.8
30E _{2%} -O ₂₀₀	0.0	0.0	4.0	9.1
30E _{2%} -O ₂₀₀ R	0.0	2.4	4.3	6.5
10M _{2%} -A ₂₀₀	0.0	5.4	4.5	8.0
10M _{2%} -A ₂₀₀ R	0.0	10.8	6.0	11.5
10E _{5%} -O ₂₀₀	0.0	10.0	3.8	7.0
10E _{5%} -O ₂₀₀ R	0.0	9.2	9.4	11.5
10E _{2%} -A ₁₀₀	0.0	8.1	12.4	8.8
10E _{2%} -A ₁₀₀ R	0.4	5.2	7.9	10.7

Fourier transform infrared spectra of all the samples are shown in Figure 6-9. The IR spectra of all the samples shown three main bands around 520 cm⁻¹, 950 cm⁻¹ and 1450 cm⁻¹, belonging to silicate tetrahedron and carbonate vibrations, respectively. Silicate structures present two reflections with maximum values near to 523 cm⁻¹ and 1004 cm⁻¹, which correspond to two active frequencies of a tetrahedral group [163]–[165]. The first band between 430 and 600 cm⁻¹, with a maximum around 523 cm⁻¹ is attributed to bending vibrations generated by Si–O–Si [159], [166], [167], while, two close bands located in 936 cm⁻¹ and 1004 cm⁻¹ correspond to symmetrical Si-O stretching vibrations of SiO₄ [157], [158], where the band located around 936 cm⁻¹ can be attributed to Ca-O-Si vibrations [12] and the band located at 1004 cm⁻¹ corresponds to ν₃(Si-O) stretching vibrations [168]. The shoulder located in 1096 cm⁻¹ is attributed to Si-O stretching vibrations of amorphous silica, which could be part of the non-diffracting material in the samples [169].

Additionally, all the samples show the presence of the calcite, which is the most stable polymorph of calcium carbonate. The bands located at 711, 873 and 1440 cm^{-1} are attributed to C-O vibrations of CO_3^{2-} ions from ν_4 (doubly degenerate in-plane bending), ν_2 (out-of-plane) and ν_3 (doubly degenerate asymmetric stretching) vibrations of calcite. Also, there are identified minor bands of this polymorph, located in 848 cm^{-1} and 1798 cm^{-1} [170], [171]. On the other hand, small bands between 2500 cm^{-1} to 2974 cm^{-1} present in some samples are associated to C-O vibrations of soot as impurities from the combustion processes, like the bands located around 846 and 1245 cm^{-1} [172].

Most of the samples show a broad band located at 3461 cm^{-1} , attributed to stretching vibrations of O-H mainly by the presence of hydroxyl ions from portlandite and absorbed molecular water from the environment, while the small band or in some spectra the small shoulder around 1651 cm^{-1} is attributed to O-H bending vibrations [12], [169]. Finally, the sharp band at 3643 cm^{-1} is associated to O-H stretching vibrations from hydroxyl ions of portlandite and hydroxyl ions strongly bound to calcite [171].

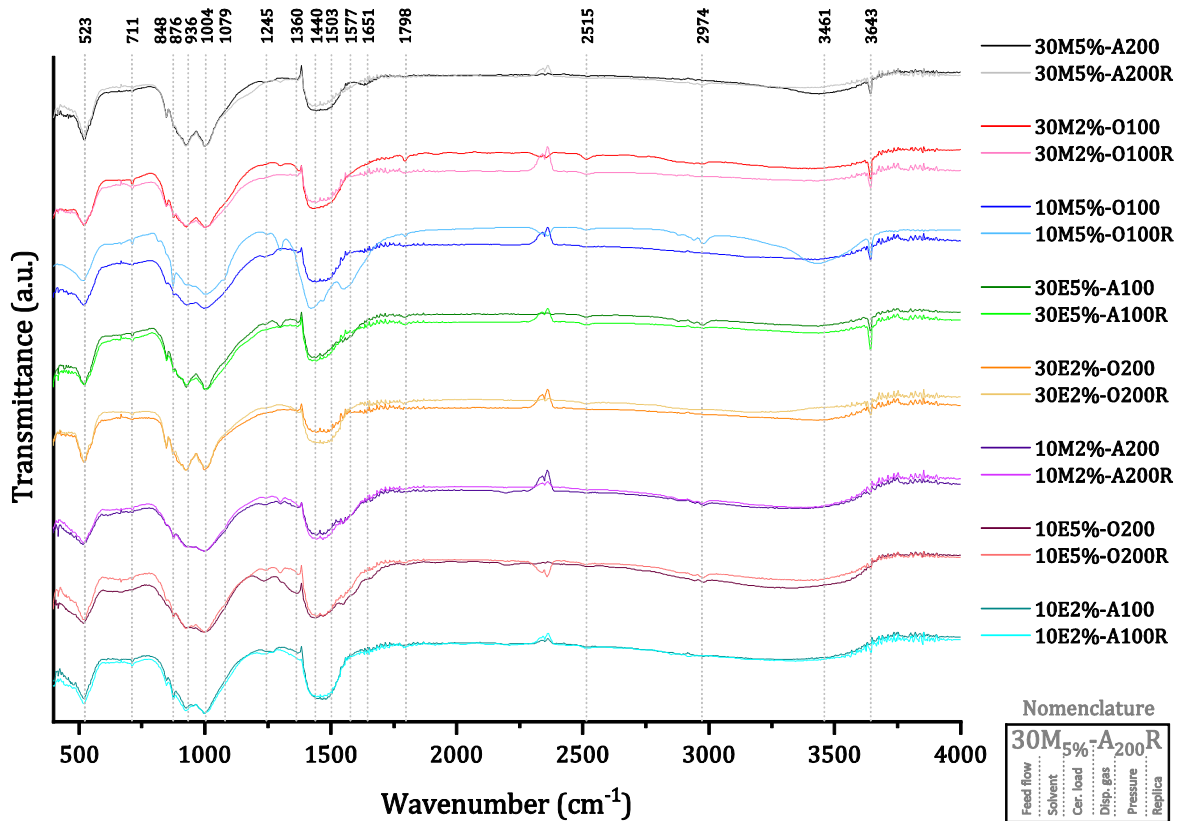
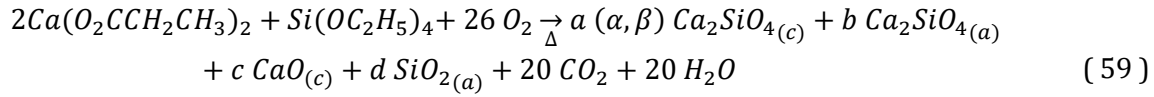
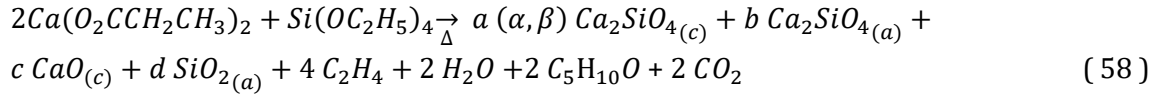


Figure 6-9. Fourier transform infrared spectroscopy spectra of calcium silicates

Considering the results obtained by XRD, TGA-DSC/MS-IR and FT-IR, it is possible to affirm that the chemical reactions in the processes differ from the theoretical reactions showed in equations (55)

and (56). The chemical reactions suggested during the synthesis process after analyzed the results are presented in the equations (58) to (61). These chemical reactions will be explaining in detail in Chapter 8.



Equations (58) and (59) show the thermal decomposition and oxidation reactions of the precursors in the flame, respectively, to produce the compounds founded in the mineralogical characterization of the samples, where *a*, *b*, *c* and *d* represent the stoichiometry coefficients of each product. The characterization shows the formation calcium oxide, Portlandite and calcium carbonate as byproducts of the reactions, however, considering the high temperatures of the reaction and the conditions of the combustion, it is not possible to form Ca(OH)₂ and CaCO₃ in the flame. Nevertheless, the precursors could be decomposed and oxidizing in dicalcium silicate polymorphs and CaO. Under high humidity conditions, from water vapor released in the combustion, CaO particles react with water to form calcium hydroxide as it is shown in equation (60), which in turns reacts with the carbon dioxide of the environment to form calcium carbonate like in equation (61).

Considering these equations and the chemical data obtained from the Rietveld refinement, the real amount of calcium oxide produced in each reaction was calculated. For this, the calcium oxide necessary to form CaCO₃ and Ca(OH)₂ was calculated in each reaction and added to the value of calcium oxide from the refinement. The calcium oxide amounts of each reaction are shown in Table 6-3.

The samples 10M_{5%}-O₁₀₀, 30M_{2%}-O₁₀₀, 30E_{5%}-A₁₀₀ and 30M_{5%}-A₂₀₀ and its respective replicates 10M_{5%}-O₁₀₀R, 30M_{2%}-O₁₀₀R, 30E_{5%}-A₁₀₀R and 30M_{5%}-A₂₀₀R present high amounts of calcium oxide formed in the flame (from 8 % to 17 %). Most of these compounds have as common factor a high feed flow rate, which could indicate that a fast flow of precursors does not permit a proper evaporation of the droplets, allowing a slow decomposition of the starting solution, which could lead to the formation of heterogeneous products. Furthermore, from Table 4-2 is observed that high flow rates form droplets with higher mean drop size than low feed flows. In addition, the pressure of dispersion

gas of these samples, tends to be the lower pressure evaluated (100 kPa), indicating that the mean drop size of the aerosol can have an important effect in the mineralogy of the formed particles.

Table 6-3. Percent of calcium oxide formed during the reaction processes

Sample	Percentages from Rietveld refinement			% CaO produced in the flame
	% CaO	% CaO from CaCO ₃	% CaO from Ca(OH) ₂	
30M _{5%} -A ₂₀₀	1.6	4.0	2.6	8.2
30M _{5%} -A ₂₀₀ R	1.7	3.3	4.1	9.1
30M _{2%} -O ₁₀₀	2.0	5.5	3.6	11.1
30M _{2%} -O ₁₀₀ R	2.6	6.1	4.6	13.3
10M _{5%} -O ₁₀₀	2.4	10.2	2.5	15.1
10M _{5%} -O ₁₀₀ R	1.6	11.9	3.7	17.2
30E _{5%} -A ₁₀₀	3.1	3.5	4.8	11.4
30E _{5%} -A ₁₀₀ R	1.1	4.8	7.1	13.0
30E _{2%} -O ₂₀₀	2.1	2.3	-	4.4
30E _{2%} -O ₂₀₀ R	1.2	2.4	-	3.6
10M _{2%} -A ₂₀₀	0.4	2.5	-	2.9
10M _{2%} -A ₂₀₀ R	-	3.4	-	3.4
10E _{5%} -O ₂₀₀	-	2.1	-	2.1
10E _{5%} -O ₂₀₀ R	1.5	5.2	-	6.7
10E _{2%} -A ₁₀₀	-	6.9	-	6.9
10E _{2%} -A ₁₀₀ R	-	4.4	0.3	4.7

6.2. Degree of reactivity

The C-S-H is the primary binding phase in Portland cement. One of the aims to produce nanoparticles of calcium silicates is the rapid hydration because of the high surface area, stimulating nucleation and growth processes of calcium silicate hydrate (C-S-H) in early stages of the hydration [173]. This reactivity is strongly dependent of the mineralogy and specific surface area of the samples. However, whether the mineralogy of the samples is not adequate, having a high specific surface area is not enough.

Table 6-4 shows the results obtained for the specific surface area of the samples. The average particle sizes (APS) of the samples was determinate using the equation (62), assuming spherical, monodisperse particles. Where APS is the average particle size, SSA is the specific surface area, x is the mass fraction and ρ is the density of the compound ([128]).

$$APS = \frac{6}{SSA \cdot \sum(x_i \cdot \rho_i)} \quad (62)$$

The average particle sizes were between 26.8 nm to 110.1 nm, for 10M_{2%}-A₂₀₀ and 30E_{5%}-A₁₀₀R, respectively. The samples 10M_{2%}-A₂₀₀, 10E_{5%}-O₂₀₀, 10M_{2%}-A₂₀₀R, 10E_{2%}-A₁₀₀, 10E_{5%}-O₂₀₀R and 10E_{2%}-A₁₀₀R, presented values under 50 nm, while the rest of the samples are upon this value. The standard deviation of the specific surface area of the first run of experiments and their replication are under ± 7 m²/g, indicating a good reproducibility of the results. Results indicate that the samples with higher specific surface area are obtained when the pressure of dispersion gas and feed flow rate take values of 200 kPa and 10 mL/min, respectively. This combination corresponds to the aerosol with smaller mean drop size from the Sauter mean diameter calculations. Additionally, the lower specific surface area was obtaining by the combination of 100 kPa and 30 mL/min, corresponding to the bigger droplets in agreement with the Sauter mean diameter, concluding that bigger droplets affect the features of the particles, even when metallorganic compounds with high enthalpy of volatility were used as starting materials.

Table 6-4. Specific surface area and average particle size distribution

Sample	SSA (m ² /g)	APS (nm)
30M _{5%} -A ₂₀₀	31.0	60.5
30M _{5%} -A ₂₀₀ R	32.6	57.9
30M _{2%} -O ₁₀₀	27.1	69.8
30M _{2%} -O ₁₀₀ R	28.6	66.6
10M _{5%} -O ₁₀₀	28.5	68.8
10M _{5%} -O ₁₀₀ R	19.6	99.2
30E _{5%} -A ₁₀₀	18.0	104.6
30E _{5%} -A ₁₀₀ R	17.3	110.1
30E _{2%} -O ₂₀₀	34.3	54.3
30E _{2%} -O ₂₀₀ R	26.2	70.2
10M _{2%} -A ₂₀₀	68.6	26.8
10M _{2%} -A ₂₀₀ R	66.7	27.6
10E _{5%} -O ₂₀₀	49.6	37.1
10E _{5%} -O ₂₀₀ R	39.8	46.7
10E _{2%} -A ₁₀₀	47.8	39.1
10E _{2%} -A ₁₀₀ R	38.9	47.7

The hydration process is usually divided in four periods, corresponding to the initial period, the induction period, the acceleration period and the retardation period, where the last to stages can be overlade and denominated main period or second peak. All the samples were submitted under isoperibolic calorimetry to observe their hydration behavior, reveling the complete formation of the initial period after 30 minutes and the subsequent formation of the second peak with an accelerated

behavior. It is knowing that β -dicalcium silicate present slow reactivity with water, requiring around 28 days to achieve the 30 % of the reaction and 1 year to achieve the 90 %, however the reactivity depends on the surface area of the particles [24].

The area under the curves in Figure 6-10 and Figure 6-11 represent the cumulative heat flow release during the hydrolysis reaction. The results obtained for each sample in the first and second peaks are presented in Table 6-5.

In the first peak of hydration take place the dissolution of calcium silicates. The complete formation of this peak took a minimum time of 11 minutes for the faster reaction and maximum time of 24 minutes for the slower reaction, achieving the maxima values after 47 seconds and 2 minutes of contact with water. The heat flow released in this stage was between 13.51-25.32 mJ/g for samples 30E_{2%}-O₂₀₀R and 10E_{5%}-O₂₀₀, respectively.

Table 6-5. Heat flow released during the hydrolysis of calcium silicates

Sample	First peak		Second peak	
	Max Height (mW/g)	Heat flow (mJ/g)	Max Height (mW/g)	Heat flow (mJ/g)
30M _{5%} -A ₂₀₀	413.02	18.88	1.07	15.57
30M _{5%} -A ₂₀₀ R	400.49	18.36	0.81	13.71
30M _{2%} -O ₁₀₀	441.89	20.89	0.82	6.62
30M _{2%} -O ₁₀₀ R	417.83	19.01	0.73	7.35
10M _{5%} -O ₁₀₀	500.37	24.62	1.33	8.95
10M _{5%} -O ₁₀₀ R	312.08	23.65	0.58	3.21
30E _{5%} -A ₁₀₀	514.11	22.67	0.76	4.94
30E _{5%} -A ₁₀₀ R	487.32	22.60	0.51	3.08
30E _{2%} -O ₂₀₀	410.34	14.75	2.72	21.95
30E _{2%} -O ₂₀₀ R	317.73	13.51	0.73	9.88
10M _{2%} -A ₂₀₀	543.71	22.07	6.86	45.58
10M _{2%} -A ₂₀₀ R	559.32	24.27	6.22	48.10
10E _{5%} -O ₂₀₀	365.87	25.32	4.63	38.46
10E _{5%} -O ₂₀₀ R	425.58	21.10	3.95	33.21
10E _{2%} -A ₁₀₀	308.78	15.37	5.75	38.90
10E _{2%} -A ₁₀₀ R	429.11	16.09	3.07	37.48

The sample 10M_{2%}-A₂₀₀R presented the higher maximum height in the first peak with a value of 559.32 mW/g and a heat flow of 24.27 mJ/g. This sample is one of the samples with the largest amount of amorphous material, low number of secondary phases (6%) and high surface area (49.6 m²/g). The replication of this sample present similar responses, being the next sample with greater

reactivity. In addition, in Figure 6-12 is possible to observe that these two samples present the higher heat flow release during the second peak.

The samples 30M_{5%}-A₂₀₀, 30M_{2%}-O₁₀₀, 10M_{5%}-O₁₀₀ and 30E_{5%}-A₁₀₀ and their respective replications 30M_{5%}-A₂₀₀R, 30M_{2%}-O₁₀₀R, 10M_{5%}-O₁₀₀R and 30E_{5%}-A₁₀₀R did not show the formation of the second peak after 200 hours of reaction, whereby this samples have non-hydraulic behavior after 8 days of reaction. Otherwise, the samples 30E_{2%}-O₂₀₀ and its replication 30E_{2%}-O₂₀₀R present an atypical behavior, due to the second peak of the replication is too small. Similar results were observed in the SSA of these samples, where the sample 30E_{2%}-O₂₀₀R has a specific surface area of 26.2 m²/g, while the original run 34.2 m²/g. Regarding to the phases identified, both products showed the higher crystallinity and lower amount of amorphous in comparison to the other samples, however, among them were observed differences in the number of polymorphs α -Ca₂SiO₄ and β -Ca₂SiO₄. The total sum of these polymorphs was close, but the amount of α -Ca₂SiO₄ was higher in the most reactive sample (30E_{2%}-O₂₀₀), while the amount of β -Ca₂SiO₄ was higher in the replication. These differences in the number of polymorphs and SSA can explain this result, considering that the polymorphs α -Ca₂SiO₄ react faster than β -Ca₂SiO₄ and the SSA was lower for the sample with less heat flow release.

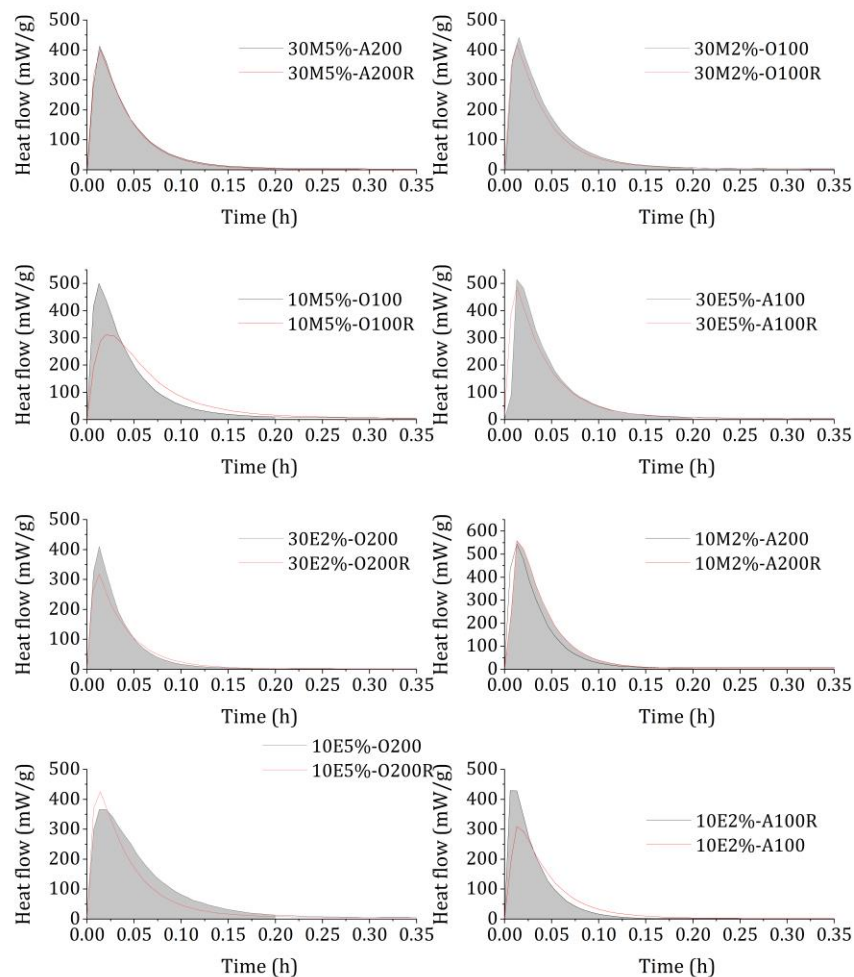


Figure 6-10. First peak of heat flow curves of calcium silicates

As it was expected, the samples with higher amount of calcium oxide (upon 8 % reported in Table 6-3), present the lower degree of reactivity due to the percentage of amorphous material and calcium silicates is lower. The sample 30E_{2%}-O₂₀₀R, was an exception to this behavior, considering that the sample has a low number of secondary phases and a high degree of crystallinity, but the degree of reactivity after 48 h was small.

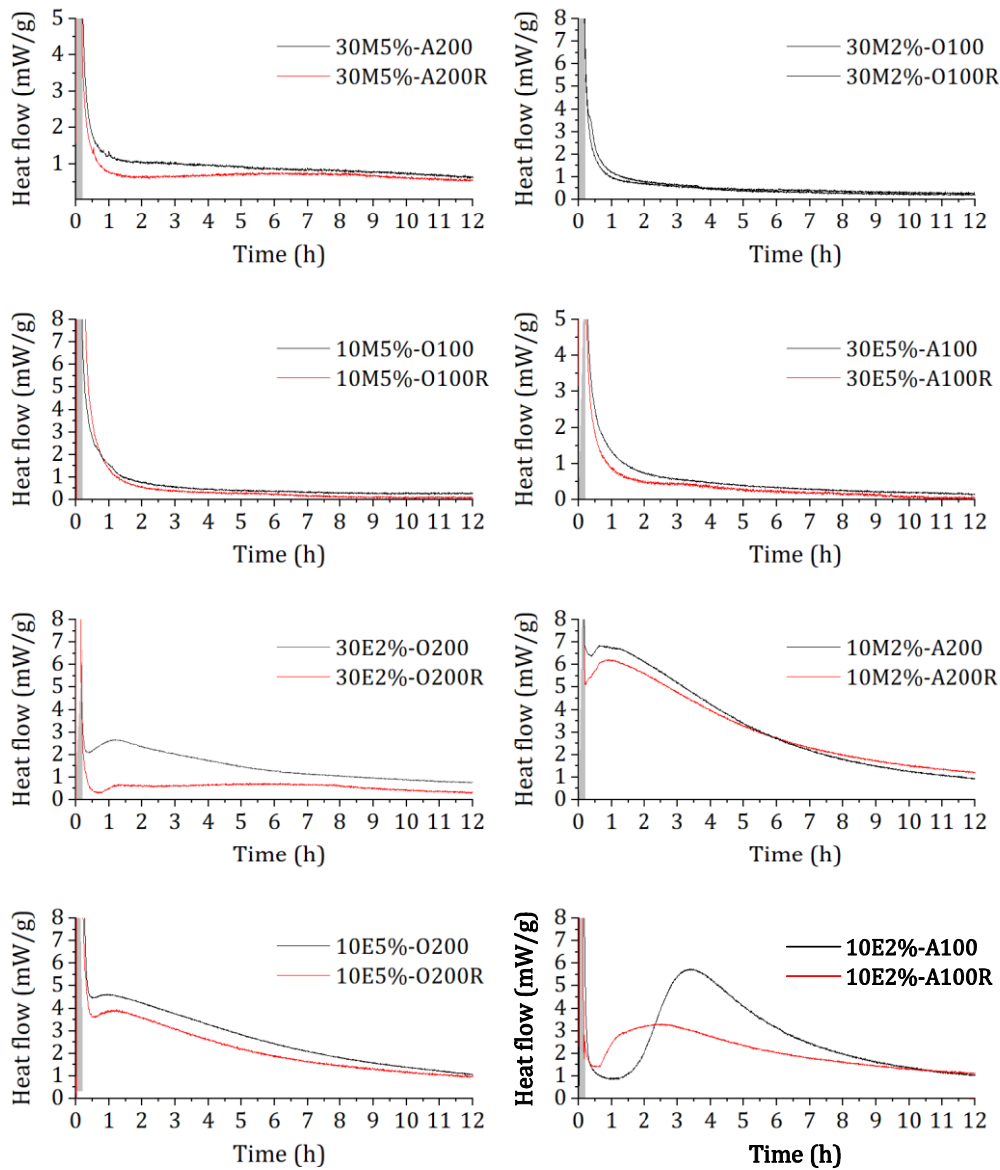


Figure 6-11. Second peak of heat flow curves of calcium silicates

The samples with higher amount of amorphous material (59.9 %-78.3 %) were 10M_{2%}-A₂₀₀, 10E_{5%}-O₂₀₀ and 10E_{2%}-A₁₀₀ and their respective replications, 10M_{2%}-A₂₀₀R, 10E_{5%}-O₂₀₀R and 10E_{2%}-A₁₀₀R,

which correspond exactly with the samples with hydraulic behavior. The rest of the samples did not show any hydraulic behavior after 8 days of contact with water (amorphous percentages between 55% to 41%), except the samples 30E_{2%}-O₂₀₀ and its replication 30E_{2%}-O₂₀₀R (amorphous values around 30%), which present a slightly hydraulic behavior and present special conditions of synthesis discussed below in Chapter 7.

The curves of the samples with reactive behavior (Figure 6-12), corresponding to 10M_{2%}-A₂₀₀, 10M_{2%}-A₂₀₀R, 10E_{5%}-O₂₀₀, 10E_{5%}-O₂₀₀R, 10E_{2%}-A₁₀₀, 10E_{2%}-A₁₀₀R, 30E_{2%}-O₂₀₀ and 30E_{2%}-O₂₀₀R show the formation of a very short or nonexistent dormant period, since the time consuming nucleation reactions does not have place, however the heat release of 10E_{2%}-A₁₀₀R was smaller than the rest of the samples. These samples start the formation of the second peak after 25 minutes to 1.5 hours of contact with water, achieving the maximum height between 43 minutes to 4 hours. After that, the heat released decrease rapidly until 10 hours and continues to decrease gradually until ~40 hours.

Finished the calorimetry assay, these samples formed a slightly hard paste that was allowed to penetrate. The amorphous percentage of the samples show a direct impact in the reactivity of the samples, with a stronger effect than the number of crystalline polymorphs of belite. This amorphous material could be constituted by polymorphs of belite with low crystallinity since the particle size and the velocity of the process, which favor the formation of metastable phases. Nevertheless, samples 30E_{2%}-O₂₀₀ and 30E_{2%}-O₂₀₀R are an exception, because were the samples with lower amount of amorphous material, but higher number of polymorphs of belite.

The hydrolysis reactions start at the surface of the samples, controlling the effectiveness of the cement hydration kinetics. During the first stage was observed the release of heat from all the samples, which is the result of humectation processes and dissolution of reactive phases. There is important to notice that most of the samples have a percentage of calcium oxide, which reacts with water in an exothermic process to form portlandite. Then, there is observe the reduction in the heat flow until 30 minutes, where the latent period was observed only in the sample 10E_{2%}-A₁₀₀ (Figure 6-12). The rest of the hydraulic samples did not show this stage, starting immediately with the formation of hydrolysis products. This behavior indicates that dissolved species in the media, where highly enough to start the nucleation processes required to produce the C-S-H gel.

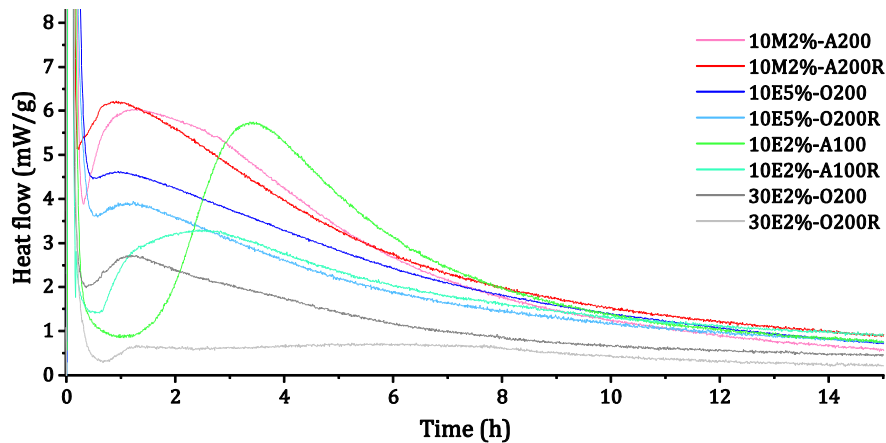


Figure 6-12. Second peak of samples with hydraulic behavior

After 48 hours of contact with water, all the reactions were stopped, and the hydrated materials were analyzed by XRD (Figure 6-13).

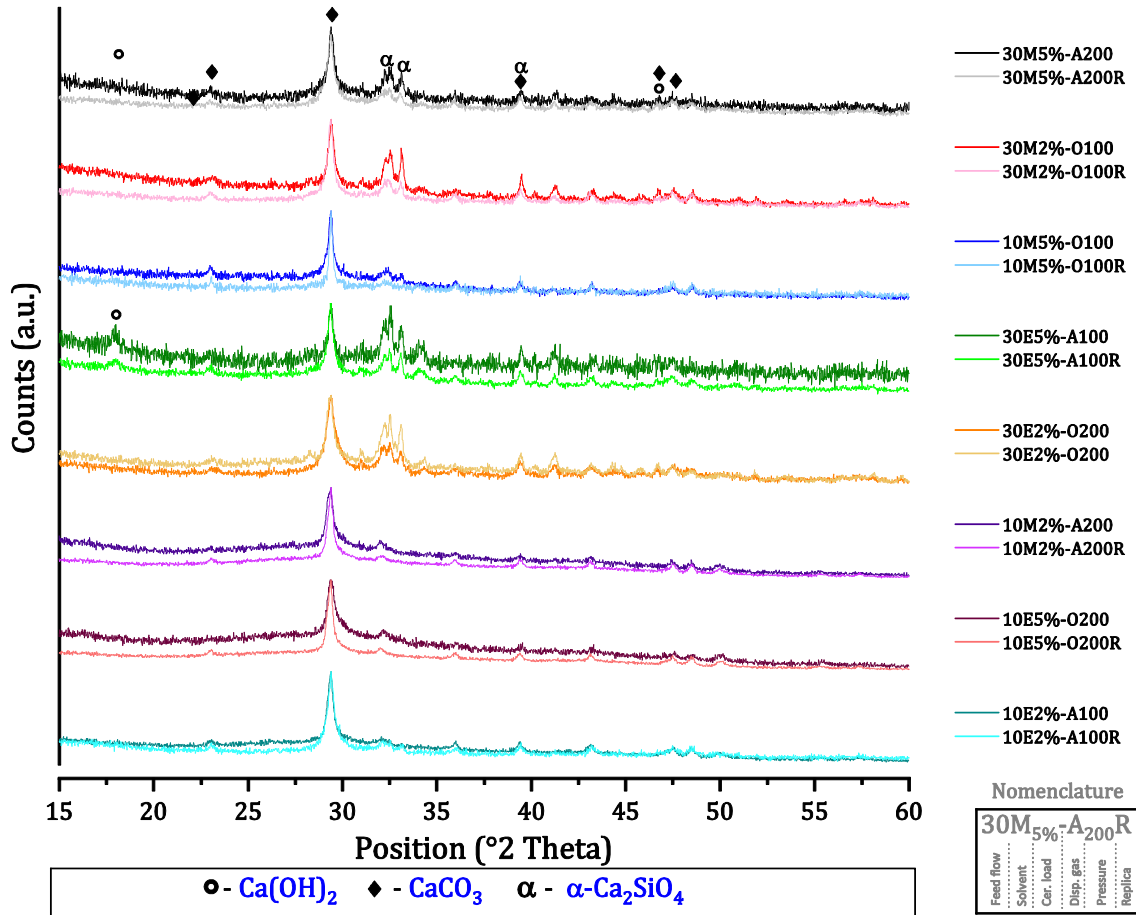


Figure 6-13. XRD patterns of the samples after 2 days of hydration

All samples contain calcium carbonate after the calorimetry, which was expected due to the unreactive behavior of this phase, which was identified in the un-hydrated samples. The samples 30M_{5%}-A₂₀₀, 30M_{2%}-O₁₀₀, 30E_{5%}-A₁₀₀ and 30E_{2%}-O₂₀₀ and their respective replications, 30M_{5%}-A₂₀₀R, 30M_{2%}-O₁₀₀R, 30E_{5%}-A₁₀₀R and 30E_{2%}-O₂₀₀R 109, show the presence of three peaks between 31.5 to 33.5 (2θ) attributed to dicalcium silicate phases with high crystallinity, which require longer reaction times to react completely with water. These samples showed the lower presence of amorphous material (below 56 %) in comparison with the phases with reactive behavior in which the non-diffraction fraction is upon 61 %. Otherwise, samples 10M_{2%}-A₂₀₀, 10E_{5%}-O₂₀₀ and 10E_{2%}-A₁₀₀ and their respective replications, 10M_{2%}-A₂₀₀R, 10E_{5%}-O₂₀₀R and 10E_{2%}-A₁₀₀R, show the presence of calcite and C-S-H (33-0306). During the hydration of dicalcium silicates, the reaction products should be calcium silicate hydrate (C-S-H) and calcium hydroxide, however the XRD patterns obtained at 48 h and later ages do not show the presence of calcium hydroxide, which could be carbonated with the

exposition to the air. Otherwise, the peaks of dicalcium silicate which did not react correspond to the β - Ca_2SiO_4 phase, which has slower rate of hydration than α - Ca_2SiO_4 phase.

XRD measurements after 28 days of hydration (Figure 6-14) reveal a complete reaction of all the products, indicating that the two groups of samples (early-reactive and late-reactive) present different kinetics during the hydration. The diffractograms show a clear presence of calcium carbonate and the formation of the three peaks C-S-H.

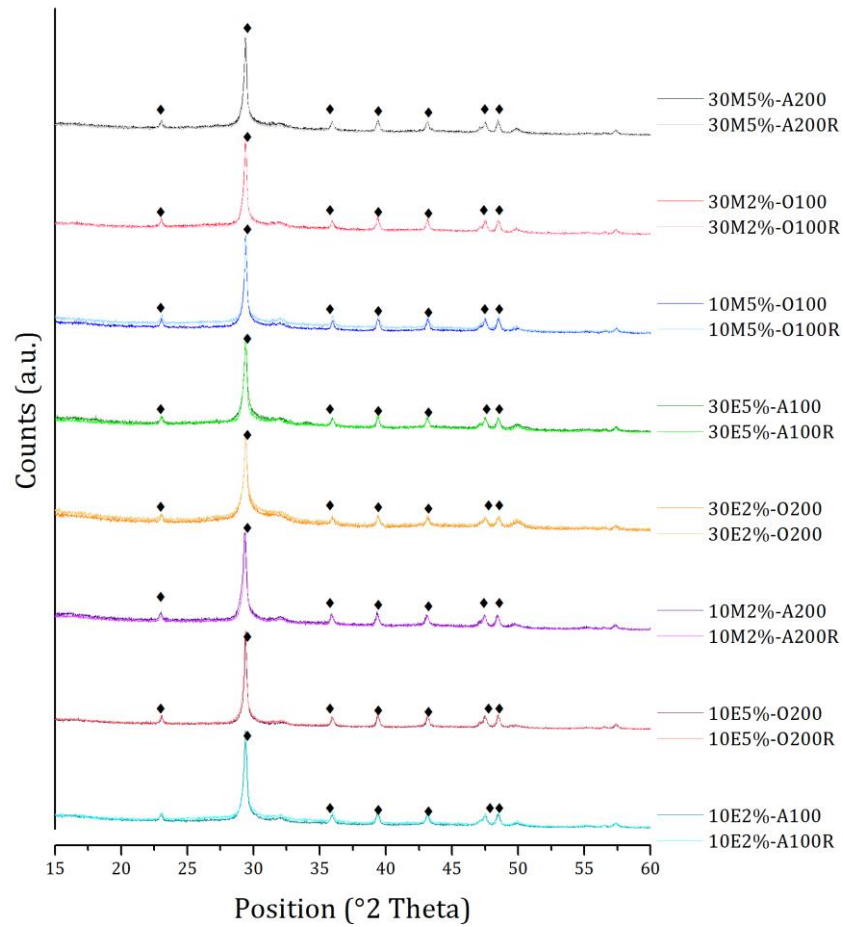


Figure 6-14. XRD patterns of the samples after 28 days of hydration

6.3. Morphological characterization

SEM and TEM techniques were used to observe the morphology of anhydrous and hydrated samples. Figure 6-15 shows the micrographs of anhydrous 10M_{5%}-O₁₀₀ at different magnifications, which was a sample with late-reactive behavior.

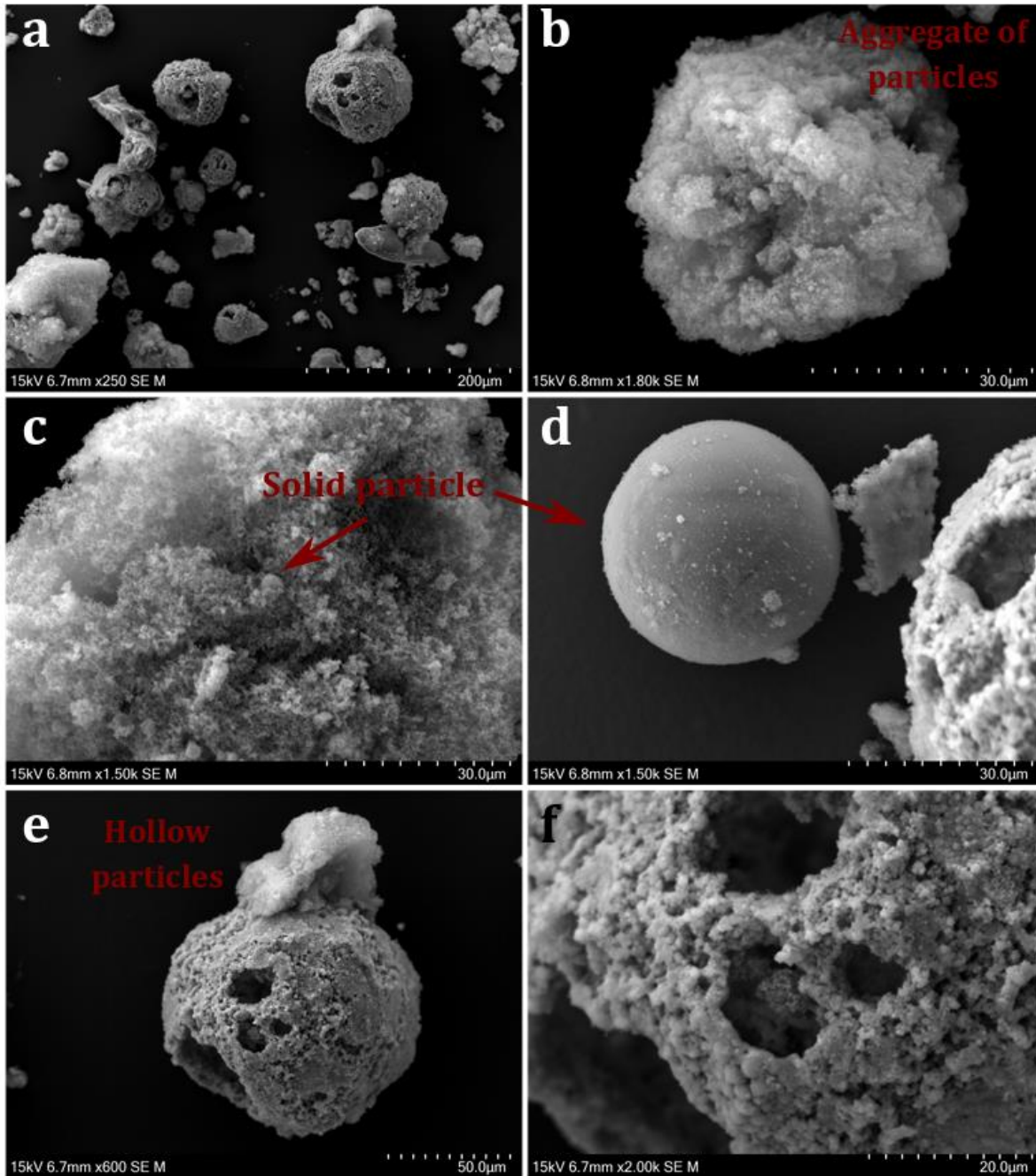


Figure 6-15. Micrographs of anhydrous 10M_{5%}-O₁₀₀

The micrograph *a* shows the formation of the three kind of particles produce by FSP following the gas-to-particle and drop-to-particle mechanisms, presenting hollow particles, large particles and aggregates of small particles. The images *b* and *c* show the aggregates of small particles, in which is possible to observe small solid particles of around 3 μm in size (image *c*). Image *d* shows a large solid particle of around 30 μm in size, which could correspond to calcium oxide formed by the precipitation of the calcium precursor, before a proper formation of the gas phase, as also occurs during the

formation of hollow particles [99], which are observed in images *e* and *f*. These hollow particles show sizes between 30 to 100 μm of diameter, which are formed by the aggregation of smaller solid particles (around 3 μm). The hollow particles found in the samples were analyzed by EDS, suggesting that these particles are mainly composed by calcium carbonate. These results are in coherence with the compositional and calorimetric results, where the slow hydraulic behavior could be attributed to a high amount of hollow and large particles, which decrease the reactivity of the samples due to the non-hydraulic feature of the secondary phases ($\text{Ca}(\text{OH})_2$ and CaCO_3).

In Figure 6-16 is shown the micrographs of $10\text{M}_{2\%}\text{-A}_{200}\text{R}$ at different magnifications, which presented early-reactive behavior. This sample shows a higher amount of aggregates of small particles as a foam-like (Images *a* and *b*). In addition, it is observed the presence of solid large particles (image *c*), surrounded by the foam material (Image *d*). The lowest presence of hollow particles in this sample, could be associated with the high pressure of dispersion gas (200 kPa) used during its synthesis, contrary to the sample $10\text{M}_{5\%}\text{-O}_{100}$ in which the pressure of dispersion was lower (100 kPa), due to this parameter influence the formation of the droplets, their rate of evaporation and the time in the high temperature zone.

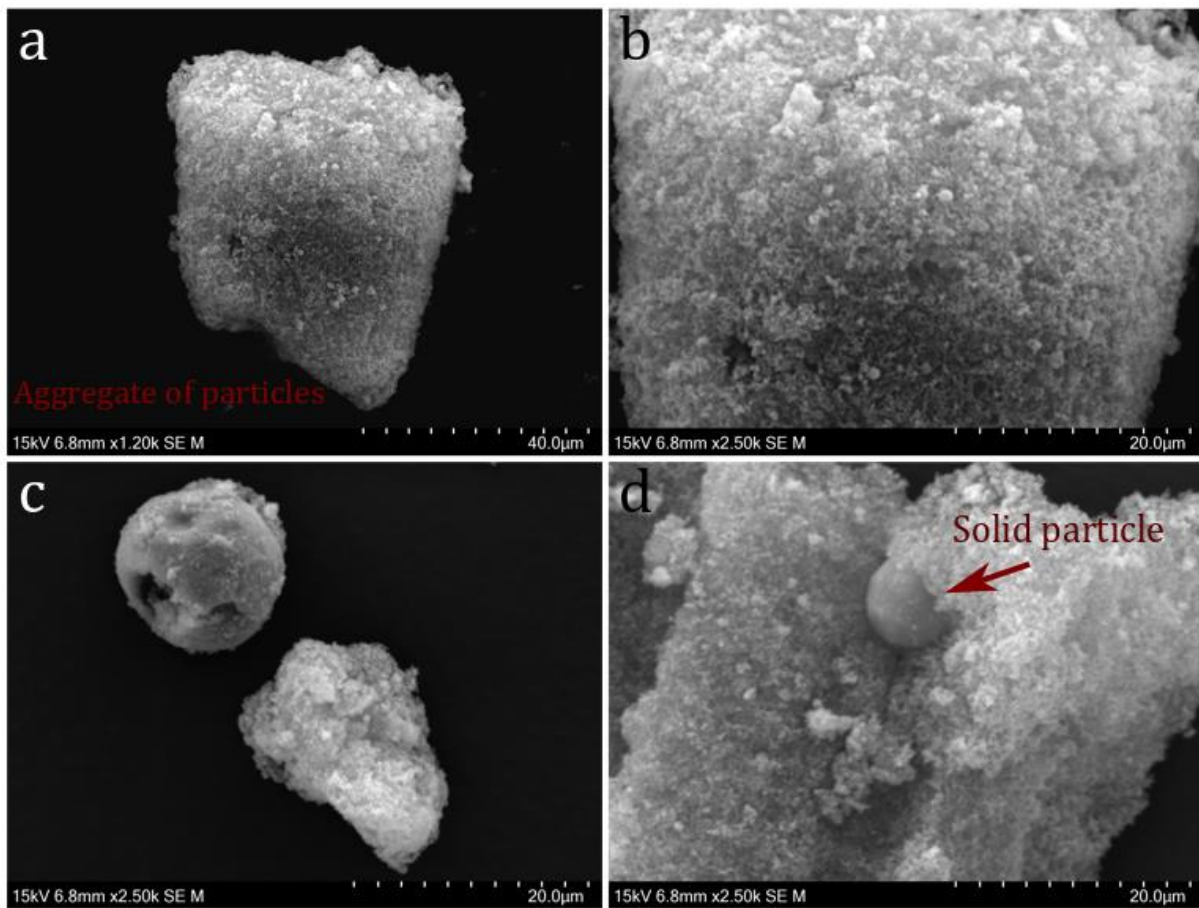


Figure 6-16. Micrographs of anhydrous $10\text{M}_{2\%}\text{-A}_{200}\text{R}$

The morphology of the hydrated samples, with late-hydraulic behavior at 48 h, 30M_{5%}-A₂₀₀ and 10M_{5%}-O₁₀₀, after 40 d is shown in Figure 6-17. The micrographs *a* and *b* correspond to 30M_{5%}-A₂₀₀, while the micrographs *c* and *d* correspond to 10M_{5%}-O₁₀₀. These samples did not show hydraulic behavior after 48 hours of hydration. However, after longer times (28 days) the small number of dicalcium silicate present in the samples reacts to form C-S-H. The micrograph *a* shows the formation of aggregates of material formed by smaller particles, without the formation of a particular morphology, nevertheless, micrograph *b* shows a slight formation of spider-like morphologies joining the small particles with each other. The micrographs *c* shows a sphere-like formation in the center of the figure, with a size of ~100 μm, while the micrograph *d* is a magnification of this sphere. The same behavior of 10M_{5%}-O₁₀₀ is observed in this sample, but the formation of the spider-like morphologies is clearer observed. These spider-like formation correspond to C-S-H formation in the surface of the aggregates.

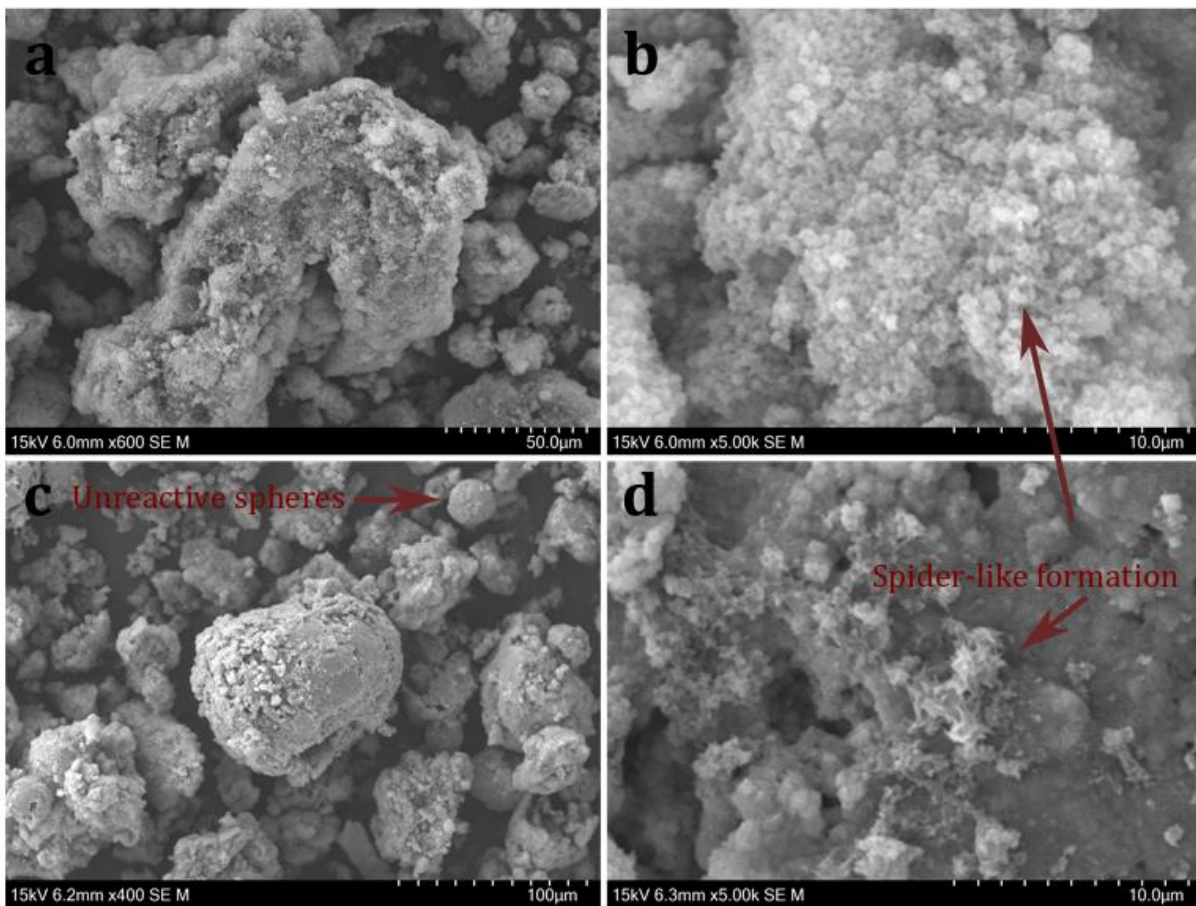


Figure 6-17. Micrographs of late-hydraulic samples after 40 d. (*a - b*) 30M_{5%}-A₂₀₀; (*c - d*) 10M_{5%}-O₁₀₀

Otherwise, the morphology of the hydrated samples, with early-hydraulic behavior at 48 h, 30E_{2%}-O₂₀₀, 10M_{2%}-A₂₀₀ and 10M_{2%}-A₂₀₀R, after 40 d is shown in Figure 6-18. The sample 30E_{2%}-O₂₀₀, correspond to the product with higher crystallinity of all the samples, showing the formation of a small second peak during the calorimetry measurements.

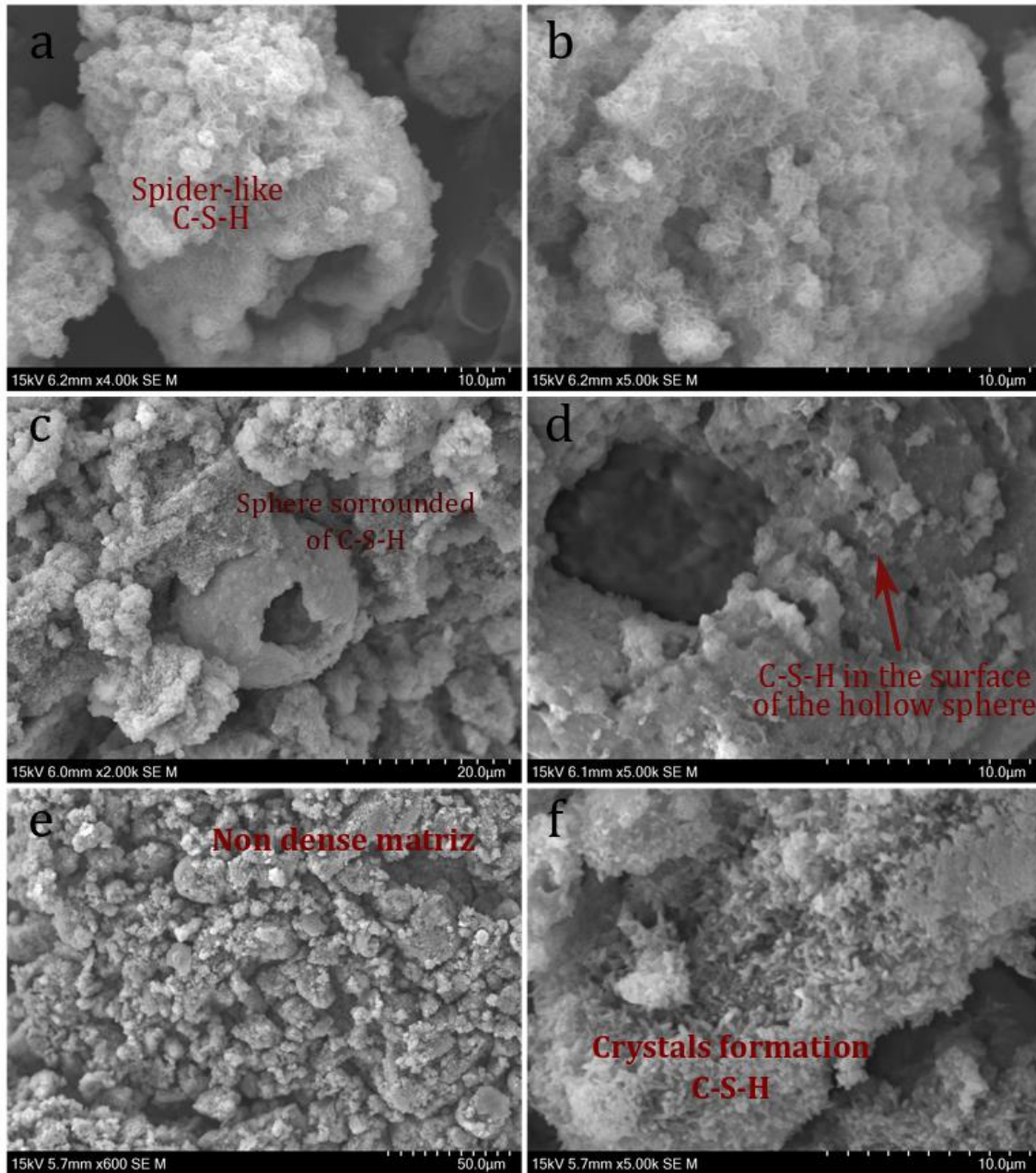


Figure 6-18. Micrographs of early-reactive samples after 40 d. (a - b) 30E_{2%}-O₂₀₀; (c - d) 10M_{2%}-A₂₀₀, (e - f) 10M_{2%}-A₂₀₀R

Sample 30E_{2%}-O₂₀₀ shows the formation of similar spider-like crystals or fibrous crystals in all the surface of the sample, which is attributed to C-S-H formation (images *a* and *b*) [174], [175]. On the other hand, samples 10M_{2%}-A₂₀₀ and 10M_{2%}-A₂₀₀R were the samples with higher amount of amorphous material before hydration and higher release of heat flow during the calorimetry measurements. After 40 d, these samples present a different morphology of 30E_{2%}-O₂₀₀. At the same magnifications, (micrographs *b*, *d* and *f*) the micrographs show a non-denser paste with the formation

of crystals in the surface. The graph *c* shows the formation of a hollow sphere surrounded by aggregates with non-dense undefined morphologies. Spheres were observed in several parts of the sample, which were formed during the flame reaction. These morphologies correspond to the liquid-to-particle mechanism resulted by the use of water in the starting solution. Otherwise, the micrograph *f* shows the formation of crystals associated to the formation of C-S-H.

Energy dispersive X-ray analysis was used on sample 10M_{2%}-A₂₀₀, to obtain chemical information about the hollow spheres and aggregates observed in anhydrous (Table 6-6) and hydrated (Table 6-7) samples as well as the formation of crystal observed in 10M_{2%}-A₂₀₀R hydrated (Table 6-8). The EDS measurements were done in a low vacuum SEM depositing the samples in carbon adhesive tapes without coating. Considering these conditions and the fact that EDS is not accurate for low atomic number elements as carbon and oxygen, the high values of carbon in the measurements are explained. Nevertheless, these results bring an idea of the composition of these hollow spheres and aggregates observed.

Table 6-6 indicates that the hollow particles observed in the anhydrous material are mainly composed by carbon, oxygen and calcium with low traces of silicon, while the aggregates have higher percent of silicon. This could suggest that the hollow spheres correspond to secondary phases as calcium carbonate particles while the aggregates are composed by nanoparticles of compounds as dicalcium silicate.

Table 6-6. EDS results for the anhydrous sample 10M_{2%}-A₂₀₀ (atomic %)

Shape	Point	C	O	Si	Ca	Micrographs
Spheres	1	57.94	28.48	0.92	12.66	
	2	62.38	27.34	0.48	9.80	
	3	55.00	32.81	0.77	11.42	
Aggregates	4	55.59	29.93	5.92	8.56	
	5	52.10	34.18	5.04	8.68	
	6	54.39	31.14	5.21	9.26	

On the other hand, the results of the hydrated samples shown in Table 6-7 and Table 6-8, show an increase of silicon in the surface of the hollow particles, which could be result of the formation of C-S-H on the surface of the spheres as observed in the SEM micrographs. Regarding to the aggregates, the percentages of silicon are higher than in anhydrous samples, which could be associated to a higher transformation of the anhydrous sample in calcium silicate hydrates.

Table 6-7. EDS results for the hydrated sample 10M_{2%}-A₂₀₀

Shape	Point	C	O	Si	Ca	Micrographs
Spheres	1	30.63	35.97	6.09	27.31	
	2	37.48	24.21	7.01	31.29	
	3	30.04	39.02	3.80	27.15	
	4	39.18	39.02	2.60	19.21	
Aggregates	5	37.48	23.23	12.45	26.84	
	6	50.04	22.50	9.95	17.51	
	7	51.04	21.86	7.82	19.28	

Table 6-8. EDS results for the hydrated sample 10M_{2%}-A₂₀₀R

Shape	Point	C	O	Si	Ca	Micrograph
Spheres	1	28.19	41.17	5.51	25.14	
	2	21.61	35.24	6.99	36.16	
Crystal	3	21.81	46.07	5.95	26.17	
	4	22.84	46.08	3.33	27.75	

TEM images and SAED (Selected Area Electron Diffraction) patterns of samples 30E_{2%}-O₂₀₀ and 10M_{2%}-A₂₀₀ as-prepared and after hydration are shown below. Considering XRD results of anhydrous phases, sample 30E_{2%}-O₂₀₀ showed the higher crystallinity regarding to the rest of the samples, while sample showed the higher number of amorphous phase or ACn content. In Figure 6-19 are shown TEM images of anhydrous 30E_{2%}-O₂₀₀. In images **a** and **b** are observed the formation of nanoparticles with spherical shape and irregular aggregates formed by sintering of them. There is observed a broad particle distribution with diameters between 20 nm to 90 nm. The formation of necks (Image **d**) could be attributed to the high temperature of the oxy-acetylene flame, which promotes sintering processes at the beginning of the synthesis process. These necks were also observed in samples made with a feed flow rate of 10 mL/min, whereby the flame may be the most relevant factor in this growth phenomenon. Images **e** and **f** show higher magnifications of a particle, in which is possible to observe its atomic arrangement. This particle (Image **e**) shows crystalline arrangements of the atoms close to the center, while in the border it is mainly amorphous. The crystalline section is detailed in Image **f**.

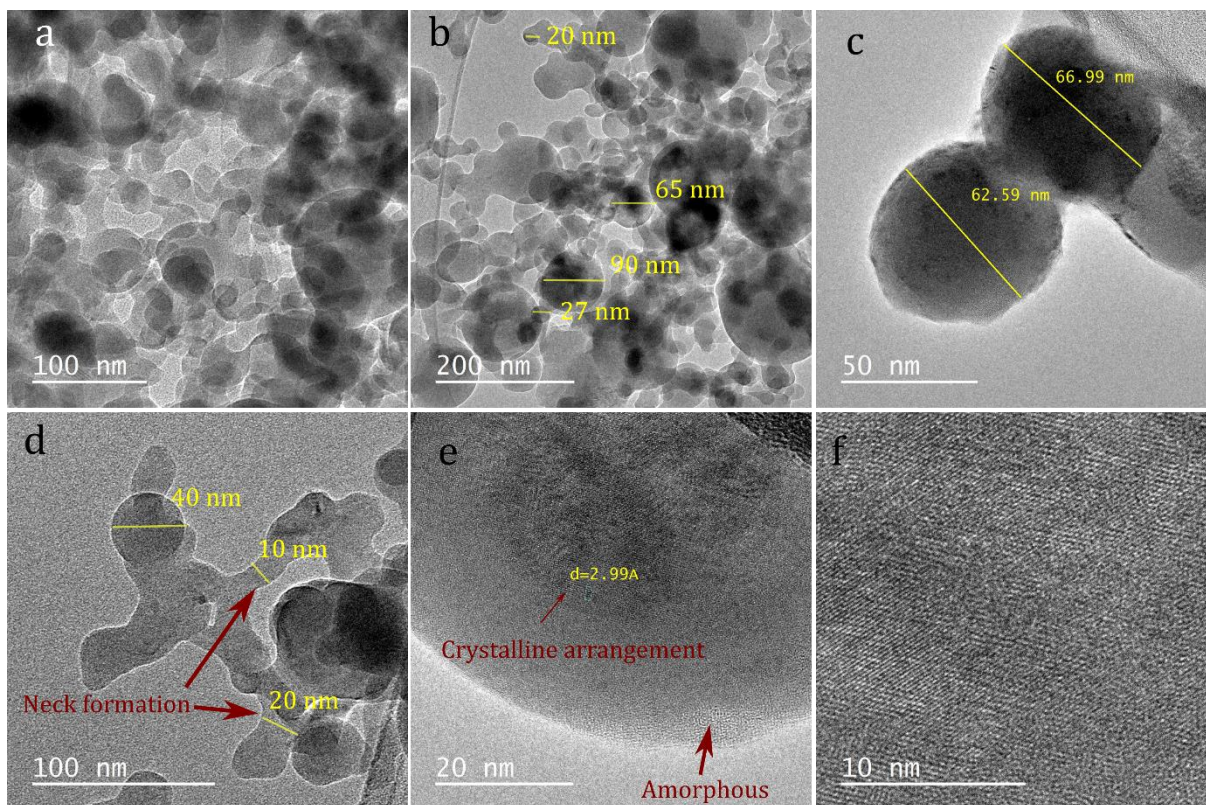


Figure 6-19. TEM images of sample 30E_{2%}-O₂₀₀

In Figure 6-20 are observed the TEM images of 10M_{2%}-A₂₀₀. Like 30E_{2%}-O₂₀₀, 10M_{2%}-A₂₀₀ shows a broad particle size distribution in nanometric scale, but for this sample, the number of smaller particles is higher, coherently with the specific surface area and calorimetric results (Figure 6-20 (**a**)). In addition, image **b** shows the formation of necks between particles with sizes between 10 to 20 nm, increasing the porosity of the sample, which increase the reactivity of the sample, but can decrease the mechanical behavior of the sample after hydration. Images **c** and **d** show higher

magnifications of the particles, in which is observed an ordered pattern of atoms. However, not all the particles and not all the area of each particle show the same pattern.

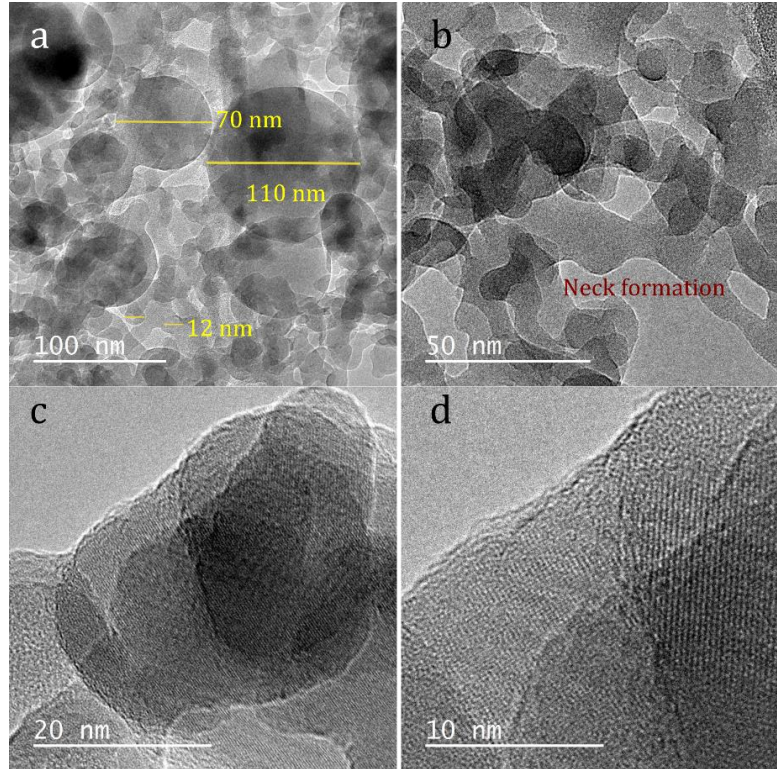


Figure 6-20. TEM images of sample 10M_{2%}-A₂₀₀

In Figure 6-21 is shown the SAED patterns of samples 30E_{2%}-O₂₀₀ (*a, b, c*) and 10M_{2%}-A₂₀₀ (*d, e, f*). Imagine *a* shows the interplanar spacing between the spots in the pattern, corresponding to α^H -CaSiO₄ in which $d=2.07\text{\AA}$ is attributed to plane (1 1 4) and $d=2.87\text{\AA}$ is attributed to plane (1 0 2). Considering the heterogeneity of the sample, images *b* and *c* show that the diffraction spots tend to arrange in circular rings, indicating the poly-nanocrystalline nature of the sample, which is well defined in image *c*. Image *c* shows the interplanar distance of $d=2.68\text{\AA}$ attributed to the plane (0 1 3) of α^H -CaSiO₄, while the interplanar distance of $d=3.81\text{\AA}$ correspond to the plane (0 1 2) of CaCO₃. On the other hand, the pattern show in image *b* shows a crystalline distribution, with a interplanar spacing of 13.98 A. Similarly, the spots in the SAED patterns of 10M_{2%}-A₂₀₀ present circular rings, indicating that the sample is formed by small crystals with random orientations (poly-nanocrystalline). Image *e* shows the interplanar distance of $d=1.63\text{\AA}$ attributed to the plane (3 0 0) and $d=2.78\text{\AA}$ of the plane (1 0 2) of β -CaSiO₄, while the interplanar distance of $d=1.96\text{\AA}$ correspond to the plane (2 2 2) of α^H -CaSiO₄. In addition, Image *f* allows the identification of the interplanar distance of $d=2.09\text{\AA}$ of the plane (2 0 2) of CaCO₃ and the interplanar distances of $d=2.54\text{\AA}$ of the plane (2 1 -2) and $d=2.78\text{\AA}$ of the plane (1 0 2) of β -CaSiO₄.

In Figure 6-22 are shown the TEM images of samples 30E_{2%}-O₂₀₀ (a, b, c) and sample 10M_{2%}-A₂₀₀ (d, e, f) after hydration. The images reveal the formation of C-S-H foil-like, but some differences between the samples are observed. Sample 30E_{2%}-O₂₀₀ shows the formation of fibrous shape in all the area (image a), but higher magnifications show similar particles as observed in the anhydrous sample. Nevertheless, magnifications of this sample suggest a low degree of crystallinity (Image c)

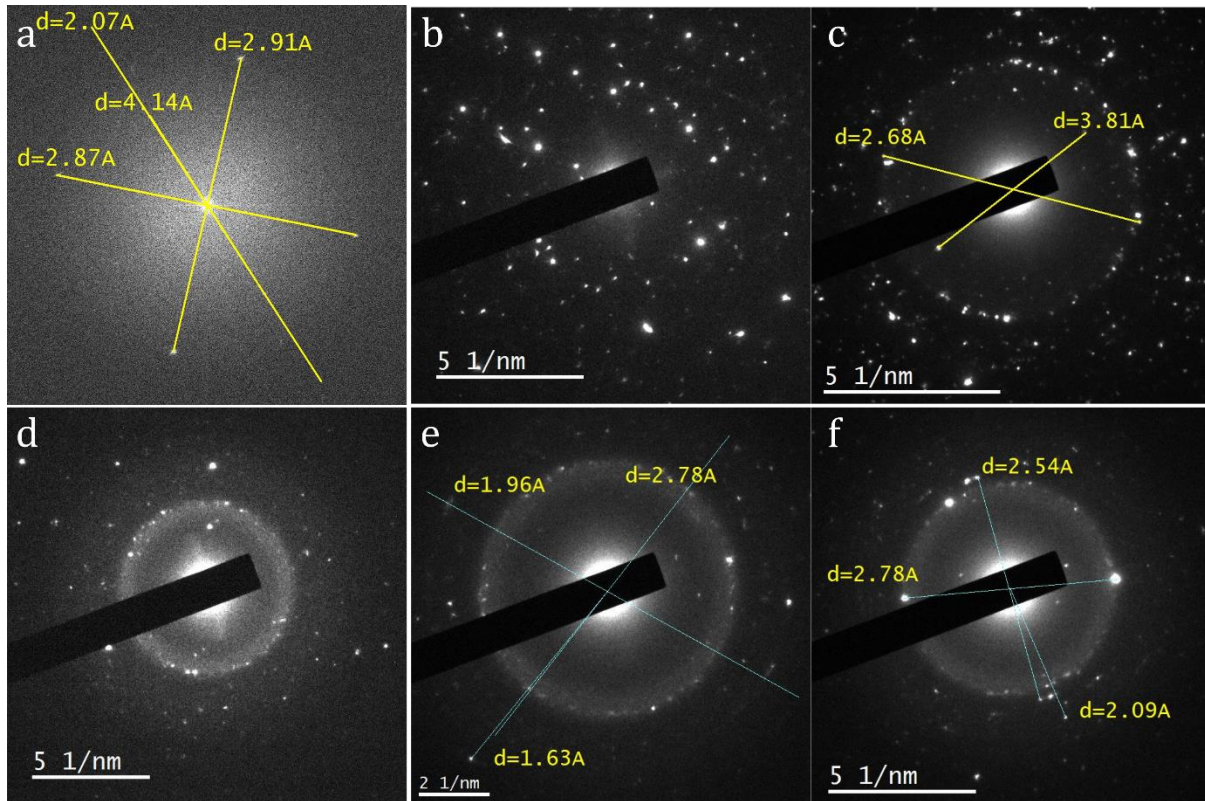


Figure 6-21. SAED patterns of anhydrous samples. (a, b, c) Sample 30E_{2%}-O₂₀₀; (d, e, f) Sample 10M_{2%}-A₂₀₀

On the other hand, these micrographs suggest the formation of the inner and outer products of C-S-H (image e) by showing the formation of granular structures. Magnifications of the inner part of the sample, show that this material has zones with a defined crystallinity (image f), but with different arrangements. This result indicates that the C-S-H formed tends to produce higher amount of inner product than outer product.

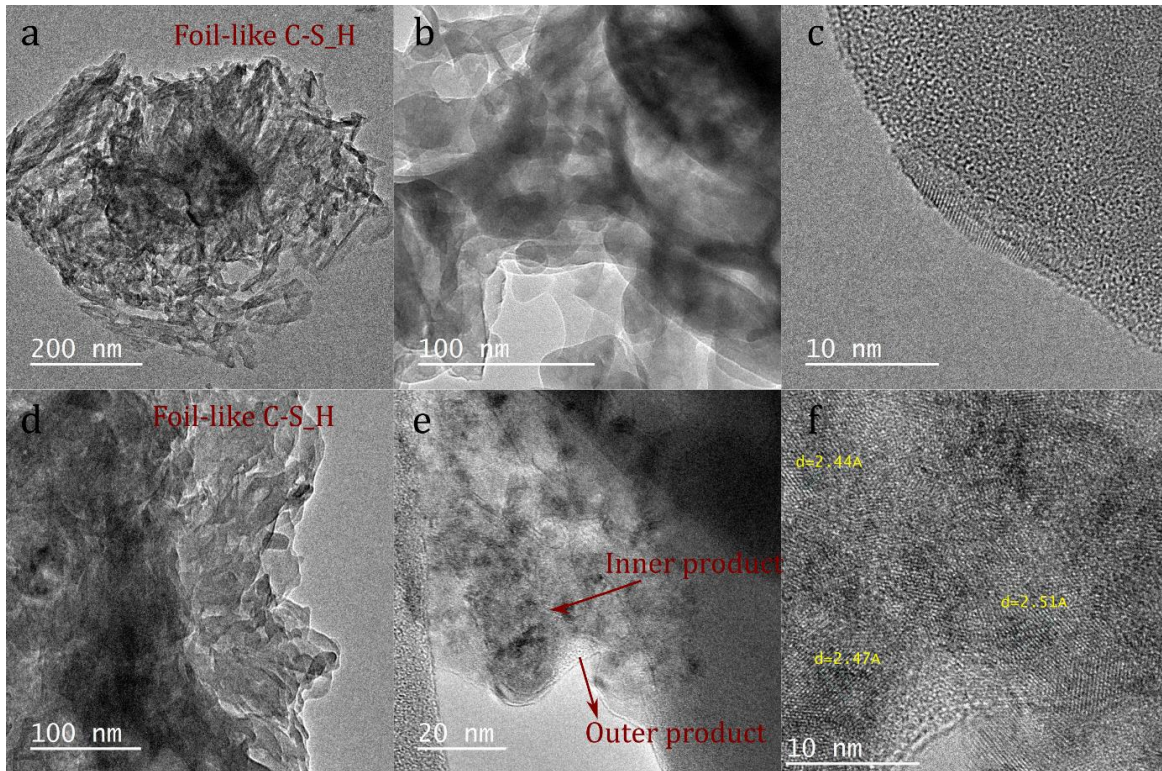


Figure 6-22. TEM images of hydrated samples (2 days). (a, b, c) Sample 30E_{2%}-O₂₀₀; (d, e, f) Sample 10M_{2%}-A₂₀₀

In Figure 6-23 are shown the SAED patterns of hydrated samples after 2 days of reaction, where images (a, b, c) correspond to sample 30E_{2%}-O₂₀₀ and images (d, e, f) to sample 10M_{2%}-A₂₀₀. In these images are observed diffuse rings indicating the formation of amorphous phases after the hydration, as it was expected for C-S-H. On the other hand, some bright spots attributed to non-hydrated dicalcium silicates phases and secondary phases are observed, which are supported by the interplanar distances identified. The interplanar spacing of $d=2.87\text{\AA}$ is attributed to plane (1 0 2) of $\alpha^{\text{H}}\text{-CaSiO}_4$, while the interplanar distances of $d=2.54\text{\AA}$ corresponds to the plane (2 1 -2) and $d=1.54\text{\AA}$ of the plane (1 3 3) of $\beta\text{-CaSiO}_4$. It was also observed the interplanar distance of $d=3.01\text{\AA}$ corresponding to the plane (1 0 4) of CaCO_3 , which does not have hydraulic properties and remain in the samples.

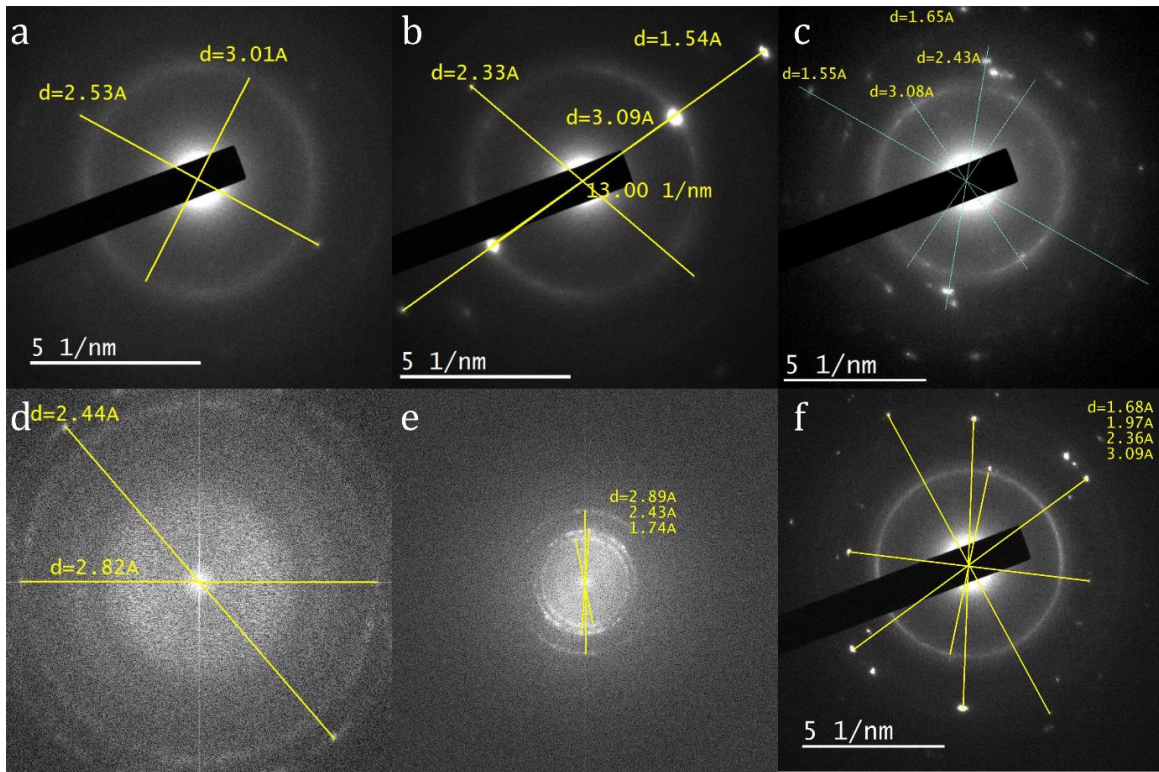


Figure 6-23. SAED patterns of hydrated samples (2 days). (a, b, c) Sample 30E_{2%}-O₂₀₀; (e, f, g) Sample 10M_{2%}-A₂₀₀

6.4. Discussion

The synthesis process shows the successful formation of calcium silicate phases by flame spray pyrolysis, with the presence of calcium compounds as secondary phases. The results suggest that the process has a good reproducibility of the experiments, with a remarkable importance of the process parameters over the final properties of the samples, considering that changes in these conditions affect the phases composition and the reactivity degree of the samples. Therefore, the samples obtained can be divide in the two groups, samples with hydraulic behavior and late-hydraulic behavior.

The samples with hydraulic behavior have in common the high quantity of amorphous material and the high specific surface area. In general, the number of polymorphs of belite in the samples, did not suggest a strong influence on the reactivity degree of the samples, at early ages. Nevertheless, it was observed an atypical sample with good hydraulic behavior, which show low amount of amorphous, high percentages of crystalline belite and median specific surface area in comparison to the rest of the samples.

On the other hand, the samples with higher number of secondary phases were the samples with non-hydraulic behaviors, as it could be expected. The secondary phases were constituted by calcium

oxide, calcium carbonate and calcium hydroxide. As it was explained above, during the flame reaction, the starting solution is decomposed and evaporated. During these stages, the components of the new gas phase react to form the nucleus and primary particles. However, some factor as the nature of the starting materials and the solvents used in the reaction can affect the proper formation of this gas phase. The mixture of solvents used to form the starting solution contained water and ethanol, while the precursors were tetraethyl orthosilicate and calcium propionate. These precursors have a preference of the solvents used, so that, the tetraethyl orthosilicate is well dissolved in ethanol, while the calcium propionate, as organic salt, prefers the water as solvent. In addition, TEA was added to the solution to improve its homogeneity and stability. Despite this, the phases composition showed that these precursors combination needs improvements to avoid the production of non-desire compounds. The evaporation of water demands higher amount of energy than the ethanol, therefore, even when the solution looks homogeneous, could be possible that a higher concentration of silicon ions evaporates easily since the affinity with ethanol, leaving a higher concentration of calcium ions in the water portion. This concentration of calcium ions in the water, will take longer times to create a proper gas phase to react with the silicon ions and form the calcium silicates, thus, the tetraethyl orthosilicate will partially produce amorphous silica and calcium silicates, while the calcium propionate will partially form calcium silicates and calcium oxide. In this sense, the nanoparticles of calcium oxide formed during the synthesis are exposed to an environment rich in vapor of water and carbon dioxide from the combustion. During this exposition, the calcium oxide adsorbs moisture to form calcium hydroxide, which could suffer carbonation reactions to produce calcium carbonate by fixation of CO_2 .

In order to observe whether the concentration of calcium carbonate in the samples was related with the order of synthesis, and for instance with a possible exposition to carbon dioxide, the Figure 6-24 shows the mineralogical results of the secondary phases, in the chronological order of synthesis. It is important to say that after the synthesis process, the samples were exposed ~ 1 hour to the environment, while the equipment was at room temperature. After that, the samples were stored and saved in a desiccator.

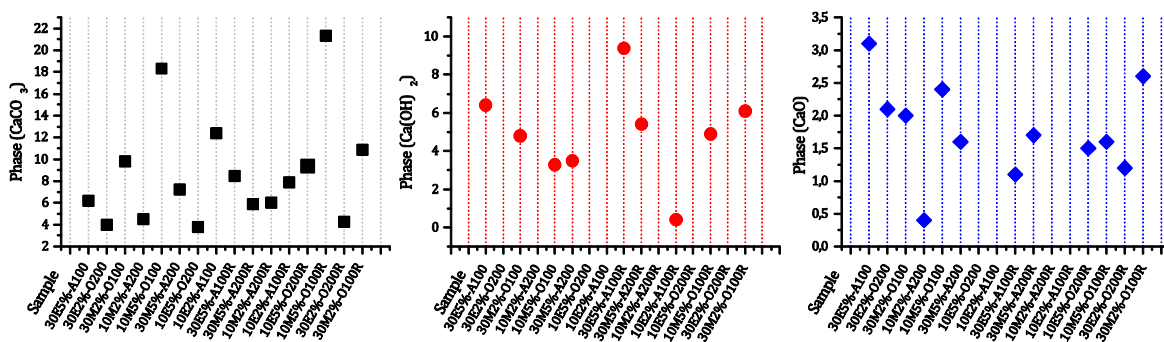


Figure 6-24. Mineralogical results of the secondary phases in the chronological order of synthesis

These figures show a random amount of the secondary phases in the samples, indicating that the calcium carbonate does not increase after the synthesis, once it is stored in a controlled environment, therefore, the hydration and carbonation can be related to the initial specific surface area, mineralogy

of the samples and their exposition to the gases during the reaction time and before the collection. In addition, the reaction process over the calcium oxide must increase the SSA of the samples [176], however any correlation between the SSA and the calcium carbonate amounts were found, which is explained by the initial differences of the samples.

The results show that the samples with lower amount of calcium carbonate were made with oxygen as dispersion air at 200 kPa (term O₂₀₀). As explained above, the high dispersion pressure promotes the disintegration of the jet of solution to form smaller droplets, but also, this pressure gives higher kinetic energy to the particles, decreasing their time in high temperature zones, where sintering and crystallization processes take place. In addition, the use of oxygen as dispersion gas gives high energy to the flame, which favors the evaporation of the droplets in the flame. Therefore, the use of water in the starting solution lost importance when the reaction zone provides high energy levels to form a homogeneous gas phase which will react, resulting in the formation of nanoparticles with less amount of calcium oxide. Consequently, even when all the synthesis starts from the same starting solution, the variations in the process parameters, affect conditions as the time in high temperature zones and the evaporation velocity by changing the size of the drops, giving to each sample particular characteristics.

The samples with hydraulic behavior show that the experimental conditions have influence on the hydration characteristics. The experimental conditions have almost no influence on the first peak of hydration of the samples. Nevertheless, the second peak of hydration shows important differences. The hydraulic behavior of these samples is very interesting, considering that in cement the belite phase has slow degree of reactivity having only significant effect after 10 days [177], while the calorimetry curves of these samples reveals the formation of the second peak of hydration after 30 minutes of contact with water, indicating that enough calcium and silicon species in the solution are available to start the nucleation and growth of C-S-H species, without the observation of the induction period. The belite compounds produced by FSP shown an improvement in the hydraulicity of the phase, since the complete hydration reaction is complete in less than 24 hours.

The samples with higher cumulative heat of hydration were 10M_{2%}-A₂₀₀ and its replication which correspond to the samples with higher SSA and higher amount of amorphous material. These samples do not have the dormant period after the dissolution of the ions in the first stage, resulting in an immediate formation of C-S-H, which can be explained by the high degree of surface in contact with water to create C-S-H nucleus, which leads to overcome the critical amount of C-S-H before the acceleration of the phase formation [177].

Regarding to the process, a deeper analysis of the effects of its conditions will be addressed in the next chapter using an analysis of variance of the data, nevertheless, general observations of the results in terms of the reactivity gives previous information about their importance (Table 6-9). All the samples show that when the five variables evaluated are varied, at least 3 of 5 variables must favor the formation of low particle sizes to obtain hydraulic materials. In this sense, the literature suggests that low ceramic loading values, high pressures of dispersion, low feed flow rates, solvent with high enthalpy of evaporation and gases of dispersion with high enthalpy, promotes the formation of nanoparticles.

Therefore, samples with reactive behavior were obtained when 4 of 5 and 3 of 5 factors favor the formation of nanoparticles, while in process conditions were less than 3 variables favored the formation of small particles (combinations of 2/5 or 1/5) no reactive behavior was observed.

In addition, when 4 of 5 variables favor the formation of small particles, but the variable favoring high particle sizes is the ceramic loading or the feed flow rate, the influence of the feed flow rate is stronger than the ceramic loading. Table 6-9 shows how the variables of the design affect the particle size and the number of variables, which favor and disfavor the formation of reactive particles (the green color indicates the degree of reactivity of the samples, which is less intense when the reactivity is lower, while the reddish colors indicates the negative effects of the values adopted for these variables, where more intensive red indicates a stronger bad effect).

Table 6-9. General evaluation of the favorable process conditions to obtain small particles

Hydraulic behavior	Sample	Favorable conditions to obtain small particles				Number of favorable variables	Number of unfavorable variables	Ratio under favorable variables	
		Solvent	Ceramic loading	Pressure of dispersion gas	Feed flow rate				Dispersion gas
Reactive samples	10M _{2%} -A ₂₀₀	↓	↑	↑	↑	↓	3	2	3/5
	10M _{2%} -A ₂₀₀ R	↓	↑	↑	↑	↓	3	2	3/5
	10E _{5%} -O ₂₀₀	↑	↓	↑	↑	↑	4	1	4/5
	10E _{5%} -O ₂₀₀ R	↑	↓	↑	↑	↑	4	1	4/5
	10E _{2%} -A ₁₀₀	↑	↑	↓	↑	↓	3	2	3/5
	10E _{2%} -A ₁₀₀ R	↑	↑	↓	↑	↓	3	2	3/5
	30E _{2%} -O ₂₀₀	↑	↑	↑	↓	↑	4	1	4/5
	30E _{2%} -O ₂₀₀ R	↑	↑	↑	↓	↑	4	1	4/5
Unreactive samples	30M _{2%} -O ₁₀₀	↓	↑	↓	↓	↑	2	3	2/5
	30M _{2%} -O ₁₀₀ R	↓	↑	↓	↓	↑	2	3	2/5
	30M _{5%} -A ₂₀₀	↓	↓	↑	↓	↓	1	4	1/5
	30M _{5%} -A ₂₀₀ R	↓	↓	↑	↓	↓	1	4	1/5
	10M _{5%} -O ₁₀₀	↓	↓	↓	↑	↑	2	3	2/5
	10M _{5%} -O ₁₀₀ R	↓	↓	↓	↑	↑	2	3	2/5
	30E _{5%} -A ₁₀₀	↑	↓	↓	↓	↓	1	4	1/5
	30E _{5%} -A ₁₀₀ R	↑	↓	↓	↓	↓	1	4	1/5

↑ Favor small particle sizes

↓ Disfavor small particle sizes

It is possible to conclude that the best combination of process conditions to obtain hydraulic materials is obtained when the ceramic loading, pressure of dispersion gas and feed flow rate are favoring the formation of small particles. The samples obtained under these conditions, 10M_{2%}-A₂₀₀ and its replication 10M_{2%}-A₂₀₀R, presented the higher reactivity. Regarding to the other conditions, when at least half of the variables plus one favor the formation of small particles, reactive samples are obtaining.

10E_{5%}-O₂₀₀ and 10E_{5%}-O₂₀₀R are the following samples with higher degree of reactivity. These samples were produced under favorable conditions to form nanoparticles, (4/5), where two of these 3 main variables (ceramic loading, pressure of dispersion gas and feed flow rate) were in favorable values. The drop in the reactivity with respect to the sample 10M_{2%}-A₂₀₀, can be explained by the disfavor values adopted for the ceramic loading. Otherwise, the lower reactivity of samples 10E_{2%}-A₁₀₀ and its replication (with 3/5 favorable variables), could be attributed to stronger effects of the pressure of dispersion than the effect of the ceramic loading.

CHAPTER 7. EFFECTS OF THE OPERATION VARIABLES ON THE CALCIUM SILICATE PROPERTIES

The effects of the operation variables of FSP process during the production of calcium silicates were evaluated using an analysis of variance (ANOVA) by comparing the response variable means at the different factor levels. To this purpose, Pareto charts of standardized effects, main effects plots and interaction plots of mineralogical, physical and chemical responses were analyzed. The residual plots of the fractional factorial, for all the responses to determine that the models are satisfied and validate the results are present in the annexes.

7.1. Effects on mineralogical, physical and chemical responses

To analyze the effects of the process on the mineralogy of the samples, three responses were chosen, corresponding to the polymorphs of belite (sum of α -Ca₂SiO₄ and β -Ca₂SiO₄), amorphous material and secondary phases (sum of calcium oxide, calcium carbonate and calcium hydroxide).

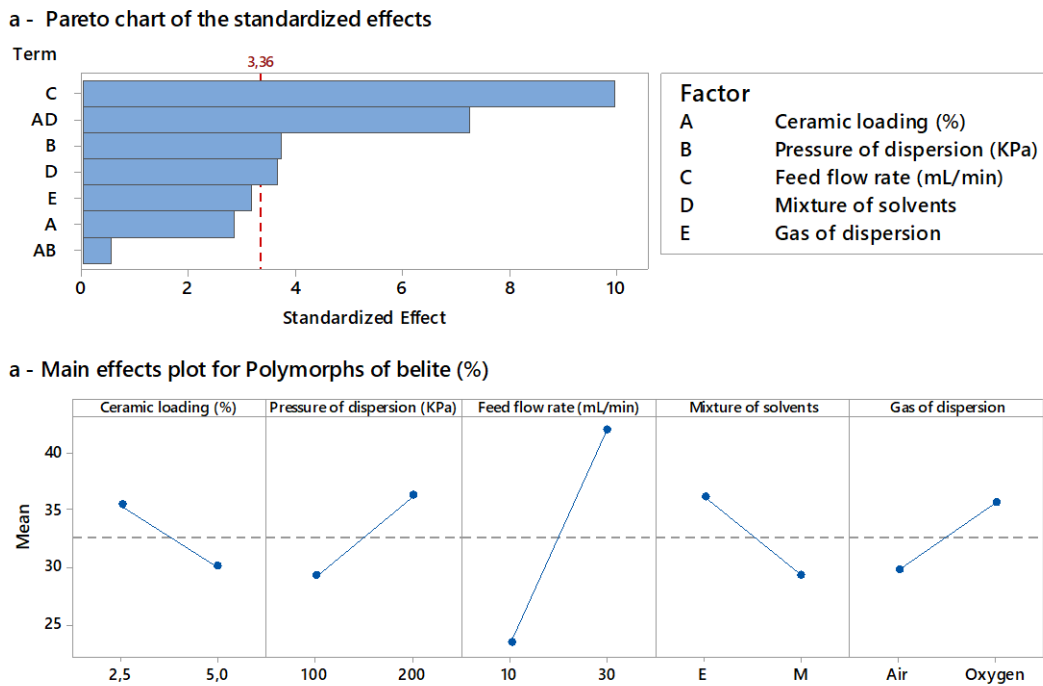


Figure 7-1. Effects plot of Polymorphs of belite

The upper part of the Figure 7-1 shows the Pareto chart of the Polymorphs of belite. This plot indicates which terms have a higher contribution in the variability of the responses, considering a

significance level of 0.01. The bars of C (feed flow rate), AD (ceramic loading/mixture of solvents), B (pressure of dispersion) and D (mixture of solvents) cross the reference line indicating that these factors are statistically significant, however to determine whether individual effects increase or decrease the response is necessary to observe the plot in the lower part, corresponding to the main effects. The factors pressure of dispersion, feed flow rate and gas of dispersion present positive slopes indicating that higher values of the variables favor the formation of higher amounts of polymorphs of belite. Otherwise, ceramic loading and the mixture of solvents show negative slopes, indicating that lower values favor a better response. Nevertheless, the steeper slope for main effects is observed for the feed flow rate, which is the most important variable to this response according to Pareto chart.

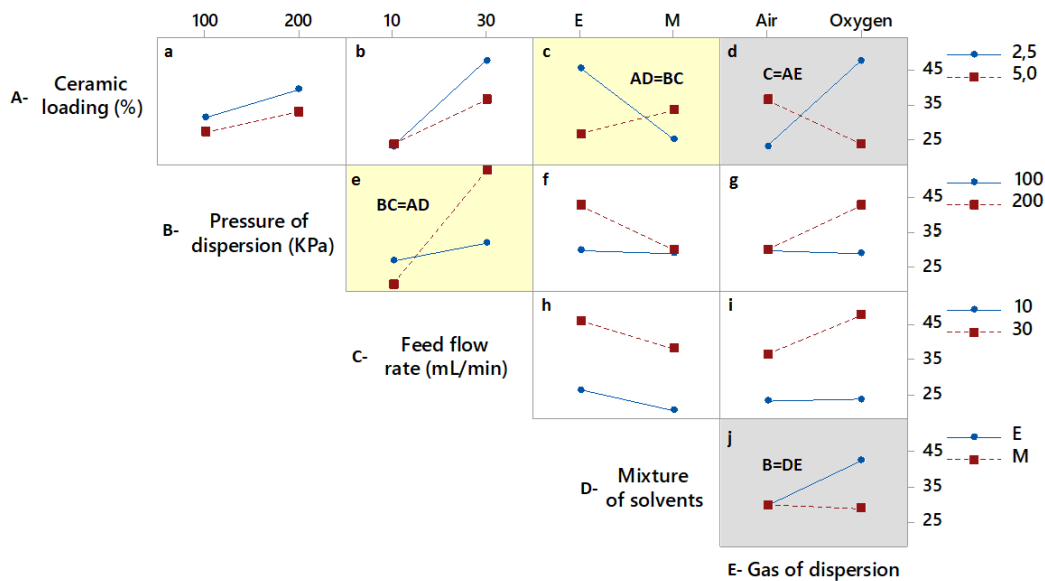


Figure 7-2. Interaction plot for Polymorphs of belite

Figure 7-2 shows the interaction plot in which is possible to analyze the combined effect of the factors. The plots *a*, *b*, *f*, *g*, *h* and *i* show a parallel-like behavior, indicating no significant interactions between the factors. Otherwise, the plots *c*, *d*, *e* and *j* (yellow plots) present interaction between the factors. The main interaction according to Pareto chart is observed in plot *c*, where the combination of the solvents and the concentration of ions in the starting solution have an effect in the quantity of belite. In this sense, the use of low ceramic loadings and solvents with high enthalpy increase the probability to produce higher percentages of belite. As a result of the aliases of the experimental design, the interactions presented in graphs *d*, *e*, and *j* correspond to confounding between the main effects and the interactions, which is implicit in fractional factorial design. However, in this case the main effects are only cofounded with non-significant interactions, which do not affect the results of the design.

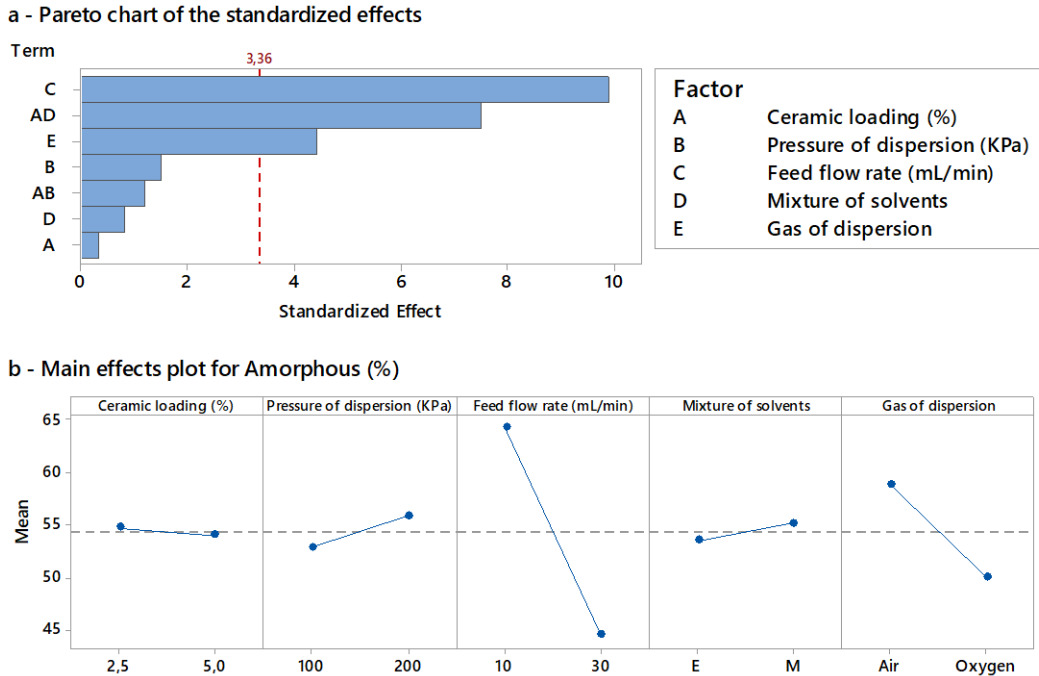


Figure 7-3. Effects plot of Amorphous

Figure 7-3 shows the Pareto chart and main effect plot for the amorphous fraction in the samples. The Pareto chart indicates that the most significant variable is the feed flow rate (C) of the starting solution, follow by the interaction AD (ceramic loading/mixture of solvents), presenting the same behavior than the polymorphs of belite. However, in this case the gas of dispersion (E) has a bigger effect than the pressure of dispersion of the gas. The main effects plot in the lower part of the graph shows that the ceramic loading, the pressure of dispersion and the mixture of solvents do not have a significant effect, considering that the line is almost parallel to the x-axis. On the other hand, the feed flow rate presents a remarkable negative slope, indicating that lower values of feed allow the formation of higher amount of amorphous material, which could be related to an easier evaporation of the drops to favor a gas-to-particle mechanism of conversion.

On the other hand, the interaction plots (Figure 7-4) shows the main interaction described in the Pareto chart, AD (ceramic loading – Mixture of solvents), which is cofounded with the interaction BC (Pressure of dispersion – feed flow rate). This interaction, highlight in yellow, suggests that the concentration of ions in the starting solution is affected by the solvent, which together conform the chemical system. The use of low concentrations of precursors favor the formation of higher amounts of amorphous materials when low enthalpy solvents are used, in contrast, the use of high ceramic loading requires the use of high enthalpy solvents. These interactions could be related to the energy requirement of the solution to form the gas phase. Otherwise, the aliasing BC is an interesting combination due to high pressure of dispersion with low feed flow rate, results in the formation of smaller droplets during the spraying process, implying a faster evaporation of the starting solution to favor the gas-to-particle mechanism.

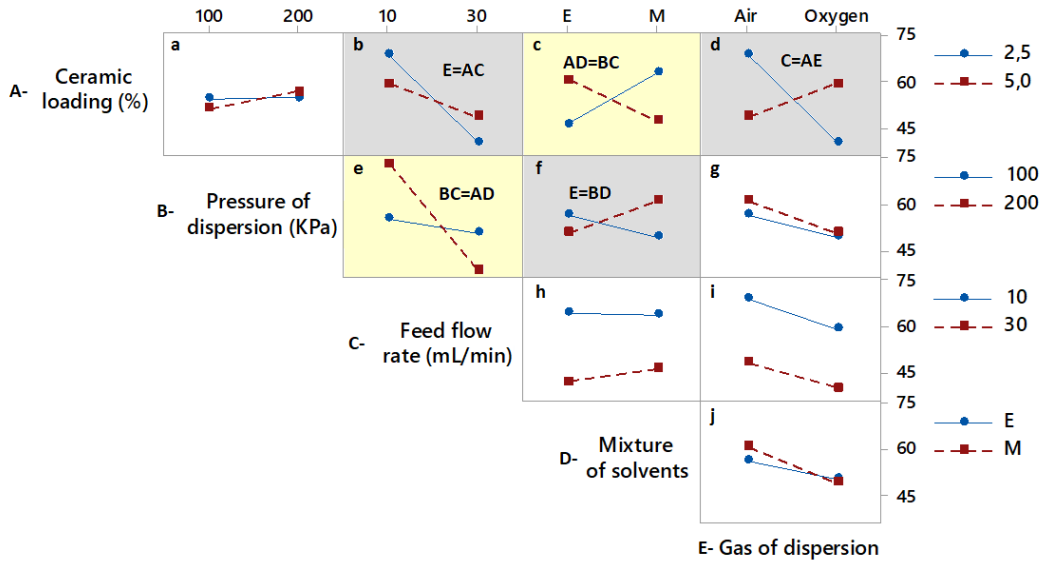


Figure 7-4. Interaction plot for Amorphous

The interactions AC (ceramic loading – feed flow rate) and BD (pressure of dispersion gas – gas of dispersion) observed in plot *b* and *f*, respectively, correspond to aliasing to the main effect gas of dispersion (E), while the interaction observed in plot *d*, AE (ceramic loading – gas of dispersion) correspond to an alias of the main effect feed flow rate (C). The only significant interaction observed in this response was AD (ceramic loading – Mixture of solvents), whereby the alias structure does not have an important impact in the results.

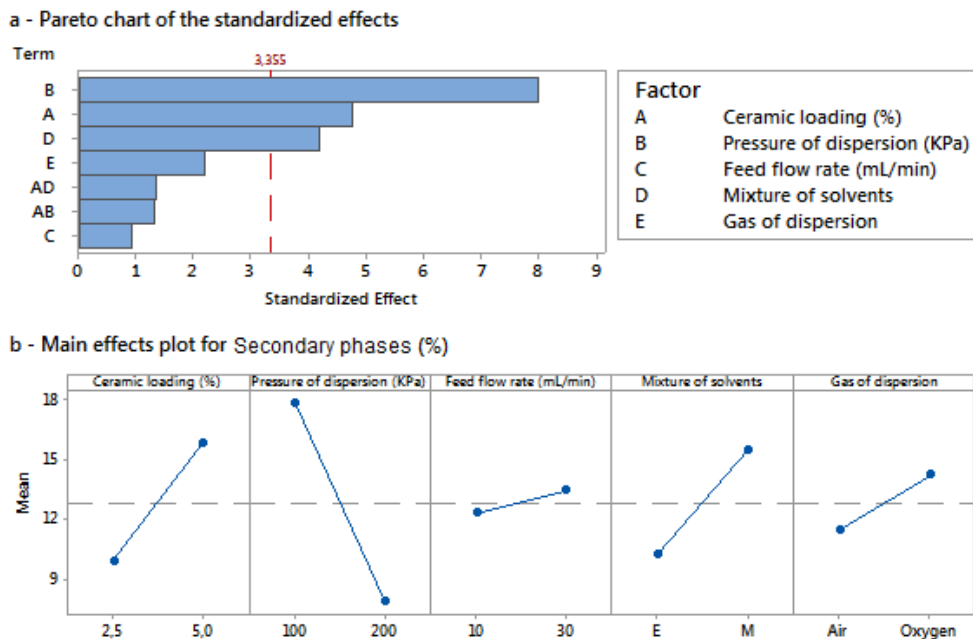


Figure 7-5. Effects plot of Secondary phases

The production of secondary phases as response was evaluated in Figure 7-5. The Pareto chart indicates that the pressure of dispersion gas (B) strongly affect the formation of these secondary phases, directly related to the formation of calcium oxide. Then, the ceramic loading (A) and the mixture of solvents (C) are the factors that most affect this response, in order of importance, while not combined effects are observed. The main effects, observed in the bottom part of the plot indicates that for minimize the production of secondary phases, higher pressure of dispersion gas must be used, favoring the formation of smaller drops and lower residence time in zones of high temperature. On the other hand, the ceramic loading most have low values, favoring a quickly decomposition of the species to form primary particles, while the mixture of solvents which allows a lower formation of these secondary phases is the mixture ethanol – water, which provides a higher energy of volatility to the system. Besides, the enthalpy of volatility of both mixtures is very close, whereby, it is possible to suppose that the precursors have a better interaction when it is use the mixture ethanol – water.

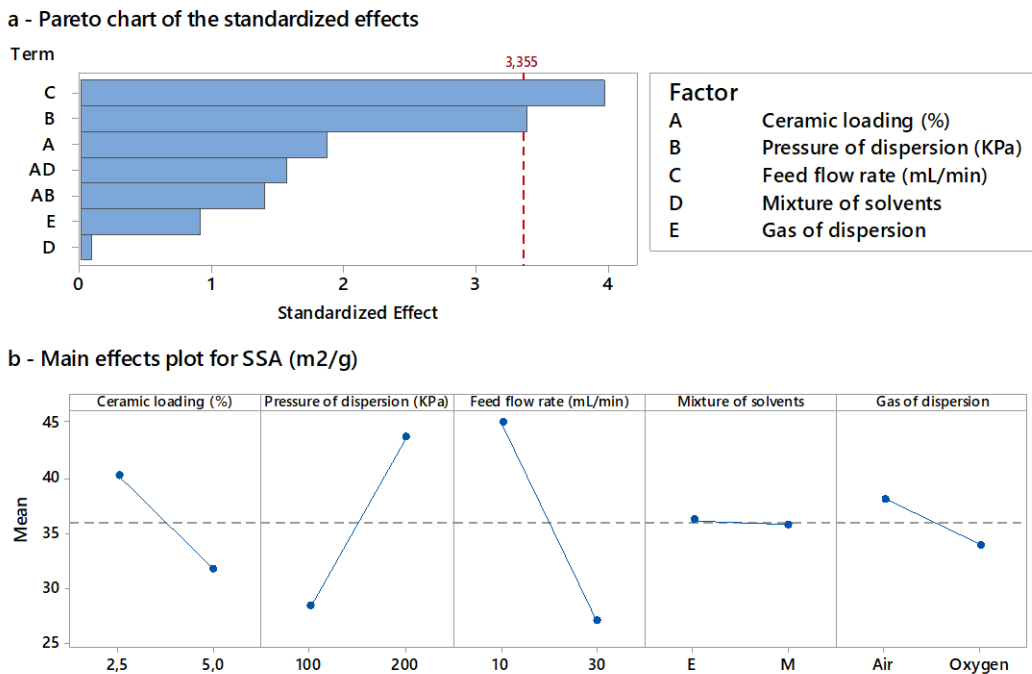


Figure 7-6. Effects plot of Specific surface area

The specific surface area of the samples was choosing as physical response. The average particle size reported in the Chapter 6 was not evaluated as response, because it was calculated from the SSA measurements. The Pareto chart observed in the upper part of Figure 7-6, shows that the feed flow rate (C) is the factor with higher impact in the specific surface area of the samples, having a significant level of 0.01. Additionally, the pressure of dispersion gas (B) shows an effect in this response, while significant interactions between the variables were not observed. The main effects plot in the lower part of the plot, indicates that low feed flow rates and high pressure of dispersion gas, favor the formation of smaller particles. As explained above, this phenomenon can be relating to the formation

of smaller droplets during the aerosol formation, allowing a better evaporation processes during the first stage of the reaction.

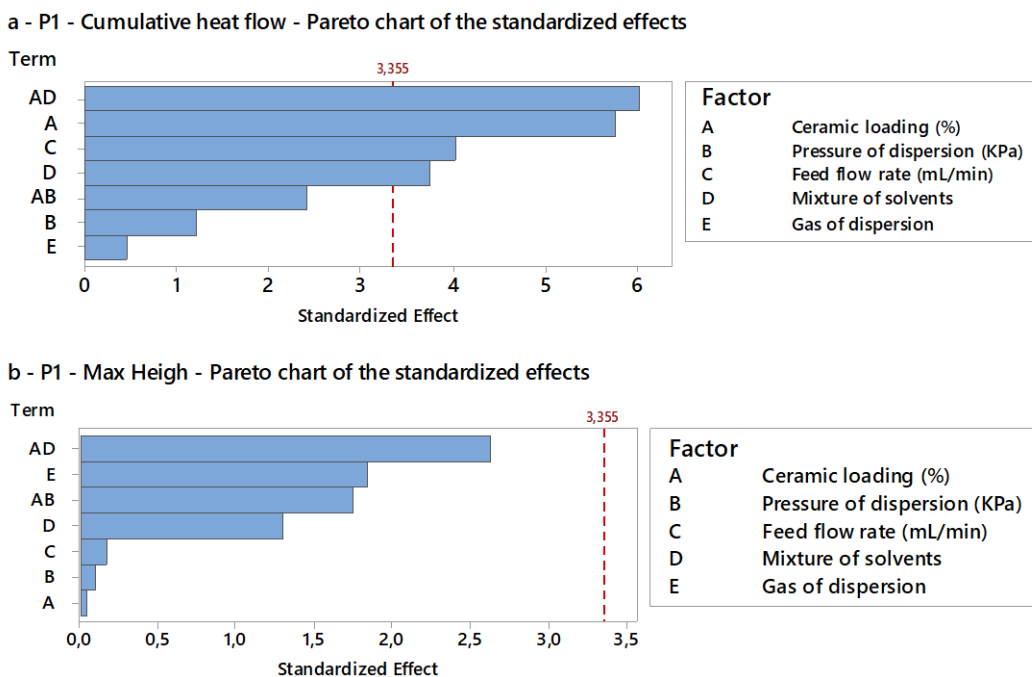


Figure 7-7. Pareto charts of the first peak responses

For the statistical analysis of the reactivity, four responses were chosen. These variables correspond to the maximum height and total area of the first and second peaks obtained during the calorimetric measurements. The residual plots of all the responses, the Pareto charts of the area and maximum height of the first peak are shown in Figure 7-7. These plots indicate which terms have a higher contribution in the variability of the responses, considering a significance level of 0.01. The Figure 7-7 (a) shows the standardized effects on the Area of the first peak. In this plot the effect for the ceramic loading by solvent interaction (AD) is statistically significant followed by the main effects of ceramic loading (A), feed flow rate (C) and mixture of solvents (D). On the other hand, the Pareto chart for the maximum height of the first peak (Figure 7-7 (b)) indicates that any factor or their interactions have a significant effect in this response. Similar than in Figure 7-7 (a), the interaction between ceramic loading and dispersion pressure (AB=CD) present the smallest effect in the maxima height of both peaks. These results indicate that the first peak is mainly affected by the features of the starting solution, while interactions between this chemical system and aerosol formation are negligible (interactions AB and CD).

In Figure 7-8 are shown the main effects plots of the first peak. Figure 7-8 (a) shows that the highest area values are associated with high values of ceramic loading, low feed flow rate and the use of the methanol-ethanol-water solvents mixture. Regarding to the dispersion pressure and gas of dispersion, not significant changes in the total area of the peak are observed. Respecting to the Figure 7-8 (b) to the maximum height of the first peak, the use of air as dispersion gas tends to increase it,

however, the Pareto chart of this response indicates that no main effects are significant for a confidence level of 0.01.

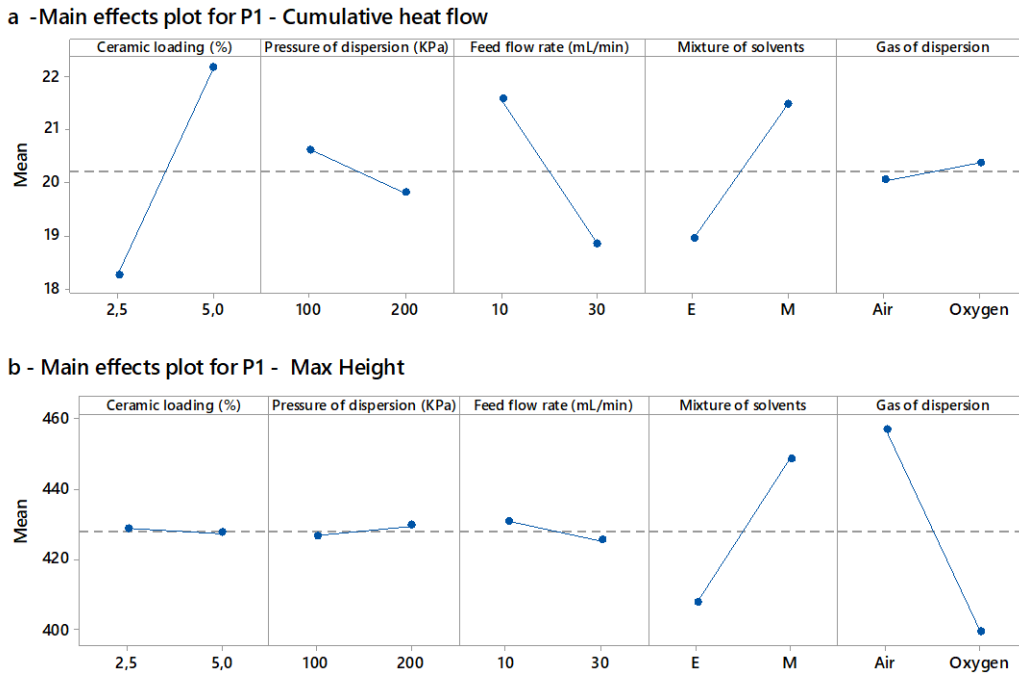


Figure 7-8. Main effects plot of the first peak responses

Figure 7-9 shows the interaction plot for the area of the first peak. As it was observed in Pareto chart, the interaction Ceramic loading by mixture of solvents (AD) has the main effect on this response.

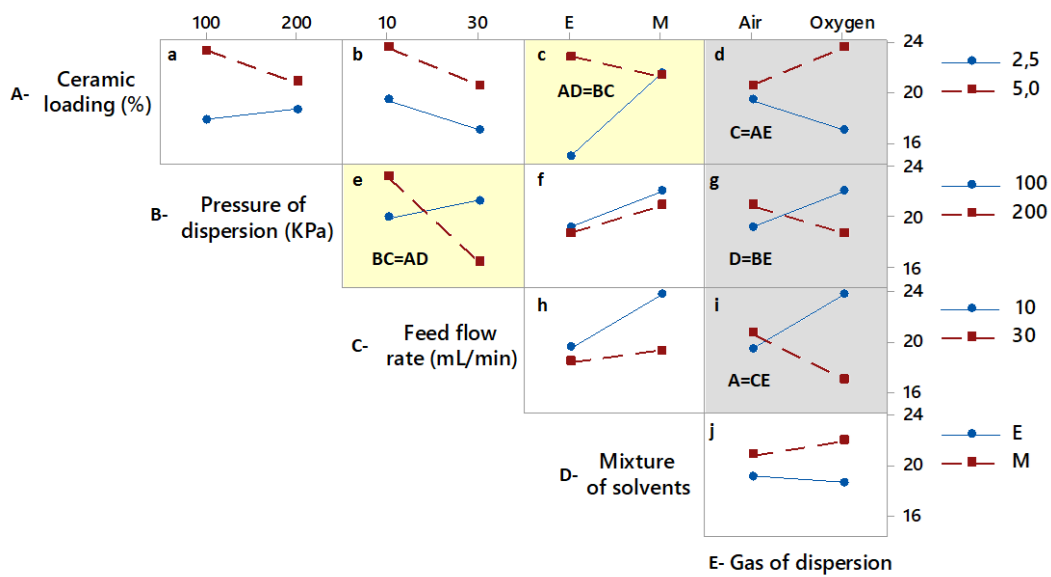


Figure 7-9. Interaction plot for First peak - cumulative heat flow

The plot *c* of this graph shows this interaction, indicating that the combination of high ceramics loading and ethanol-water as mixture of solvents, favor a higher release of energy during the hydration of the samples, while low ceramic loadings with the same mixture of solvents results in low energy release. On the other hand, the use of methanol-ethanol-water as mixture of solvents, makes that the ceramic loading has not effect on the system. As has been observed in several graphs, this combined effect is cofounded with the interaction BC corresponding to the pressure of dispersion gas and the feed flow rate, which shows a higher release of energy when high pressures and low flow rates are used. This result agrees with the production of high percentages of amorphous materials, which has shown an important effect of the final features of the samples.

The main effect plots for the second peak responses are shown in Figure 7-10. The Pareto charts indicate that the feed flow rate (C) used during the synthesis process has a remarkable effect on the area and maximum height of the second peak, this factor is followed by the pressure of dispersion gas and ceramic loading, as single factors, which also shown significant influence in both responses. On the other hand, the gas of dispersion shows a low impact in the second peak responses, but it only exceeds the level of significance for the area of the peak. Significant interactions between the factor were not observed for these responses.

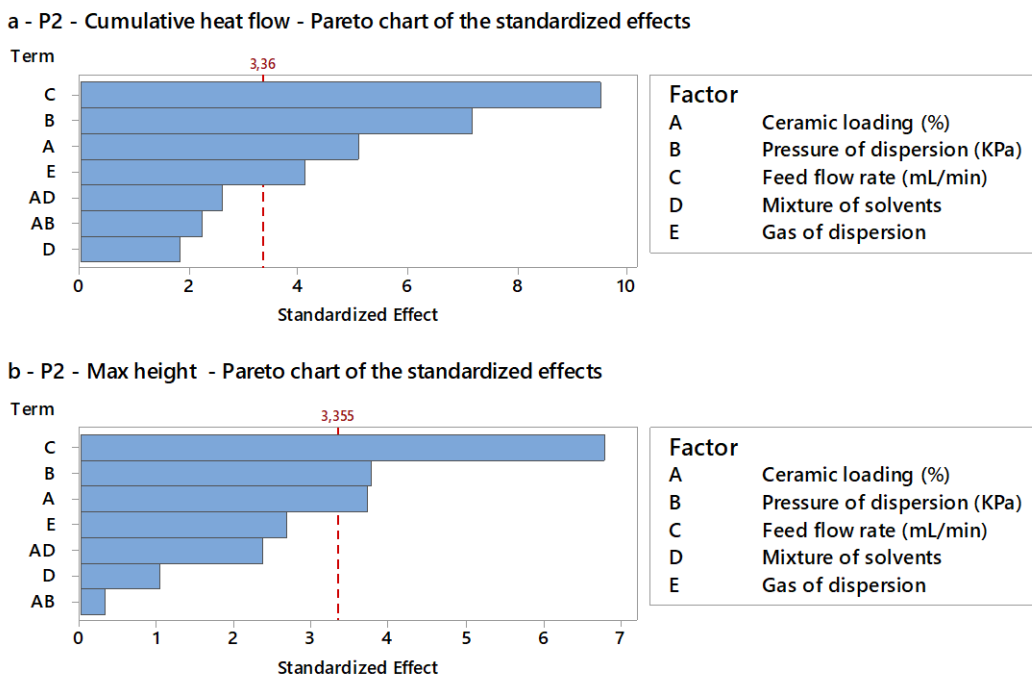


Figure 7-10. Pareto charts of the second peak responses

The main affects plot for both responses, area and maximum height of the second peak, shows the same behavior (Figure 7-11). The steeper slope is observed for the feed flow rate, showing the main importance of these synthesis conditions. The slope for the ceramic loading, the feed flow rate and

the gas of dispersion have negative values, indicating that the low level of these factor favor a higher release of energy during the hydration reaction. On the other hand, the pressure of dispersion gas has a positive slope, which indicates that high values promote the release of energy. These main effects present the same behavior than the specific surface area main effects, which was expected considering that the reactivity is directly linked to the surface of contact of the samples with the water.

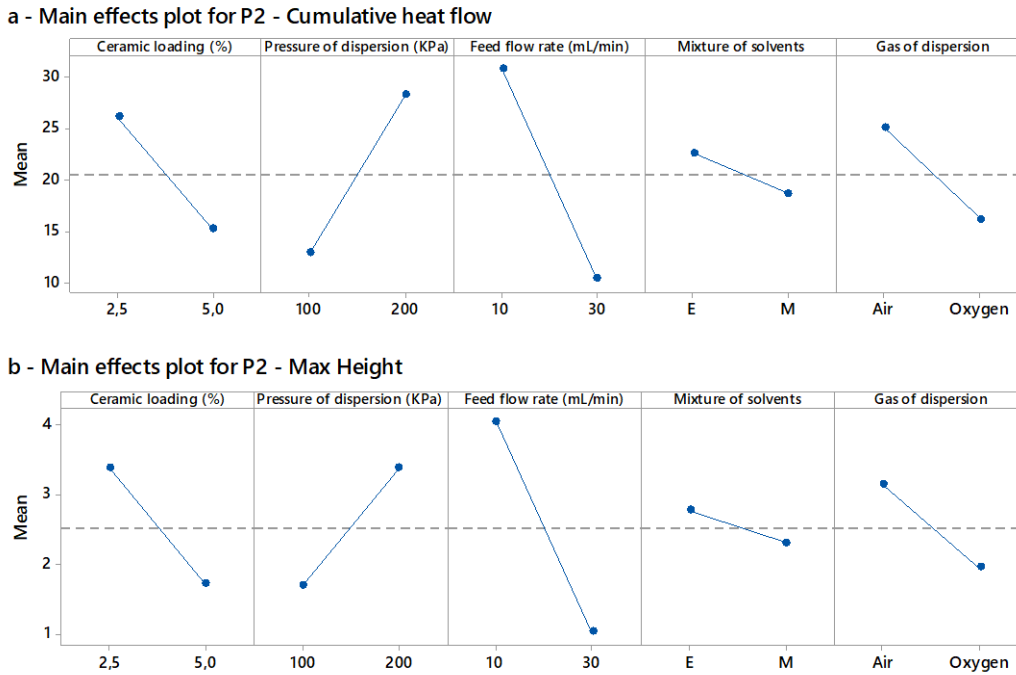


Figure 7-11. Main effects plot of the Second peak responses

7.2. Optimization of the responses

The optimal settings of the experimental design is shown in Figure 7-12. This graph shows how the variables were affected by the predicted responses, being composed by six columns and seven rows. The first column gives the desirability of the responses, while the columns 2 to 6 shows the response values at each level of each factor. Otherwise, the first row shows the desirability of the model and the follow rows, the optimal values for each factor (red color values).

The composite desirability of the design was of 0.7103 which indicates a good solution of the process, considering that the maximum value of these parameter is 1. This desirability is obtain when the factors take the red values show in the first column of the graph, corresponding to ceramic loading=2.5 %, pressure of dispersion gas=200 kPa, feed flow rate=10 mL/min, Mixture of solvents= ethanol/water, and gas of dispersion=air. The responses chosen for the optimization were the

percent of the phases (polymorphs of belite, amorphous and secondary phases), the specific surface area and area of the second peak during the hydration reaction. All the responses were maximize, except the secondary phases which were minimize. The area of the first peak was not consider due the factor in the design were not statistically significant in this response.

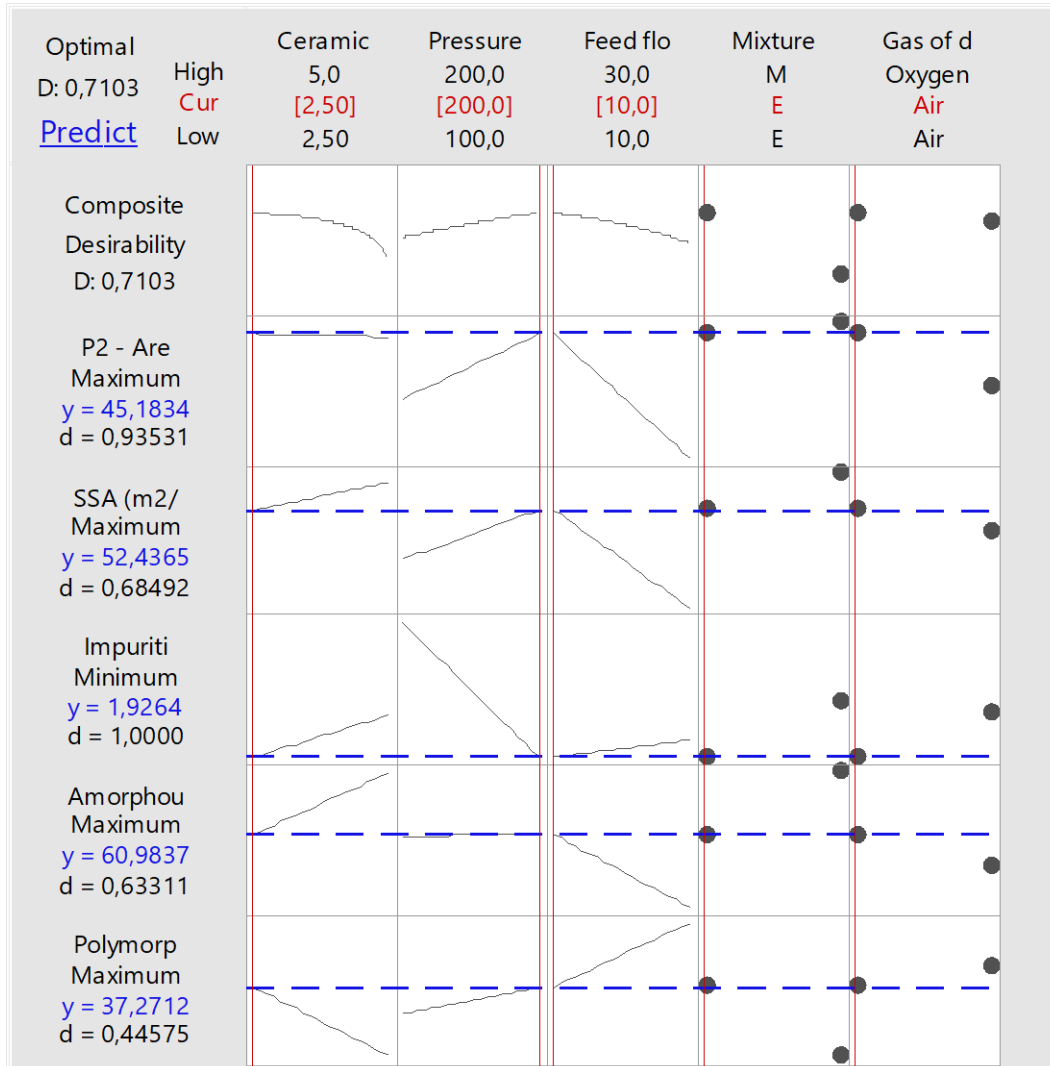


Figure 7-12. Optimization plot

The first row in right part shows the predicted values for all the responses. The most important response in terms of cementitious applications is the reactivity of the samples, therefore the main goal was to optimize this value. The predicted value for the area of the second peak was 45.1834, with an individual desirability of 0.9353. As it was observed in the Pareto charts of all the responses, the most important variable in the process is the feed flow rate, which is directly related to the droplet size in the aerosol, and therefore, to the efficiency of the vaporization process at the beginning of the reaction. The row 4 shows that decreasing the feed flow rate, all the responses are maximize except by the polymorphs of belite and the secondary phases. Regarding to the secondary phases it

is a favorable result, due to the objective of the design is minimize the amount of unreactive/undesirable compounds. Otherwise, regarding to the polymorphs of belite, the results suggest that this is not the most important crystalline phase to obtain higher reactivities, since the amount of amorphous materials seems to be the most influential variable. This result suggest that the use of lower feed flow rates could favor the formation of most reactive materials, but it will require longer reaction times, implying a higher consumption of energy.

The pressure of dispersion gas was another parameter with strong influence in the responses of the process. As it is show in the row 3 of the graph, high values of pressure favor the maximization of all the responses, while the production of secondary phases are minimized. During the process high values of this variable promotes a higher disintegration of the jet of liquid, allowing the formation of smaller droplets. Additionally, high pressures of dispersion give higher kinetic energy to the particles, decreasing the residence times in high temperature zones, preventing the crystallization of the powders and the growth process by sintering.

Regarding to the categorical response, gas of dispersion (row 6), it is interesting to see that the best results are obtained by using air, which provides lower enthalpy to the reaction, by the dissolution of the flame. This result could be linked to the type of gases used during the combustion, because the acetylene is one of the most powerful fuel gases. On the other hand, the even when the enthalpy of vaporization of the mixture of solvents, (row 5), is very close, it seems to have an important effect on the process, which could be associated to the affinity of the precursors in the solvents. Under the optimal conditions of synthesis show in the Figure 7-12, but changing the mixture of solvents, the SSA (59.11 m²/g), area of the second peak (46.8 mJ/g) and production of amorphous material are favored (77.7 %), however, the amount of secondary phases in the system increase to values close to 6%, which could have a bigger impact in the quality of the product. On the other hand, the minimum value of the secondary phases is the 1.92 %, by using a ceramic loading of 2.5 %. Similarly, an increase of this factor to 5%, represents an increase of the secondary phases to 4.57% (138% of increment), which could be undesirable, however, the increment of these factor substantially decreases the reaction time.

7.3. Correlation between the responses

Figure 7-13 shows the responses variables of the experiments with their standard deviation, regarding to the replication of the experiments. Most of the data show a good degree of agreement, indicating the repeatability of the experiments. Considering the good replicability showed in the results, it is possible to suggest that the differences observed in samples 30E_{2%}-O₂₀₀ and 30E_{2%}-O₂₀₀R (group 5), could have been due to experimental errors during their execution, whereby, in order to correlate the results, these experiments were excluded.

Figure 7-14 shows four graphs in which the responses SSA, heat flow of the second peak, % of amorphous and % of secondary phases were correlate to observe a general tendency of the data. The rest of the responses did not show any tendency between them, whereby these graphs did not take place.

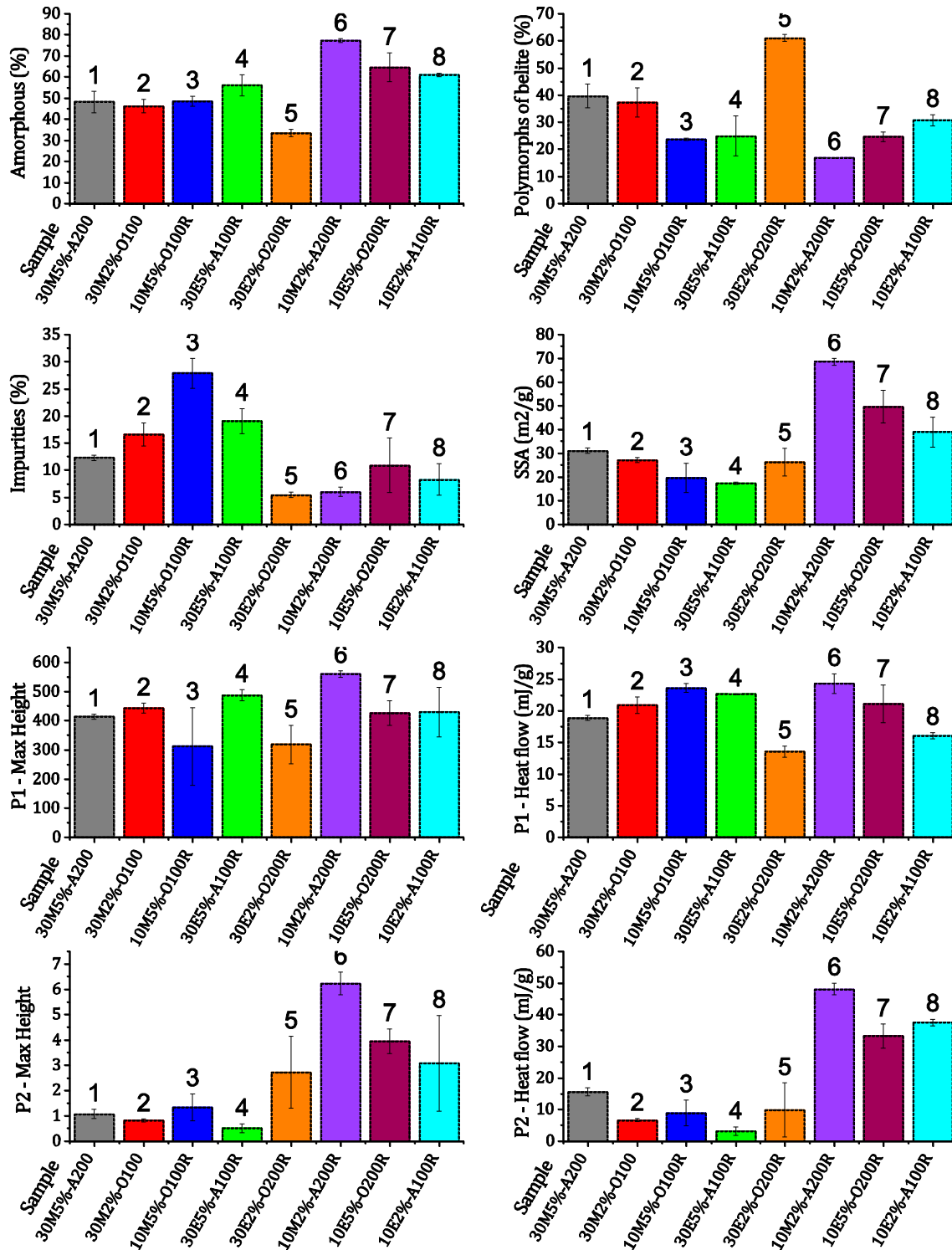


Figure 7-13. Standard deviation of the response variables (*secondary phases named as impurities)

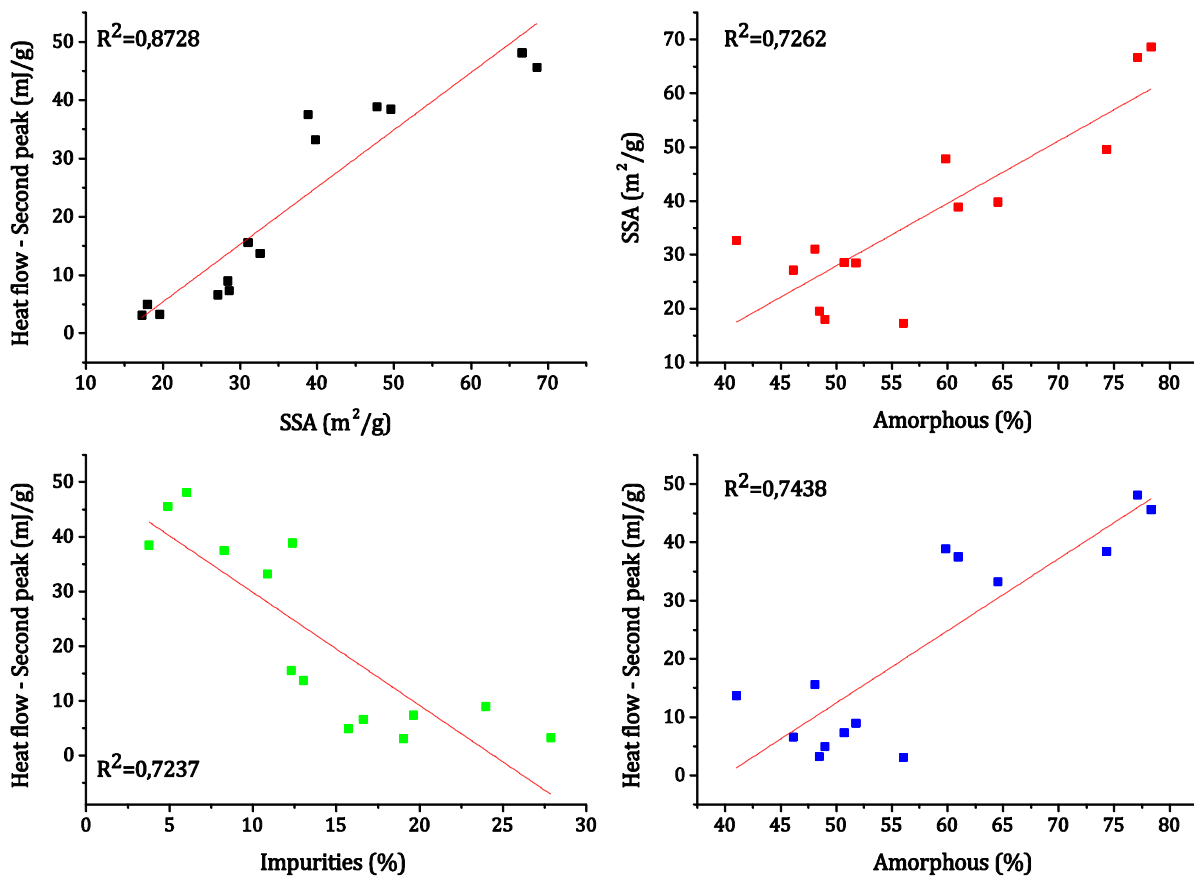


Figure 7-14. Correlation between the variables

The specific surface area was correlated with the heat flow of the second peak and the amorphous % in the samples (Figure 7-14 *a* and *b*). Both graphs show a positive proportional relationship, indicating that the amorphous material amount and the heat flow of the second peak increase with the increment of the specific surface area of the samples. It is possible to suggest that an important fraction of the amorphous materials in the sample is associated with the formation of particles of calcium silicates in nanometric sizes, due to the heat flow of the second peak is associated with the formation of C-S-H. Additionally, as it was expected, higher surface areas promote a better and faster interaction of the products and water, releasing a higher amount of energy in short times. The plots *c* and *d* are a consequence of the plots *a* and *b*, since the amorphous and heat flow have a proportional relationship with SSA, the relationship between them will be a proportional relationship. Regarding to the secondary phases, high percentages of secondary phases imply less reactive material in the sample, whereby the heat flow is lower in samples with high amount of them.

7.4. Discussion


The study of the effects of the variables during the synthesis processes was one of the main objectives of this work, considering that every chemical system present particular features at the end of the process. As explained above, the production of calcium silicates has been less explored by flame spray pyrolysis and researchers agree that one of the main challenges of this synthesis process is find relation between intrinsic and extrinsic conditions [19]. In this sense, the statistical design chooses to study the process is based in *test of significance*, in which a null hypothesis and an alternative hypothesis are accepted or rejected. In this test, the significant level for a given hypothesis test is a value for which a P-value less than or equal to α (significance level) is statistically significant. The design was evaluated with a significance level of 0.01, considering the fraction of the design. This value indicates that the probability to obtain a valid result is 99 %, therefore the risk to label an effect as significant by chance is only 1 %. The combination of variables involved in the flame spray process presented interesting results. Each variable was evaluated in two levels, in which the intrinsic value changed was the energy gave to the process. These values have important effects in the chemical composition and specific surface area of the products. The results show that a proper combination of these responses, promotes the formation of materials with better cementitious features.

The correlation of the variables shows that products with higher specific surface area have higher amount of amorphous material and higher reactivity. In this sense, process conditions, which favor the production of smaller particles, will give products with high quality for cement applications.

Table 7-1 summarizes the responses evaluated and the variables who affect them, according to the statistical design results. This table shows that the process is mostly affected by individual effects, while few interactions between the factors evaluated were found. The most important interaction was the ceramic loading with the mixture of solvents, which together correspond to the chemical system. On the other hand, this interaction is cofounded with the interaction between the pressure of dispersion gas and the feed flow rate, which are the most important variable to define the droplet particle in the aerosol. In general, the variable with stronger influence in the responses is the feed flow rate, follow by the pressure of dispersion gas.

The responses with higher relevance to identify a good cementitious material were the amount of amorphous, the SSA and the cumulative heat flow of the second peak. These responses have in common that low feed flow rates in the process favor the formation of materials with cementitious features. This variable is acting as main condition in the process, therefore its definition since the beginning of the reaction could determine the quality of the product for special applications. Considering the literature about the effects of process conditions on the products features showed in the Chapter 2, it was expected that the specific surface area of the samples will decrease with the increment of the feed flow rate; however, the dependence of the reactivity was not expected. In addition, the ranges of particle diameter obtain in this experimental design were broader and bigger than the particle diameter showed in Figure 3-3. As it was observed in the results, the features of the products are stronger dependent on the equipment characteristics and particular process conditions.

Table 7-1. Summarize of the variables with significant effects on the responses

Response	Variables with significant effects			
	 Increment of the effect			
Polymorphs of belite	C	AD=BC	B	D
Amorphous	C	AD=BC	E	-
Secondary phases	B	A	D	-
SSA	C	B	-	-
P1 - Cumulative heat flow	AD=BC	A	C	D
P1 - Height	-	-	-	-
P2 - Heat flow	C	B	A	E
P2 - Height	C	B	A	-

- A - Ceramic loading
- B- Pressure of the dispersion gas
- C- Feed flow rate
- D- Solvent
- E- Gas of dispersion

Regarding to the feed flow rate, the results indicate that under same conditions of gas of dispersion, pressure of dispersion and mixture of solvents, the products made with 10 mL/min of feed flow rate, show lower average particle size than the products made at 30 mL/min. These differences in the particle size are attributed to two conditions. First, low feed flow rates promote the formation of small droplets, facilitating their heat up, later evaporation and reactions in gas phase. Second, high feed flow rates increase the amount of fuel in the flame, resulting in longer flames and larger high temperature zones to favor the growth processes of the particles, decreasing the specific surface area of the particles [127]. Otherwise, the combustion flame during the process was slightly oxidant to avoid the formation of soot material in the samples, but the increase in the feed flow rate increase the amount of fuel in the combustion environment, promoting conditions to form organic compounds.

Concerning to the gas of dispersion, it was used oxygen and air, which provides oxygen to the combustion environment in different proportions. The negative impact over the specific surface area by the increment of fuel from a higher amount of solvent in the combustion environment was less when air was used as dispersion gas. This suggests that the 21 % of excess of oxygen supply by the air is enough to combust the excess of fuel, avoiding the formation of long flames, which promotes the sintering processes. Otherwise, the use of oxygen as dispersion gas promotes an oxidant environment, which creates most energetic flames, as it was show in Table 3-2. In this sense, Figure 7-15 shows the variations in the average particle size (APS) using air as dispersion gas at a pressure of 100 kPa with the mixture of solvent ethanol:water (plot *a*) and 200 kPa with the mixture of solvents methanol:ethanol:water (plot *b*).

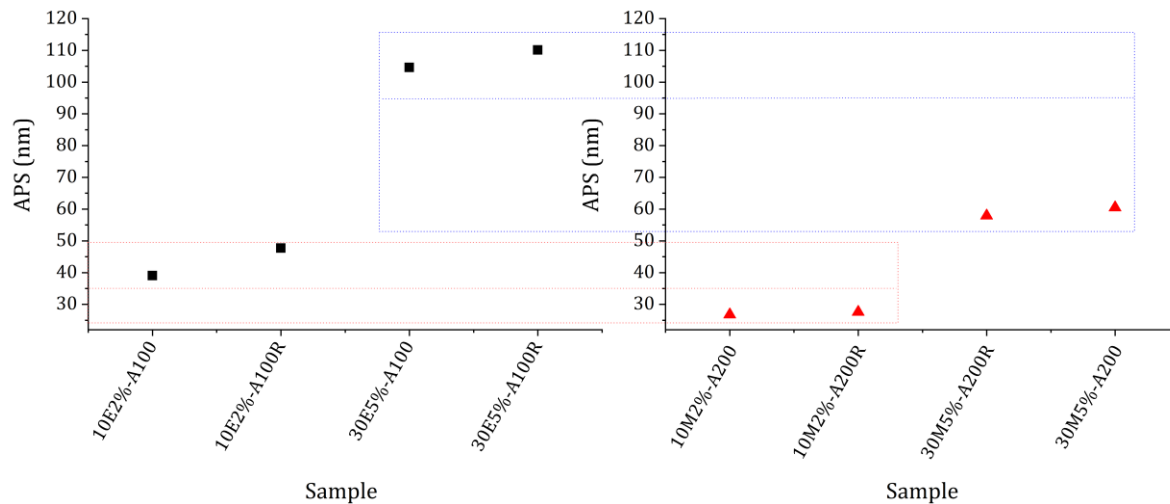


Figure 7-15. Variations in the average particle size using air as dispersion gas

From these plots are clearly observed the effects of the feed flow rate and the pressure of dispersion, overlooking the effect of the mixture of solvents. There is observed that flow rates of 10 mL/min always produce smaller nanoparticles than at 30 mL/min. Additionally, the horizontal lines between the graphs, under the same feed flow rate, clearly show the positive effect of high pressures of dispersion in the APS. In FSP, the production of nanoparticles is favored using solvents and precursors with high enthalpy of volatility and low concentration of starting materials. Theoretically, whether these two conditions are met, the other operating conditions for the aerosol formation are less relevant. However, the process may be conditioned by the availability, costs and type of raw materials, which may require, as in this case, the use of low volatility solvents as water, giving more importance to the variables involved in the formation of the aerosol. For these cases, the study shows that the first stage of the process, in which the aerosol is formed, takes a remarkable importance, giving to the pressures of the dispersion gas and feed flow rates a leading role as operational variables. Nevertheless, the specific response expected in the products defines the influence of the parameter, because the effect of some variables is stronger than those of others.

Regarding to the production of secondary phases in the samples, the results suggest that lower pressures of dispersion favor their formation, which could be attributed to the formation of an inefficient spray, with large droplets and low kinetic energy. The large drops in the spray difficult the formation of a gas phase with good distribution of the ions, limiting the formation of homogeneous particles. On the other hand, the low kinetic in the droplets, and subsequent particles, allows a long permanence of the particles in high temperature zones, where occur the sintering processes.

The effects of the concentration are not easily observed by comparison of the experimental results. Nevertheless, the experimental design indicates that the use of low ceramic loadings, favor the formation of smaller products and more amorphous, whereby more reactive products. This result agrees with the phenomenon describe in the Chapter 3, in which is explained that high concentration

of precursors, increase the amount of collisions in the gas phase, increasing the particle size by coalesce processes.

Concluding, the results indicate a strong dependence of the characteristics of the products by the process conditions, determining their reactivity. It was observed that is possible to fabricate highly reactive dicalcium silicate using an adequate combination of the process conditions, while the degree of reactivity can be manipulated by the changes in the parameters of the process. These experimental conditions are easily manipulated using gauges, valves and proper regulator equipment, reason for why the scale-up of the process to obtain nanoparticles of these cementitious materials should be reasonable.

CHAPTER 8. FORMATION OF CALCIUM SILICATES BY FLAME SPRAY PYROLYSIS

The formation of the starting solution and the chemical reactions during thermal decomposition and oxidation processes, considering the mineralogical results, are described in this chapter. Then, an explanation of the phenomena in the flame is giving, supported by the results of the statistical analysis and general characterization. Finally, a general methodology to the production of calcium silicates with general parameters are raised.

8.1. Mechanism of formation of calcium silicates by FSP

During the preparation of the starting solution, two metallorganic compounds were used as precursors, corresponding to calcium propionate and tetraethyl orthosilicate. As explain above, the calcium propionate was initially dissolved in water, while the tetraethyl orthosilicate was dissolved in ethanol.

Calcium propionate is only slightly soluble in ethanol; therefore, the use of water as solvent was required. Nevertheless, it was used in the lower amount possible, considering that the evaporation of water is an endothermic process affecting the enthalpy of the flame and the stability of TEOS in water is not good, resulting in precipitation of silica [102], [178]. Calcium propionate is a salt of carboxylic acid with short chain, which suffer hydration of the cations and anions of the structure by contact with water. The oxygen of the water surrounds the calcium cations, while the propionic chain is attracted by the hydrogen ions, resulting in a solution (Figure 8-1 *a*). On the other hand, the tetraethyl orthosilicate was dissolved in ethanol, in which the non-organic part of the molecules are surrounded by ethanol (Figure 8-1 *b*).

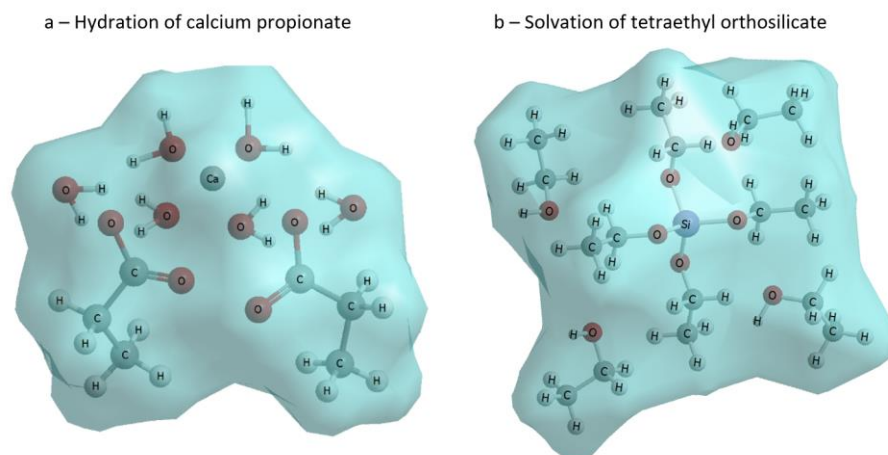


Figure 8-1. Solvation of precursors

The organic and inorganic solutions were mixed; however a slight liquid-liquid phase separation was observed, which was solved using triethanolamine (TEA) to improve the miscibility of the phases. The amount of TEA was determinates drop by drop, until obtain a homogenous and stable solution, keeping its amount proportionally to the volume of solvent, whereby this compound was part of the mixture of solvents. Considering this, during the synthesis process, the solution was always under magnetic stirring to avoid problems related to the homogeneity of the solution. Nevertheless, TEA could acts as complexing agent [179], [180], affecting the interaction behavior between the cations in the starting solution for different percentages of ceramic loadings, due to the amount of reagents remains constant for the formulations of 2.5 wt % and 5 wt % ceramic loadings, but the amount of solvent is the half for 5 wt %. In this sense, higher amount of chelates are formed for solutions with 2.5 wt % of ceramic loading than the synthesis with 5 %. Figure 8-2 shows two complexes which could be form with TEA and Ca^{2+} and Si^{4+} ions, however this compound can form monomers, dimers and trimers with these cations.

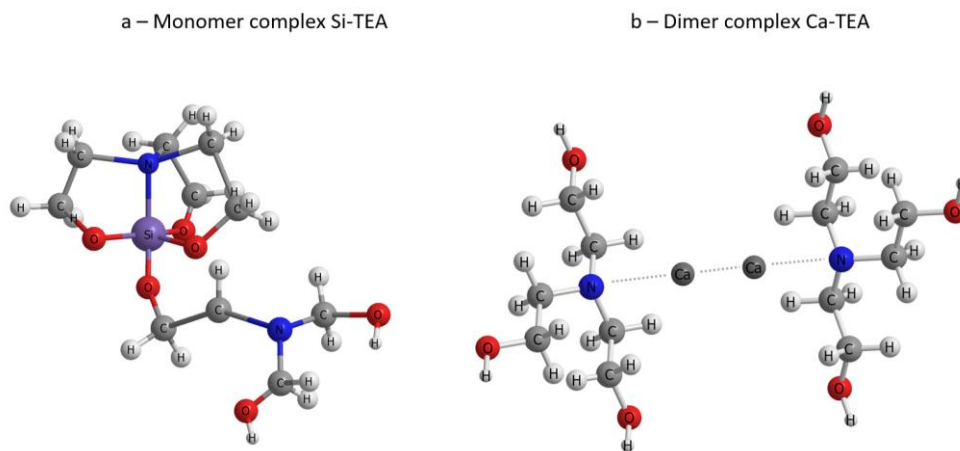


Figure 8-2. Complex of TEA; a – Monomer complex Si- TEA , b- Dimer complex Ca-TEA (Adapted from [179], [180])

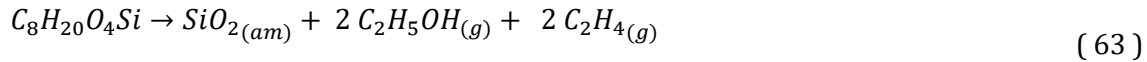
The observations about the use of TEA suggest that this compound could change the chemistry of the solution, by promoting a better interaction of the metal ions, coherently with the mineralogical results, in which is observed that the lower amounts of calcium oxide were obtain when ceramic loadings of 2.5 wt % percent were used. However, as this compound was used at the beginning to have a good miscibility of the phases, not enough amount was added to favor the total complexation of the cations in the solution. Additionally, it could be inferring that the effects observed by the interaction between the mixture of solvents and the ceramic loading could be strongly related to the interaction of the cations with TEA.

Dissolving metallorganic compounds in organic solvents, the mechanism of formation of the nanoparticles, should follow the gas-to-particle route, however, the use of water decreases the energy of the flame, promoting the formation of large particles, as it was observed in the BET measurements of the samples. Nevertheless, more factors are involving in the formation of the

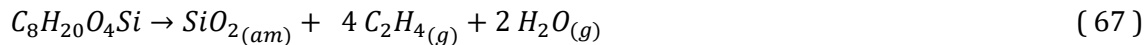
nanoparticles, like the combustion environment, which was acetylene/oxygen, providing enough energy to the flame to avoid the formation route of drop-to-particle.

In the flame, the components of the solution could be thermally decomposed or/and oxidized [72], [84], [155], [181], [182]. Whereby, the decomposition and oxidation reactions of the precursors and solvents mentioned are shown below [84], [125], [183]. With these equations, the overall reaction in the flame is shown in equations (81) and (82), corresponding to the thermal decomposition and oxidation, respectively.

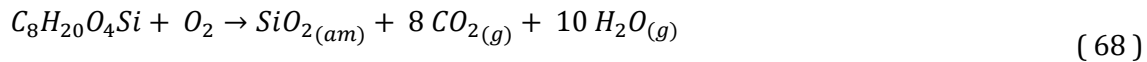
The thermal decomposition of tetraethyl orthosilicate results in the formation of SiO₂, H₂O, CO₂, CO, C₂H₅OH, C₂H₄ and H₂ [183]. During the first stage of the thermal decomposition is formed amorphous silica, while the alkyl chains decompose in ethanol and ethane (equation (63)). Then, ethanol could present two decomposition routes, producing ethene (C₂H₄) and water (64) or hydrogen and (CH₃CHO) (65), which will suffer a later decomposition to produce methane and carbon monoxide (66) [183], [184].



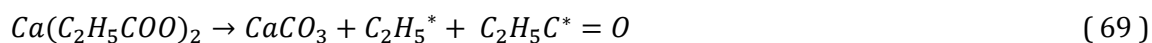
The equation (67) shows the overall reaction of the thermal decomposition of TEOS considering only the formation of ethene and water.



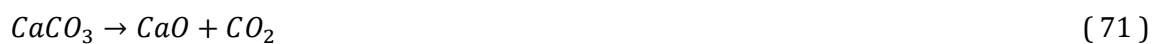
On the other hand, under oxidizing environment TEOS is decomposed in silica and ethanal (CH₃CHO), followed by the oxidation of ethanal in methanal (CH₂O), which will decompose in CO₂ and water [183], [185].



Regarding to calcium propionate, its thermal decomposition is divided in three stages, follows the mechanism of Hites and Biemann. The decomposition process starts with the formation of acyl and alkyl radicals (51) between 292-486 °C, which could react to form ketones as 3-pentanone (70) [151]-[153].



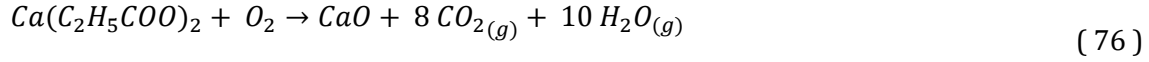
Increasing the temperature, between 570-739 °C, the calcium carbonate decomposes in lime and CO₂ [151], [186].



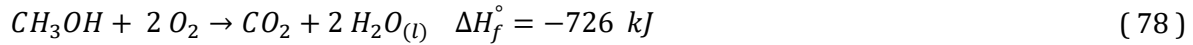
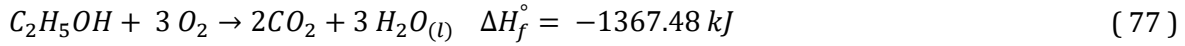
In addition, others hydrocarbons as 2-butanone and propanal can be formed by the reaction of ethyl radicals as is shown in (72) and (73), resulting in the formation of methyl and hydrogen radicals which will form 2-butanone and propanal as it is shown in (74) and (75) [152], [153].



The oxidation reaction of the calcium propionate is show in equation (76).



The decomposition reactions of ethanol were described in equations (64), (65) and (66), while its oxidation reaction is shown in equation (77). Furthermore, the oxidation of methanol is shown in equation (78) and the thermal decomposition and evaporation of water in (79) and (80), respectively.



Considering the equations shown above, the equation (81) shows the overall thermal decomposition of the precursors in the starting solution, while equation (82) shows its oxidation. Taking into account the results of the mineralogical characterization, in the equations (81) and (82) it was assumed that the amorphous material is composed by dicalcium silicate with low crystallinity and silicon oxide, based on the fact that higher amounts of amorphous material results in better hydraulic responses and the principle of mass conservation. The stoichiometry coefficients *a*, *b*, *c*, and *d*, for this equations were calculated for each reaction considering the chemical composition obtained by Rietveld refinement, supposing that all the calcium resource that was not part of the crystalline products (calcium oxide and polymorphs of belite) was transformed in belite with low crystallinity as part of the amorphous material (Table 8-1). However, the calcium resource left could form of dicalcium silicate, calcium oxide, calcium carbonate and portlandite, nevertheless, for practical purposes it was considered that all the calcium was converted in dicalcium silicate with low crystallinity.

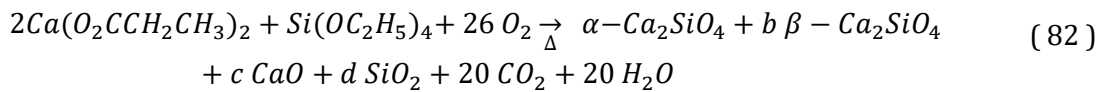
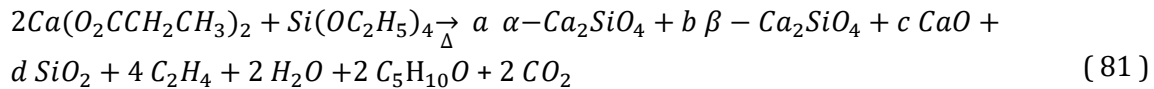


Table 8-1. Calculated stoichiometry coefficients of the products

Sample	Stoichiometric coefficient			
	<i>a</i>	<i>b</i>	<i>c</i>	<i>d</i>
30M _{5%} -A ₂₀₀	0.39	0.49	0.25	0.14
30M _{5%} -A ₂₀₀ R	0.45	0.41	0.27	0.15
30M _{2%} -O ₁₀₀	0.37	0.47	0.34	0.19
30M _{2%} -O ₁₀₀ R	0.29	0.51	0.40	0.22
10M _{5%} -O ₁₀₀	0.35	0.48	0.34	0.19
10M _{5%} -O ₁₀₀ R	0.25	0.56	0.39	0.22
30E _{5%} -A ₁₀₀	0.62	0.31	0.13	0.08
30E _{5%} -A ₁₀₀ R	0.60	0.34	0.11	0.06
30E _{2%} -O ₂₀₀	0.23	0.51	0.52	0.29
30E _{2%} -O ₂₀₀ R	0.24	0.54	0.46	0.25
10M _{2%} -A ₂₀₀	0.17	0.80	0.10	0.07
10M _{2%} -A ₂₀₀ R	0.30	0.63	0.14	0.09
10E _{5%} -O ₂₀₀	0.22	0.76	0.06	0.05
10E _{5%} -O ₂₀₀ R	0.24	0.66	0.20	0.12
10E _{2%} -A ₁₀₀	0.17	0.80	0.09	0.06
10E _{2%} -A ₁₀₀ R	0.28	0.63	0.21	0.12

Moreover, being consistent with the mineralogical results, equations (83) and (84) show the hydration of calcium oxide produced during the reaction and the carbonation of the calcium hydroxide, forming the observed secondary phases, calcium hydroxide and calcium carbonate. The hydration and carbonation reactions of calcium oxide, occurs in two regimes, the first one controlled by the chemical reaction with the moisture, the second regime controlled by the formation of a passive layer in the compound, limiting the diffusion of ions through the structure [176]. Additionally, the kinetics of these reactions depends on the concentration of gases in the environment and the morphological features as specific surface area and porosity of the compounds. V. Morales et al., study the kinetic of hydration and carbonation reactions of nanoparticles of calcium oxide by weathering, finding that the first regime of the hydration occurs between few minutes to hundreds of hours to achieve a complete hydration, while the carbonation can require months, which is linked to the concentrations of water vapor and carbon dioxide in the atmosphere [176].



When the solution is sprayed in the flame, the evaporation and chemical reaction are considering instantaneous processes. The lifetime of the droplets in the flame is divided in two stages, in which the evaporation depends of the velocity of the droplet in the flame. This velocity expressed in equation (8), shows that the velocity of the droplets is proportional inverse to the droplets diameter, whereby, smaller droplets have higher velocities, therefore, are evaporated easily in the flame. In this sense, the particles made under a dispersion pressure of 200 kPa and 10 mL/min of feed flow rate, present the higher rate of evaporation (Table 4-2), having less chance to have higher differences in the rate of evaporation of the components, which in this case could be partially responsible of the formation of calcium oxide during the reaction. In contrast, the samples made under 100 kPa and 30 mL/min of pressures of dispersion and feed flow velocity, respectively, show the higher formation of calcium oxide in the flame, for both values of ceramic loadings, nevertheless, it is show also a tendency of higher amount of this impurity in the samples with 5 wt % of ceramic loading, attributed above to a better interaction of the cations in presence of higher percentages of chelating agents. On the other hand, the morphological results show the formation of hollow and solid particles, which could indicate that the mechanism of formation of the particles follow both mechanism, i.e. gas-to-particle and drop-to-particle.

Subsequently to the evaporation and decomposition of the precursors, the media becomes rich in monomers, increasing the Gibbs free energy, permitting the formation of primary particles. The equations (18) to (23), describes the formation of the primary particles. These equations depend of the temperature of the system and the concentration of species in the media. Thus, high ceramics loadings result in higher Gibbs free energy, promoting adequate conditions to form higher amounts of primary particles. However, like it was explained before, this condition not necessarily favor the process, because high concentration of primary particles in the flame increment the number of collisions of particles, resulting in coalesce processes with decrease the surface area of the samples, and consequently, decreasing their reactivity with water.

Finally, after the formation of the primary particles, the growth process by coagulation and coalescence start. Equations (30) to (39) describe the coagulation processes during the growth of the particles. From these equations, the most important term is the particle velocity, c , which increase the coagulation rate (β) in the Fuchs equation, when the particle velocity is high. This particle velocity depends of the kinetic energy of the drop in the flame, which is influence by the feed flow rate and the pressure of dispersion. Figure 8-3 shows the schema of the whole process reaction with the mechanism of formation of the calcium silicates.

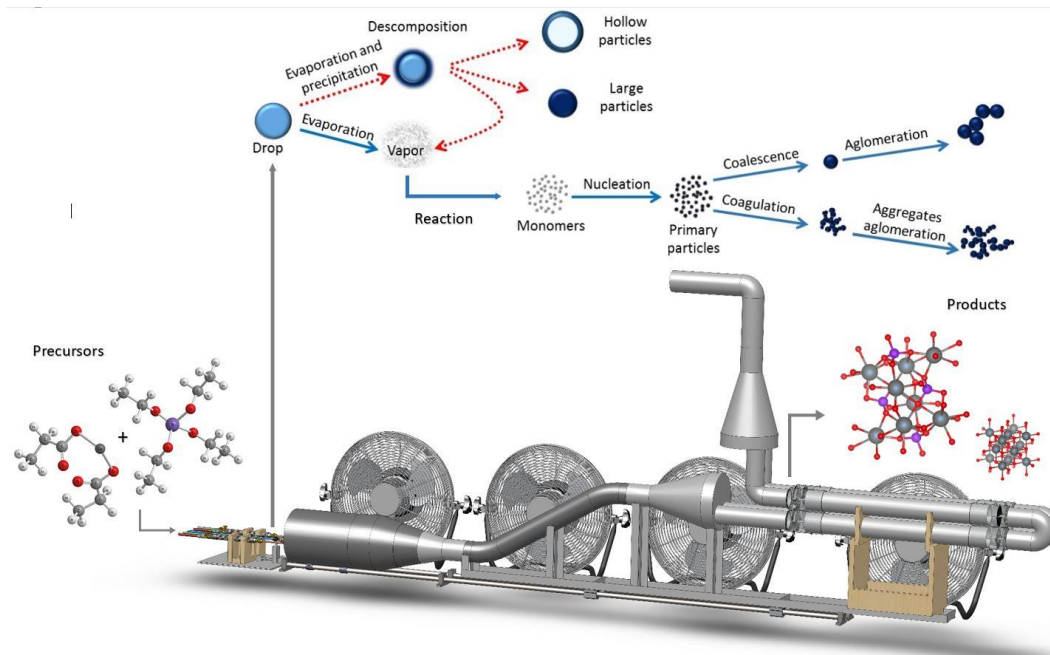


Figure 8-3. Schema of the reaction process

8.2. Methodology of synthesis conditions in flame spray pyrolysis

Considering the results obtained during the experimentation, characterization and analysis of results and fulfilling the general objective of this thesis, it is presented a methodology, which allows the production of a material with cementing properties, making it suitable for possible applications in the cement industry. The diagram of the methodology is shown in Figure 8-4.

The definition of the methodology starts with the formulation of the starting solution. In this case, the main purpose is the production of calcium silicate phases, for this reason they were chosen calcium propionate and tetraethyl orthosilicate as precursors. To improve the interaction between the cations to form the structure, it is suggested the use of stoichiometric amounts of TEA to promote the formation of ligands in the solution. On the other hand, the use of calcium 2-ethylhexanoate is still consider as a good option but using different solvents. During the set-up of the process, this reagent was evaluated in mixtures of water/ethanol and toluene without good results, however, a mixture of solvents as xylene/ethanol could be a better option to avoid the use of water in the starting solution. Considering the use of xylene in the starting solution, instead of water, can avoid the precipitation problems show by the use of water and TEOS in the same solution as possible avoiding the use of TEA as stabilizing agent. Nevertheless, its evaluation is part of the recommend future works in this thesis.

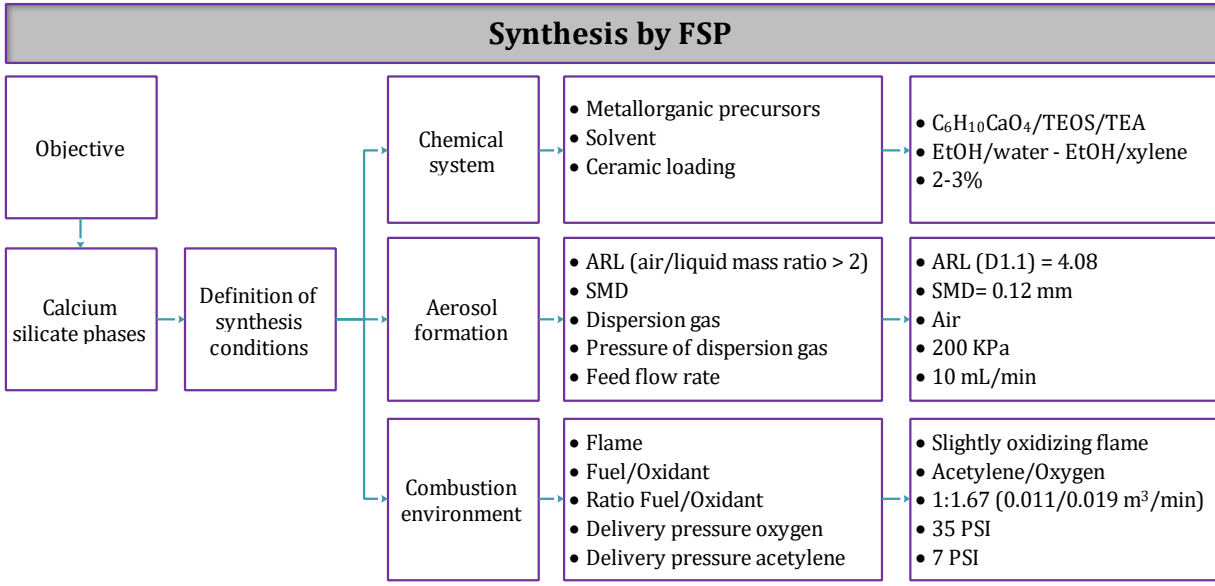


Figure 8-4. Methodology of synthesis of calcium silicates by FSP

The ceramic loading of the solution should be under 3 wt %, avoiding the growth process by higher concentration of primary particles in the flame, due to high rates of collisions. Low ceramic loadings imply longer times of reaction, however, the increase of this parameter have an impact in the reactivity of the samples. Under ceramic loadings of 3 wt %, the number of secondary phases in the product remains below 2.5 wt %, increasing in 1wt % with the increase of the ceramic loading. Table 8-2 shows the variation of the responses with the increase of the ceramic loading

Table 8-2. Variations in the responses with the variation of ceramic loading

Response	Ceramic loading (%)			
	2.5	3	4	5
SSA	52.43	53.43	55.41	57.37
P2 - Cumulative heat flow	45.18	45.07	44.86	44.65
Amorphous	60.98	64.38	71.14	77.79
Polymorphs of belite	37.27	33.24	25.22	17.34
Secondary phases	1.92	2.46	3.52	4.57

During the formation of the aerosol, the dimensions and configuration of the equipment are very important, since it defines the droplet size of the aerosol. An airblast nozzle was used to generate the aerosol. The air/liquid mass ratio (ALR) govern the mass median drop size, which should be between 0.1 to 10, in which lower values will not produce proper drops, while higher values waste energy [105]. Although, during the experimentation the aerosol formed using a pressure of dispersion of 100 kPa and a feed flow rate of 30 mL/min show unfavorable results, with an ALR of 0.96 for an airblast nozzle with external diameter of 1.1 mm. Similarly, the combination 200 kPa and 30 mL/min with an ALR of 1.36. Otherwise, the combinations of pressure of dispersion and feed flow rate of 200-10 and

100-10 showed better results, with ALR values of 4.08 and 2.89, respectively. For this reason, here is suggested the use of ALR values upon 2.89, as a general parameter for the formation of droplets in airblast nozzles. As explained above, the ALR values were calculated using air and water as fluids; this calculation depends on the density of the fluids, reason for why the values could have slight differences if the fluids are change for air and ethanol. The same situation is applying for the calculation of the SMD.

Regarding to the combustion environment, it is suggested the use of slightly oxidizing flames to avoid the formation of high amounts of soot in the samples. Additionally, a stoichiometric mixture of gases for neutral flames in combustion do not works well, due to the excess of fuel provided by the starting solution. As fuel, it was choosing acetylene, due to the configuration of the burner system and the availability of gases. This gas has as advantage the high availability and the high energy of the flame, however, it has as disadvantage the 2 atoms of carbon in the structure, implying the production of 2 mole of CO_2 per mole of C_2H_2 . Methane could be another option, which have only one atom of carbon in the structure, however, the temperature of the flame is lower than acetylene. On the other hand, hydrogen as fuel could be the best option, since it is a zero-emission fuel, which generates water vapor during the combustion and reach temperature of combustion of 2900 °C. Nevertheless, the manufacture cost of this fuel is higher than other fuels and it requires special storage systems.

Using the mixture acetylene/oxygen to the combustion, the delivery pressures, ratio of gases and their flow are defined in Figure 8-4. However, it is possible to increase the amount gases of combustion, keeping their ratio, in order to use higher pressures of dispersion gas. The increment of this parameter, allows a better liquid disintegration of the liquid jet, increasing the turbulence and kinetic energy of the droplets, favoring the formation of smaller particles, which as seen throughout the development of this thesis, favors the formation of products with higher reactivity.

CHAPTER 9. CONCLUSIONS AND FUTURE WORK

In this research it was addressed the study of the effects of the process conditions of flame spray pyrolysis in the production of calcium silicate phases, their chemical composition and hydraulic behavior. This chapter highlights the conclusions obtained during the development of the research and some recommendations and future works that could be perform.

9.1. Conclusions

Flame spray pyrolysis method was used to prepare calcium silicates phases starting form metallorganic and organometallic precursors changing five experimental conditions. The anhydrous products were evaluated with XRD, TGA-DSC coupled with mass spectrometer, FT-IR, SEM and TEM, showing the presence of polymorphs of dicalcium silicate, calcium oxide, calcite and portlandite in micrometer and nanometer sizes. TGS-DSC measurements were an important support to verify the amounts of calcium carbonate and calcium hydroxide obtained by Rietveld refinement. The small differences observed between XRD and TGS-DSC measurements were attributed to their formation in nanoscale phases of these components, which were not possible to identify by x-ray diffraction. On the other hand, the FT-IR showed that all the precursors were consume in the flame, due to any band of these organic compounds were observed.

Five experimental conditions of the process were evaluated using an experimental design, two-level fractional factorial design with resolution III, 2^{5-2} . Thus, several responses were considering, in order to observe effects on the mineralogy, particle size and reactivity of the samples. The application of the ANOVA test shows the significance of the process conditions evaluated, permitting to observe correlations between the process conditions and the responses evaluated. From this statistical analysis was observed that products with higher specific surface area have higher amount of amorphous material and higher reactivity, whereby process conditions to produce smaller particles must favor the production of hydraulic materials. Considering this, the most important variables are the feed flow rate, follow by the pressure of dispersion gas, which must be defined favoring the formation of small droplets during the formation of the spray (Low feed flow rates and high pressure of dispersion gas). The interaction of these variables can be expressed by the air/liquid mass ratio (ALR) which is an operation factor in the formation of sprays governing the mass median drop size.

Additionally, the results obtained for the effect of the feed flow rate in this thesis, agree with the results of H. Chang *et al.*, M. Aromaa *et al.* and Lovell *et al.* [81], [127], [131], in which the increment in the feed flow rate leads to increments in the particle size. This condition favors the formation of large droplets in which the evaporation process is less effective, disfavoring the formation of the gas phase and promoting the coalescence of the particles in high temperature zones.

Considering the results of the characterization a mechanism of formation of the products were described, based on the chemistry of the process and phenomenological equations involve during the formation of the particles. This analysis suggested that the reactions could be strongly influenced by the presence of TEA, favoring the formation of complex with the Ca^{2+} and Si^{4+} ions. Nevertheless, in this study this compound was added with different purposes, reason for why future research on its influence is proposed. The products showed heterogeneous composition as result of the use of a mixture of solvents in the starting solution with different evaporation rates. Choosing proper precursors and solvents for the FSP synthesis can determinate the amount of desirable and undesirable phases in the product. During this project, it was necessary the use of mixtures of organic and inorganic solvents, which could favor the production of heterogeneous phases and resulting in the formation of calcium oxide as main impurity. Nevertheless, intrinsic and extrinsic conditions as process parameters and chemistry of the starting solution demonstrate to be very significant to produce calcium silicates.

Based on the results of the characterization and statistical analysis, a methodology to obtain dicalcium silicates with hydraulic behavior was proposed, giving the experimental conditions and suggesting alternative conditions in which it could be possible to improve their hydraulic behavior, satisficing the hypothesis of the thesis. After analyzed the several synthesis conditions it was observed that it is possible to obtain early-hydraulic and late-hydraulic products, depending of the definition of the parameters of the process, indicating their strong influence in the final properties of the products. The optimize process conditions for produce calcium silicate phases with hydraulic behavior using the equipment describe in Chapter 4, are a ceramic loading=2.5 wt %, pressure of dispersion gas=200 kPa, feed flow rate=10 mL/min, mixture of solvents= ethanol/water, and gas of dispersion=air. The constant conditions of the process were the dimmesions of the nozzle, the combustion gases, their pressure and flow rate. These gases were oxygen and acetylene with a flow rate of 0.019 m^3/min and 0.011 m^3/min , respectively, corresponding to an oxidizing flame. Additionally, the samples with hydraulic behavior have in common an arrangement of conditions, in which at least 3 of 5 conditions tend to produce smaller nanoparticles. In contrast, the non-hydraulic samples were produced with less than 3 process parameters favoring the decrease of particle size. These conditions are low ceramic loading values, high pressures of dispersion, low feed flow rates, solvent with high enthalpy of evaporation and gases of dispersion with high enthalpy. Nevertheless, the optimization of the results indicates that the use of air as dispersion gas is better for the process, when a fuel as acetylene is use in the combustion flame.

9.2. Recommendations

Evaluate the effect of the addition of TEA or additional chelating agent in the synthesis of calcium silicates through flame spray pyrolysis.

Consider the use of mixtures of solvents using xylene instead of water.

Perform a deeper study of the hydraulic behavior of the samples obtained by flame spray pyrolysis as products with interesting properties to be use in the cement industry. Additionally, a study of their mechanical properties most be developed.

Consider the use of alternative fuels as hydrogen or methane, which release less GHGs during the synthesis process. Additionally, it could be considering the use of higher amounts of fuel/oxidant and higher pressure of dispersion gas, which could favor the formation of materials with better hydraulic performance.

The use of digital controllers could improve the reproducibility of the results, because the mechanical controllers are more susceptible to human errors.

In this chapter is shown the complementary information of the project as supporting information to the characterization results and statistical analysis.

10.1. Ratio of combustion gases

In order to define the feed flow of the gases, several tests were carried out looking for a complete evaporation of the solvent and precursors. The gases flow tested are shown in the Table 10-1.

Table 10-1. Flames tested in the production of particles with a Terodyn system

Flame number	Acetylene (m ³ /min)	Oxygen (m ³ /min)	C ₂ H ₂ :O ₂ (m ³ : m ³)
Flame 1	20	30	1:1.5
Flame 2	18.6	29.7	1:1.67

Initially, it was tested a neutral flame (Flame 1) with a C₂H₂:O₂ ratio of 1:1.5, in which all the fuel is consumed by the oxygen in the flame. This flame had an acetylene flow rate of 20 m³/min and 30 m³/min for oxygen, commonly used in flame guns during the application of coatings. Figure 10-1 shows the formation of coal particles in the product, which were observed in a stereoscope, probably produced by the additional fuel in the system provide by the starting solution, whereby the flow of acetylene was decreased until have a slightly oxidant flame, providing an oxygen excess burning all the carbon ions in the combustion environment.

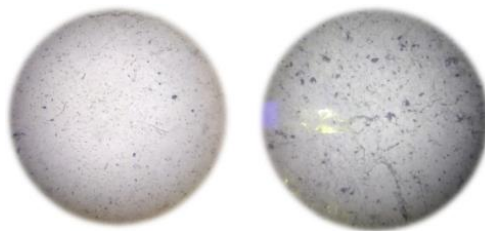


Figure 10-1. Particles obtained with Flame 1 (1:1.5)

In this sense, applying a flame with smaller amount of fuel flow (Flame 2), was obtained a powder without the presence of coal (Figure 10-2). Using the coaxial flame assemble, several flames using the ratio 1:1.67 gases were probed with lower consumption of gases; however the reactions were unsuccessful. This led to the construction of the assembly dual-flame burner.

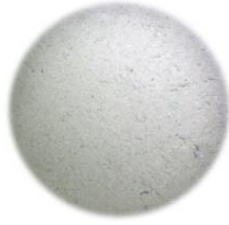
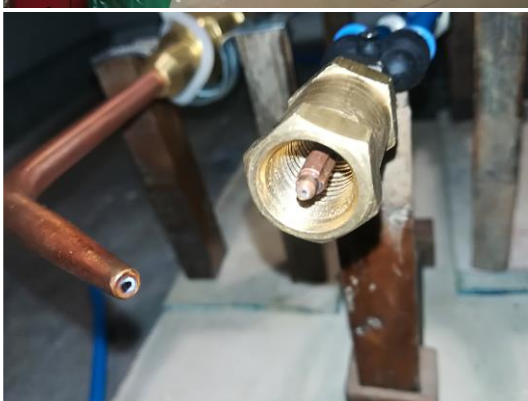
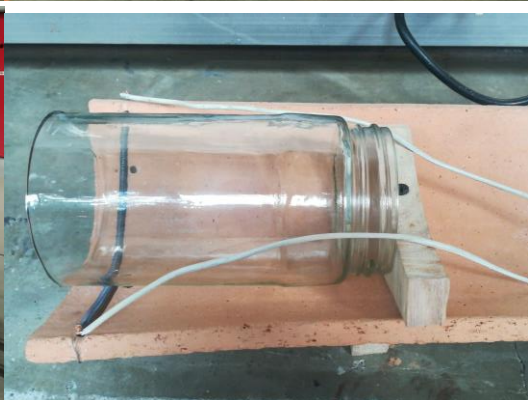


Figure 10-2. Particles obtained with Flame 2 (1:1.67)

10.2. Photographic record of the building and use of the FSP equipment

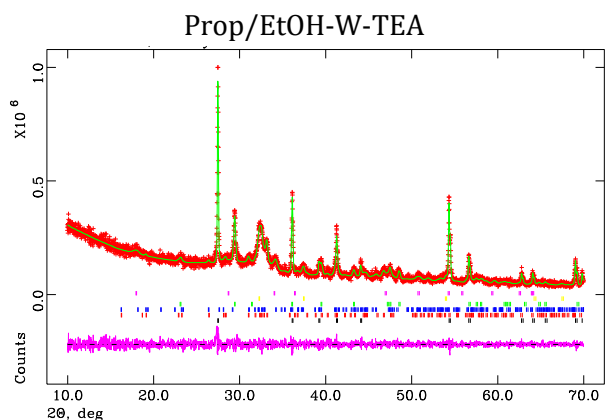
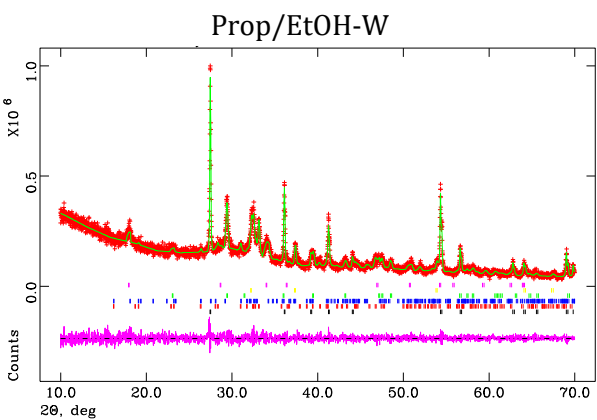
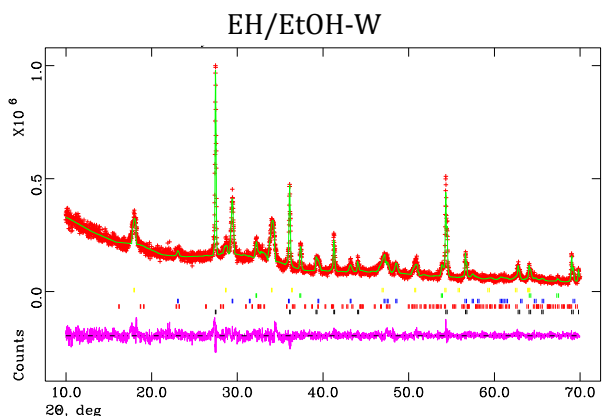
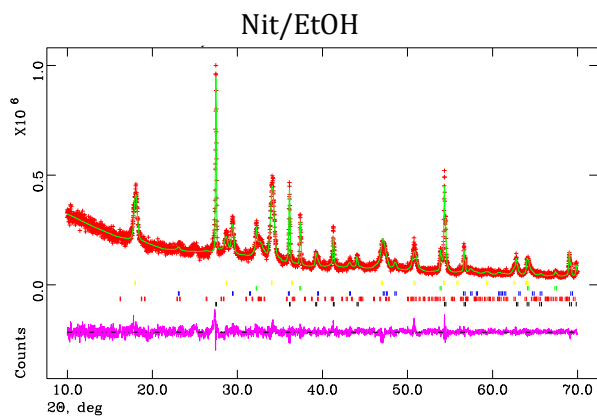
In this section are shown some photographs taken during the construction of the equipment and its use to synthesize nanoparticles.



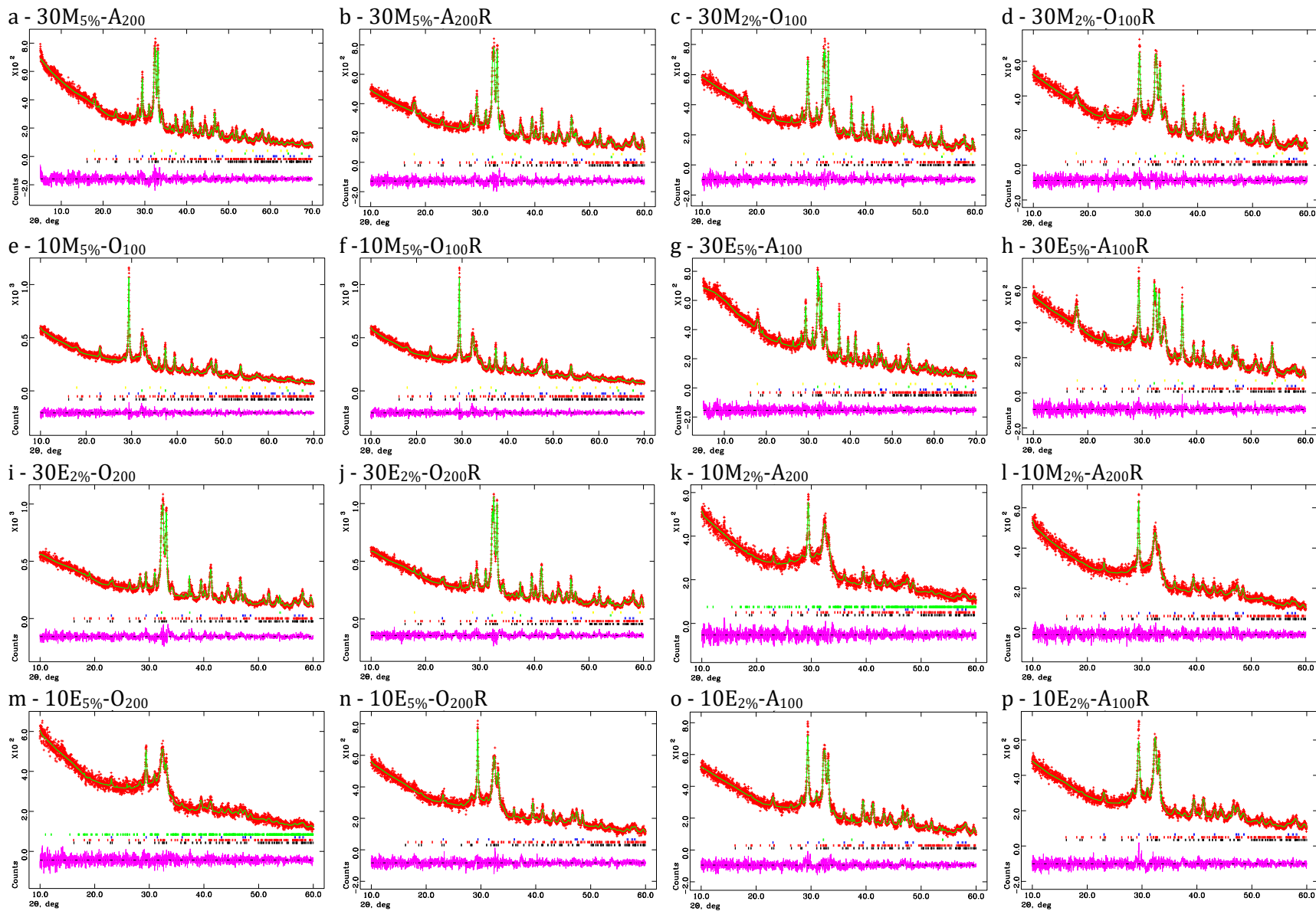




10.3. Rietveld refinement during the evaluation of different chemical systems

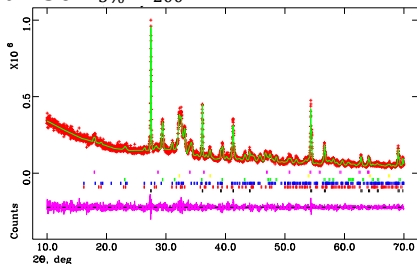


10.4. Diffractograms of Rietveld refinement of calcium silicates by FSP as-prepared

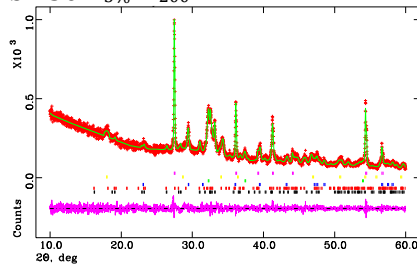


10.5. Diffractograms of Rietveld refinement of calcium silicates by FSP with internal standard.

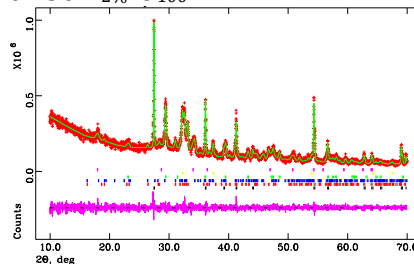
a - 30M_{5%}-A₂₀₀



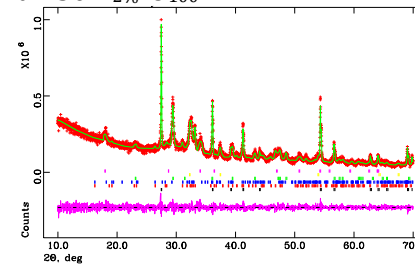
b - 30M_{5%}-A₂₀₀R



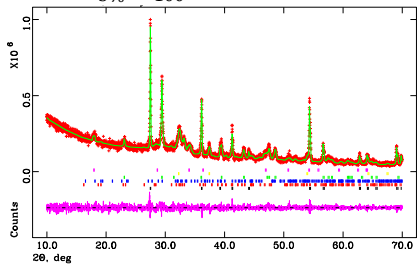
c - 30M_{2%}-O₁₀₀



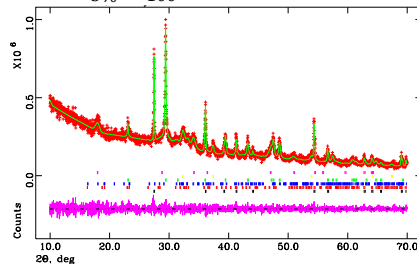
d - 30M_{2%}-O₁₀₀R



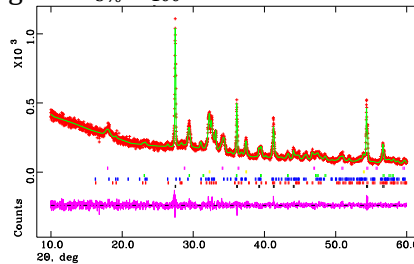
e - 10M_{5%}-O₁₀₀



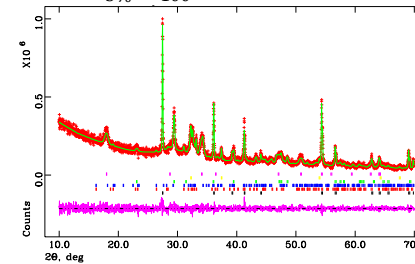
f - 10M_{5%}-O₁₀₀R



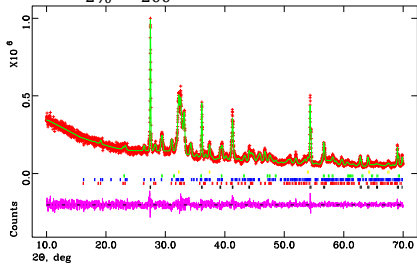
g - 30E_{5%}-A₁₀₀



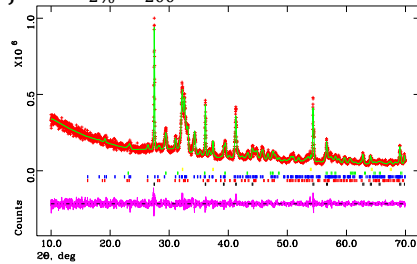
h - 30E_{5%}-A₁₀₀R



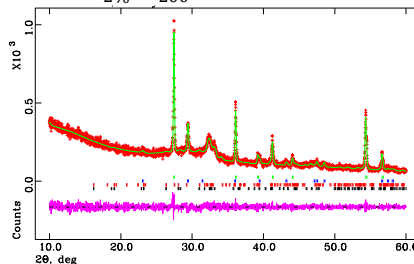
i - 30E_{2%}-O₂₀₀



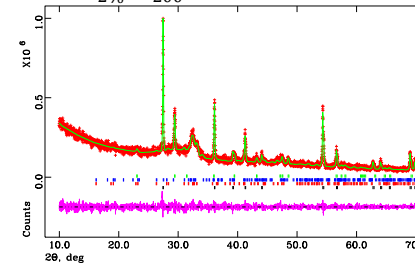
j - 30E_{2%}-O₂₀₀R



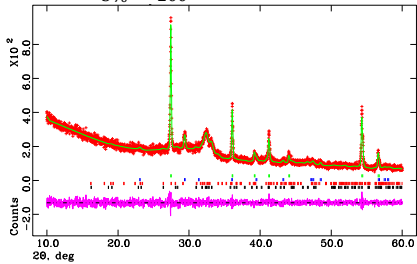
k - 10M_{2%}-A₂₀₀



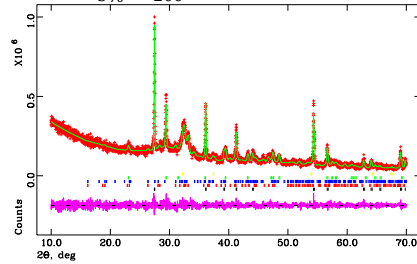
l - 10M_{2%}-A₂₀₀R



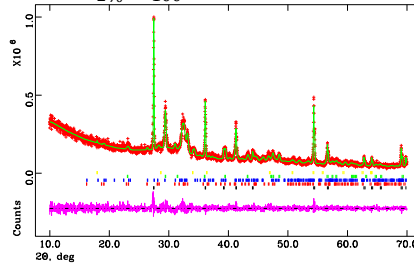
m - 10E_{5%}-O₂₀₀



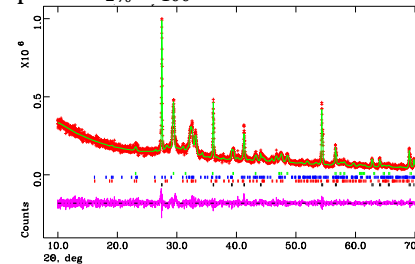
n - 10E_{5%}-O₂₀₀R



o - 10E_{2%}-A₁₀₀



p - 10E_{2%}-A₁₀₀R



10.6. Assumptions of the analysis of variance (ANOVA)

10.6.1. Polymorphs of belite

Table 10-2. Analysis of Variance of Polymorphs of belite

Source	D F	Adj SS	Adj MS	F- Value	P- Value
Model	7	2655.7 5	379.39	12.19	0.001
Linear	5	2043.7 6	408.75	13.14	0.001
Ceramic loading (%)	1	90.09	90.09	2.90	0.127
Pressure of dispersion (kPa)	1	315.14	315.14	10.13	0.013
Feed flow rate (mL/min)	1	1351.5 1	1351.5 1	43.43	0.000
Mixture of solvents	1	139.87	139.87	4.50	0.067
Gas of dispersion	1	147.15	147.15	4.73	0.061
2-Way Interactions	2	612.00	306.00	9.83	0.007
Ceramic loading (%)*Pressure of disp. (kPa)	1	22.96	22.96	0.74	0.415
Ceramic loading (%)*Mixture of solvents	1	589.03	589.03	18.93	0.002
Error	8	248.93	31.12		
Total	15	2904.6 8			

Table 10-3. Model Summary of Polymorphs of belite

S	R-sq	R-sq(adj)	R-sq(pred)
5.57819	91.43%	83.93%	65.72%

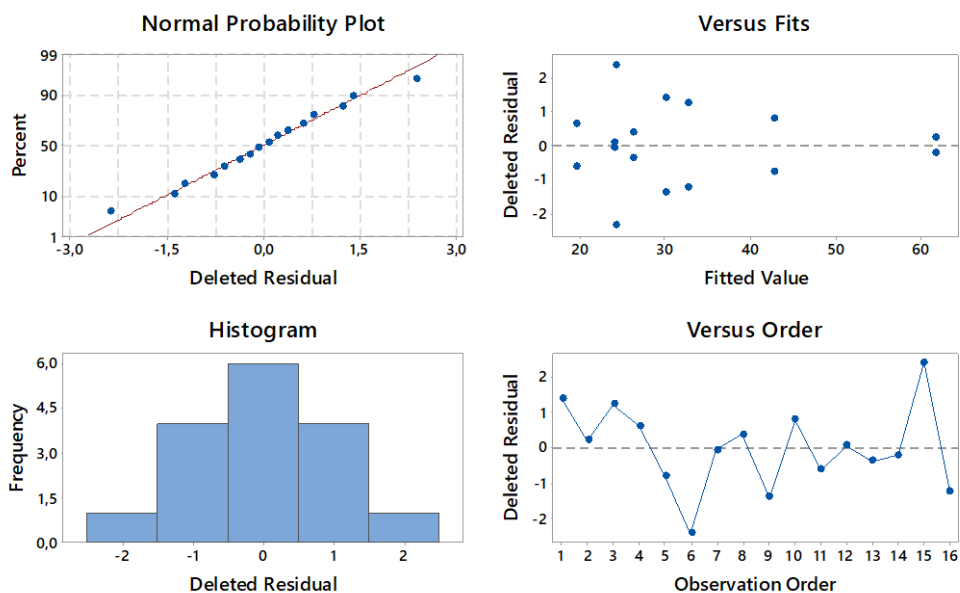


Figure 10-3. Residual plots for Polymorphs of belite

10.6.2. Amorphous

Table 10-4. Analysis of Variance of Amorphous

Source	DF	Adj SS	Adj MS	F-Value	P-Value
Model	7	2650.33	378.62	9.53	0.002
Linear	5	1803.78	360.76	9.08	0.004
Ceramic loading (%)	1	5.70	5.70	0.14	0.715
Pressure of dispersion (kPa)	1	8.64	8.64	0.22	0.653
Feed flow rate (mL/min)	1	1474.65	1474.65	37.12	0.000
Mixture of solvents	1	6.64	6.64	0.17	0.693
Gas of dispersion	1	308.15	308.15	7.76	0.024
2-Way Interactions	2	846.55	423.28	10.65	0.006
Ceramic loading (%)*Pressure of dispersion (kPa)	1	46.66	46.66	1.17	0.310
Ceramic loading (%)*Mixture of solvents	1	799.89	799.89	20.13	0.002
Error	8	317.84	39.73		
Total	15	2968.17			

Table 10-5. Model Summary of Amorphous

S	R-sq	R-sq(adj)	R-sq(pred)
6.30315	89.29%	79.92%	57.17%

Table 10-6. Fits and Diagnostics for Unusual Observations of Amorphous

Obs	Amorphous	Fit	Resid	Std Resid	
6	78.32	67.85	10.48	2.35	R
15	57.37	67.85	-10.48	-2.35	R

R Large residual

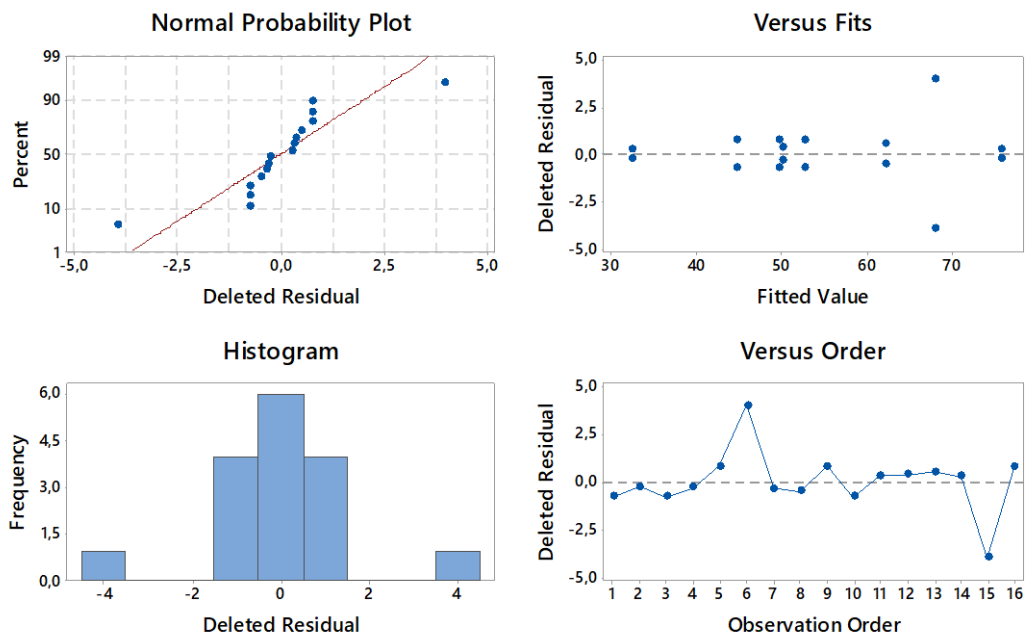


Figure 10-4. Residual plots for Amorphous

10.6.3. Secondary phases

Table 10-7. Analysis of Variance of Secondary phases

Source	DF	Adj SS	Adj MS	F-Value	P-Value
Model	7	307.520	43.931	22.30	0.000
Linear	5	302.417	60.483	30.70	0.000
Ceramic loading (%)	1	69.012	69.012	35.03	0.000
Pressure of dispersion (kPa)	1	179.552	179.552	91.14	0.000
Feed flow rate (mL/min)	1	9.146	9.146	4.64	0.063
Mixture of solvents	1	33.334	33.334	16.92	0.003
Gas of dispersion	1	11.373	11.373	5.77	0.043
2-Way Interactions	2	5.103	2.551	1.30	0.326
Ceramic loading (%)*Pressure of dispersion (kPa)	1	1.672	1.672	0.85	0.384
Ceramic loading (%)*Mixture of solvents	1	3.431	3.431	1.74	0.223
Error	8	15.761	1.970		
Total	15	323.281			

Table 10-8. Model Summary of Secondary phases

S	R-sq	R-sq(adj)	R-sq(pred)
1.40361	95.12%	90.86%	80.50%

Table 10-9. Fits and Diagnostics for Unusual Observations of Secondary phases

Obs	CaO real	Fit	Resid	Std Resid	
6	2.911	5.057	-2.146	-2.16	R
15	7.202	5.057	2.146	2.16	R

R Large residual

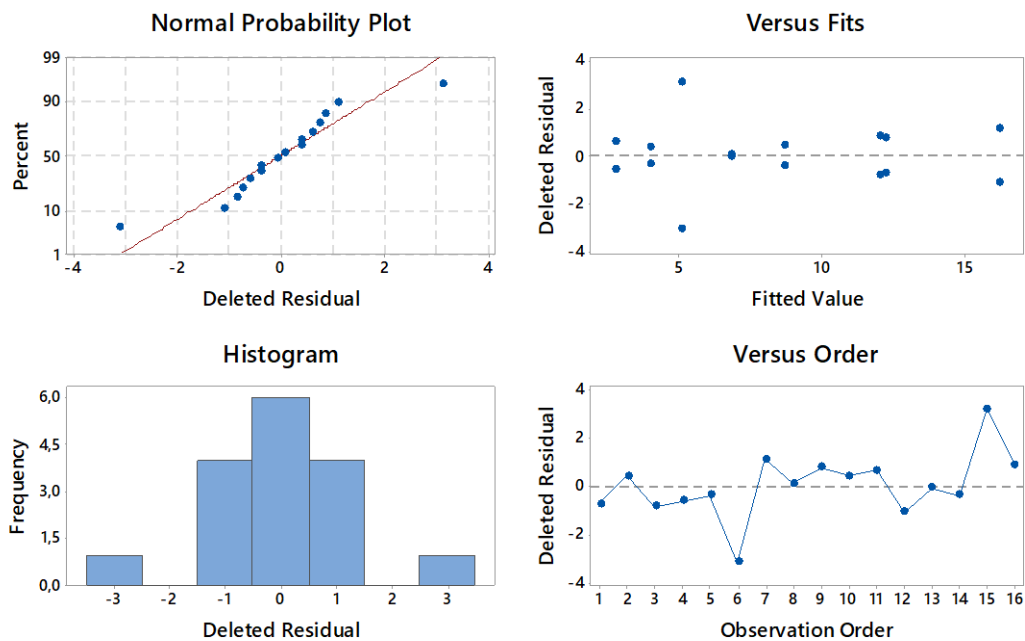


Figure 10-5. Residual plots for secondary phases

10.6.4. Specific surface area

Table 10-10. Analysis of Variance of SSA

Source	DF	Adj SS	Adj MS	F-Value	P-Value
Model	7	3272.78	467.54	7.93	0.005
Linear	5	2770.00	554.00	9.40	0.003
Ceramic loading (%)	1	202.45	202.45	3.43	0.101
Pressure of dispersion (kPa)	1	1057.02	1057.02	17.93	0.003
Feed flow rate (mL/min)	1	1463.43	1463.43	24.83	0.001
Mixture of solvents	1	15.98	15.98	0.27	0.617
Gas of dispersion	1	31.12	31.12	0.53	0.488
2-Way Interactions	2	502.78	251.39	4.26	0.055
Ceramic loading (%)*Pressure of dispersion (kPa)	1	249.24	249.24	4.23	0.074
Ceramic loading (%)*Mixture of solvents	1	253.54	253.54	4.30	0.072
Error	8	471.54	58.94		
Total	15	3744.33			

Table 10-11. Model Summary of SSA

S	R-sq	R-sq(adj)	R-sq(pred)
7.67743	87.41%	76.39%	49.63%

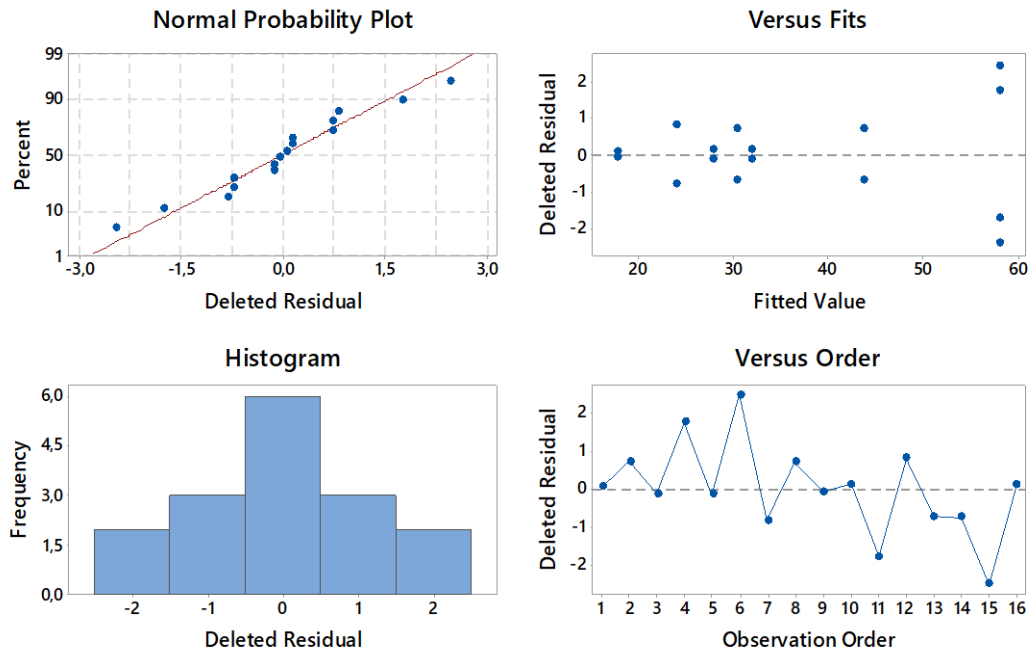


Figure 10-6. Residual plots for Specific surface area

10.6.5. P1 – Cumulative heat flow

Table 10-12. Analysis of Variance – P1 – Cumulative heat flow

Source	DF	Adj SS	Adj MS	F-Value	P-Value
Model	7	209.773	29.968	3.19	0.063
Linear	5	156.281	31.256	3.33	0.064
Ceramic loading (%)	1	28.864	28.864	3.08	0.117
Pressure of dispersion (kPa)	1	1.471	1.471	0.16	0.702
Feed flow rate (mL/min)	1	70.639	70.639	7.53	0.025
Mixture of solvents	1	25.185	25.185	2.68	0.140
Gas of dispersion	1	30.122	30.122	3.21	0.111
2-Way Interactions	2	53.492	26.746	2.85	0.116
Ceramic loading (%)*Pressure of dispersion (kPa)	1	47.623	47.623	5.08	0.054
Ceramic loading (%)*Mixture of solvents	1	5.869	5.869	0.63	0.452
Error	8	75.048	9.381		
Total	15	284.821			

Table 10-13. Model Summary - P1 – Cumulative heat flow

S	R-sq	R-sq(adj)	R-sq(pred)
3.06285	73.65%	50.60%	0.00%

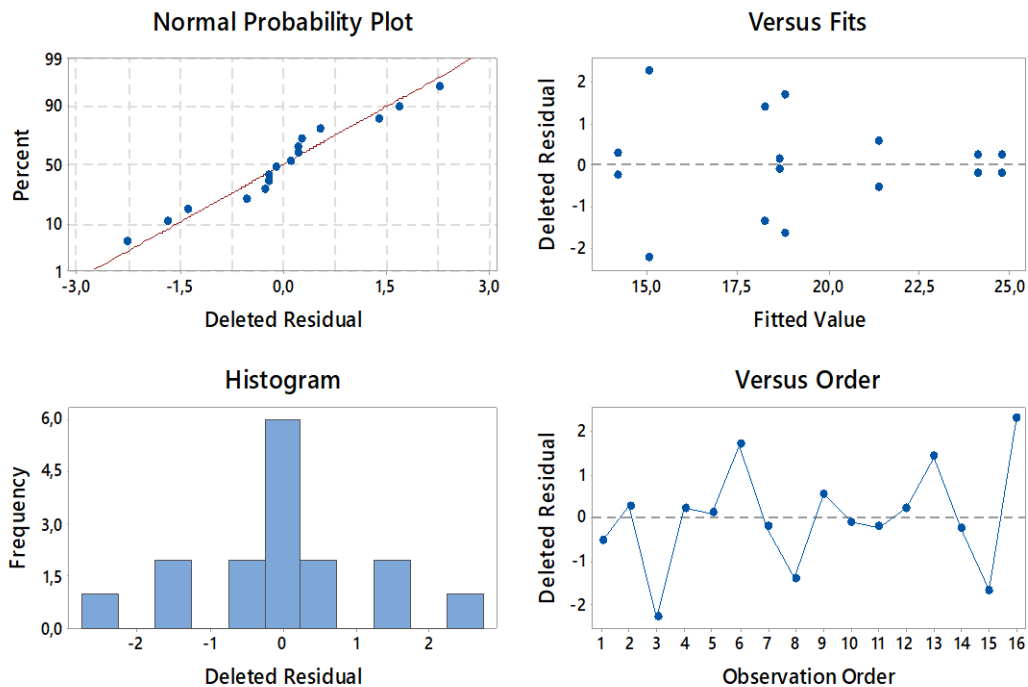


Figure 10-7. Residual plots for P1 – Cumulative heat flow

10.6.6. P2 – Cumulative heat flow

Table 10-14. Analysis of Variance – P2 – Cumulative heat flow

Source	DF	Adj SS	Adj MS	F-Value	P-Value
Model	7	3237.15	462.45	6.93	0.007
Linear	5	3114.11	622.82	9.33	0.003
Ceramic loading (%)	1	457.24	457.24	6.85	0.031
Pressure of dispersion (kPa)	1	708.76	708.76	10.62	0.012
Feed flow rate (mL/min)	1	1458.94	1458.94	21.86	0.002
Mixture of solvents	1	97.51	97.51	1.46	0.261
Gas of dispersion	1	391.65	391.65	5.87	0.042
2-Way Interactions	2	123.04	61.52	0.92	0.436
Ceramic loading (%)*Pressure of dispersion (kPa)	1	79.39	79.39	1.19	0.307
Ceramic loading (%)*Mixture of solvents	1	43.64	43.64	0.65	0.442
Error	8	533.80	66.73		
Total	15	3770.95			

Table 10-15. Model Summary – P2 – Cumulative heat flow

S	R-sq	R-sq(adj)	R-sq(pred)
8,16855	85,84%	73,46%	43,38%

Table 10-16. Fits and Diagnostics for Unusual Observations – P2 – Cumulative heat flow

Obs	- P2 – Cumulative heat flow	Fit	Resid	Std Resid	R
6	45.58	32.08	13.50	2.34	R
15	18.58	32.08	-13.50	-2.34	R

R Large residual

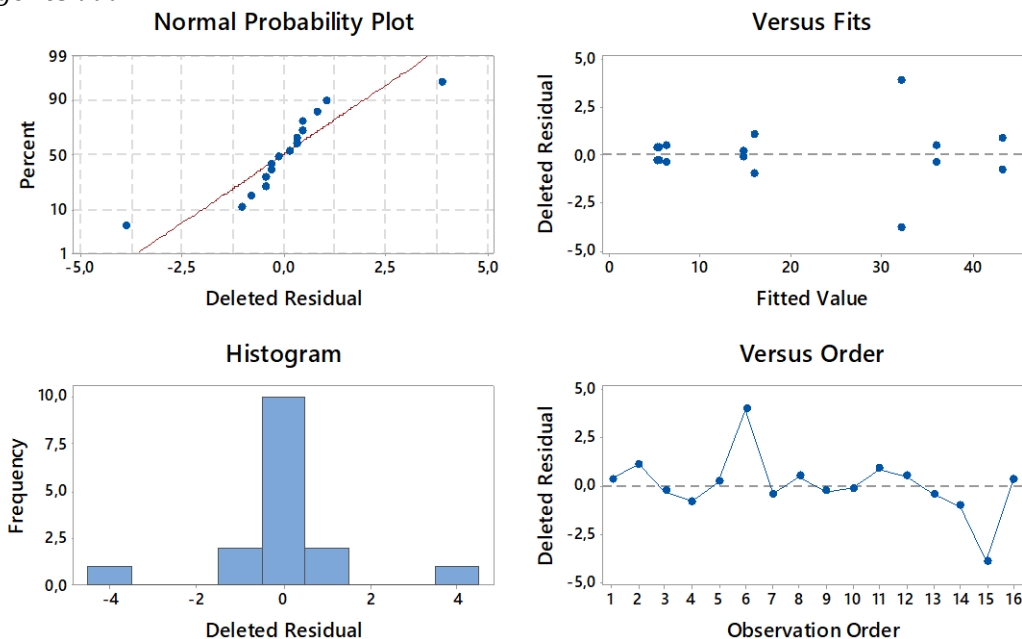


Figure 10-8. Residual plots for - P2 – Cumulative heat flow

10.6.7. P1 – Max height

Table 10-17. Analysis of Variance- P1 – Max height

Source	DF	Adj SS	Adj MS	F-Value	P-Value
Model	7	39819	5688.4	0.47	0.829
Linear	5	21352	4270.4	0.36	0.865
Ceramic loading (%)	1	8930	8929.7	0.74	0.413
Pressure of dispersion (kPa)	1	153	153.0	0.01	0.913
Feed flow rate (mL/min)	1	225	224.6	0.02	0.895
Mixture of solvents	1	162	162.1	0.01	0.910
Gas of dispersion	1	11883	11882.6	0.99	0.349
2-Way Interactions	2	18467	9233.3	0.77	0.495
Ceramic loading (%)*Pressure of dispersion (kPa)	1	11095	11095.0	0.93	0.364
Ceramic loading (%)*Mixture of solvents	1	7372	7371.6	0.61	0.456
Error	8	95933	11991.6		
Total	15	135752			

Table 10-18. Model Summary- P1 – Max height

S	R-sq	R-sq(adj)	R-sq(pred)
109.506	29.33%	0.00%	0.00%

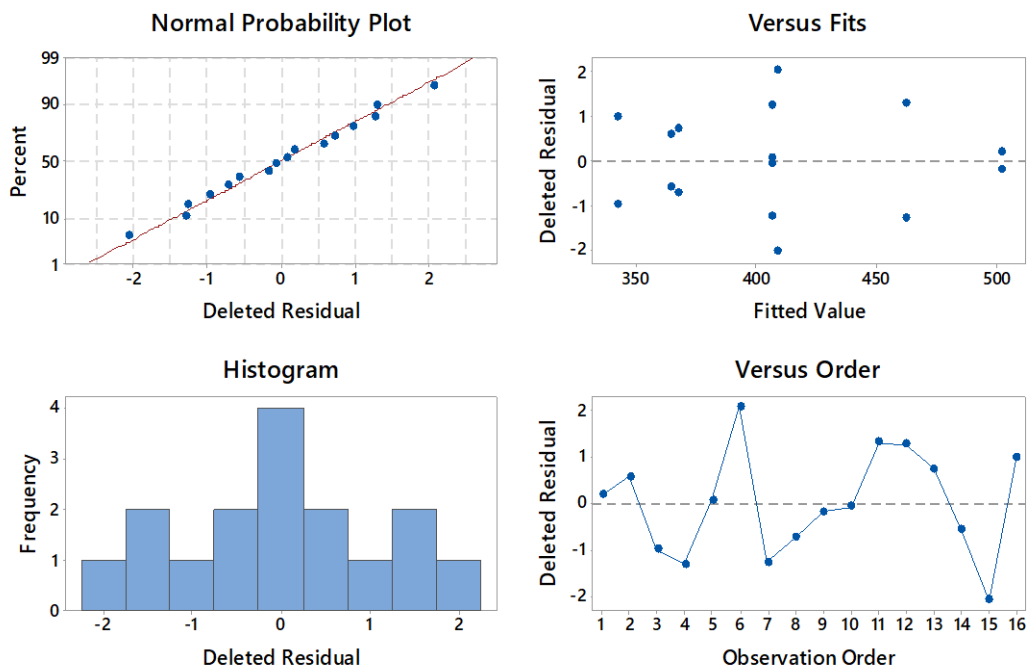


Figure 10-9. Residual plots for - P1 – Max height

10.6.8. P2 – Max height

Table 10-19. Analysis of Variance P2 – Max height

Source	DF	Adj SS	Adj MS	F-Value	P-Value
Model	7	57.4553	8.2079	3.15	0.065
Linear	5	55.4241	11.0848	4.25	0.035
Ceramic loading (%)	1	8.7713	8.7713	3.37	0.104
Pressure of dispersion (kPa)	1	6.3745	6.3745	2.45	0.156
Feed flow rate (mL/min)	1	32.0456	32.0456	12.30	0.008
Mixture of solvents	1	2.9687	2.9687	1.14	0.317
Gas of dispersion	1	5.2641	5.2641	2.02	0.193
2-Way Interactions	2	2.0312	1.0156	0.39	0.689
Ceramic loading (%)*Pressure of dispersion (kPa)	1	0.6643	0.6643	0.25	0.627
Ceramic loading (%)*Mixture of solvents	1	1.3669	1.3669	0.52	0.490
Error	8	20.8453	2.6057		
Total	15	78.3006			

Table 10-20. Model Summary – P2 – Max height

S	R-sq	R-sq(adj)	R-sq(pred)
1.61421	73.38%	50.08%	0.00%

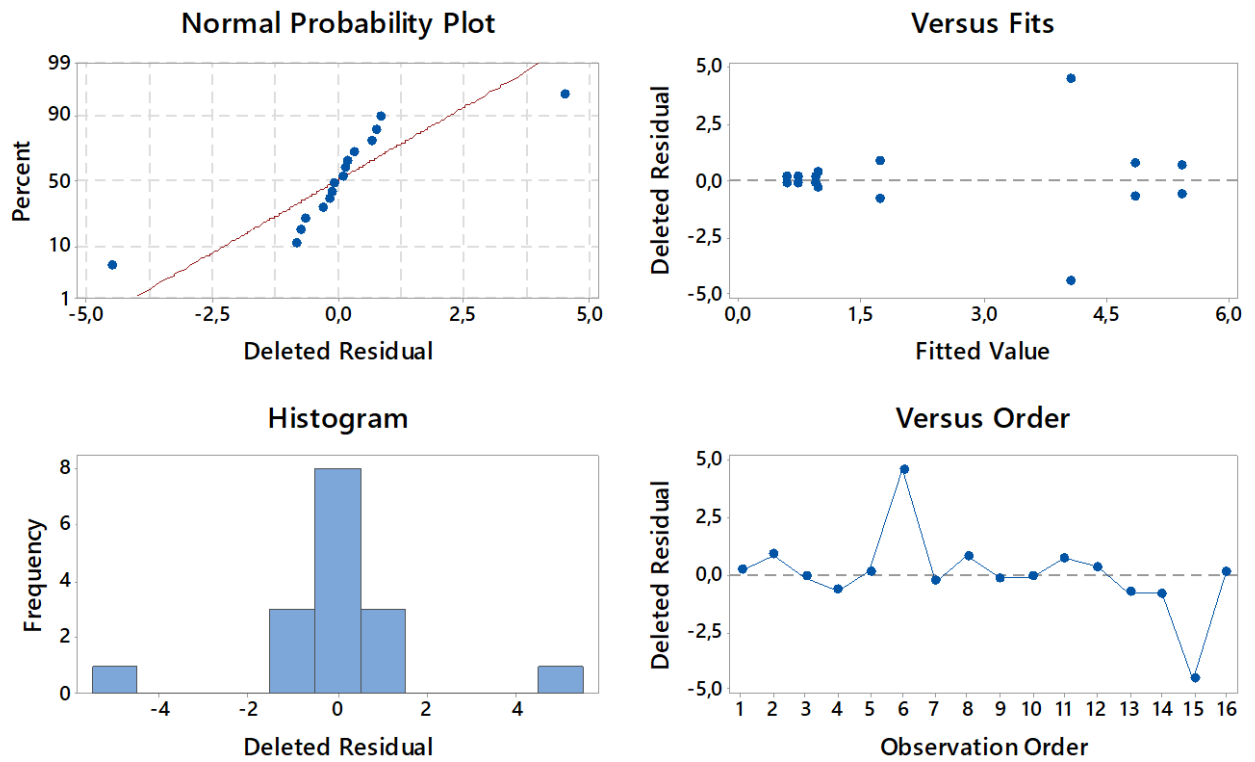


Figure 10-10. Residual plots for – P2 – Max height

REFERENCES

- [1] D. N. Huntzinger and T. D. Eatmon, "A life-cycle assessment of Portland cement manufacturing: comparing the traditional process with alternative technologies," *J. Clean. Prod.*, vol. 17, no. 7, pp. 668–675, 2009.
- [2] K. Begg, F. van der Woerd, and D. L. (David L. Levy, *The business of climate change : corporate responses to Kyoto.* .
- [3] "Cement Sustainability Initiative (CSI) - World business council for sustainable development." .
- [4] W. B. C. for S. D. (WBCSD), "Toward a sustainable cement industry," 2002.
- [5] A. Hasanbeigi, L. Price, and E. Lin, "Emerging energy-efficiency and CO2 emission-reduction technologies for cement and concrete production: A technical review," *Renew. Sustain. Energy Rev.*, vol. 16, no. 8, pp. 6220–6238, 2012.
- [6] G. Constantinides, "Nanoscience and nanoengineering of cement-based materials," *Nanotechnol. Eco-Efficient Constr.*, pp. 9-37a, 2013.
- [7] G. Voicu, C. D. Ghițulică, and E. Andronescu, "Modified Pechini synthesis of tricalcium aluminate powder," *Mater. Charact.*, vol. 73, pp. 89–95, Nov. 2012.
- [8] A. Wesselsky and O. M. Jensen, "Synthesis of pure Portland cement phases," *Cem. Concr. Res.*, vol. 39, no. 11, pp. 973–980, 2009.
- [9] D. M. Roy and S. O. Oyefesobi, "Preparation of Very Reactive Ca₂SiO₄ Powder," *J. Am. Ceram. Soc.*, vol. 60, no. 3–4, pp. 178–180, 1977.
- [10] D. Stephan and P. Wilhelm, "Synthesis of pure cementitious phases by sol-gel process as precursor," *Zeitschrift fur Anorg. und Allg. Chemie*, vol. 630, no. 10, pp. 1477–1483, 2004.
- [11] A. Meiszterics and K. Sinkó, "Sol-gel derived calcium silicate ceramics," *Colloids Surfaces A Physicochem. Eng. Asp.*, vol. 319, no. 1–3, pp. 143–148, 2008.
- [12] A. Meiszterics *et al.*, "Structural Characterization of Gel-Derived Calcium Silicate Systems," *J. Phys. Chem.*, vol. 114, pp. 10403–10411, 2010.
- [13] R. Chrysafi, T. Perraki, and G. Kakali, "Sol-gel preparation of 2CaO.SiO₂," *J. Eur. Ceram. Soc.*, vol. 27, no. 2–3, pp. 1707–1710, 2007.
- [14] I. Nettleship, J. L. Shull, and W. M. Kriven, "Chemical preparation and phase stability of Ca₂SiO₄ and Sr₂SiO₄ powders," *J. Eur. Ceram. Soc.*, vol. 11, no. 4, pp. 291–298, 1993.
- [15] S. H. Hong and J. F. Young, "Hydration kinetics and phase stability of dicalcium silicate synthesized by the Pechini process," *J. Am. Ceram. Soc.*, vol. 82, no. 7, pp. 1681–1686, 1999.
- [16] X.-H. Huang and J. Chang, "Low-temperature synthesis of nanocrystalline β-dicalcium silicate with high specific surface area," *J. Nanoparticle Res.*, vol. 9, pp. 1195–1200, 2007.
- [17] J. C. Restrepo, "Síntesis de silicatos cálcicos hidraulicamnete activos producidos a partir de métodos químicos de combustión," Universidad Nacional de Colombia, 2015.
- [18] N. Betancur, "Síntesis de pigmentos ceramicos a partir de cromitas de estructura tipo espinela por el método no convencional de pirólisis de aerosol con llama con alimentación líquida,"

Universidad Nacional de Colombia, 2014.

- [19] W. Y. Teoh, R. Amal, and L. Mädler, "Flame spray pyrolysis: An enabling technology for nanoparticles design and fabrication.," *Nanoscale*, vol. 2, no. 8, pp. 1324–1347, 2010.
- [20] S. C. Halim, T. J. Brunner, R. N. Grass, M. Bohner, and W. J. Stark, "Preparation of an ultra fast binding cement from calcium silicate-based mixed oxide nanoparticles.," *Nanotechnology*, vol. 18, no. 39, p. 395701, 2007.
- [21] L. Nicoleau, A. Nonat, and D. Perrey, "The di- and tricalcium silicate dissolutions," *Cem. Concr. Res.*, vol. 47, pp. 14–30, 2013.
- [22] Y. P. Arías Jaramillo, "Incidencia de la temperatura ambiente en la formación de compuestos cementantes mediante la activación alcalina de ceniza de carbón," Universidad Nacional de Colombia, 2013.
- [23] X. Li, X. Shen, M. Tang, and X. Li, "Stability of tricalcium silicate and other primary phases in portland cement clinker," *Ind. Eng. Chem. Res.*, vol. 53, no. 5, pp. 1954–1964, 2014.
- [24] H. F. W. Taylor, *Cement Chemistry*. 1997.
- [25] H.-M. Ludwig and W. Zhang, "Research review of cement clinker chemistry," *Cem. Concr. Res.*, vol. 78, pp. 24–37, 2015.
- [26] A. Bazzoni, S. Ma, Q. Wang, X. Shen, M. Cantoni, and K. L. Scrivener, "The effect of Magnesium and Zinc Ions on the Hydration kinetics of C3S," *J. Am. Ceram. Soc.*, vol. 97, no. 11, pp. 3684–3693, 2014.
- [27] M.-N. de Noirfontaine, F. Dunstetter, M. Courtial, G. Gasecki, and M. Signes-Frehel, "Polymorphism of tricalcium silicate, the major compound of Portland cement clinker," *Cem. Concr. Res.*, vol. 36, no. 1, pp. 54–64, 2006.
- [28] K. Urabe, T. Shirakami, and M. Iwashima, "Superstructure in a triclinic phase of tricalcium silicate," *J. Am. Ceram. Soc.*, vol. 83, no. 5, pp. 1253–1258, 2000.
- [29] F. Dunstetter, M. N. De Noirfontaine, and M. Courtial, "Polymorphism of tricalcium silicate, the major compound of Portland cement clinker: 1. Structural data: Review and unified analysis," *Cem. Concr. Res.*, vol. 36, no. 1, pp. 39–53, 2006.
- [30] Á. G. De la Torre, R. N. De Vera, a. J. M. Cuberos, and M. a G. Aranda, "Crystal structure of low magnesium-content alite: Application to Rietveld quantitative phase analysis," *Cem. Concr. Res.*, vol. 38, no. 11, pp. 1261–1269, 2008.
- [31] M. BIGARÉ *et al.*, "Polymorphism of Tricalcium Silicate and Its Solid Solutions," *J. Am. Ceram. Soc.*, vol. 50, no. 11, pp. 609–619, 1967.
- [32] V. K. Peterson, B. a Hunter, and A. Ray, "Tricalcium Silicate T1 and T2 Polymorphic Investigations: Rietveld Refinement at Various Temperatures Using Synchrotron Powder Diffraction," *J. Am. Ceram. Soc.*, vol. 87, no. 9, pp. 1625–1634, 2004.
- [33] M. D. L. Á. Gómez de la Torre, "Estudio de cementos y materiales relacionados por el método de Rietveld," Universidad de Málaga, 2003.
- [34] N. B. Singh, S. Rai, and N. Singh, "Highly Reactive B-Dicalcium Silicate," *J. Am. Ceram. Soc.*, vol. 85, no. 9, pp. 2171–2176, 2002.
- [35] N. A. Yamnova, N. V. Zubkova, N. N. Eremin, A. E. Zadov, and V. M. Gazeev, "Crystal structure of

larnite β -Ca₂SiO₄ and specific features of polymorphic transitions in dicalcium orthosilicate," *Crystallogr. Reports*, vol. 56, no. 2, pp. 210–220, 2011.

- [36] A. M. Cuesta-García, "Preparation and hydration of model ecocement phases. Characterization by diffraction and cognate methods," Universidad de Málaga, 2015.
- [37] C. Guozhong, *Nanostructures & Nanomaterials- Synthesis, Properties & Applications*, World Scie. University of Washington, USA: Imperial College Press, 2004.
- [38] J. C. Restrepo, A. A. Chavarriaga, O. J. Restrepo, J. I. Tobón, J. I. Tobon, and J. I. Tobón, "Synthesis of Hydraulically Active Calcium Silicates Produced by Combustion Methods," *MRS Proc.*, vol. 1768, pp. imrc2014-6d – 008, Mar. 2015.
- [39] P. Deb, "Kinetics of Heterogeneous Solid State Processes," in *Kinetics of Heterogeneous Solid State Processes*, Springer, 2014, pp. 13–18.
- [40] N.-V. Buchete, "Santosh K. Upadhyay. Chemical Kinetics and Reaction Dynamics.," *J. Stat. Phys.*, vol. 129, no. 2, pp. 407–408, 2007.
- [41] J. Calbo, "Desarrollo de ecopigmentos negros de espinela dopada alternativos a los ferritos tradicionales mediante presión y procesados sol-gel," Universitat Jaume I de Castelló, 2003.
- [42] C. H. Bamford and C. F. H. Tipper, "Reactions in the Solid State - Google Books," in *Comprehensive chemical kinetics*, Elsevier, 1980, p. 339.
- [43] J. H. Welch and W. Gutt, "Tricalcium Silicate and Its Stability Within the System CaO-SiO₂," *J. Am. Ceram. Soc.*, vol. 41, no. 1, pp. 11–15, 1959.
- [44] E. T. Carlson, "the Decomposition of Tricalcium Silicate," *Bur. Stand. J. Res.*, vol. 33, no. 8, pp. 78–79, 1930.
- [45] B. Phillips and A. Muan, "Phase Equilibria in the System CaO-Iron Oxide-SiO₂, in Air," *J. Am. Ceram. Soc.*, vol. 42, no. 9, pp. 413–423, 1959.
- [46] W. C. Hasen, "Further studies on portland cement compounds by the X-Ray diffraction method," *Bur. Stand. J. Res.*, vol. 1, no. 12, 1928.
- [47] F. A. Rodrigues, "Synthesis of chemically and structurally modified dicalcium silicate," *Cem. Concr. Res.*, vol. 33, no. 6, pp. 823–827, 2003.
- [48] L. QUÉMÉNEUR, J. CHOISNET, B. RAVEAU, J. M. THIEBAUT, and G. ROUSSY, "Microwave Clinkering with a Grooved Resonant Applicator," *J. Am. Ceram. Soc.*, vol. 66, no. 12, pp. 855–859, 1983.
- [49] H. Li, D. K. Agrawal, J. Cheng, and M. R. Silsbee, "Microwave sintering of sulphoaluminate cement with utility wastes," *Cem. Concr. Res.*, vol. 31, no. 9, pp. 1257–1261, 2001.
- [50] H. Li, D. K. Agrawal, J. Cheng, and M. R. Silsbee, "Formation and hydration of C3S prepared by microwave and conventional sintering," *Cem. Concr. Res.*, vol. 29, no. 8, pp. 1611–1617, 1999.
- [51] S. Long, C. Yan, and J. Dong, "Microwave-promoted burning of Portland cement clinker," *Cem. Concr. Res.*, vol. 32, no. 1, pp. 17–21, 2002.
- [52] L. Kacimi, a. Simon-Masseron, a. Ghomari, and Z. Derriche, "Reduction of clinkerization temperature by using phosphogypsum," *J. Hazard. Mater.*, vol. 137, no. 1, pp. 129–137, 2006.
- [53] D. a. Fumo, M. R. Morelli, and A. M. Segadães, "Combustion synthesis of calcium aluminates," *Mater. Res. Bull.*, vol. 31, no. 10, pp. 1243–1255, 1996.

- [54] L. L. Hench and J. K. West, "The sol-gel process," *Chem. Rev.*, vol. 90, no. 1, pp. 33–72, 1990.
- [55] G. Laudisio and F. Branda, "Sol-gel synthesis and crystallisation of $3\text{CaO}\cdot 2\text{SiO}_2$ glassy powders," *Thermochim. Acta*, vol. 370, no. 1–2, pp. 119–124, 2001.
- [56] Z. Gou and J. Chang, "Synthesis and in vitro bioactivity of dicalcium silicate powders," *J. Eur. Ceram. Soc.*, vol. 24, no. 1, pp. 93–99, 2004.
- [57] Z. Gou, J. Chang, and W. Zhai, "Preparation and characterization of novel bioactive dicalcium silicate ceramics," *J. Eur. Ceram. Soc.*, vol. 25, no. 9, pp. 1507–1514, 2005.
- [58] W. Zhao and J. Chang, "Sol-gel synthesis and in vitro bioactivity of tricalcium silicate powders," *Mater. Lett.*, vol. 58, no. 19, pp. 2350–2353, 2004.
- [59] W. Zhao, J. Wang, W. Zhai, Z. Wang, and J. Chang, "The self-setting properties and in vitro bioactivity of tricalcium silicate," *Biomaterials*, vol. 26, no. 31, pp. 6113–6121, 2005.
- [60] C.-C. Chen, C.-C. Ho, S.-Y. Lin, and S.-J. Ding, "Green synthesis of calcium silicate bioceramic powders," *Ceram. Int.*, vol. 41, no. 4, pp. 5445–5453, 2015.
- [61] M. P. Pechini, "Method of preparing lead and alkaline earth titanates and niobates and coating method using the same to form a capacitor," 1967.
- [62] A. Gaki, R. Chrysafi, and G. Kakali, "Chemical synthesis of hydraulic calcium aluminate compounds using the Pechini technique," *J. Eur. Ceram. Soc.*, vol. 27, no. 2–3, pp. 1781–1784, Jan. 2007.
- [63] A. C. Tas, "Chemical Preparation of the Binary Compounds in the Calcia–Alumina System by Self-Propagating Combustion Synthesis," *J. Am. Ceram. Soc.*, vol. 81, no. 11, pp. 2853–2863, 1998.
- [64] A. G. Merzhanov and I. P. Borovinskaya, "Self-propagated high-temperature synthesis of refractory inorganic compounds." 1972.
- [65] J. C. Restrepo, A. Chavarriaga, O. J. Restrepo, and J. I. Tobón, "Synthesis of Hydraulically Active Calcium Silicates Produced by Combustion Methods," *MRS Proc.*, vol. 1768, pp. imrc2014-6d – 008, Mar. 2015.
- [66] H. Ishida, K. Mabuchi, and K. Sasaki, "Low-Temperature Synthesis," no. 1, 1992.
- [67] M. Georgescu, J. Tipan, A. Badanoiu, D. Crisan, and I. Dragan, "Highly reactive dicalcium silicate synthesized by hydrothermal processing," *Cem. Concr. Compos.*, vol. 22, no. 5, pp. 315–319, 2000.
- [68] L. Kacimi, M. Cyr, and P. Clastres, "Synthesis of alfa-C2S cement from fly-ash using the hydrothermal method at low temperature and atmospheric pressure," *J. Hazard. Mater.*, vol. 181, no. 1–3, pp. 593–601, 2010.
- [69] S. C. Halim, W. J. Stark, and E. T. H. Zurich, "In - Situ Preparation of Nano - Portland Cement Via Flame Spray Pyrolysis : Processing , Characterization and Mechanical Properties," *TMS 2006*, vol. 1356, no. 2002, p. 5184, 2006.
- [70] R. Strobel, A. Alfons, and S. E. Pratsinis, "Aerosol flame synthesis of catalysts," *Adv. Powder Technol.*, vol. 17, no. 5, pp. 457–480, 2006.
- [71] X. Qin, Y. Ju, S. Bernhard, and N. Yao, "Europium-doped yttrium silicate nanophosphors prepared by flame synthesis," *Mater. Res. Bull.*, vol. 42, no. 8, pp. 1440–1449, 2007.
- [72] A. J. Gröhn, S. E. Pratsinis, and K. Wegner, "Fluid-particle dynamics during combustion spray aerosol synthesis of ZrO_2 ," *Chem. Eng. J.*, vol. 191, pp. 491–502, 2012.

- [73] T. J. Brunner, R. N. Grass, and W. J. Stark, "Glass and bioglass nanopowders by flame synthesis," *Chem. Commun. (Camb)*, pp. 1384–1386, 2006.
- [74] T. J. Brunner, R. N. Grass, M. Bohner, and W. J. Stark, "Effect of particle size, crystal phase and crystallinity on the reactivity of tricalcium phosphate cements for bone reconstruction," *J. Mater. Chem.*, vol. 17, no. 38, p. 4072, 2007.
- [75] M. Bohner, T. J. Brunner, and W. J. Stark, "Controlling the Reactivity of Calcium Phosphate Cements," *Key Eng. Mater.*, vol. 361–363, no. iii, pp. 295–298, 2008.
- [76] H. Zhong *et al.*, "Mechanical properties and bioactivity of β -Ca₂SiO₄ ceramics synthesized by spark plasma sintering," *Ceram. Int.*, vol. 37, no. 7, pp. 2459–2465, 2011.
- [77] S. Nath, R. Tu, and T. Goto, "Apatite formation in Hanks' solution on β -Ca₂SiO₄ films prepared by MOCVD," *Surf. Coatings Technol.*, vol. 206, no. 1, pp. 172–177, 2011.
- [78] N. Betancur-Granados, J. I. Tobón, and O. J. Restrepo-Baena, "Alternative Production Processes of Calcium Silicate Phases of Portland Cement : A Review," *Civ. Eng. Res. J.*, vol. 5, no. 3, pp. 1–6, 2018.
- [79] O. J. Restrepo Baena and E. R. Baena Murillo, "Synthesis of spinels by thermal spray flame," *TMS Annu. Meet.*, 2010.
- [80] L. Mädler, "Liquid-fed Aerosol Reactors for One-step Synthesis of Nano-structured Particles †," *Kona*, vol. 22, no. 22, pp. 107–120, 2004.
- [81] H. Chang, J.-H. Park, and H. D. Jang, "Flame synthesis of silica nanoparticles by adopting two-fluid nozzle spray," *Colloids Surfaces A Physicochem. Eng. Asp.*, vol. 313–314, pp. 140–144, Feb. 2008.
- [82] T. Sahn, L. Mädler, A. Gurlo, N. Barsan, S. E. Pratsinis, and U. Weimar, "Flame spray synthesis of tin dioxide nanoparticles for gas sensing," *Sensors Actuators B Chem.*, vol. 98, no. 2–3, pp. 148–153, Mar. 2004.
- [83] S. E. Pratsinis, "Flame synthesis of nanosize particles: Precise control of particle size," *J. Aerosol Sci.*, vol. 27, no. 96, pp. S153–S154, Sep. 1996.
- [84] V. S. Buddhiraju and V. Runkana, "Simulation of nanoparticle synthesis in an aerosol flame reactor using a coupled flame dynamics–monodisperse population balance model," *J. Aerosol Sci.*, vol. 43, no. 1, pp. 1–13, Jan. 2012.
- [85] S. Lee, K. Schneider, J. Schumann, A. K. Mogalicherla, P. Pfeifer, and R. Dittmeyer, "Effect of metal precursor on Cu/ZnO/Al₂O₃ synthesized by flame spray pyrolysis for direct DME production," *Chem. Eng. Sci.*, vol. 138, pp. 194–202, 2015.
- [86] N. Betancur-Granados and O. J. Restrepo-Baena, "Flame spray pyrolysis synthesis of ceramic nanopigments CoCr₂O₄: The effect of key variables," *J. Eur. Ceram. Soc.*, 2017.
- [87] M. Kim, S. Lai, and R. M. Laine, "Combinatorial Nanopowder Synthesis Along the ZnO-Al₂O₃ Tie Line Using Liquid-Feed Flame Spray Pyrolysis," *J. Am. Ceram. Soc.*, vol. 94, no. 10, pp. 3308–3318, Oct. 2011.
- [88] A. K. Rai, K. . Mandal, D. Kumar, and O. Parkash, "Characterization of nickel doped CCTO: CaCu_{2.9}Ni_{0.1}Ti₄O₁₂ and CaCu₃Ti_{3.9}Ni_{0.1}O₁₂ synthesized by semi-wet route," *J. Alloys Compd.*, vol. 491, no. 1–2, pp. 507–512, Feb. 2010.
- [89] R. M. Laine, C. R. Bickmore, D. R. Treadwell, and F. Waldner, "Ultrafine metal oxide powders by

Flame Spray Pyrolysis," 5958361, 1999.

- [90] R. M. Laine, S. C. Rand, T. Hinklin, and G. Williams, "Ultrafine powders and their use as lasing media," 6656588 B1, 2003.
- [91] A. C. Sutorik, R. M. Laine, J. Marchal, T. Johns, and T. Hinklin, "Mixed-metal oxide particles by Liquid Feed Flame Spray Pyrolysis of oxide precursors in oxygenated solvents," 7220398, 2007.
- [92] M. Sokolowski, A. Sokolowska, A. Michalski, and B. Gokieli, "The 'In-flame-reaction' method for Al₂O₃ aerosol formation," *J. Aerosol Sci.*, vol. 8, no. 1946, 1977.
- [93] R. Strobel, A. Baiker, and S. E. Pratsinis, "Aerosol flame synthesis of catalysts," *Adv. Powder Technol.*, vol. 17, no. 5, pp. 457–480, Aug. 2006.
- [94] W. Teoh, "A Perspective on the Flame Spray Synthesis of Photocatalyst Nanoparticles," *Materials (Basel)*, vol. 6, no. 8, pp. 3194–3212, Jul. 2013.
- [95] T. Hinklin *et al.*, "Liquid-Feed Flame Spray Pyrolysis of Metalloorganic and Inorganic Alumina Sources in the Production of Nanoalumina Powders," *Chem. Mater.*, vol. 16, no. 12, pp. 21–30, 2004.
- [96] J. Azurdia *et al.*, "Liquid-Feed Flame Spray Pyrolysis as a Method of Producing Mixed-Metal Oxide Nanopowders of Potential Interest as Catalytic Materials . Nanopowders along the NiO-Al₂O₃ Tie Line Including," *Chem. Mater.*, no. 6, pp. 731–739, 2006.
- [97] H. Vera Diaz, "Fabricación de películas delgadas de ZnS por la técnica MOCVD," Instituto Politécnico Nacional de México, 2010.
- [98] P. Molina, P. Barbeito, and G. Alabart, "Preparación de precursores metalorgánico anhidridos y su uso para la deposición y crecimiento de capas y cintas superconductoras," 2259919, 2006.
- [99] S. Li, Y. Ren, P. Biswas, and S. D. Tse, "Flame aerosol synthesis of nanostructured materials and functional devices: Processing, modeling, and diagnostics," *Prog. Energy Combust. Sci.*, vol. 55, pp. 1–59, 2016.
- [100] M. S. Wooldridge, "GAS-PHASE COMBUSTION SYNTHESIS," *Prog. Energy Combust. Sci.*, vol. 24, pp. 63–87, 1998.
- [101] S. E. Pratsinis, "Flame aerosol synthesis of ceramic powders," *Prog. Energy Combust. Sci.*, vol. 24, no. 3, pp. 197–219, 1998.
- [102] R. Jossen, S. E. Pratsinis, W. J. Stark, and L. Mädler, "Criteria for flame-spray synthesis of hollow, shell-like, or inhomogeneous oxides," *J. Am. Ceram. Soc.*, vol. 88, no. 6, pp. 1388–1393, 2005.
- [103] R. M. Trommer and C. P. Bergmann, *Flame Spray Technology - Method for production of nanoparticles*. Springer, 2015.
- [104] A. Lefebvre and V. McDonell, *Atomization and Sprays, Second Edition*. 2017.
- [105] A. H. Lefebvre, "Airblast atomization," *Prog. Energy Combust. Sci.*, vol. 6, pp. 233–261, 1980.
- [106] J. Tikkanen *et al.*, "Characteristics of the liquid flame spray process," *Surf. Coat. Technol.*, vol. 90, pp. 210–216, 1997.
- [107] M. C. Heine, L. Mädler, R. Jossen, and S. E. Pratsinis, "Direct measurement of entrainment during nanoparticle synthesis in spray flames," *Combust. Flame*, vol. 144, no. 4, pp. 809–820, Mar. 2006.
- [108] A. J. Gröhn, S. E. Pratsinis, and K. Wegner, "Scale-up for Nanoparticle Synthesis by Flame Spray

- Pyrolysis: The High Temperature Particle Residence Time," *Ind. Eng. Chem. Res.*, vol. 53, pp. 10734–10742, 2014.
- [109] O. Waser, A. J. Groehn, M. L. Eggersdorfer, and S. E. Pratsinis, "Air Entrainment During Flame Aerosol Synthesis of Nanoparticles," *Aerosol Sci. Technol.*, vol. 48, no. 11, pp. 1195–1206, 2014.
- [110] F. Migliorini, S. De Iuliis, F. Cignoli, and G. Zizak, "How 'flat' is the rich premixed flame produced by your McKenna burner?," *Combust. Flame*, vol. 153, no. 3, pp. 384–393, 2008.
- [111] T. Rudin, K. Wegner, and S. E. Pratsinis, "Uniform nanoparticles by flame-assisted spray pyrolysis (FASP) of low cost precursors," *J. Nanoparticle Res.*, vol. 13, no. 7, pp. 2715–2725, 2011.
- [112] N. Betancur-Granados, J. C. Restrepo, J. I. Tobón, and O. J. Restrepo-Baena, "Dicalcium silicate (2CaO·SiO₂) synthesized through flame spray pyrolysis and solution combustion synthesis methods (CB-6:IL10)," *Ceram. Int.*, vol. 45, no. July, pp. 9589–9595, 2019.
- [113] T. Tani, L. Madler, and S. E. Pratsinis, "Homogeneous ZnO nanoparticles by flame spray pyrolysis," *J. nan.*, pp. 337–343, 2002.
- [114] "Oxyfuel Cutting - Process and Fuel Gases - TWI." [Online]. Available: <https://www.twi-global.com/technical-knowledge/job-knowledge/oxyfuel-cutting-process-and-fuel-gases-049>. [Accessed: 20-Jan-2020].
- [115] L. L. Campbell, *Oxy-acetylene Welding Manual*, Primera ed. London, 1919.
- [116] A. C. (Arthur C. Davies, *The science and practice of welding.*, Cambridge University Press, 1972.
- [117] F. Vargas, "Élaboration De Couches CéRamiques ÉPaisées à Structures MicroméTriques Et NanoméTriques Par Projections Thermiques Pour Des Applications Tribologiques," 2010.
- [118] W. Encyclopedia, "Encyclopedia | Upgrade your welding supplies knowledge -Oxyacetylene flame." [Online]. Available: https://www.weldcor.ca/encyclopedia.html?alpha=O&per_page=2.
- [119] D.-I. B. Rumpf, *Thermochemical data of pure substances*, vol. 55, no. 4. 1997.
- [120] "NIST-JANAF Thermochemical Tables."
- [121] D. Patiño, B. Crespo, J. Porteiro, E. Villaravid, and E. Granada, "Experimental study of a tubular-type ESP for small-scale biomass boilers: Preliminary results in a diesel engine," *Powder Technol.*, vol. 288, no. November 2015, pp. 164–175, 2016.
- [122] C. R. Bickmore, K. F. Waldner, D. R. Treadwell, and R. M. Laine, "Ultrafine Spinel Powders by flame Spray Pyrolysis of a Magnesium Aluminum Double Alkoxide." 1996.
- [123] C. R. Bickmore, K. F. Waldner, D. R. Treadwen, and R. M. Láine, "Ultrafine Spinel Powders by Flame Spray Pyrolysis of a Magnesium Aluminium Double Alkoxide," *J. Am. Ceram. Soc.*, vol. 3, no. 2, pp. 1419–1423, 1996.
- [124] R. Mueller, L. Mädler, and S. E. Pratsinis, "Nanoparticle synthesis at high production rates by flame spray pyrolysis," *Chem. Eng. Sci.*, vol. 58, no. 10, pp. 1969–1976, May 2003.
- [125] M. Olivas-Martinez, H. Y. Sohn, H. D. Jang, and K.-I. Rhee, "Computational fluid dynamic modeling of the flame spray pyrolysis for silica nanopowder synthesis," *J. Nanopart Res*, vol. 17, no. 324, 2015.
- [126] A. J. Gröhn, M. L. Eggersdorfer, S. E. Pratsinis, and K. Wegner, "On-line monitoring of primary and agglomerate particle dynamics," *J. Aerosol Sci.*, vol. 73, pp. 1–13, 2014.

- [127] E. Lovell, J. Scott, and R. Amal, "Ni-SiO₂ Catalysts for the Carbon Dioxide Reforming of Methane: Varying Support Properties by Flame Spray Pyrolysis," *Molecules*, vol. 20, no. 3, pp. 4594–4609, 2015.
- [128] H. Schulz, L. Mädler, S. E. Pratsinis, P. Burtscher, and N. Moszner, "Transparent nanocomposites of radiopaque, flame-made Ta₂O₅/SiO₂ particles in an acrylic matrix," *Adv. Funct. Mater.*, vol. 15, no. 5, pp. 830–837, 2005.
- [129] G. Chiarello, I. Rossetti, and L. Forni, "Flame-spray pyrolysis preparation of perovskites for methane catalytic combustion," *J. Catal.*, vol. 236, no. 2, pp. 251–261, Dec. 2005.
- [130] A. I. Tok, F. Y. Boey, S. Du, and B. Wong, "Flame spray synthesis of ZrO₂ nano-particles using liquid precursors," *Mater. Sci. Eng. B*, vol. 130, no. 1–3, pp. 114–119, Jun. 2006.
- [131] M. Aromaa, H. Keskinen, and J. Mäkelä, "The effect of process parameters on the Liquid Flame Spray generated titania nanoparticles," *Biomol. Eng.*, vol. 24, no. 5, pp. 543–8, Nov. 2007.
- [132] N. Ashgriz, *Handbook of Atomization and Sprays*. Springer Netherlands, 2011.
- [133] A. Camenzind, W. R. Caseri, and S. E. Pratsinis, "Flame-made nanoparticles for nanocomposites," *Nano Today*, vol. 5, no. 1, pp. 48–65, 2010.
- [134] S. Processing and O. F. Liquid, "J. Karthikeyan, C.C. Berndt, J. Tikkanen, J.Y. Wang, A.H. King and H. Herman Department of Materials Science & Engineering, SUNY Stony Brook, Stony Brook, NY," *Science (80-.)*, vol. 9, pp. 137–140, 1997.
- [135] W. A. Sirignano, *Fluid dynamics and transport of droplets and sprays*, Second edi. Cambridge University Press, 2010.
- [136] L. Mädler, H. K. Kammler, R. Mueller, and S. E. Pratsinis, "Controlled synthesis of nanostructured particles by Flame spray pyrolysis," *J. Aerosol Sci.*, vol. 33, pp. 369–389, 2002.
- [137] P. Roth, "Particle Synthesis in Flames Keywords," pp. 1–43, 2006.
- [138] G. D. Ulrich, "Theory of Particle Formation and Growth in Oxide Synthesis Flames Theory of Particle Formation and Growth in Oxide Synthesis Flames," *Combust. Sci. Technol.*, vol. 4, no. 1, pp. 47–57, 1971.
- [139] A. Gutsch, H. Mühlenweg, and M. Krämer, "Tailor-made nanoparticles via gas-phase synthesis," *Small*, vol. 1, no. 1, pp. 30–46, 2005.
- [140] W. Koch and S. K. Friedlander, "The effect of particle coalescence on the surface area of a coagulating aerosol," *J. Colloid Interface Sci.*, vol. 140, no. 2, pp. 419–427, 1990.
- [141] F. E. Kruis, K. a. Kusters, S. E. Pratsinis, and B. Scarlett, "A Simple Model for the Evolution of the Characteristics of Aggregate Particles Undergoing Coagulation and Sintering," *Aerosol Sci. Technol.*, vol. 19, no. 4, pp. 514–526, 1993.
- [142] R. Gopalakrishnan and C. J. Hogan, "Determination of the transition regime collision kernel from mean first passage times," *Aerosol Sci. Technol.*, vol. 45, no. 12, pp. 1499–1509, 2011.
- [143] S. Nukiyama and Y. Tanasawa, "Experiments on the atomization of liquids in an air stream," 1950.
- [144] Victor ®, "Cutting, Heating and Welding Guide. Set-Up and Safe Operating Procedures OXY-FUEL EQUIPMENT." 2009.
- [145] "Design of electrostatic precipitator." .

- [146] K. R. Parker, *Applied electrostatic precipitation*. 1997.
- [147] S. B. Desu, "Decomposition Chemistry of Tetraethoxysilane," *J. Am. Ceram. Soc.*, vol. 72, no. 9, pp. 1615–1621, 1989.
- [148] D. Nurkowski, P. Buerger, J. Akroyd, M. Kraft, and P. Street, "A detailed kinetic study of the thermal decomposition of tetraethoxysilane," *Proc. Combust. Inst.*, vol. 35, no. 137, pp. 2291–2298, 2013.
- [149] J. Spitzmüller, J. Braun, H. Rauscher, and R. J. Behm, "Thermal decomposition of tetraethoxysilane (TEOS) on Si(111)-(7×7)," *Appl. Phys. A Mater. Sci. Process.*, vol. 66, no. SUPPL. 1, pp. 1021–1024, 1998.
- [150] A. Elements', "Calcium 2-Ethylhexanoate." .
- [151] S. L. Niu, K. H. Han, and C. M. Lu, "Kinetic calculations for the thermal decomposition of calcium propionate under non-isothermal conditions," *Chinese Sci. Bull.*, vol. 56, no. 12, pp. 1278–1284, 2011.
- [152] R. A. Hites and K. Biemann, "On the Mechanism of Ketonic Decarboxylation. Pyrolysis of Calcium Decanoate," *J. Am. Chem. Soc.*, vol. 94, no. 16, pp. 5772–5777, 1972.
- [153] P. A. Barnes, G. Stephenson, and S. B. Warrington, "The use of TA - GLC - MS as a quantitative specific EGA technique for the investigation of complex thermal decomposition reactions: The thermal decomposition of calcium propanoate," *J. Therm. Anal.*, vol. 25, no. 2, pp. 299–311, 1982.
- [154] C. T. Moynihan, "A low temperature fused salt experiment: The conductivity, viscosity, and density of molten calcium nitrate tetrahydrate," *J. Chem. Educ.*, vol. 44, no. 9, p. 531, 1967.
- [155] W. Brockner, C. Ehrhardt, and M. Gjikaj, "Thermal decomposition of nickel nitrate hexahydrate , $Ni(NO_3)_2 \cdot 6H_2O$, in comparison to $Co(NO_3)_2 \cdot 6H_2O$ and $Ca(NO_3)_2 \cdot 4H_2O$," vol. 456, no. 3, pp. 64–68, 2007.
- [156] A. M. C. Dumitriu, M. Cazacu, A. Bargan, S. Shova, and C. Turta, "Cu(II) and Ni(II) complexes with a tri-, tetra- or hexadentate triethanolamine ligand: Structural characterization and properties," *Polyhedron*, vol. 50, no. 1, pp. 255–263, 2013.
- [157] K. Garbev, B. Gasharova, G. Beuchle, S. Kreis, and P. Stemmermann, "First Observation of α - $Ca_2[Si_3O_7](OH)[Si_2O_7][Si_2O_7](OH)_2$ Phase Transformation upon Thermal Treatment in Air," *J. Am. Ceram. Soc.*, vol. 91, no. 1, pp. 263–271, 2007.
- [158] K. Garbev, G. Beuchle, U. Schweike, D. Merz, O. Dregert, and P. Stemmermann, "Preparation of a novel cementitious material from hydrothermally synthesized C-S-H phases," *J. Am. Ceram. Soc.*, vol. 97, no. 7, pp. 2298–2307, 2014.
- [159] K. Garbev, B. Gasharova, and P. Stemmermann, "A modular concept of crystal structure applied to the thermal transformation of $Ca_2[Si_3O_7](OH)[Si_2O_7](OH)_2$," *J. Am. Ceram. Soc.*, vol. 97, no. 7, pp. 2286–2297, 2014.
- [160] K. Wegner, B. B. Schimmoeller, B. B. Thiebaut, C. Fernandez, and T. N. Rao, "Pilot plants for industrial nanoparticle production by flame spray pyrolysis," *Kona Powder Part. J.*, vol. 29, no. 29, pp. 251–265, 2011.
- [161] A. G. De La Torre, S. Bruque, and M. A. G. Aranda, "Rietveld quantitative amorphous content analysis," *J. Appl. Crystallogr.*, vol. 34, no. 2, pp. 196–202, 2001.
- [162] D. Londono-Zuluaga, J. I. Tobón, M. A. G. Aranda, I. Santacruz, and A. G. De la Torre, "Clinkering and hydration of belite-alite-ye'elimit cement," *Cem. Concr. Compos.*, vol. 80, pp. 333–341, 2017.

- [163] L. Fernández-Carrasco, D. Torrens-Martín, L.M. Morales, and Sagrario Martínez-Ramírez, "Infrared spectroscopy in the analysis of building and construction materials," *Infrared Spectrosc. - Mater. Sci. Eng. 370 Technol. Technol.*, pp. 369–382, 2012.
- [164] F. Matossi, "Vibration frequencies and binding forces in some silicate groups," *J. Chem. Phys.*, vol. 17, no. 8, pp. 679–685, 1949.
- [165] M. J. Varas, M. A. De Buergo, and R. Fort, "Natural cement as the precursor of Portland cement: Methodology for its identification," *Cem. Concr. Res.*, vol. 35, no. 11, pp. 2055–2065, 2005.
- [166] C. Shi, a. F. Jiménez, and A. Palomo, "New cements for the 21st century: The pursuit of an alternative to Portland cement," *Cem. Concr. Res.*, vol. 41, no. 7, pp. 750–763, Jul. 2011.
- [167] W. Booncharoen, A. Jaroenworoluck, and R. Stevens, "A synthesis route to nanoparticle dicalcium silicate for biomaterials research," *J. Biomed. Mater. Res. - Part B Appl. Biomater.*, vol. 99 B, no. 2, pp. 230–238, 2011.
- [168] A. Fernández-Jiménez and F. Puertas, "Effect of activator mix on the hydration and strength behaviour of alkali-activated slag cements," *Adv. Cem. Res.*, vol. 15, no. 3, pp. 129–136, 2003.
- [169] Y. Yin *et al.*, "FT-IR and micro-Raman spectroscopic characterization of minerals in high-calcium coal ashes," *J. Energy Inst.*, vol. 91, no. 3, pp. 389–396, 2018.
- [170] A. G. Xyla and G. Koutsoukos, "Quantitative Analysis of Calcium Carbonate Polymorphs by Infrared Spectroscopy," *J. Chem. Soc. Faraday Trans.*, vol. 85, no. 10, pp. 3165–3172, 1989.
- [171] D. Chakrabarty, S. I. Kuriyavar, R. Vetrivel, S. G. Hegde, S. Mahapatra, and A. V. Ramaswamy, "Insights into the formation of hydroxyl ions in calcium carbonate: temperature dependent FTIR and molecular modelling studies," *J. Mater. Chem.*, vol. 10, no. 8, pp. 1835–1840, 2002.
- [172] J. P. Cain, P. L. Gassman, H. Wang, and A. Laskin, "Micro-FTIR study of soot chemical composition - Evidence of aliphatic hydrocarbons on nascent soot surfaces," *Phys. Chem. Chem. Phys.*, vol. 12, no. 20, pp. 5206–5218, 2010.
- [173] J. Björnström, A. Martinelli, A. Matic, L. Börjesson, and I. Panas, "Accelerating effects of colloidal nano-silica for beneficial calcium-silicate-hydrate formation in cement," *Chem. Phys. Lett.*, vol. 392, no. 1–3, pp. 242–248, 2004.
- [174] H. Ishida, K. Sasaki, and T. Mitsuda, "Highly Reactive β -Dicalcium Silicate: I, Hydration Behavior at Room Temperature," *J. Am. Ceram. Soc.*, vol. 75, no. 2, pp. 353–358, 1992.
- [175] K. Fujii and W. Kondo, "Rate and Mechanism of Hydration of B-C2S," *J. Am. Ceram. Soc.*, vol. 161, no. 3, pp. 161–167, 1979.
- [176] V. Morales-Flórez, A. Santos, I. Romero-Hermida, and L. Esquivias, "Hydration and carbonation reactions of calcium oxide by weathering: Kinetics and changes in the nanostructure," *Chem. Eng. J.*, vol. 265, pp. 194–200, 2015.
- [177] K. L. Scrivener, P. Juilland, and P. J. M. Monteiro, "Advances in understanding hydration of Portland cement," *Cem. Concr. Res.*, vol. 78, no. JUNE, pp. 38–56, 2015.
- [178] T. Kawahara, A. Yuuki, and Y. Matsui, "Reaction Mechanism of Chemical Vapor Deposition Using Tetraethylorthosilicate and Ozone at Atmospheric Pressure," *Jpn. J. Appl. Phys.*, vol. 31, no. 9 R, pp. 2925–2930, 1992.
- [179] K. Cho, H. Chang, J. H. Park, B. G. Kim, and H. D. Jang, "Effect of molar ratio of TiO₂/SiO₂ on the properties of particles synthesized by flame spray pyrolysis," *J. Ind. Eng. Chem.*, vol. 14, no. 6, pp.

860–863, 2008.

- [180] P.-T. F *et al.*, “Silica with 3D Mesocellular Pore Structure Used as Support for Cobalt Fischer-Tropsch Catalyst,” *Synth. Catal. Open Access*, vol. 02, no. 03, pp. 15–19, 2017.
- [181] H. Torabmostaedi, T. Zhang, P. Foot, S. Dembele, and C. Fernandez, “Process control for the synthesis of ZrO₂ nanoparticles using FSP at high production rate,” *Powder Technol.*, vol. 246, pp. 419–433, 2013.
- [182] C. Ettarh, “A kinetic and mechanistic study of the thermal decomposition of calcium nitrate,” *Thermochim. Acta*, vol. 288, pp. 203–219, 1996.
- [183] M. G. M. VAN DER VIS, E. H. P. CORDFUNKE, and R. J. M. KONINGS, “The thermodynamic properties of tetraethoxysilane (TEOS) and an infrared study of its thermal decomposition,” *Le J. Phys. IV*, vol. 03, no. C3, pp. C3-75-C3-82, 1993.
- [184] B. Delperier, C. Vinante, and R. Morancho, “Analysis and modelling of tetraethoxysilane pyrolysis,” *J. Anal. Appl. Pyrolysis*, vol. 13, no. 1–2, pp. 141–149, 1988.
- [185] F. Fracassi, “Plasma-Enhanced Chemical Vapor Deposition of Organosilicon Thin Films from Tetraethoxysilane-Oxygen Feeds,” *J. Electrochem. Soc.*, vol. 139, no. 9, p. 2636, 2006.
- [186] C. A. O’Connell and D. Dollimore, “A study of the decomposition of calcium propionate, using simultaneous TG-DTA,” *Thermochim. Acta*, vol. 357–358, pp. 79–87, 2000.